

# DSE - UAV Cargo Delivery System

*Group 3 - Delft, The Netherlands*

Derek Beeftink	4012291	Roderik Oude Ophuis	1507559
Mika Bots	4011007	Martijn Potuijt	4013840
Dion Hordijk	4081307	Menco Schuurman	4103076
Thomas Koopman	4017412	Daan Smit	1536494
Heleen Middel	4003721	Lubi Spranger	4124359



Final Report  
AE3200 Design Synthesis Exercise



# Preface

Four years after the 7.0-magnitude earthquake in Haiti, there are still approximately 170,000 people living in makeshift tents [1]. Sanitation is poor, with almost no access to drinking water, toilets, and waste disposal. Natural disasters such as the Haiti earthquake leave its victims in dire conditions. To offer a solution to the poor housing conditions, a cargo delivery unmanned aerial vehicle (UAV) has been designed. The UAV carries a cargo package of half a ton in weight which transforms into an expandable modular house unit, covering more than the basic needs of three people. The cargo is delivered with a parachute system and cushioned with an airbag to ensure its safe delivery. Due to its compact size, the UAV can be transported to the international airport closest to the natural disaster zone. The UAV can operate over a range of 2,000 *km* and is able to deliver at least two cargo packages per day over the maximum range. The housing unit is equipped with a solar system, generating sufficient energy to power all electronic systems inside, including a small fridge, cooking plates, and lighting. Designed as a permanent living space for at least 10 years, the house offers a flexible and comfortable housing solution to the victims of any natural disaster.

Group three of the fall DSE 2013 would like to thank Dr. M.J. Martinez as the head coordinator of the project and the coaches D.M.J. Peeters and N.B. dos Santos for their enthusiasm, consistent support, and guidance. Furthermore, the group would like to thank all the staff members of the faculty of Aerospace Engineering who helped with their valuable input and spend their time to support the design process.

# Contents

<b>1</b>	<b>Introduction</b>	<b>1</b>
<b>I</b>	<b>Systems engineering</b>	<b>3</b>
<b>2</b>	<b>Project organisation</b>	<b>4</b>
2.1	Gantt Chart . . . . .	4
2.2	Compliance matrix . . . . .	4
2.3	Human resource budgeting . . . . .	5
<b>3</b>	<b>Market analysis</b>	<b>6</b>
3.1	SWOT analysis . . . . .	6
3.2	UAV market segment . . . . .	8
3.3	Air cargo market . . . . .	8
3.4	Demand in case of disasters . . . . .	8
3.5	UAVs with comparable cargo capabilities . . . . .	8
3.6	Stakeholders . . . . .	9
3.7	Delivery system . . . . .	9
3.8	Development on the market . . . . .	10
3.9	Permanent shelter . . . . .	10
<b>4</b>	<b>Mission analysis</b>	<b>10</b>
4.1	Mission outline . . . . .	10
4.2	Functional flow diagram . . . . .	12
4.3	Functional breakdown structure . . . . .	12
4.4	Operations and logistics . . . . .	12
<b>II</b>	<b>Conceptual design phase</b>	<b>14</b>
<b>5</b>	<b>Preliminary analysis</b>	<b>15</b>
5.1	Environmental and geographical analysis . . . . .	15
5.2	Sustainable development strategy . . . . .	16
<b>6</b>	<b>UAV concepts</b>	<b>18</b>
6.1	Concept 1: Airship . . . . .	18
6.2	Concept 2: Tiltrotor . . . . .	19
6.3	Concept 3: Fixed wing . . . . .	20
6.4	Trade-off . . . . .	22
<b>7</b>	<b>Conceptual design cargo</b>	<b>22</b>
7.1	Housing concept 1: Foldable cabin design . . . . .	22
7.2	Housing concept 2: Modular cabin design . . . . .	23
7.3	Housing concept 3: Permanent tent design . . . . .	23
7.4	Housing trade-off . . . . .	24
7.5	Subsystems . . . . .	24
<b>8</b>	<b>Delivery system concepts</b>	<b>25</b>
<b>III</b>	<b>Detailed design UAV</b>	<b>27</b>
<b>9</b>	<b>Detailed design input</b>	<b>28</b>

<b>10 Weight estimation</b>	<b>28</b>
10.1 Methodology . . . . .	28
10.2 Class I weight estimation . . . . .	29
10.3 Preliminary layout . . . . .	30
10.4 Class II weight estimation . . . . .	30
10.5 Results of the weight estimation . . . . .	32
10.6 Discussion of the weight estimation . . . . .	32
10.7 Balance . . . . .	33
<b>11 Aerodynamics</b>	<b>34</b>
11.1 Wing parameters . . . . .	34
11.2 Tail design . . . . .	36
11.3 Aerofoil selection . . . . .	37
11.4 High lift devices . . . . .	39
11.5 Aerodynamic simulation . . . . .	40
11.6 Take-off and landing distances . . . . .	41
11.7 Sensitivity study . . . . .	42
11.8 Recommendations . . . . .	43
<b>12 Propulsion analysis</b>	<b>43</b>
12.1 Engines . . . . .	43
12.2 Fuel type . . . . .	46
12.3 Engine selection . . . . .	46
12.4 Propeller design . . . . .	48
12.5 Verification . . . . .	49
12.6 Conclusion . . . . .	49
<b>13 Structural and material analysis</b>	<b>50</b>
13.1 Reference frames . . . . .	50
13.2 Assumptions . . . . .	50
13.3 Dimensions . . . . .	51
13.4 Load cases . . . . .	52
13.5 Failure modes . . . . .	52
13.6 Material properties . . . . .	52
13.7 Applied theory . . . . .	52
13.8 Analytical tool . . . . .	55
13.9 Analytical results . . . . .	55
13.10Sensitivity study . . . . .	58
13.11Structural analysis - finite element analysis . . . . .	58
13.12Landing gear . . . . .	64
13.13Wing mounting . . . . .	66
13.14Cargo drop system . . . . .	66
<b>14 Stability and control</b>	<b>66</b>
14.1 Tail sizing . . . . .	67
14.2 Elevator sizing . . . . .	69
14.3 Aileron sizing . . . . .	70
14.4 Determining the coefficients of the state-space system . . . . .	71
14.5 Longitudinal stability during cruise . . . . .	72
14.6 Longitudinal stability during cargo drop . . . . .	74
14.7 Verification of the program . . . . .	75
14.8 Recommendations . . . . .	76
<b>15 Performance analysis</b>	<b>76</b>
15.1 Maximum load factor . . . . .	76
15.2 Standard rate turns . . . . .	76
15.3 Climbing performance . . . . .	77

<b>16 Avionics</b>	<b>77</b>
16.1 Requirements analysis . . . . .	78
16.2 System selection & overview . . . . .	78
16.3 Component selection . . . . .	79
16.4 Landing gear actuator . . . . .	83
16.5 Fuel pump . . . . .	83
16.6 Reliability . . . . .	83
16.7 Interfaces and system layout . . . . .	84
16.8 Triple redundant autopilot layout . . . . .	85
16.9 Power budget . . . . .	85
16.10Electrical circuit . . . . .	86
16.11System placement . . . . .	86
16.12Conclusions . . . . .	86
16.13Recommendations . . . . .	87
<b>17 Final configuration</b>	<b>87</b>
17.1 External configuration . . . . .	87
17.2 Internal configuration . . . . .	88
<b>IV Detailed design cargo delivery system</b>	<b>90</b>
<b>18 Cargo delivery system</b>	<b>91</b>
18.1 Drop-off method . . . . .	91
18.2 Trajectory determination . . . . .	91
18.3 Impact attenuation design . . . . .	92
18.4 Landing precision . . . . .	93
18.5 Verification & validation . . . . .	94
18.6 Conclusion & recommendations . . . . .	94
<b>V Detailed design cargo</b>	<b>96</b>
<b>19 Wind loading</b>	<b>97</b>
19.1 Frictional effects . . . . .	97
19.2 Design wind speed and design pressure . . . . .	97
19.3 Wind loading . . . . .	98
<b>20 Housing - Structural analysis</b>	<b>98</b>
20.1 Model . . . . .	99
20.2 Modeled wind loading . . . . .	99
20.3 Design optimisation . . . . .	99
20.4 Wind loading results . . . . .	99
20.5 Wind loading verification . . . . .	100
20.6 Conclusion . . . . .	100
<b>21 Housing - Detailed design</b>	<b>100</b>
21.1 Floor panels . . . . .	101
21.2 Anchors . . . . .	101
21.3 Wooden columns . . . . .	101
21.4 Bolting . . . . .	102
21.5 Wall panels . . . . .	102
21.6 Wooden beams . . . . .	103
21.7 Roof panels . . . . .	103
<b>22 Subsystems</b>	<b>104</b>
22.1 Power supply . . . . .	104
22.2 Water treatment . . . . .	106
22.3 Interior . . . . .	106
22.4 Emergency supplies . . . . .	107

<b>23 Weight and cost estimation</b>	<b>107</b>
23.1 Weight estimation . . . . .	107
23.2 Cost estimation . . . . .	107
23.3 Packaging . . . . .	107
<b>VI Final design considerations</b>	<b>109</b>
<b>24 Technical risk assessment</b>	<b>110</b>
24.1 Categories of risk . . . . .	110
24.2 Events . . . . .	110
24.3 Conclusions and design guidelines . . . . .	111
<b>25 Project design &amp; development logic</b>	<b>111</b>
<b>26 Production plan</b>	<b>112</b>
26.1 Production . . . . .	112
26.2 Integration and assembly . . . . .	112
26.3 Lean manufacturing . . . . .	113
<b>27 Costs</b>	<b>115</b>
<b>28 Conclusion</b>	<b>116</b>
<b>VII Appendices</b>	<b>117</b>
<b>A Functional flow diagrams and functional breakdown structure</b>	<b>118</b>
<b>B Structural analysis input and output</b>	<b>121</b>
<b>C Equations of motion parachute</b>	<b>122</b>
<b>D Landing precision</b>	<b>123</b>
<b>E Numerical values used for the areodynamic analysis</b>	<b>124</b>
<b>F Values of stability and control coefficients</b>	<b>125</b>
<b>G Avionics system components</b>	<b>126</b>
<b>H Layout of the electrical power system</b>	<b>127</b>
<b>I Layout of the triple redundant autopilot</b>	<b>128</b>
<b>J Layout of the entire avionics system</b>	<b>129</b>
<b>K Flowcharts operations &amp; logistics</b>	<b>130</b>
<b>L Gantt charts</b>	<b>132</b>

# List of Figures

2.1	Hours worked per person per week during the detailed design phase of the project	5
2.2	Hours worked per person per task during the detailed design phase of the project	6
3.1	The three leading airdrop systems	9
4.1	The mission profile for the cargo delivery with a loitering phase at the disaster site and the home base international airport.	11
4.2	Examples of transportation options for rail, road, water (left) commercial air transport (middle) and transportation as done by the department of defence (DOD) (right)	13
5.1	Climate graph Haiti (altitude 41 m)	15
6.1	Rendering of a simplified airship	18
6.2	Rendering of the tiltrotor concept	19
6.3	Rendering of the fixed wing concept	20
6.4	Loading diagram for the UAV to be designed (using propellers)	21
7.1	A visualisation of the foldable cabin design	23
7.2	A visualisation of the modular cabin design	23
7.3	A visualisation of the permanent tent design	24
10.1	Design methodology to estimate the weight and layout of the aeroplane	29
10.2	Top view of the UAV with the CG locations of all the components	34
11.1	Wing loading diagram	35
11.2	The aerofoils used for the horizontal and vertical tailplane of the UAV [2]	37
11.3	Visualisation of the NLF(1) – 0416 aerofoil used for the wing [2]	38
11.4	Overall wing layout with lift and drag distributions generated by XFLR5	39
11.5	Change in lift coefficient and angle of attack for the drop/worst case landing and the take-off scenario	40
12.1	Graphical representation of the longitudinal cross section and workings of a piston engine	43
12.2	Graphical representation of the longitudinal cross section of a double spool turboprop engine [3]	44
12.3	Graphical representation of the longitudinal cross section of a single spool propfan engine [3]	45
12.4	Lifecycle emissions from fossil fuels and biofuels [4]	46
12.5	Front- and side-view of the selected M250-B17F model	47
12.6	Plot of the total engine thrust and accompanying propeller thrust of the final engine	47
12.7	Plot of the ideal disk power for varying surface area	49
13.1	Reference frames wing	50
13.2	Reference frames fuselage	50
13.3	Derivation of wingbox dimensions from aerofoil dimensions	51
13.4	Non-idealised and idealised cross-section	53
13.5	The lift distribution along the wing span and the (negative) shear force distribution caused by the weight of the fuel	53
13.6	Shear and moment diagram for fuselage	54
13.7	Plots on chord length, force distribution, moments and moment of inertia along span length	56
13.8	Bending-, shear-, torsion and von Mises stress of the wingbox for the highest load case	57
13.9	Von Mises stress for fuselage during cruise conditions	58
13.10	Discretisation of a circle	59
13.11	Shape deformation of elements under an applied bending moment with visible shear locking in (B) and hour-glassing in (C)	60
13.12	FEM model of a loaded beam and thin plate	62
13.13	Skeleton view of the final model	63
13.14	FEM models with the final results	64
13.15	FEM model displaying the cross sectional view of the final stress in the wingbox	64
13.16	Top view of the UAV with the cg. locations of all the components	65
13.17	Illustration of the wing mounting principle	66
13.18	Rail system for the cargo drop system	66
14.1	Three different types of stability	67
14.2	Free body diagram of UAV including neutral point	68
14.3	X-plot, indicating the stability and controllability lines	68
14.4	Tail loads during various conditions	69
14.5	Pitch moment coefficients for different groups of the UAV, elevator deflection is zero here	70
14.6	Response of the aircraft to a $10^\circ$ step input to the elevator	73
14.7	Eigenvalues of the phugoid during the drop	74
14.8	Eigenvalues of the short period motion during the drop	74
16.1	The working principle of a dual-redundant EHA	82
16.2	The recommended type of USB connector	84
17.1	Illustration of the external configuration	87
17.2	Illustration of the internal configuration	89

18.1	The two motions of the delivery system: the swinging motion (1), and the falling motion (2) . . . . .	91
19.1	Near ground surface frictional effects on the wind speed . . . . .	97
19.2	External pressure coefficients for walls of rectangular buildings. h is the height, l is the greater horizontal dimension and w is the lesser horizontal dimension of the building [5] . . . . .	98
19.3	Values of the force coefficient versus a/b for h/b <1 . . . . .	98
20.1	a: Model of the modular cabin design created in Visual Analysis 11; b: Result view of the critical 0 degrees wind, negative internal pressure loading case. The dotted lines indicate the unloaded model . . . . .	99
21.1	a: The entire floor made out of 7 panels. b: The tongue and groove connection between different floor panels. c: Grooves and holes in the floor panels for the anchors, columns and wall panels to slide into . . . . .	101
21.2	a: Anchor with general dimensions. b: Anchor precisely fitted into the hole in the floor panel. c: The 70 cm pins will ensure a fixed connection to the ground . . . . .	101
21.3	a: Standard column. b: Corner column. c: Door column left. d: Door column right . . . . .	101
21.4	a: Bolted connection between the column, floor panel and anchor. b: Load distribution in the bolted connection. c: Shear flow in wooden column due to bolting . . . . .	102
21.5	a: Standard wall panel. b: Window panel. c: Door panel. d: Wall panels fitted into the grooves in the columns . . . . .	103
21.6	a: Bottom door beam. b: Standard beam. c: Corner beam 1. d: Corner beam 2. e: Top door beam. f: Top window beam. g: Roof beam . . . . .	103
21.7	a: Steel connection at the long side of the building. b: Steel corner connection. c: Steel connection at the small side of the building . . . . .	103
21.8	a: Watertight aluminium roof profile. b: Watertight aluminium roof end profile. c: Roof panels slid into the profiles . . . . .	104
21.9	Final empty design of the permanent house . . . . .	104
22.1	Schematic view of the solar home system . . . . .	105
22.2	The Hydrad biosand water filter [6] . . . . .	106
22.3	Interior design of the housing unit . . . . .	107
23.1	a: Smallest pile of all the housing parts. b: The final transport package . . . . .	108
25.1	Schematic representation of the project design and development logic . . . . .	112
26.1	Production plan for the assembly of the UAV. . . . .	114
A.1	Functional flow diagram for the complete operation of the UAV, part 1 . . . . .	118
A.2	Functional flow diagram for the complete operation of the UAV, part 2 . . . . .	119
A.4	Functional breakdown structure for the essential parts of the UAV operation . . . . .	120
A.3	Functional flow diagram for the operation of the cargo unit . . . . .	120
B.1	Structural analysis tool input and output . . . . .	121
C.1	The free-body diagram for the combined cargo-parachute system . . . . .	122
G.1	List of all avionics system components. The datasheets corresponding to the components are found in the bibliography. They are linked to the component id in the following list: 1: [7], 2: [8], 5: [9], 6: [10], 7: [11], 8: [12], 9: [13], 10: [14], 11: [15], 12: [16], 13: [17], 14 [18], 16 [19], 17 [20], 18 [21], 19 [22], 20 [23], 21 [24], 22, 23, 24, 25: [25], 26 [26], 33 [27], 35 [28], 36 [29], 37 [30], 39 [31]. . . . .	126
H.1	The layout of the electrical power system . . . . .	127
I.1	The layout of the triple redundant autopilot . . . . .	128
J.1	The layout of the entire avionics system . . . . .	129
K.1	Operations & logistics flowcharts . . . . .	130
K.2	Operations & logistics flowcharts . . . . .	131
L.1	Gantt chart of the DSE project from the mid-term report up until the symposium . . . . .	132

## List of Tables

2.1	Compliance matrix for both the UAV and the cargo unit . . . . .	5
3.1	The SWOT analysis performed for the UAV cargo delivery system . . . . .	7
4.1	Design inputs for UAV . . . . .	10
4.2	The allocated times for different processes to be performed during the mission . . . . .	11
6.1	Final tiltrotor concept design parameters . . . . .	19
6.2	Results of the class I weight estimation for both the propeller and the jet aircraft . . . . .	20
6.3	Aerodynamic conceptual parameters . . . . .	21
6.4	Mission requirements feasibility for the concepts . . . . .	22
7.1	Trade-off table for the housing concepts . . . . .	25
10.1	Constants used to calculate the landing gear weights . . . . .	31
10.2	Final results of the weight estimation . . . . .	32
10.3	Comparison between component and group weights of the design and reference long-haul turboprop cargo aeroplanes . . . . .	32
10.4	CG locations of the different components . . . . .	33
11.1	Wing loading comparison with reference aircraft . . . . .	35

11.2	$C_{D_0}$ components for different parts of the UAV	41
11.3	Take-off distance for a few aeroplanes of comparable size as the UAV designed	42
12.1	Engine specification	45
12.2	Selected engine versus similar engines	48
12.3	Results of Javaprop and Equation 12.4 combined	49
12.4	Engine values before and after final engine and propeller choice	50
13.1	Material properties aluminium 7075-T6 [32]	52
13.2	Final design considerations wingbox	55
13.3	Analytical results wingbox	56
13.4	Final design considerations fuselage	57
13.5	Results comparison for sensitivity study	58
13.6	Solid wingbox model stress evaluation	62
13.7	Solid wingbox displacement evaluation	62
13.8	Thin plate stress evaluation	63
13.9	Thin plate displacement evaluation	63
13.10	Analytical and FEM simulation end result comparison	63
14.1	Longitudinal stability characteristics of the UAV for the phugoid and short period motion	73
14.2	Damping factors calculated analytically and numerically	75
14.3	Damping ratios calculated using Matlab and those in the reader for the Flight Dynamics course (AE3202)	75
15.1	Variables used in determining the maximum load factor	77
15.2	Variables used in determining the maximum load factor	77
15.3	Variables used in determining the maximum load factor	78
16.1	UAV radio transmission and reception systems	80
16.2	LOS link budget	80
16.3	Comparison of three different actuation systems	82
16.4	Control surface actuators power estimation	83
16.5	Avionic system reliability measures	84
16.6	Power budget estimations	85
16.7	Emergency descent power requirement assumptions	86
17.1	Specification and description "Aidplane"	88
18.1	Errors in the modelled terminal velocities with respect to the numerical values	94
18.2	Characteristics of reference PLADS missions [33] [34], the designed mission of this project is displayed in bold numbers	94
20.1	Extreme force, moment and stress results for the four wind loading cases: 0 and 90 degrees wind and positive [+] and negative [-] internal pressure	100
22.1	Required energy for different appliances	104
23.1	Weight and cost of different parts of the housing design	108
24.1	Identified technical risks	111
27.1	Cost breakdown structure for the housing unit and UAV	115
E.1	Numerical values used for the aerodynamic analysis	124
F.1	Values of stability and control coefficients influencing the resulting force in X-direction during cruise	125

# List of symbols

Symbols	Description	Symbols	Description
$A$	Surface area	$DoD$	Depth of discharge
$A_e$	Effective frontal area	$E$	Modulus of elasticity
$A_{sec}$	Section area	$F_n$	Wind load
$AF$	Activity factor	$F_{tot}$	Total wind load
$AR$	Aspect ratio	$G$	Gain
$B$	Boom area	$I$	Moment of inertia
$B$	Tire width	$K$	Constant factor
$C$	Battery capacity	$L$	Lift
$C_d$	Drag coefficient	$L/D$	Aerodynamic efficiency
$C_f$	Force coefficient	$L_s$	Free space loss
$C_L$	Lift coefficient	$M$	Moment
$C_{m_0}$	Coefficient of moment around Y-axis during steady flight	$M$	Mach number
$C_{m_\alpha}$	Relation between moment around Y-axis and angle of attack	$N$	Blade speed
$C_{m_{\dot{\alpha}}}$	Relation between moment around Y-axis and angular acceleration	$P$	Power
$C_{m_{\delta_e}}$	Relation between moment around Y-axis and elevator angle	$R$	Radius
$C_{m_q}$	Relation between moment around Y-axis and pitch acceleration	$R$	Range
$C_{m_u}$	Relation between moment around Y-axis and horizontal speed	$RC$	Rate of climb
$C_p$	External pressure coefficient	$Re$	Reynolds number
$C_p$	Specific fuel consumption	$S$	Surface area
$C_{X_\alpha}$	Relation between forces in X-direction and angle of attack	$T$	Thrust
$C_{X_{\dot{\alpha}}}$	Relation between forces in X-direction and angular acceleration	$T$	Torque
$C_{X_{\delta_e}}$	Relation between forces in X-direction and elevator angle	$V$	Shear force
$C_{X_0}$	Coefficient of forces in X-direction during steady flight	$V$	Velocity
$C_{X_q}$	Relation between forces in X-direction and pitch angle	$V_D$	Design wind speed
$C_{X_u}$	Relation between forces in X-direction and horizontal speed	$V_Z$	Real wind speed
$C_{Z_0}$	Coefficient of forces in Z-direction during steady flight	$W$	Weight
$C_{Z_\alpha}$	Relation between forces in Z-direction and angle of attack	$W/P$	Power loading
$C_{Z_{\dot{\alpha}}}$	Relation between forces in Z-direction and angular acceleration	$W/S$	Wing loading
$C_{Z_{\delta_e}}$	Relation between forces in Z-direction and elevator angle	$Z$	Height
$C_{Z_q}$	Relation between forces in Z-direction and pitch angle	$Z_G$	Gradient height
$C_{Z_u}$	Relation between forces in Z-direction and horizontal speed		
$D$	Tire diameter		

Symbols	Description	Symbols	Description
$b$	Wing span	$\Gamma_0$	Circulation
$c$	Chord length	$\Lambda$	Sweep angle
$c_r$	Root chord	$\alpha$	Angle of attack
$c_t$	Tip chord	$\alpha$	Mean speed component
$f$	Frequency	$\beta$	Side slip angle
$g$	Gravitational acceleration	$\gamma$	Flight path angle
$h$	Altitude	$\delta$	Deflection
$l$	Length	$\zeta$	Damping ratio
$m$	Mass	$\eta$	Efficiency
$\dot{m}$	Mass flow	$\eta$	Imaginary part of the eigenvalue
$n_{ult}$	Ultimate load factor	$\theta$	Pitch angle
$p$	Angle of roll	$\lambda$	Eigenvalue
$p_D$	Design wind pressure	$\lambda$	Wavelength
$p_Z$	Wind pressure at any height	$\mu$	Dynamic viscosity
$q$	Dynamic pressure	$\xi$	Real part of the eigenvalue
$q$	Pitch rate	$\rho$	density
$q$	Shear flow	$\sigma$	Bending stress
$r$	Angle of yaw	$\tau$	Shear stress
$r$	Transmission distance	$\varphi$	Bank angle
$s$	Deceleration stroke	$\omega$	Natural frequency
$t$	Thickness		
$t$	Time		
$u$	Horizontal airspeed		

# List of abbreviations

<b>Abb.</b>	<b>Description</b>	<b>Abb.</b>	<b>Description</b>
ABS	Acrylonitrile-Butadiene-Styrene	LAPES	Low Altitude Parachute Extraction System
ADS	Automatic Dependent Surveillance	LE	Leading Edge
AR	Aspect Ratio	LOS	Line of Sight
ARP	Aerospace Recommended Practice	MAC	Mean Aerodynamic Chord
ATC	Air Traffic Control	MIL-STD	Military-Standard
BER	Bit Error Rate	MSF	Médecins Sans Frontières
CAN	Controller Area Network	MTOW	Maximum Take-Off Weight
CFD	Computational Fluid Dynamics	NACA	National Advisory Committee for Aeronautics
CG	Center of Gravity	NLF	Natural Laminar Flow
DB	Drop-off Base	OCHA	Office Coordination of Humanitarian Affairs
DC	Direct Current	OEW	Operating Empty Weight
DVI	Digital Visual Interface	PLADS	Parachute Low Altitude Delivery System
EASA	European Aviation Safety Agency	PVC	Polyvinyl Chloride
EH	Electrohydraulic Actuators	PVF	Polyvinylfluoride
EHA	Electrohydrostatic Actuators	SAE	Society of Automotive Engineers
EMA	Electromechanical Actuators	SATCOM	Satellite Communication Link
EOM	Equations of Motion	SMAD	Space Mission Analysis and Design
FAA	Federal Aviation Authority	SPI	Serial Peripheral Interface
FBS	Functional Breakdown Structure	SWOT	Strengths, Weaknesses, Opportunities, Threats
FEM	Finite Element Method	TBO	Time Between Overhaul
FFD	Functional Flow Diagram	TCAS	Traffic Alert and Collision Avoidance System
GCS	Ground Control Station	TCAS	Traffic Alert and Collision Avoidance System
GPIO	General Purpose Input/Output	TOP	Take-Off Parameter
GPS	Global Positioning System	TU	Technical University
HB	Home Base	UART	Universal Asynchronous Receiver/Transmitter
HLD	High Lift Devices	UAV	Unmanned Aerial Vehicle
IFR	Instrument Flight Rules	ULD	Unit Load Devices
IFRC	International Federation Red Cross	UN	United Nations
IMU	Inertial Measurement Unit	US	United States
ISM	Industrial Scientific Medical	USB	Universal Serial Bus
JPADS	Joint Precision Airdrop System	VTOL	Vertical Take-Off and Landing
		WVI	World Vision International

# 1 | Introduction

One of the five worst disasters in 2013 was Typhoon Haiyan with 14.1 million people affected and at least 4.1 million people displaced [35] [36]. The 560 *km*-wide typhoon with gusts reaching up to 380 *km/h* destroyed large parts of the City of Tacloban [37]. Tacloban is the capital and most densely populated area of the Region of Eastern Visayas, approximately 580 *km* southeast of the capital of the Philippines, Manila. However, not only the Philippines were struck by disaster in the last year; also, Typhoon Phailin- the strongest cyclone to hit India in 14 years- affected more than 13 million people. Another large-scale disaster were the two hurricanes Manuel and Ingrid in Mexico in September with more than 200,000 people affected by widespread flooding and landslides.

What all these disasters have in common are the severe consequences on the lives of the people affected: the people are left without shelter, cut off from traffic and without access to food or equipment. Furthermore, the disasters occurred in areas unequipped to support all the people affected due to the lack of well-established relief organisations.

To be able to save the lives of the people left helpless after a natural disaster strikes, it is immensely important to have the mobility to provide help in the form of food and shelter to the victims from overseas. Especially the fast, well-organised and efficient distribution to immediately cover their basic needs is important. Next to providing elementary help, it becomes increasingly important to provide the people with a permanent solution in term of housing and sustainability on the long-run.

Relief organisations such as the International Federation of Red Cross and Red Crescent Societies (IFRC) or bodies such as the United Nations Office for the Coordination of Humanitarian Affairs (OCHA) already coordinate and actively provide support to victims of natural disasters over the globe. Help services and packages are often transported by large military aircraft such as the Lockheed C-130. However, these aircraft need a long time for loading and a crew of at least three people.

To be able to optimally distribute permanent shelter to the victims of natural disasters, an unmanned aerial vehicle (UAV) is an optimal solution, since it can operate continuously. Especially fast, small and flexible aircraft are desired, able to operate non-stop. These cargo UAVs could be transported to the nearest international airport to the disaster zone and from there continuously fly emergency relief missions.

This report presents the design of a cargo transportation UAV able to carry a 500 *kg* payload. This load was optimised to transform into a modular house unit for three people upon delivery, containing all required systems to be used for more than 10 years.

The UAV is designed similar to a conventional fixed-wing aircraft with a single propeller and a specially designed cargo release parachute system. The cargo unit provides a unique solution to the permanent housing problem, since its modular design allows for units to be joined into bigger community buildings and be expanded.

**Mission Need Statement:** To perform an automated, sustainable and economical delivery of a multifunctional cargo system that provides humanitarian aid and permanent housing for three people using an Unmanned Aerial Vehicle Cargo Delivery System. The UAV system has been designed to take off from an international airport in the Dominican Republic while capable of flying to a disaster zone in neighbouring Haiti.

**Project Objective Statement:** Design an automated UAV system in combination with a a modular, multifunctional cargo system that provides humanitarian aid in the Haiti disaster zone. Ten students from Delft University of Technology Faculty of Aerospace Engineering took on the design challenge during a ten week project.

The main requirements for the UAV are:

- Each UAV has to be able to deliver at least two cargo units per day.
- The UAV should be able to operate past line of sight.
- The mission range set by the client was set to 2,000 *km*.
- The UAV is designed to take off from an international airport runway (Punta Cana International Airport).
- The UAV has to be able to be transported by a Lockheed C-130 Hercules.
- The minimum production series is 200 UAVs, each with corresponding replaceable cargo containers.

The main requirements for the cargo are:

- The cargo delivery unit has a weight of 500 *kg*.

- The cargo has to be able to be assembled into a permanent (>10 years) house for three people.
- The cargo needs to be equipped with basic survival equipment as well as all the systems required for the permanent stay of three people.
- The cargo container needs to be dropped off with a precision of 50 m.

The objective of this Final Design Report is to provide information on the detailed design of the UAV cargo delivery system. The design itself has been done by a group of ten Aerospace Engineering students over ten weeks as a collective final bachelor thesis, called the Design Synthesis Exercise (DSE).

This section gives an overview of the structure of the report. The report is divided into 7 parts enumerated in Roman numerals. Following up from the introduction in Chapter 1, part *I* contains the systems engineering aspects of the project. Chapter 2 gives an overview of the project organisation, Chapter 3 presents the market analysis that has been carried out during the initial phase of the project and Chapter 4 contains the mission analysis.

Part *II* contains information on the conceptual design phase. Chapter 5 presents the preliminary analysis, Chapter 6 the UAV concepts during this phase, Chapter 7 deals with the conceptual design of the cargo and Chapter 8 gives information on the delivery system concepts.

Part *III* of the report contains information on the detailed design of the UAV. Chapter 9 gives an overview of the design input to the detailed design phase of the UAV. Chapter 10 presents the weight estimation, Chapter 11 contains information on the aerodynamic analysis and Chapter 12 deals with the propulsion analysis. Chapter 13 presents the structural and material analysis, Chapter 14 deals with the stability and control aspects of the detailed design and Chapter 15 presents the performance analysis. Chapter 16 goes into detail about the avionics systems on board of the aircraft and Chapter 17 presents the final configuration.

Part *IV* of the report contains the detailed design of the cargo delivery system with Chapter 18 describing all the design aspects involved.

Part *V* deals with the detailed design of the cargo. Chapter 19 contains information on the most critical loading for the house unit, wind loading. Chapter 20 contains the structural analysis of the house, Chapter 21 deals with the detailed design of the house, Chapter 22 presents all its subsystems and Chapter 23 presents the weight and cost estimation.

Part *VI* gives an overview of the final design considerations. Chapter 24 contains the technical risk assessment, Chapter 25 presents the project design & development logic and Chapter 26 contains the production plan. Chapter 27 gives an overview of the costs involved and Chapter 28 contains an overall conclusion.

Finally, part *VII* contains appendices with additional information about the UAV cargo delivery system design and are referred to throughout the report.

Part I

Systems engineering

## 2 | Project organisation

This chapter comments on the planning, fulfilment of requirements and group organisation. The used planning is displayed in Section 2.1 by means of a Gantt chart. The compliance matrix shows whether or not the requirements have been met and by what means. Section 2.3 shows which person worked on what parts in the report, it also shows how many hours every person worked on a weekly basis.

### 2.1 Gantt Chart

One of the most important aspects of project management is to keep track of the performed activities and the upcoming events. This full overview is realised using a Gantt chart, which is a graphical representation of the project schedule. By making an initial estimation of the time needed for every task and phase, the chairman has an effective tool to monitor the progress of the project. The project is divided into five different phases, containing three milestones; the baseline, mid-term, final report, and the symposium. These milestones are indicated by the diamond shaped indicators in the Gantt chart.

The work planned for every sub-task of the design phases also takes the writing effort into account. Therefore, there is no separate task allocated for writing. Since the mid-term and final report are extensive and the quality of the reports is important, dedicated tasks are created for the evaluation of the reports. In the planning of the project, overtime hours are taken into account. Every team-member is aware of the fact that an effort rate of 140% may be required to avoid any delay during the critical parts of the project. Towards the final report, this 140% proved to be needed, but sufficient to finish every task in time.

The Gantt chart of the detailed phase of the project can be found in the Appendix, in Figure L.1. The hours used per task are indicated in the first column of the Gantt chart.

### 2.2 Compliance matrix

At the start of this design project a number of requirements were formulated by the client. Requirements were set for both the UAV and the cargo unit. This section will discuss, by means of presenting a compliance matrix, the way in which, or to what extent these requirements have been met for the successful completion of this mission. Furthermore, it is stated in which chapter the information can be found. The compliance matrix can be found in Table 2.1.

From this compliance matrix, one can conclude that the cargo UAV delivery mission can be performed within the constraints and requirements imposed on this project by the client. With the cruise velocity of the UAV and the consequently computed block time it can be said that if operation would be allowed to take place day and night, one UAV would be able to deliver three cargo units per day. Guided parachutes are not necessary in the performance of this mission, since the drop will take place at low altitudes.

**Table 2.1:** Compliance matrix for both the UAV and the cargo unit

Requirement description		Compliance		Chapter
UAV	Required value	Value achieved/ method used	Compliant	
Operation of the UAV using open-source technology whenever possible	–	Use of Lisa/L	Yes	16
Lean and sustainable manufacturing concepts	–	–	Yes	26
Deliveries per UAV per day	2	Block time: 7.25 hrs	Yes	4
Operation of the UAV past line of sight (transmission of important data)	–	Satellite communication	Yes	16
Provide surveillance information (HD photograph) of struck area	–	Cloud Cap Technolgy Tase400	Yes	16
Range	2,000 km	2,000 km	Yes	10
Eco-friendly material selection	–	–	Yes	5
Take-off and landing from Punta Cana Int. Airport (Dominican Republic)	< 3,100 m	Take-off distance: 1,097 m Landing distance: 877 m	Yes	11
Propulsion selection based on mission requirements and weight	–	Max power delivered: 450hp	Yes	12
Minimum production of 200 units with replaceable cargo container	–	–	Yes	26
Fit inside the C-130 Hercules	–	–	Yes	13
<b>Cargo</b>				
Cargo delivery unit	max. 500 kg	< 500 kg	Yes	23
Open-source based guidance system for drop		Unguided parachute used	Not applicable	18
Lean and sustainable manufacturing concepts	–	–	Yes	21
Number of people housed per cargo unit	3	3	Yes	1
Water, food, power communication equipment				22
Water filtration and desalination	–	–	Yes	22
Blankets and first aid emergency kit	–	–	Yes	22
Energy systems (i.e.solar power)	–	–	Yes	22
Other emergency supply identified by the team	–	–	Yes	22
Cargo drop precision	radius < 50 m	–	Yes	18

### 2.3 Human resource budgeting

In Figure 2.1 the hours that the team members spent on the project per week during the detailed design phase are shown. In Figure 2.2 the same is done for the tasks performed during the project. The most important tasks are grouped alone, where the more generic tasks are grouped together in order to keep a good overview.

Hours spent per week	Week number					
	6	7	8	9	10	Total
Daan	38	62	59	50	32	240.1
Derek	36	41	47	45	32	201
Dion	43	44	47	45	32	211.6
Heleen	43	45	39	41	32	199.3
Lubi	44	39	48	47	32	209.5
Martijn	40	44	42	42	32	200
Menco	43	47	50	41	32	212
Mika	40	40	58	47	32	217
Roderik	34	41	48	41	32	195
Thomas	43	44	52	50	32	221
<b>Total</b>	<b>403</b>	<b>446</b>	<b>489</b>	<b>449</b>	<b>320</b>	<b>2106</b>

**Figure 2.1:** Hours worked per person per week during the detailed design phase of the project

Hours spent per task		Task															Sections worked on	
		Baseline report part	Mid-term report part	Systems engineering	Aerodynamic analysis	Propulsion analysis	Structural analysis	Flight dynamics & stability	Avionics	Performance analysis	Airplane configuration	Cargo design	Cargo delivery system	Meetings	Other deliverables	Editing		Total
Person	Daan	0	0	0	0	0	0	0	170	0	0	0	0	30	0	40	240	4.4, 5.2, 16
	Derek	3	3	17	0	0	0	70	20	0	10	0	0	38	12	28	201	2.1, 2.3, 14.1, 14.4-14.8, 17.1, 25
	Dion	0	0	16	147	0	0	0	0	0	9	0	0	26	0	20	218	3.1-3.6, 4.1- 4.4, 6.3, 11.1-11.4, 11.7, 11.8, 26
	Heleen	6	8	0	0	0	0	0	0	0	0	7	82	22	35	41	199	4.2, 4.3, 7, 8, 18, 22
	Lubi	0	0	0	135	0	0	0	0	10	5	0	0	25	15	20	210	1,3.1-3.6,4.1-4.3, 6.2, 11.1, 11.3, 11.5, 11.6, 28
	Martijn	0	0	0	0	0	0	0	0	0	0	94	3	65	0	38	200	7,19,20,21,22
	Menco	4	15	0	0	0	128	0	0	0	0	0	0	28	15	23	212	6, 9, 13.1-13.10, 13.12-13.14
	Mika	0	15	0	0	1	150	0	0	0	0	0	0	26	0	25	217	5.1, 13.11, 12.1.2, 12.1.3
	Roderik	0	0	0	0	86	0	0	0	14	0	0	0	24	32	44	200	12,15
	Thomas	0	5	50	0	0	0	55	0	0	20	0	0	33	8	50	221	3.7, 6.3, 10, 13,12, 14.1-14.4, 24
	Total	13	46	83	282	87	278	125	190	24	44	101	85	317	117	328	2118	

Figure 2.2: Hours worked per person per task during the detailed design phase of the project

### 3 | Market analysis

This chapter will focus on the current demand for a UAV cargo delivery system and explore the options for new markets on which this concept can be established in the future. The chapter will start with a SWOT (Strengths, Weaknesses, Opportunities and Threats) analysis and continue with an overview of the different market segments, stakeholders, the delivery system and the permanent shelter options.

#### 3.1 SWOT analysis

To begin with, a SWOT analysis was carried out for the design of the cargo delivery UAV. The SWOT analysis lists the different advantages and disadvantages as well as the possibilities and threats emerging from the design of a UAV directed at humanitarian aid missions such as for the International Federation of Red Cross (IFRC).

**Table 3.1:** The SWOT analysis performed for the UAV cargo delivery system

	Helpful	Harmful
Internal origin	<p><b>Strengths:</b></p> <ul style="list-style-type: none"> <li>- Flexibility (no cockpit crew, automated cruise)</li> <li>- Structural/aerodynamic (no cabin pressurisation or windows needed)</li> <li>- Fewer operational costs (e.g. one pilot controls a batch of UAVs by remote control)</li> <li>- ATC infrastructure for UAV already in place (communication ATC-UAV)</li> <li>- Can access disaster zones that would otherwise not be accessible</li> </ul>	<p><b>Weaknesses:</b></p> <ul style="list-style-type: none"> <li>- High level of automation means that in case of a computer error, no human is on board to take over control, which might lead to accidents that could otherwise be prevented.</li> <li>- In case ATC makes a mistake, no immediate corrective action from pilot possible</li> <li>- Long time for approval by aviation authorities</li> </ul>
External origin	<p><b>Opportunities:</b></p> <ul style="list-style-type: none"> <li>- Additional operational capabilities (commercial cargo delivery increasing in the future)/rescue missions without endangering the pilot</li> <li>- Possible operation by USAF and UN military for disaster help missions</li> <li>- Application of sustainable technologies</li> <li>- Technological breakthroughs with a wider application of UAVs as a result</li> <li>- Positive instead of negative publicity due to drone missions (e.g. current US military missions in Pakistan)</li> </ul>	<p><b>Threats:</b></p> <ul style="list-style-type: none"> <li>- Future UAV regulations in disaster zones</li> <li>- UAV manufacturers with a military mentality</li> <li>- Lack of experience on the civil market</li> <li>- Funding difficulties (Humanitarian organisations, such as the IFRC having budget issues)</li> <li>- Safety issues with UAV operations</li> </ul>

Next, all the different subsections will be explained in more detail.

### 3.1.1 Strengths

One of the main advantages of the cargo UAV is that no onboard crew is required for its operation, which allows for the performance of missions in hazardous or rough environments without endangering their lives. No onboard crew also means that no pressurised cabin or window fitting will be needed. Next to this, one pilot on the ground can keep track of multiple UAVs.

### 3.1.2 Opportunities

Opportunities coming along with the cargo delivery UAV design are for example that the life of the pilot is not affected if something goes wrong and the possibility for additional operations aside from emergency relief missions. Commercial cargo delivery, rescue missions or fire fighting are just a few examples. Aside from missions for the IFRC, the UAV could also be used by other humanitarian organisations such as the UN military or Médecins Sans Frontières (MSF). Another opportunity for the design of the UAV is that new (sustainable) technologies can be tested and incorporated. Technological breakthroughs could lead to a wider application of UAVs. The negative publicity of drones used for military attacks (such as the current attacks in Pakistan) can be considered an opportunity for the design of the cargo delivery UAV, since it would serve a good cause. Due to its use for humanitarian aid missions, the positive reception of the project could lead to new funding possibilities for UAVs altogether.

### 3.1.3 Weaknesses

When looking at the possible weaknesses, harmful aspects were identified that are caused internally. It can certainly be advantageous to have a high level of automation, given that currently most aviation crashes are caused by pilot error. However, chances are that in the case of an emergency, there is no pilot on board to take over control.

In the aviation sector it can often take a long time before a new type of system gets approval for use by the European aviation safety agency (EASA) and/or the federal aviation authority (FAA). For a completely new type of UAV this could lead to large delays.

Normally, a mistake made by the ATC can be corrected by the pilot, for instance in the case of a runway incursion, while for a UAV this might be more difficult if the other aircraft is not in sight.

### 3.1.4 Threats

In spite of the strengths of a cargo UAV design, there are also a number of threats. For example, humanitarian organisations such as the IFRC might be faced with funding difficulties for the purchase and use of a UAV. Moreover, safety issues remain [38]. Another threat is that most UAVs are used on military missions and that there is a lack of

experience for the application of UAVs on the civil market. This might be an obstacle to using UAVs on humanitarian missions. Current UAV manufacturers are building UAVs with a military mentality. To be able to produce UAVs with cargo delivery systems for civil purposes, this military attitude may have to be altered.

## 3.2 UAV market segment

On the UAV market a distinction can be made between the general market and the military market. The general market is expected to grow significantly over the next decade. Studies carried out by the Tealgroup predict that the current worldwide spendings on UAVs will increase from currently \$5.2 billion annually to \$11.6 billion in the next 10 years [39]. Furthermore, the UAV market is expected to become increasingly international. Currently, the US have a market share of approximately 70% with UAV manufacturers concentrated in the US. Israel is also a major location for UAV research and development, according to [40].

However, the main application of UAVs is currently on the military market. Besides from combat UAVs that are employed in battle, there is also a number of cargo UAVs that could be used in disaster zones to drop off equipment for people affected by natural disasters. Forecast International expects the market for UAV reconnaissance systems (including air vehicles, ground control equipment and payloads) to amount to \$13.6 billion through 2014 [41]. The market analysts, moreover, expect over 9,000 UAVs to be purchased over the next 10 years by countries all around the world.

## 3.3 Air cargo market

One main strength of the development of a cargo UAV is that once the system has been designed for the required mission, it could be adapted for commercial cargo transportation.

A study conducted in 2004 indicated that there has been a growth rate in international air cargo of an average 6% per annum over the last decades [42]. At the same time, the capacity of the largest airports in the world has not been growing at the same pace, which will ultimately result in a capacity shortage and more congestion at these airports.

The advantage of this commercial option for the cargo UAV is that the UAV can takeoff and land from much smaller, cheaper, and far less congested regional airports. This new kind of cargo transportation can be useful for companies that are involved in delivering parcels internationally (domestically in large countries like the US), since for these companies it is important to have a fast and reliable system.

Currently, the largest cargo airline in the world is FedEx. Companies like FedEx could benefit from this technology. To show that this is indeed a viable option, the air cargo transportation data for FedEx has been collected and analysed. FedEx Freight was established in 2001 and up to the year 2007 there has been a large annual growth (on average 4% to 5% annually). After that there were 2 years of declining demand of which the largest one can be explained by the start of the global financial crisis in 2008. FedEx managed to turn this into a 13% growth in 2009 and by 2012 they had reached the highest number of tonne-miles (more than 11 million tonne-miles) in the company history. This indicates that a commercial air cargo alternative could be a feasible option.

## 3.4 Demand in case of disasters

To give an impression of the large number of people affected by natural disasters, the largest natural disasters over the past two decades have been considered [43]. From this it can be said that in the period from 1990 to 1999 approximately 2.22 billion people were affected worldwide by these natural disasters. In the period from 2000 to 2009 approximately 2.55 billion people were affected. This is an increase of 15%. Over the same time period the number of people on Earth increased from 5.29 billion to 6.79 billion, which is an increase of approximately 28.4% [44] [45].

With an increasing number of people in the world, combined with the issues of global warming, the number of people affected by such tragedies is highly likely to increase in the future. This will also increase the need for humanitarian aid systems such as the UAV.

## 3.5 UAVs with comparable cargo capabilities

Current UAVs with similar flight characteristics and capabilities as the delivery UAV to be deployed on Haiti are rotorcraft. The following three vehicles were identified as possible options for a humanitarian mission of similar scope:

### **Boeing A160 Hummingbird**

The Hummingbird is a multi-mission rotorcraft system that can take off vertically. It is runway-independent and able to operate in rough environments. It can operate for intelligence, surveillance, reconnaissance and direct attack missions. In addition, the A160 is able to deliver unmanned ground vehicles and ground sensors and can perform precision resupply. It reaches a maximum speed of 305 *km/h* with a range of 4,162 *m*. The maximum payload that

can be carried is 1,130 *kg* [46].

#### **Kaman K-Max (Lockheed Martin Corp./Kaman Aerospace Corp.)**

The Kaman K-Max is designed for precision aerial delivery of supplies such as food, water, fuel, blood or bullets (for military operations). In addition, it can insert and retrieve unmanned ground vehicles, place data relay stations and communication equipment. It can fly at a maximum speed of 185 *km/h* with a range of 495 *km*. The maximum payload that can be carried is 3,109 *kg* [47] [48].

#### **Boeing AH-6 (Little Bird)**

The Boeing AH-6 is a modified MD 530F single-turbine helicopter designed for optionally manned flight. It is capable of dual pilot, single pilot or no pilot flight operations. The AH-6 can be remotely operated or programmed for automated operations. The maximum speed that can be achieved is 282 *km/h* with a range of 430 *km* and a maximum payload of 1,090 *kg* [49] [50].

### **3.6 Stakeholders**

Aside from the IFRC, there are other humanitarian aid organisations as well as the military to use cargo UAVs to deliver goods to sufferers of a natural disaster. Possible organisations are: the United Nations, Médecins Sans Frontières (MSF), CARE International and World Vision International (WVI). Other stakeholders involved in this project are:

- Delft University of Technology (TU Delft)
- The governments and people affected by the disasters
- Aircraft suppliers and manufacturers

### **3.7 Delivery system**

The UAV market analysis, that was conducted in the previous sections, did not include the cargo delivery system in detail, which will be discussed in the following section. Furthermore, the market for permanent shelters will be analysed.

#### **3.7.1 Joint Precision Airdrop System market**

The market for Joint Precision Airdrop System (JPADS) started growing rapidly after the year 1997, when the US Army and USAF launched a funding program to develop JPADS for dropping cargo of a wide range of weight [51]. There are three main companies that produce these kind of systems: Atair Aerospace, MMIST, and Parafly. All three companies produce dropping systems, that utilise a parachute with an automated guiding unit and different standard dropping containers. Payload-wise, the companies are offering similar options, ranging from 0.2 tons up to 1 tons for the standard configuration [52]. The maximum payload is approximately 16 tons. The precision of the three systems is very similar, varying between 50 to 150 metres. From an economical point of view, this type of delivery system might not be feasible, since the costs are approximately \$60,000 [53].

The Sherpa Provider was outperformed by the other two and therefore will not be discussed further.



(a) Onyx Ultra Light by Atair [54]



(b) Sherpa Provider by MMIST [55]



(c) FireFly by Parafly [56]

**Figure 3.1:** The three leading airdrop systems

### Atair Aerospace with the Onyx

With an accuracy of 50 *m*, the Onyx is the best system on the market in terms of precision. The system is designed and fully tested at 24,500 feet [7.47 *km*] to fly with gross variances in wing loading and asymmetrically rigged payloads caused by either preflight rigging errors as well as damage induced while in flight. Onyx has an operating system capable of collision avoidance and swarm-flying with multiple systems in a decentralised fashion to reduce the number of operators needed [57].

### Parafly with the FireFly

An interesting feature introduced with the FireFly is the roadway landing feature, enabling the user to designate an azimuth for landing, resulting in a rectangular dropping zone rather than a circular one. This way the FireFly can take advantage of roads for cargo retrieval [58].

## 3.8 Development on the market

The market for the JPADS is growing rapidly. Up to 2013, more than 2,500 FireFly systems and 250 DragonFly systems (for cargo loads up to 4,536 *kg*) have been sold. Halfway through 2011, more than 18 million kg of cargo have been airdropped in Afghanistan, which is an increase of 1000% compared to the 1.6 million kg in 2006.

## 3.9 Permanent shelter

The market for providing permanent shelter in natural disaster areas is actually inexistent at this moment. Humanitarian aid organisations concentrate on providing temporary shelter like tents. The IFRC is the largest humanitarian organisation using the emergency shelter market. In the last 5 years they accommodated about 140,000 families with temporary shelters on Haiti. The IFRC supplies so called ‘shelter kits’ in disaster areas [59] [60]. These shelter kits consist of two waterproof tarpaulins (4 x 6 *m*) and a tool kit (including fixing materials). The kit does not provide any materials to build a structure. Debris material can be used as structure, or the kit can be used to repair broken houses. The total shelter kit weighs about 20 *kg* and costs CHF50 [\$65.90].

The market for permanent shelters only covers conceptual models. There are two models which already exist as prototypes: the Life Cube [61] and the Reaction Housing System [62]. Specific information on these concepts can be found in the Baseline report.

# 4 | Mission analysis

The purpose of this chapter is to provide an analysis of the mission that needs to be performed to allow for a successful cargo delivery. The chapter will start with an outline of the mission. Thereafter, the functional flow diagram and the functional breakdown structure for the mission will be discussed. The last part will describe the operations and logistics concept for both the housing unit and the UAV.

## 4.1 Mission outline

This section gives an overview of the details of the cargo delivery mission to be performed. It presents all design inputs for the detailed design, including contingencies where needed, and it describes the mission profile. In addition, the most important assumptions important for the successful execution of the mission are explained. An overview of the design inputs is given in Table 4.1.

**Table 4.1:** Design inputs for UAV

Design aspect	Value	Unit
Range	2,000	km
Payload	600	kg
Hercules cargo hold (l x w x h)	12.3 x 3.1 x 2.7	<i>m</i> <sup>3</sup>
Payload dimensions	2 x 0.7 x 0.8	<i>m</i> <sup>3</sup>

The client requested that the UAV should be able to carry and drop a cargo of 500 *kg*. To allow for some extra room in the design of the housing unit the UAV will be designed to carry 600 *kg* of cargo.

The maximum distance from Punta Cana International Airport to the furthest part of Haiti is less than 1,000 *km*,

therefore it has been decided not to add a contingency on the range.

Figure 4.1 displays the general mission profile for the UAV. After engine start-up, taxi and take-off, the aircraft has to climb to its cruise altitude, cruise to Haiti and deliver the cargo. The delivery of the cargo will be done using an unguided parachute system that will drop the cargo at a predetermined location controlled by the local authorities. A loiter time of 30 minutes at the drop zone is taken into account in order to perform this task. Thereafter, the UAV climbs back to its cruise altitude and returns to Punta Cana International Airport, where it lands.

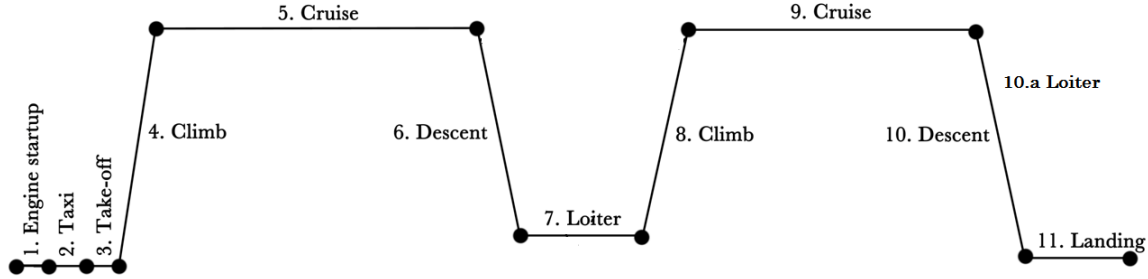


**Figure 4.1:** The mission profile for the cargo delivery with a loitering phase at the disaster site and the home base international airport.

Regulations for operating at an airport stipulate that an aircraft should have reserve fuel on board that will allow the aircraft to loiter at the airport if needed. For this mission a loiter time of 45 minutes will be assumed [63].

In Section 12.1.3 it is determined that the cruise velocity will be  $400 \text{ km/h}$ . Table 4.2 presents the block time based on a range of  $2,000 \text{ km}$ .

**Table 4.2:** The allocated times for different processes to be performed during the mission

Cruise time:	$5 \text{ h}$
drop time:	$0.5 \text{ h}$
loiter time airport:	$0.75 \text{ h}$
cargo refill/checks:	$1.0 \text{ h}$
<b>Total:</b>	$7.25 \text{ h}$

Based on the block speed it will be possible to perform two missions per UAV per day.

For the given mission frame, the assumption is made that the area where the cargo needs to be delivered is cleared by the UN Humanitarian Aid Forces before the UAV begins its cargo delivery. Basic equipment such as a receiver for communicating the clearance signal to the UAV from the delivery area is assumed to be delivered by the first (military) aircraft sent to Haiti.

Furthermore, it is assumed that the parachutes used for the delivery process will be retrieved by other transportation vehicles employed in the disaster area and returned to Punta Cana International Airport.

Additional general assumptions concerning the cargo delivery to the disaster zone are the following:

- The drop-off site will be a fenced region out of reach of civilians so that the cargo can be received by military personnel on the ground (for example by UN Peacekeeping soldiers) and distributed amongst the population as needed.
- Personnel and other basic equipment required to perform the cargo drop will be transported to the delivery zone by military vehicles prior to the cargo delivery mission is executed.
- It is important to notice that the trade-off of the UAV was done according to the following design consideration: the cargo delivery aircraft is designed to be able to be employed on humanitarian aid missions in the near future. The current level of technology available plays an important factor in realising this goal.
- The logistic solution for the retrieval of the parachutes is beyond the scope of this project.

## 4.2 Functional flow diagram

For the functional flow diagram (FFD), all the different phases of the mission are identified. It encompasses the entire project from the design phase up to the retirement phase. The mission was split up in functions of the UAV and functions of the cargo delivery system. For the UAV part, the operational phase is critical for the mission success. The operational phase is the biggest part of the entire mission and is therefore discussed in an FFD. This diagram can be found in Figure A.1 and Figure A.2 in Appendix A. The FFD for the cargo drop-off procedure can be found in Figure A.3. Colours in these FFDs are used to discern different functional levels. They hold no further meaning.

Every UAV that is built follows the same flow in the FFD. The operational phase consists of different functions that every UAV should perform during a normal mission. These functions describe the individual parts of the mission, such as payload attachment and landing. In Figure A.2 in Appendix A these generic operational aspects are elaborated on in more detail to identify all the necessary parts for the different mission segments.

The FFD in Figure A.3 in Appendix A presents the cargo landing procedure and the operations on the ground. During the landing procedure, all functions are required in order to land the cargo at the correct position and in a safe manner. On the ground the cargo has to be opened and distributed. After that, the main functions of providing shelter, water, power, and communication should be executed.

## 4.3 Functional breakdown structure

Figure A.4 in Appendix A contains the functional breakdown structure (FBS), incorporating the major technical functionalities that the UAV cargo delivery system will provide. The functionalities of the system are split into different categories, which are ground operation, remote control during take-off and landing phase, cruise, cargo deployment, cargo landing, ground operations of the cargo, and operational support functionalities. Depending on the consequence of a failure, the sub-functionalities are coloured either in yellow (\*), orange (\*\*), or red (\*\*\*). These indicate minor, moderate and major consequences, respectively.

## 4.4 Operations and logistics

The purpose of the present section is to provide insight in the operations and logistics aspects that will need to be dealt with in order to allow for a smooth operation of the UAV cargo delivery system. For this, a division has been made between the operational aspects of the UAV and the cargo as described in subsequent sections.

### 4.4.1 UAV operations and logistics

This section describes the logistics and operational aspects of developing, producing and operating the cargo delivery UAV. This allows for the effective use and incorporation of the product by the client.

Appendix K provides a general overview of all stages in the life cycle of the cargo delivery aircraft. Each of the stages are worked out in subsequent flowcharts and explained in more detail in this section, where necessary. The numbers in this section refer to the numbered blocks in the flowcharts found in Appendix K.

Stage one is design & development. This stage includes the assembly of prototypes and continues until the prototypes have been successfully tested and certified for use.

In stage two the UAVs are being produced. This includes the selection of manufacturers and suppliers, setting up logistic lines, and production schedules and finally producing the UAVs.

Stage three deals with the systems incorporation with the client. It could be beneficial to run this stage parallel to stage two. The client needs trained personnel, storage for the UAV cargo delivery systems, and operational protocols for the UAV. These protocols are based on stage four.

In stage four the system becomes operational. This includes operating the system after a disaster (4.1a), performing maintenance, and managing supplies. The operation of the cargo UAV poses a logistical challenge with many aspects to consider and is presented in a detailed flow diagram. After mapping the disaster area and assessing the needs of the dislocated population, ground support crews have to be sent to the selected drop-off zones. While a drop-off base (DB) is set up, the UAVs have to be transported to the closest international airport. Once the home base (HB) is operational it can send UAVs to the DB upon request. The staff at the DB has to remove the parachutes from the cargo units and store them before distributing the cargo units among the population. The parachutes will be returned to the HB from the DB in batches using appropriate means of transportation. The HB needs to manage its supplies such as cargo containers and order new supplies when necessary. After the completion of these tasks the operation is evaluated in stage 4.2.

Maintenance needs to be performed periodically and upon system failure, as described in flowchart 4.1b. This has to be done in such a way that at least a critical number of UAVs is available for operational purposes at all times, in order to avoid the time delay in case of a sudden need of the system.

The system is retired in stage five when it reaches the end of its operational lifetime or when the product is no longer a viable solution to the problem. The system will be retired according to the sustainability strategy worked out in Section 5.2. The goal during retirement is to maximise economical and ecological sustainability.

#### 4.4.2 Cargo operations and logistics

The individual housing units will be transported to the disaster zone by the UAVs, however, these units also need to be stored in a warehouse and be flown to the airport that will be used for the distribution operation. This section will discuss the different ways in which the units can be transported.

After production by the manufacturer, the housing units need to be stored in a warehouse facility so that they can be used immediately in case of an emergency. Transportation of the units, from the production site to the storage site, can be done by rail, road, water, air, or any combination of these.

For the first three options the best method for transportation would be intermodal containers (standardised reusable steel boxes that can go from ship to train to truck). This allows for better product security, reduced chances of damages and losses, and a faster way of freightage.

The interior dimensions of these containers range from  $5.7\text{ m} \times 2.3\text{ m} \times 2.3\text{ m}$  (length  $\times$  width  $\times$  height) to  $13.5\text{ m} \times 2.3\text{ m} \times 2.6\text{ m}$ . Depending on the final dimensions of the housing unit the most suitable container can be chosen for transport [64] [65]. The intermodal containers are illustrated in Figure 4.2a [66].

Intermodal containers are, unfortunately, not an option for air transportation. For this, unit load devices (ULDs) are commonly used (special containers and pallets for civil aviation). These are again standardised to fit in wide-body aircraft [67] [68]. An example can be found in Figure 4.2c [69]. The standardised pallets used in military transport aircraft are slightly smaller than the ones used in civil aviation and are referred to as 463 *L* pallets [67] [70].

Depending on the type of Hercules used, six to eight of these pallets can be loaded on board (six for the Hercules C-130E/H/J and eight for the C-130J-30) up to a maximum allowable payload weight of 19,090 *kg* or 19,958 *kg* respectively [71].

Aside from the Hercules aircraft these 463 *L* pallets are also certified for use on board of the following aircraft: C-5, C-27, CH-47, KC-10, C-17 and C-9 [70].



**Figure 4.2:** Examples of transportation options for rail, road, water (left) commercial air transport (middle) and transportation as done by the department of defence (DOD) (right)

## Part II

# Conceptual design phase

# 5 | Preliminary analysis

Before the start of the design phases of the project it is important to know in what environment the UAV will operate and in what environment the housing unit will be used. This will be the focus of the first part of this chapter. The second part will discuss the strategy that will be used for the development of a sustainable design for both systems.

## 5.1 Environmental and geographical analysis

The UAV cargo delivery mission is influenced by the environmental and geographical conditions in Haiti and the Dominican Republic. To make sure that the design fulfils the needs of the mission and the refugees, some specific background information has been retrieved.

### 5.1.1 Climate

Haiti has a tropical wet and dry, savannah-like climate. It has a pronounced dry season in the summer months, no cold season and a wet season in the winter months. A graphical representation of the climate of Haiti is shown in Figure 5.1. These conditions have to be taken into account when considering the design. They play a role in designing the housing in for example the amount of insulation that is needed and the type of materials that are suited to tropical climates. Climate control for the inhabitants will be extremely important and could influence the shape of the cargo to include shaded areas and/or open areas within the design.

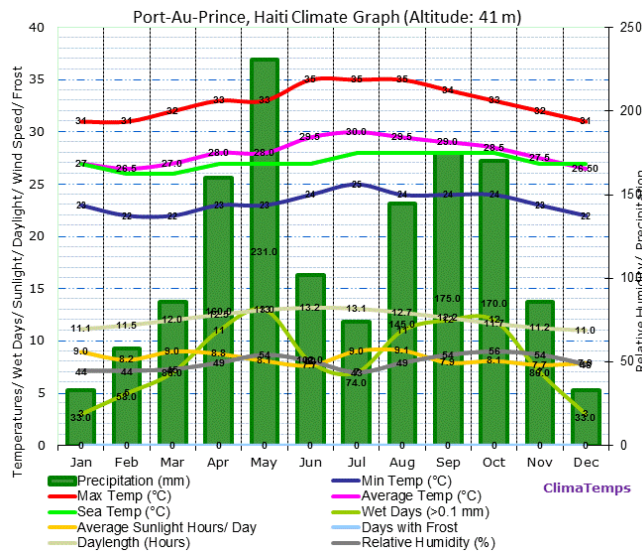


Figure 5.1: Climate graph Haiti (altitude 41 m)

### 5.1.2 Infrastructure

Haiti's infrastructure is primitive, which is the result of decades of environmental damage and poor maintenance. Most roads, even those linking Port-au-Prince to other large cities, cannot be navigated by ordinary vehicles. Of a total of 4,160 km of registered road, only 1,011 km is paved. Those that are paved suffer from landslides and potholes making their condition of the same grade as the unpaved ones.

### 5.1.3 Physical geography

Haiti and the Dominican Republic together are called Island Hispaniola. The physical geography is very diverse, with five mountain ranges covering the island. The largest mountain range is The Central Range. This mountain range boasts the highest peak in the Antilles, Pico Duarte at 3,087 m above sea level. Pico Duarte is centrally positioned on the island and is on the path that the UAV would follow were it to fly in a straight line. Based on this the UAV can be designed to have a flight ceiling above this altitude, allowing it to fly an optimal flight path.

### 5.1.4 Natural resources

Haiti used to be a very green island with more than 60% of the island being covered with forest in 1925. Deforestation without regard for the consequences has now resulted in the deforestation of 98% of the original forest cover. This huge amount of deforestation is due to the increasing demand for fuel, wood and due to tropical storms. The current primary energy source on Haiti is charcoal. Due to rapid population growth the demand for charcoal has risen so dramatically that deforestation was accelerated even further. It is very important for the design of the cargo that it

does not further enhance this problem.

Haiti is blessed with over 3,000 sunlight hours per year. This makes solar power a viable option. The average is  $5.3kWh/m^2/day$ . Trade winds in the Caribbean cause light winds around Haiti all year round. These winds are mild of nature and have a yearly average of 4.6 m/s. Winds mainly come from the west. Maximum wind speeds measured are 51.6 m/s which correspond to hurricane strength. 4.6 m/s is too little for self-sufficient power supply. These maximum winds will be taken into account when designing the shelter concerning the anchoring of the house.

## 5.2 Sustainable development strategy

This section describes the strategy to develop a sustainable design. Sustainable development is generally defined as follows [72]:

*Development that meets the needs of the present without compromising the ability of future generation to meet their own needs.*

The following three pillars can be distinguished in sustainability:

- Ecological sustainability
- Economical sustainability
- Social sustainability

Each of these aspects of sustainability are considered while designing the UAV cargo delivery system. The sustainable design philosophy behind this design is explained in Section 5.2.1. Section 5.2.2 explains the actual strategy that will be used to design a sustainable solution.

### 5.2.1 Sustainable solution to shelter for refugees

One of the primary goals of this project is to design a more sustainable solution to the provision of shelter to disaster refugees. Current solutions provide temporary shelter in the form of tents and housing until refugees have found a new permanent home. What happens in reality is that the international community quickly loses interest and attention shifts to the next problem. Out of the 1.5 million refugees who lived in temporary shelters in Haiti just after the disaster struck in January 2010, 320,050 individuals still remained in those shelters in April 2013 [73]. One of the aims of this project is to develop shelters that can function as permanent housing for the disaster refugees. This leads to improvements in ecological, economical and social sustainability compared to the current alternatives.

### 5.2.2 General rules of the sustainable design strategy

This section provides the general rules of the sustainable design strategy. This is done for all phases that the UAV cargo delivery system goes through in its existence: production, operation and disposal.

#### **Sustainable production of the UAV cargo delivery system**

Most products could make large gains in their sustainability by altering their production techniques. The strategy to produce the UAV cargo delivery system in a way that is ecologically, economically and socially sustainable is outlined below:

- Ecological sustainability
  - Minimise power consumption
  - Consume power from a 'sustainable' source
  - Minimise use of production processes that produce hazardous side products
  - Minimise material waste
- Economical sustainability
  - Minimise material and manufacturing costs
  - Pay appropriate wages to the workers
- Social sustainability
  - Create jobs for people in different layers of society
  - Guarantee the safety of the workers
  - Guarantee the safety of the surroundings of the production plant

### **Sustainable operation of the UAV cargo delivery system**

This section investigates in what ways the three pillars of sustainability can be addressed during operation of the UAV. The system consists of two parts: the UAV and the cargo system. In some follow-up sections the sustainability for both parts is evaluated separately.

- Ecological sustainability
  - An aerodynamically efficient UAV
  - Use of green fuels to propel the UAV
  - Use of an efficient power plant in the UAV
  - Efficient flight plans
  - Minimise loss of waste substances such as oil, coolant, etc.
  - Use of a renewable energy source in the cargo system
  - Limit waste substances from the operation of the cargo system
  - Development of the cargo for a long lifetime, which reduced the need for replacements
- Economical sustainability
  - Provide a concept that is economically competitive to alternatives
  - Minimise fuel costs
  - Minimise maintenance costs of the UAV by the operator
  - Minimise maintenance costs of the cargo system for the refugees
- Social sustainability
  - Operate the UAV cargo delivery system by suitable people that need the work
  - Guarantee the safety of the operating environment
  - Provide the resources to those who need them the most
  - Use the cargo system to provide the refugees with a high level of welfare

### **Sustainable disposal of the UAV cargo delivery system**

Any product will eventually reach the end of its operational lifetime, which is defined by the term disposal. The disposal can be done in a sustainable manner. There is an important difference between the UAV and the housing unit that needs to be considered at this stage. The UAV will remain in control of the operating organisation which can then coordinate its disposal. However, the disposal of the housing unit will be done in a way that suits the former refugees well, without any external control.

- Ecological sustainability
  - Maximise the use of biologically degradable material
  - Control the disposal of hazardous material
  - Make use of recycling
- Economical sustainability
  - Recycle or sell parts that still have value at disposal
  - Design for cheap disposal that meets the sustainability requirements
- Social sustainability
  - Waste is not allowed to be a hazard to any layer of society
  - Guarantee the safety of the people charged with disposal

### **5.2.3 Conclusion**

Designing a UAV cargo delivery system that meets its primary requirements while being ecologically, socially and economically sustainable is a great challenge. It will include many difficult trade-offs because the different aspects of sustainability are often in conflict. For example, the choice for methods of disposal that are ecologically sustainable will often increase the costs of disposal. This is unfortunately part of the process, and the rules of Section 5.2.2 are there to assist in this process. The provision of sustainable shelter to disaster refugees as explained in Section 5.2.1 is one of the primary deliverables of this project.

## 6 | UAV concepts

From seventeen generated concepts, three were selected based on a preliminary trade-off using the mission requirements. These three concepts and the corresponding trade-off will be briefly summarised in this chapter. In order to do a consistent trade-off, it was decided to elaborate on the same subjects for every concept. This distribution can be found in all the upcoming sections that discuss the different concepts.

This distribution also finds somehow its way back in the upcoming sections.

### 6.1 Concept 1: Airship

An airship is a 'lighter than air vehicle'. Since it generates lift from the helium inside the envelope, it is able to hover. Engines mounted on the outside of the airship give the airship its thrust. Figure 6.1 shows a render of an airship.

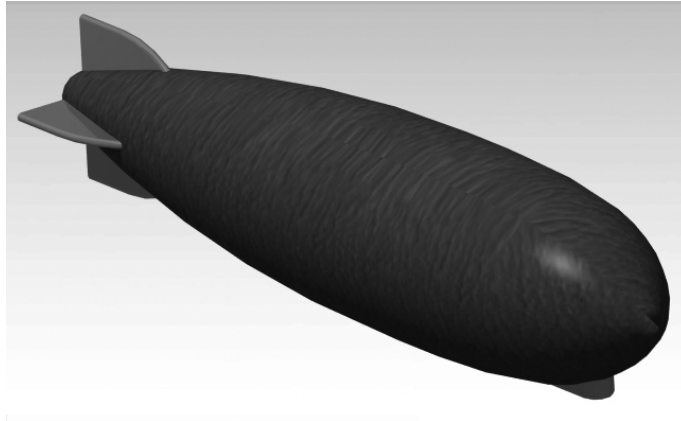


Figure 6.1: Rendering of a simplified airship

**First class weight and size estimation** - As a first step a weight and size estimation were performed. Size and weight highly depend on each other, since large volumes of gas are required to lift small payloads. Based on reference airships it was possible to come up with some values for the proposed volume ( $2,292 m^3$ ), maximum take-off weight ( $2,242 kg$ ) and lift required  $21,996 N$ ).

**Aerodynamic analysis** - According to the shape, a compromise should be found between having maximum lift capacity and low air resistance. From reference airships it is known that a streamlined spheroid body contributes to both elements quite well, this can also be seen in Figure 6.1. Based on the results from the first weight estimation (envelope volume and required lift), for a wide range of corresponding dimensions the drag coefficient was calculated.

**Propulsion analysis** - For the propulsion it is considered to have a propeller driven airship, of which the engines have the ability to rotate in order to control the airship in all directions. The selection of the engine in order to perform the estimations on fuel efficiency is based on the power required to overcome the air resistance in combination with the velocity mission requirement. From a list of engines the GarrettTPE331-12JR turned out to be the best option. However, with the combination of velocity ( $> 220 km/h$ ) and range ( $2,200 km$ ) from the mission requirements, it is impossible to fulfil this by means of an airship.

**Preliminary sizing (dimensions)** - From the propulsion analysis it is known that the required length for the airship will be around  $44 m$  and the maximum diameter will be around  $9.9 m$ .

**Stability and control** - When looking at the control of the respective attitudes of all types of airships, a widely used method is the use of vector thrusting; by rotating the engines, the airship can be controlled in almost all directions. Non-rigid airships can also be controlled by using so-called ballonets. These ballonets can be filled with air in order to decrease altitude and vice versa. For all the other flight manoeuvres, regular control surfaces can be used. Stability will also be influenced by the ballonets in case of a non-rigid airship, furthermore is proper placing of the payload an important contributor to the stability of an airship.

**Structural analysis** - Two main options according to the structure can be considered; a rigid or a non-rigid airship. The rigid ones have mainly advantages in the field of placement possibilities regarding the engines and fuel- and gas compartments. Disadvantages are related to its enormous size, ground handling for example can be problematic in

that case.

Non-rigid airships are easier to built, another advantage is its deflatability allowing great accessibility. A non-rigid airship however is not always consistent according to its shape, therefore it is not possible to fly at higher velocities. Based on the mission requirements it can be concluded that a rigid airship is the best option.

**Material analysis** - The external skin has to provide resistance against environmental degradation and structural damage, but at the same time should be as light as possible. A widely used material for this is an aramid Kevlar-ply. However for the weathering components it is better to use Polyvinylfluoride (PVF).

**Cargo delivery** - Since it is not desirable to land the airship at the drop zone, but taking its ability to hover into account, a skycrane is the most feasible option regarding the cargo delivery system.

**Costs and manufacturing** - One of the latest airships, the Zeppelin NT, incorporates all the modern technologies and has a price tag of \$19,500,000. Based on reference airships the maintenance costs will be around \$100 per flight.

## 6.2 Concept 2: Tiltrotor

The tiltrotor is a vertical take-off and landing (VTOL) vehicle, which uses the tilting abilities of the rotors to hover and to fly. A rendering of the tiltrotor concept can be found in Figure 6.2.

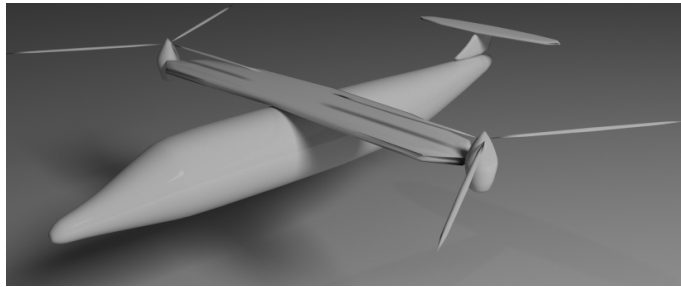


**Figure 6.2:** Rendering of the tiltrotor concept

**Sizing** - A first sizing is performed on three important elements of the tiltrotor concept; the tiltrotor, the main rotor and the wing. From this first sizing it can be concluded that in order to fulfil the mission requirements the following design parameters need to be included, see Table 6.1.

**Table 6.1:** Final tiltrotor concept design parameters

Parameter [units]	Value	Description	Parameter [units]	Value	Description
$P_r$ [kW]	431	Power required	R [m]	2.76	Blade radius
$L/D$ [-]	9	Lift over drag ratio	$N_b$	3	Number of blades
$W_G$ [kg]	4042	Gross weight	$C_T$	0.0456	Thrust coefficient

**Propulsion** - Based on the mission requirement for the tiltrotor, it has to be able to fly 275 *km/h*. When looking at reference tiltrotors the Rolls Royce AE 1107C Liberty seems to be a feasible option. Since a tiltrotor should be able to fly both like a helicopter and an aircraft, a so-called proprotor needs to be designed.

**Stability and control** - According to stability and control, the challenges can be mainly found in the hovering ability of the tiltrotor. According to the take-off and landing, it is for safety reasons preferred to do this with a slightly tilted helicopter. Shortly after take-off there is the possibility of an engine failure, the helicopter will not be able to provide shaft power in that case, hence an emergency plan must be considered. Even without shaft power, the rotor should sustain its revolutions per minute (RPM) in order to continue controlled flight and landing. By adjusting the collective pitch, forces are generated on the blades which sustain the RPM. The energy to overcome the blade drag must be provided by an airflow over the blades. In fact, the potential energy and the forward velocity are utilised to land in a controlled manner, this phenomenon is known as autorotation.

**Structural and materials analysis** - VTOL aircraft pose special challenges to structural design and material selection: the loads generated by the engines change direction, depending on the flight mode. A tiltrotor experiences

other loads than a conventional aeroplane. Especially for the wing, since the relatively large rotorblades are mounted almost at the wingtips for propeller clearance.

The most significant improvement in structural efficiency can be accomplished through the use of composites. Their static strength properties are outstanding, while fatigue properties are also measurably better than those of present materials [74].

**Cargo delivery** - One of the advantages of a tiltrotor is its ability to land and take-off vertically. Therefore the most logical way to deliver the cargo is by landing the tiltrotor at the drop zone.

**Costs and manufacturing** - The V-22 Osprey is an example of a tiltrotor aircraft used by the US military which- at a price of \$115,000,000 per aircraft (FY2005 US defence budget)- costs several times more than an average medium-weight helicopter and even several times more than a military transport aeroplane. Based on reference tiltrotor designs, the cost per flight hour can be assumed as being \$2,537 [75].

### 6.3 Concept 3: Fixed wing

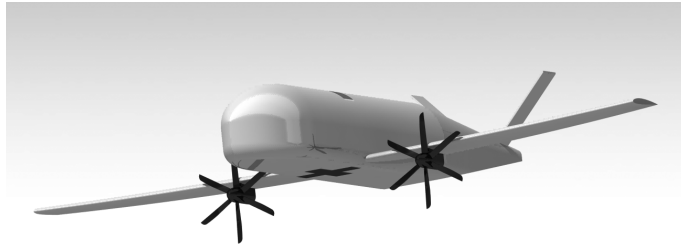


**Figure 6.3:** Rendering of the fixed wing concept

**Weight estimation** - A first class weight estimation is the first step in designing a fixed wing aircraft. In order to do a reliable weight estimation, data from reference aeroplanes is needed. Based on this data, the fuel weight fractions for each mission phase can be determined. Using these fractions a first estimation can be made of the fuel weight. To be able to make a substantiated decision on using a jet or a propeller, both options need to be considered. The results of this first class weight estimation can be found in Table 6.2.

**Table 6.2:** Results of the class I weight estimation for both the propeller and the jet aircraft

Group	Symbol	Propeller	Jet	Difference
Maximum take-off weight [kg]	$MTOW$	2,786	3,071	10%
Operational empty weight [kg]	$OEW$	1,310	1,432	9%
Fuel weight [kg]	$W_{Fuel}$	876	1,038	19 %

**Propulsion** - The propulsion system of an aeroplane must be able to provide thrust in order to balance the drag during cruise, as well as exceed the drag to accelerate. Since the mission objective does not state any restriction on the speed other than the requirement of a block time of 9.5 h, both the turbojet and propeller engine can be considered. An advantage of a turbojet is its efficiency at higher flight velocities. However, its complexity is a large disadvantage. Propellers convert rotary motion from an engine to propulsive force by accelerating large amounts of mass. The turboprop is a propeller driven by a shaft connected to a turbine. In contrast to the jet-engine, all the energy available in the flow is utilised to provide the propeller with shaft power. Based on the required two drops per day, the jet-engine can do the job faster, but less efficiently. Therefore the option jet engine is discarded.

**Loading diagram** - Based on a certain maximum stall speed from the certification procedure CS23, determined as being 31.4 m/s, it can be calculated that the maximum wing loading during landing will be in the range of 975 to 1,524 N/m<sup>2</sup> for the different flap configurations. For the take-off phase it was chosen that this would be around 600 m, using the Raymer method the corresponding take-off parameters (TOP) can be determined. This TOP turned out to be 220 lb<sup>2</sup>/(ft<sup>2</sup>hp) [0.594 (kg s<sup>3</sup>)/m<sup>4</sup>]. Together with values for efficiencies, climb rate, rate of climb, Oswald factor, aspect ratio and drag coefficients gained from reference aeroplanes or statistics, the loading diagram can be created, as seen in Figure 6.4. The sizing in this diagram has been done for take-off, landing, stall in landing configuration, climb rate and climb performance. The shaded part indicates the design range and the circle indicates the chosen design point.

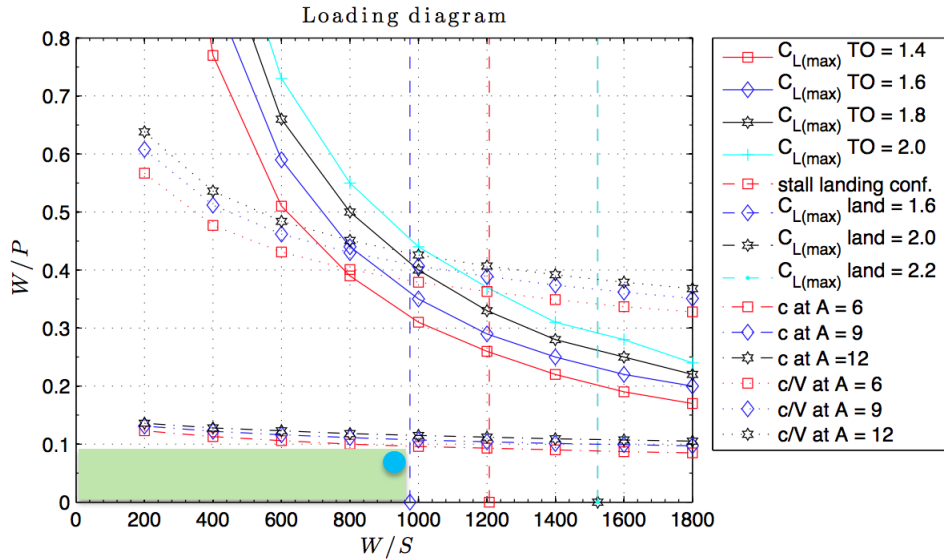


Figure 6.4: Loading diagram for the UAV to be designed (using propellers)

**Aerodynamics** - Table 6.3 shows the conclusions from the aerodynamic analysis

Table 6.3: Aerodynamic conceptual parameters

Aerodynamic conceptual parameters	Values
Highest wing loading [ $N/m^2$ ]	975
Take-off weight [ $kg$ ]	2,786
Wing surface area [ $m^2$ ]	28
Aspect Ratio [-]	6 - 12
Wing span [ $m$ ]	13 - 18.3
Chord length [ $m$ ]	2.2 - 1.5

**Fuselage sizing** - The size of the fuselage of a UAV is mainly related to the cargo dimensions and the amount of fuel stored inside the fuselage. Since there is no need to pressurise the fuselage, it is not required to have a circular shaped fuselage. When looking at the reference UAVs the average fuselage length of these type of planes vary mostly from 10 to 14  $m$ .

**Stability and control** - The stability of the aeroplane describes how well equilibrium is maintained during flight. Controllability describes how this equilibrium can be changed. The cargo drop will influence the stability of the UAV. To meet the requirements on cargo drop-off precision, the UAV should be able to fly at a certain minimum velocity. Another aspect of the drop-off that will influence stability is the change in weight. As a result it is important to place the cargo at a well determined position in the UAV.

**Structure and materials** - For the conceptual design, only the fuselage construction and wing intersection are taken into consideration. As mentioned before a circular cross section is not necessarily the most suitable design for the fuselage. Since the cargo has a rectangular shape, also a rectangular fuselage design can be considered. However, higher stresses will occur at the corners. A compromise will have to be made between load resistance and optimal use of space. Due to its determined wing span of 28  $m$  the UAV does not fit inside a Hercules. For that reason the UAV should be made foldable in some way. With regard to the materials, aluminium, and composites are widely used in the aeroplane industry.

**Cargo delivery system** - Two options according to the cargo delivery system can be considered. The first possibility is to land the aeroplane at the drop zone, the second delivery option is by dropping the cargo while the UAV is flying. There are two ways to drop the cargo from the airplane during flight. The most commonly used possibility is having a cargo hedge at the rear of the aeroplane, opening downwards. Another option would be to place the cargo around the location of the centre of gravity of the aircraft, and then opening a cargo door in a similar way as the deployment of the landing gear of a regular aircraft.

**Costs and manufacturing** - Based on reference aeroplanes, it can be assumed that the operational costs per flight

hour will vary between \$600 and \$800. The manufacturing costs will be around \$500,000, based on the Singular SA03 [76].

## 6.4 Trade-off

Using the mission requirements and mission need statement, the following four categories have been defined for the trade-off criteria:

- Automation
- Performance
- Sustainability
- Technical feasibility

Based on these criteria, sub criteria were defined and a certain weight was given to each of them. Outside this trade-off, a check was also performed on the mission requirements. If a concept failed on this check, it is not able to fulfill the mission. Table 6.4 shows the result of the first check on the mission requirements. It can be seen that the airship can be discarded from the trade-off. The final trade-off results for all three concepts can be found in the mid-term report. The fixed wing turned out to be the most feasible option and will be discussed further in part III; the detailed design of the UAV.

**Table 6.4:** Mission requirements feasibility for the concepts

Mission requirement	Airship concept	Tiltrotor concept	Aeroplane concept
600 <i>kg</i> payload	Yes	Yes	Yes
2200 <i>km</i> range	Yes	Yes	Yes
2 flights per day	No	Yes	Yes
Fit in a Hercules	No	Yes	Yes

## 7 | Conceptual design cargo

In this chapter the results of the cargo concept evaluation are briefly described. The cargo is divided into two parts: the housing, and its subsystems. For the housing, three different concepts were generated and with the use of a trade-off table, one concept was chosen to be taken into the detailed design phase. For the subsystems (water treatment system, power system, and communication) existing options were considered and the ones that are most suitable for the UAV cargo delivery mission were chosen.

### 7.1 Housing concept 1: Foldable cabin design

The foldable cabin design is based on a one-piece material that can easily be folded into a cubic cabin.

#### Configuration

The design of this concept consists of a set of multiple foldable cabins. One cabin can be equipped with beds, sanitary or kitchen devices. One family of three will at first get one cabin, and will share sanitary cabins with the other families in the community. The kitchen and dining room will be placed in a community centre, built from multiple cabins. A visualisation of the foldable cabin design can be found in Figure 7.1.

#### Sizing, structure, and materials

The minimum size of one foldable cabin is 200 *cm* x 180 *cm* x 200 *cm*. To be weather-proof, the foldable cabin will have to be anchored to the ground. Also, the roof has a slight slope in order to drain rainwater. The roof and floor panels will be made out of polyethelene plastic, which is a durable, strong, but light weight plastic. The wall panels can be made of aluminium or a plastic, Acrylonitrile-Butadiene-Styrene (ABS).

#### Transport

The folded package of the foldable cabin, for both materials has a minimum size of 0.65 *m* x 0.70 *m* x 2 *m*. The weight of the aluminium foldable concept is 154 *kg* and the weight of the ABS foldable concept is 191 *kg*. Shortly after the disaster, mainly bedrooms will be delivered. At this stage the community centre and sanitary cubicles can be shared. When everyone has a shelter, more sanitary cabins and perhaps community centres can be delivered to make this design meet the requirements for a permanent living space.

#### Construction

The foldable cabin design is easy to construct, since most of the parts are already attached to each other. However, the connection between these parts could be tricky, and have to be done correctly to make the design durable. Therefore, a manual with graphic explanations should be provided together with the necessary tools.



Figure 7.1: A visualisation of the foldable cabin design

## 7.2 Housing concept 2: Modular cabin design

The modular cabin design is a compact housing system, with expansion opportunities for the future. Its concept is based on construction with 'puzzle pieces'.

### Configuration

The modular cabin design consists of five components: a wall panel, a floor panel, a roof panel, a window panel, and a door panel. With these, a complete cabin can be build of any size and for any purpose. A visualisation of the modular cabin design can be found in Figure 7.2.



Figure 7.2: A visualisation of the modular cabin design

### Sizing, structure, and materials

As for the foldable cabin, the size of the modular cabin was based on the minimum size of a bed, together with the size of the panels. This results in a size of  $240\text{ cm} \times 180\text{ cm} \times 200\text{ cm}$  for one cabin. The material used for the floor and roof panels is the same as for the foldable cabin: polyethelene plastic. Similarly, the wall panels can be made of aluminium or a plastic. When aluminium is used, a supporting framework is needed. It is convenient to make this framework of wood, which allows easy connections (screws or nails) between the panels and the framework.

### Transport

The minimal package size, from a three dimensional analysis, is  $60\text{ cm} \times 40\text{ cm} \times 200\text{ cm}$  for the aluminium modular cabin design and  $60\text{ cm} \times 80\text{ cm} \times 200\text{ cm}$  for the ABS modular cabin design. The total package weight is  $269\text{ kg}$  for the aluminium design and  $244\text{ kg}$  for the ABS design. Shortly after a disaster, panels can be delivered for small bed cabins together with a few community kitchens and living rooms. For a more permanent solution, the small bed cabins can be extended by the delivery of extra panels to provide every family with its own kitchen and sanitary.

### Construction

The modular cabin should be designed in a way that allows easy construction. This is achieved by producing the panels as a kind of 'puzzle piece'. All links are designed to fall easily in place, and only a few connections are needed to make a strong static body. The strength of the connections is part of the detailed design phase. The construction can be guided with a clear manual or with trained personnel on the ground.

## 7.3 Housing concept 3: Permanent tent design

The third concept is the permanent tent design, which is based on existing high quality party tents or so called 'aluhalls'. Basic tents do not have the required lifetime of at least ten years. This permanent tent design provides a

variation on a tent design, with an increased lifetime.

### Configuration

The permanent tent has a supporting framework, a floor, and walls that are covered with panels at the bottom. The rest of the walls and the roof are covered by a durable cover. One tent will provide all the necessities for a family of three, except for sanitation. The sanitation will be placed in a larger tent, and has to be shared by multiple families. The permanent tent also contains a small overhanging shed. Under this shed, a water treatment system can be placed or people can sit outside in the shadow. A visualisation of the permanent tent can be found in Figure 7.3.



Figure 7.3: A visualisation of the permanent tent design

### Sizing, structure, and materials

The permanent tent design has  $9 m^2$  inside space, and a shed of  $4.5 m^2$ . The cover of the tent is made from durable polyvinylchloride (PVC), which has a lifetime of 35 years. A widely used light weight material for a tent framework is aluminium. For durability, the walls are not entirely made of PVC. The lowest part of the walls will be made from ABS.

### Transport

The main advantage of the permanent tent design is the weight and size of the package it can be delivered in. The PVC cover can be folded, and has a low weight. Together with the panels and the aluminium structure, the weight of the package is  $88 kg$ . The minimal package size is  $0.6 m \times 0.32 m \times 2 m$ .

### Construction

Putting together the components of the permanent tent might be a difficult task for people in the disaster zone. The aluminium structure contains multiple separate pieces of different sizes that have to be placed in the correct place. Putting the panels in place is quite simple, as well as covering the structure with the PVC cover. However, the cover has to be connected to the structure in the correct way to ensure a permanency of at least ten years. To make sure the permanent tent is built correctly, the construction can be guided by a clear manual or trained personnel on the ground.

## 7.4 Housing trade-off

From these three concepts, one concept had to be chosen to continue with in the detailed design phase. This was done by the use of a trade-off, which will be discussed in this section.

### 7.4.1 Trade-off method

In order to make a good comparison, a trade-off method had to be established. Using the mission requirements and mission need statement, the following four categories have been defined for the trade-off criteria: Permanency, size, complexity, and sustainability. Within these categories several criteria were defined and weights were given for each of these according to their importance for mission success.

### 7.4.2 Trade-off summary table

From Table 7.1, the aluminium modular concept scores the highest with a score of 35. Especially the expansion possibility characteristic and the weather resistance makes it best suited for this mission. Therefore, the aluminium modular concept will be designed in detail in the next phase. Although this concept only scores 70% of the total 50 points achievable, it can be optimised in the detailed design phase. For example if the package weight can be decreased, the possibility remains to increase the living space of the smallest modular unit.

## 7.5 Subsystems

Besides housing, the cargo also has to supply the basic needs of people in disaster zones. This includes clean drinking water, power, and a way to communicate with the outside world. The best options -based on permanency, weight, and sustainability- for these are discussed in this section.

**Table 7.1:** Trade-off table for the housing concepts

Criteria	Weight	Fold. Alu	Fold. ABS	Mod. Alu	Mod. ABS	Tent
Living space	8	3	3	3	3	7
Expansion possibility	10	3	3	10	10	0
Package weight	7	5	4	3	4	6
Package dimension	6	1	1	3	1	4
Low complexity housing unit	5	4	4	2	3	1
Environmental friendly material	6	5	5	5	5	5
Weather resistance	8	4	4	8	4	2
<b>Total</b>	<b>50</b>	<b>24</b>	<b>24</b>	<b>35</b>	<b>29</b>	<b>24</b>

### 7.5.1 Water treatment

The UN World Water Assessment Programme suggests that each person needs 20 L to 50 L of clean fresh water per day to ensure their basic needs for drinking, cooking, and cleaning are met [77]. To provide this, the best possible solution for purifying fresh water was found to be a family-sized, non-powered water filter. An existing option for this is the biosand water filter. It can filter approximately 20 L/h, and is designed to last a lifetime. Simple trainings can be given to the people on how to make their own filter. One of these filters costs around \$70.

To be able to desalinate sea water, a community-sized and powered system was found. This system, offered by GenPro Energy Solutions [78], can desalinate 75 L/h to sustain 45 people per day. The system costs \$15,000, which is over \$330 per person. It can also purify fresh water, so only one system is necessary to obtain drinking water from all available sources. However, compared to the biosand filter it is very expensive and less efficient. To filter the same amount of water with biosand filters, the cost would be approximately \$2,000. Also, the desalination system needs to be powered, which would increase the costs even more. It was therefore decided not to use desalination systems, but only biosand filters.

### 7.5.2 Power system

Several renewable energy solutions were considered to supply the housing with power, of which solar energy was found to be the most feasible and efficient option for Haiti. A solar panel can be placed on the roof of the modular cabin to provide power. By using a minimum radiation in Haiti from Section 5.1, a solar panel efficiency of 20 %, and an estimated required power of 1,500 W for two hours for a family of three, the required area of solar panel was calculated to be 3.4 m<sup>2</sup>. Since the roof of the smallest modular cabin design is 4.3 m<sup>2</sup>, the solar panels can fit onto that.

### 7.5.3 Communication

The cellular phone infrastructure in Haiti should be improved, making it reliable and easily recoverable after an earthquake. Right after a disaster, satellite phones should be provided for communities. Both of these options are not within the scope of this mission. Improving the infrastructure is part of the reconstruction of the country, not humanitarian aid. The satellite phones are part of ‘Telecom without Borders’, and not of the IFRC. However, if the client insists on providing a communication system, a satellite phone per community is the best option. Furthermore, a radio could be a cheap solution to have a one-way communication system, to, for example, inform the people about recent updates.

## 8 | Delivery system concepts

For the delivery system, six concepts have been generated and evaluated in the conceptual design phase. Based on the strengths and weaknesses the optimal concepts have been chosen for the different concept UAVs. The result of this selection is presented in Chapter 6, where the different UAV concepts are shown.

### Land with UAV

One of the options to deliver cargo is to land the UAV at the desired location and take it out of the aircraft. The main advantage of such a delivery system is that no extra delivery system is needed and therefore reducing the mission cost and complexity. On the other hand, this system requires the landing location to be cleared which is not feasible for every UAV concept.

### Skycrane

By lowering the cargo with a rope during hover, the cargo is delivered at the drop zone. Therefore it is not required to land the aircraft, however, it must have hover capabilities. The cargo can be either stored inside the body of the aircraft or hanging under the aircraft. When hanging the payload under the aircraft, the aerodynamic drag introduced will make this a non-efficient method.

**Free fall**

Another option is to let the cargo fall from a designed drop altitude. No extra delivery system will be necessary, which minimises complexity and costs. The forces involved in the landing, however, will be significantly high and the cargo would have to be designed for that.

**Catch concept**

For the catch concept the cargo will be decelerated by a ground device. In this way, the cargo packages will not need an individual delivery system, but can all use the same device. The device will have to be constructed before any aid can be delivered. The impact forces are also of considerable magnitude.

**Delivery using parachutes**

When the cargo is dropped from the aircraft, the impact on the cargo during landing can be decreased compared to the free fall option, by the use of a parachute. The UAV can drop its cargo during flight which reduces the block time. To ensure the drop-off precision, either a guided parachute can be used or the altitude should be low enough to make an accurate trajectory calculation.

**Conclusion**

The skycrane with hanging payload as well as the free fall method are discarded because of the large loads and the inefficiency. The catch concept is not an option since the probably large device will have to be built before any cargo can be dropped, and it is not sure if there is enough space in the disaster zone for such a structure.

Landing the UAV would be an option if the UAV is designed for a small take-off and landing distance. A skycrane with the payload incorporated in the fuselage is an option for UAVs that are able to hover. For UAVs that can not hover, dropping the cargo with a parachute (guided or non-guided) is also an option.

Part III

Detailed design UAV

## 9 | Detailed design input

Before the detailed design starts, the design outputs including contingencies gained from the conceptual design phase which will be the input for the detailed design phase. Some of the values can be subjected to changes during the detailed design phase in the following chapters.

### UAV:

- Fixed wing configuration
- Dimensions (folded):  $12.5\text{ m} \times 3.1\text{ m} \times 2.7\text{ m}$
- Range:  $2200\text{ km}$
- Block time:  $9.5\text{ hr}$
- Payload mass:  $600\text{ kg}$
- Avionics: Lisa/L flight computer

### Cargo delivery system:

- Drop cargo during flight
- Use of a parachute system

### Cargo / housing:

- Maximum payload dimensions:  $200\text{ cm} \times 70\text{ cm} \times 80\text{ cm}$
- Housing concept: modular concept
- Material: aluminium
- Minimal package size housing:  $60\text{ cm} \times 40\text{ cm} \times 200\text{ cm}$
- Water treatment system: biosand water filter
- Power generation: solar panels

## 10 | Weight estimation

In this chapter, a weight estimation of the aeroplane will be performed. It is of utmost importance to minimise the weight when designing an aeroplane. When adding extra weight to a component, it generally results in added weight for another component as well, leading to the so called snowball effect of weight growth. The reverse is also true.

The weight estimation methodology will be presented in Section 10.1. Section 10.2 presents a short summary of the class I weight estimation. In Section 10.3 the preliminary layout will be presented. Section 10.4 presents the class II weight estimation where the component weights are determined.

In Section 10.5 the results of the weight estimation will be presented which will be discussed in Section 10.6. Finally, Section 10.7 presents the centre of gravity location of the UAV.

### 10.1 Methodology

To ensure that the weight estimation is accurate, two different methods are applied, and iterated until the error between them is less than 2%. The calculation scheme is shown in Figure 10.1. The first step is to perform a class I weight estimation [63]. This estimation requires data from the mission definition, an estimation of the aerodynamics, engine performance, and the operational empty weight (OEW) to estimate the maximum take-off weight (MTOW) and the fuel weight. In the first iteration, the OEW is expressed in terms of the MTOW based on reference aeroplanes. In subsequent iterations, the OEW estimated with the class II weight estimation will be used.

After the first iteration of the class I weight estimation, a preliminary layout is made which is used to estimate the OEW with the class II weight estimation as described in 'Synthesis of subsonic airplane design' by Torenbeek [79]. The result of this class II weight estimation forms the input for a new iteration of the class I weight estimation. The weight change has its effect on the planform. Therefore, the aerodynamic properties also change with every iteration. The new aerodynamic properties are updated in the class I weight estimation together with the updated OEW of the class II weight estimation.

A MATLAB script is used to perform these iterations automatically. In Figure 10.1 the automated part is indicated with a large background. When the weight estimation is finished, the centre of gravity is calculated by using the rules of Torenbeek. With the preliminary layout a preliminary analysis is done for the stability and controllability of the aeroplane. During the optimisation process, the wing position, tail distance, tail surface area and the influence of a shift in centre of gravity due to cargo drop have been taken into account.

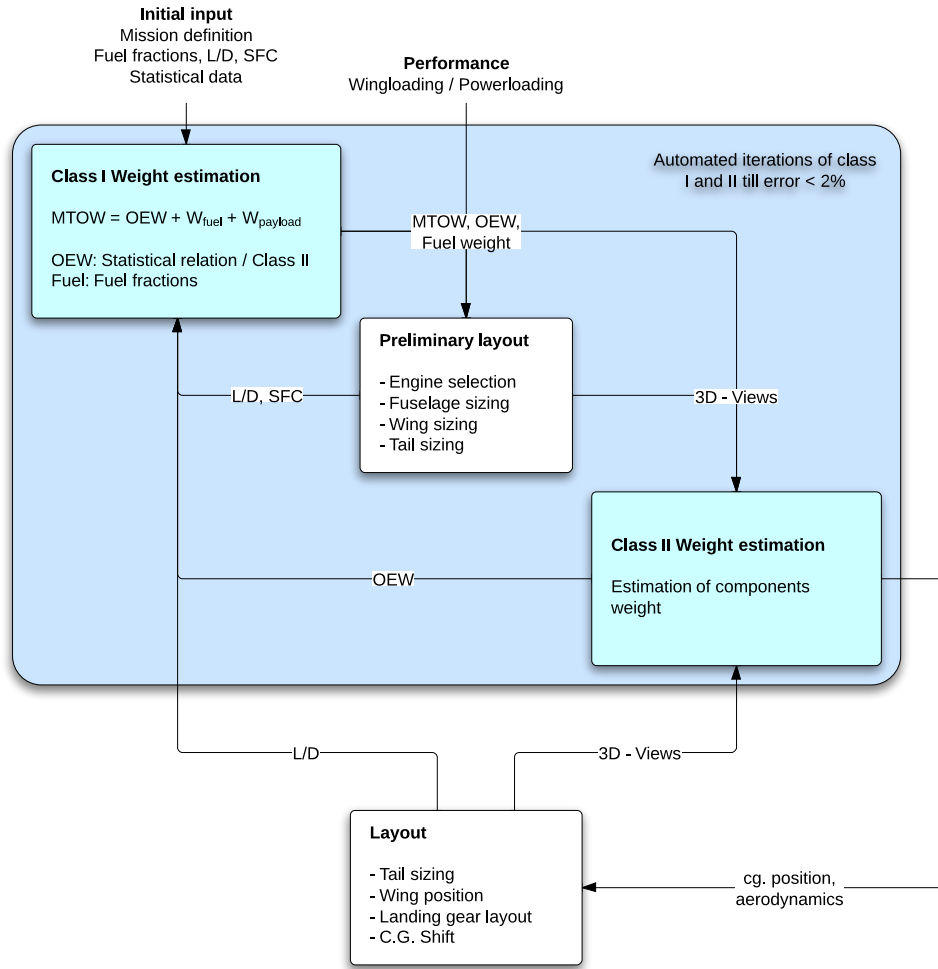


Figure 10.1: Design methodology to estimate the weight and layout of the aeroplane

## 10.2 Class I weight estimation

Since few details of the aeroplane are known in this phase of the design, the class I weight estimation method is chosen. It produces an estimation of the required fuel based on the aerodynamic efficiency, engine efficiency and the range. Equation 10.1 shows the main equation of the estimation.

$$W_{to} = W_{oe} + W_{fuel} + W_{payload} \quad (10.1)$$

Where  $W_{to}$  is MTOW,  $W_{oe}$  the OEW,  $W_{fuel}$  the fuel weight and  $W_{payload}$  the payload weight. In the first iteration the OEW is calculated using a statistical relation between the OEW and the MTOW based on reference aeroplanes. In further iterations the OEW is known directly from the second class weight estimation. The payload weight is dictated by the mission definition, and set to 600 kg. The fuel weight is calculated using Equation 13.15.

$$W_{fuel} = (1 - M_{ff}) \cdot W_n \text{ where } M_{ff} = \left( \frac{W_{n+1}}{W_n} \right) \quad (10.2a)$$

$$R = \left( \frac{\eta_p}{gC_p} \right) \left( \frac{L}{D} \right) \ln \left( \frac{W_n}{n+1} \right) \quad (10.2b)$$

Where  $M_{ff}$  is the fuel fraction which determines the amount of fuel consumed by the aeroplane during a particular phase of the mission. The product of all the fuel fractions determines the amount of fuel used during the entire mission. Equation 10.2b is used to calculate the largest contribution to the fuel fractions; the fuel used during cruise. It shows that the most important factors for the fuel weight are the range  $R$ , the engine efficiency  $\eta_p$ , the specific fuel consumption by the engine  $C_p$  and the aerodynamic efficiency  $L/D$ . More details on the class I weight estimation can be found on page 106 of the mid-term report.

## 10.3 Preliminary layout

Using the output of the class I weight estimation, it is possible to generate a preliminary layout of the aeroplane. By multiplying the wing- and power loading, which are generated in Chapter 11, with the MTOW, one obtains the required engine power and the wing surface area. Next to that, most of the dimensions are derived from literature or reference aeroplanes. It is necessary to have a preliminary idea of what the aeroplane will look like to make an initial component weight estimation. The choices made, and the initial values used for the different components of the aeroplane are described in the corresponding subsections of the class II weight estimation.

## 10.4 Class II weight estimation

In the class II weight estimation, a prediction is done for the most influential components of the aeroplane. The components are: the wing, the fuselage, the tail, the landing gear, the propulsion, the airframe services and equipment, the nacelles, and the control surfaces. They can be divided into three main groups: the airframe structure, the propulsion group and the airframe services and equipment. In this section the weight of all the components will be calculated. When summing up the weight of all the components the OEW is obtained. Since all the equipment was designed in sufficient detail during the design, the initial weight estimation has been updated to the exact value.

### 10.4.1 Wing

The weight of the wing is first calculated using Equation 10.3. In the early stage of the design process, it is not known whether high lift devices are required; hence, they are not taken into account until decided otherwise.

$$\frac{W_w}{W_G} = 4.90 \cdot 10^{-3} b_s^{0.75} \left( 1 + \sqrt{\frac{b_{ref}}{b_s}} \right) n_{ult}^{0.55} \left( \frac{b_s/t_r}{W_G/S} \right)^{0.30} \quad (10.3)$$

Where  $b_s = b/\cos(\Lambda_{1/2})$  is the structural span, and  $b_{ref} = 1.905m$  is the reference span given for this estimation method. The gross weight is assumed to be the MTOW. Equation 10.3 shows that the wing weight depends on the span ( $b$ ), the quarter-chord sweep ( $\Lambda_{1/2}$ ), the ultimate load factor ( $n_{ult}$ ), the thickness at the root ( $t_r$ ) and the surface area ( $S$ ). The wing weight may be reduced by 5% since the undercarriage is not mounted on the wing, which is the case since it will be mounted to the fuselage. This initial estimation can be refined using Equation 10.4.

$$W_{w_{basic}} = 4.58 \cdot 10^{-3} \cdot k_{no} k_\lambda k_{uc} \cdot [n_{ult} (W_{des} - 0.8W_w)]^{0.55} \cdot b^{1.675} (t/c)_r^{-0.45} \cos(\Lambda_{1/2})^{-1.325} \quad (10.4)$$

Where  $k_{no} = 1 + \sqrt{\frac{b_{ref}}{b_s}}$  represents a weight penalty due to skin joints, non-tapered skin, minimum gauge, etc..  $k_\lambda = (1 + \lambda)^{0.4}$  accounts for the taper ratio and  $k_{uc} = 0.95$  corrects for the fuselage-mounted undercarriage. The design weight ( $W_{des}$ ) is assumed to be the MTOW.

The flaps are calculated separately, using Equation 10.5.

$$\frac{W_{HLD}}{S_f} = 2.706 (S_f b_{fs})^{3/16} \cdot \left[ \left( \frac{V_{lf}^2 \sin(\delta_f) \cos(\Lambda_f)}{100 (t/c)_r} \right) \right]^{3/4} \quad (10.5)$$

Where  $V_{lf} = 1.8 \cdot V_{stall}$  is the airspeed over the flaps during landing. The formula has been chosen for single slotted trailing edge high lift devices. No leading edge devices will be used. The wing weight is the basic wing weight plus the weight of the high lift devices.

### 10.4.2 Tail

According to Torenbeek, the tail area can be estimated by taking 4% of the OEW, 2-3% of the MTOW, or with Equation 10.6.

$$W_{tail} = 0.64 \cdot (n_{ult} * S_{tail}^2)^{0.75} \quad (10.6)$$

Where the  $S_{tail}$  is the surface area of the tail. Using this formula, the tail weight is only 2% of the OEW and less than 1% of the MTOW. For that reason, 4% of the OEW is taken as an estimate.

### 10.4.3 Body

According to Torenbeek, the fuselage weight is difficult to predict with a generalised method, since there are a lot of additional weights varying with every design. Varying components from design to design are floors, cutouts, attachments and support structures and other structural features. The fuselage weight is affected primarily by the gross shell area, defined as the area in contact with the air outside. For Al-alloy fuselages, the basic fuselage weight is shown in Equation 10.7.

$$W_f = 0.23 \sqrt{V_D \frac{l_t}{b_f + h_f}} S_G^{1.2} \quad (10.7)$$

Where  $V_D$  is the design dive speed, which is 1.3 times the cruise speed. The gross shell area is defined in Equation 10.8.

$$S_G = \pi D_f l_f \left( 1 - \left( \frac{2}{\lambda_f} \right)^{2/3} \right) \cdot \left( 1 + \left( \frac{1}{\lambda_f^2} \right) \right) \quad (10.8)$$

Where the fineness ratio  $\lambda_f = l_f/D_f$ . The weight penalties are: +7% because the main landing gear is attached to the fuselage and an extra +10% for freighter aircraft. It is assumed that the gross shell area is 15% less than calculated here, since the tail-part of the fuselage will be significantly smaller than the part where the payload is located.

#### 10.4.4 Landing gear

The landing gear is one of the components of the aeroplane which needs to be designed according to safe-life criterium. It may not fail in any case, and no cracks are allowed. The landing gear can be subdivided into: wheels, main structure and items such as the retraction mechanism. The weight of the undercarriage can be calculated using Equation 10.9.

$$W_{uc} = k_{uc} \left( A + B \cdot W_{to}^{3/4} + C \cdot W_{to} + D \cdot W_{to}^{3/2} \right) \quad (10.9)$$

Where  $k_{uc} = 1.08$  for high-wing aeroplanes. By filling in different values for A, B, C and D the weights of either the main landing gear or the nose landing gear can be calculated. The values used to calculate the weights were taken from Torenbeek his method and are shown in Table 10.1.

**Table 10.1:** Constants used to calculate the landing gear weights

Landing gear configuration		A	B	C	D
Retractable	Main	18.1	0.131	0.019	$2.23 \cdot 10^{-5}$
	Nose	9.1	0.082	-	$2.97 \cdot 10^{-6}$

#### 10.4.5 Surfaces control

The surface controls group weight can be divided into three subcomponents: cockpit controls, automatic pilot and system controls. The system controls are: the manoeuvring controls, the leading edge flaps, and the brake controls. Since there is no cockpit, these controls are ignored. The automatic pilot is part of the electronics, which is accounted for in the airframe services and equipment. Therefore, the surface controls only consist of system controls, which are 0.8% of the MTOW.

#### 10.4.6 Nacelles

For aeroplanes with turboprop engines, the nacelles weight is given by Equation 10.10

$$W_n = (0.0635 + 0.018) \cdot P_{to} \quad (10.10)$$

The second value (0.018) is a weight penalty since the main landing gear is retractable into the nacelles.

#### 10.4.7 Propulsion

The propulsion group consists of the following sub-components: the engine installation, gear boxes and drives, the air induction system, exhaust system, fuel system, and more. To predict the weight of the propulsion group for a propeller aircraft Equation 10.11 can be used.

$$W_{pg} = k_{pg} N_e (W_e + 0.109 P_{to}) \quad (10.11)$$

Where  $k_{pg} = 1.16$  for a single tractor propeller in the fuselage. One part of the equation depends on the engine weight whilst the other part depends on the take-off power required.

#### 10.4.8 Airframe services and equipment

The airframe services and equipment can be divided into the following sub-components: auxiliary power unit (APU) group, instruments and navigation, hydraulics, and electronics. Since the weight of the APU depends on the bleed airflow per person required, it is neglected in a UAV. For single-engine propeller aircraft, the instruments weigh 3.6 kg per pilot and the radio weighs 13.6 kg in total. The UAV will be equipped with single NAV/COM equipment intended for invisible flight rules (IFR) operations. The weight of the NAV/COM can be calculated using Equation 10.12.

$$W_{NAV/COM} = 54.4 + 9.1N_e + 0.006W_{to} \quad (10.12)$$

The weight of the hydraulics can be calculated using Equation 10.13.

$$W_{hydraulics} = 0.277W_e^{4/5} \quad (10.13)$$

The power required by the electrical systems is at most 6 kW, while the engine delivers around 290 kW weighing around 120 kg. Since the power will be extracted from the engine using a small generator, the weight of the primary power system is assumed to be 2% of the engine weight.

## 10.5 Results of the weight estimation

During the design process of the UAV the input parameters varied several times before arriving at the final design. The first calculations on the aerodynamics showed that no flaps were required to drop the cargo and land safely, but during the design process it was decided to install flaps which changed the wing weight. The initial guess of the aerodynamic efficiency  $L/D$  was also lower than the final value. The final results of the weight estimation are shown in Table 10.2.

**Table 10.2:** Final results of the weight estimation

Components	Weight [kg]
Maximum take-off weight	2,448
Operational empty weight	1,021
Fuel	818
Wing	186
Fuselage	255
Tail	41
Nose gear	11
Main gear	119
Propulsion	183
Airframe services and equipment	180
Nacelles	26
Surfaces control	20

## 10.6 Discussion of the weight estimation

In Table 10.2, the results of the weight estimation are shown. To see whether the design is moving in the right direction, the results will be verified in this section. With a range of 2,000 km and a flight time of around six hours, one can label the UAV as a long-haul freighter aeroplane. In his work, Torenbeek presents the component weights of this type of aeroplane with respect to the MTOW. Table 10.3 shows the UAV compared to reference aeroplanes.

**Table 10.3:** Comparison between component and group weights of the design and reference long-haul turboprop cargo aeroplanes

Group	Percentage of MTOW		
	Design	Reference AC (100%)	Difference [%]
Operational empty	41.2	43.5	-5.3
Airframe structure	26.9	26.5	+1.5
Propulsion	7.5	10.0	-25.0
Equipment	7.3	7.0	+4.3
Wing	10.0	10.0	0.0
Tail	3.1	2.5	+24.0
Body	10.0	11.0	-9.0
Landing gear	5.3	6.0	-11.7

The OEW of the design is lighter than reference freighters. One of the explanations can be that the cargo of the UAV is relatively small, hence the structure of the UAV can be light compared to the amount of fuel required. The propulsion group is 25% lighter than reference freighters, which is a significant difference. The propulsion group is mainly influenced by the initial engine weight as well as the required engine power. The cruise velocity at 400 km/h is lower than the cruise speed of reference freighters which may cause the difference. The UAV will also carry relatively more/heavier equipment. This can be explained by the fact that the UAV is designed to fly fully automated beyond the line of sight. Therefore, the redundancies and flight rules are different and require more instruments.

The wing is comparable to reference freighters. The weight of the wing is largely influenced by the surface area of the wing. Since the surface area is directly related to the wing loading, which is comparable to reference aeroplanes, the weight of the wing is in the same range as the reference freighters. The tail of the UAV is 24% heavier than for reference aircraft. It can occur that a cargo package is not loaded symmetrically, resulting in a change in centre of gravity. During the drop-off, the cargo package slides backwards changing the centre of gravity again. To ensure stability, a relatively large tail is required. The body is 9% lighter than for reference freighters, which can be explained by the fact that neither a cockpit nor a pressure cabin is required for a UAV. For the landing gear, the difference can be explained due to the low MTOW of the UAV compared to reference freighters, since the landing gear can be less complex. For example, the main gear can provide a sufficient shock absorbance stroke with a cantilever beam while larger freighters need complex shock dampers.

## 10.7 Balance

When designing an aeroplane, stability is an important aspect of the flight characteristics. Although some fighter-planes are designed neutrally unstable to improve their controllability, for passenger or cargo planes it is desirable to be stable in all the flight phases. Before the stability analysis can be performed, the centre of gravity must be calculated. Torenbeek suggested some rules of thumb to estimate the locations of the different components, shown in Table 10.4.

**Table 10.4:** CG locations of the different components

	<b>Component</b>	<b>CG Location</b>	<b>Distance from nose [m]</b>
<b>Structure</b>	<i>Wing (half)</i>	40% chord from LE at 40% semi-span from center line	4.50
	<i>Fuselage</i>	36% of fuselage length from nose	3.96
	<i>Tailplane (half)</i>	42% chord from LE at 38% semi-span from center line	10.55
	<i>Nacelles</i>	40% of nacelle length from nose	4.50
	<i>Surface control system</i>	100% MAC from LEMAC	5.49
	<i>Alighting gear</i>	At the determined locations	main: 5.31, nose: 1.1
	<b>Engine</b>	50% of engine length from the nose	0.55
	<b>Airframe equipment</b>	Where most of the instruments will be placed	5.5
	<b>Fuel tanks</b>	Same as wings	4.50
<b>Aeroplane</b>	<b>Before drop</b>	At take-off, carrying payload and fuel	4.42 (34% MAC)
	<b>After drop</b>	After dropping the cargo, full fuel tanks	4.33 (29% MAC)
	<b>End of mission</b>	Before landing, almost without fuel	4.17 (20% MAC)
	<b>Extreme during drop</b>	During drop (Half cargo length shift)	4.67 (48% MAC)

The CG location of the half-wing is chosen for a straight wing configuration, of the fuselage is chosen for a single tractor engine, of the half tailplane is chosen for a conventional tail. The CG location of the landing gear is derived from the landing gear layout calculations described in Subsection 10.4.4, of the engine is derived from the propulsion analysis described in Subsection 10.4.7, and of the fuel is assumed to coincide with the wing. The CG range of the complete aeroplane is from 20 to 34% MAC. Reference aircraft according to Torenbeek have a centre of gravity range varying between 15 to 36% MAC, hence the results of the weight estimation and balance are in a reasonable range.

To support the design process, a MATLAB script has been written to visualise the layout of the UAV. The CG locations of the different components are added to support the allocation of the components. The layout of the UAV is shown in Figure 10.2.

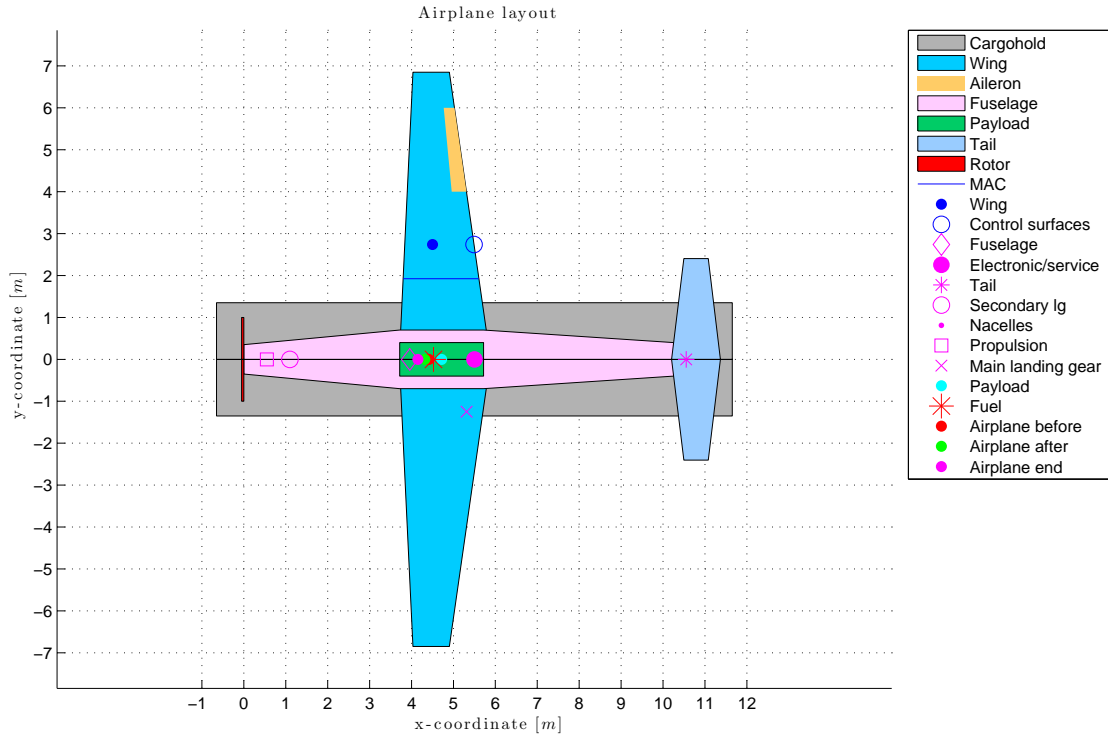


Figure 10.2: Top view of the UAV with the CG locations of all the components

## 11 | Aerodynamics

The following chapter will present the aerodynamic considerations that have been made during the detailed design of the UAV. The wing configuration with its design parameters will be explained in Section 11.1. Section 11.2 contains information on the tail design, while Section 11.3 on the selection of the aerofoil for the main wing. Section 11.4 describes the selection of the high lift devices. Section 11.5 presents the results of the aerodynamic analysis of the wing using the software XFLR5. Section 11.6 presents the methods for determining the take-off and landing distances and Section 11.7 contains a sensitivity study on the results of the aerodynamic analysis. Finally, Section 11.8 presents the main recommendations for the aerodynamic analysis.

All the parameters used in this chapter can also be found in a table in Appendix E.

### 11.1 Wing parameters

Throughout this section, design methods from the book ‘Aircraft Design: A Conceptual Approach’ by Daniel P. Raymer are used [80]. The initial step for sizing the wing area was the approximation of the maximal wing loading. A loading diagram with power loading ( $W/P$ ) plotted against wing loading ( $W/S$ ) was generated to identify the design point as shown in Figure 11.1. According to the loading diagram, with a limiting  $C_{L_{max}}$  clean of 1.5 for a cruise stall speed of  $175\text{ m/s}$ , the design wing loading was set at  $1,152\text{ N/m}^2$ . This wing loading was verified using data from reference single propeller aircraft and UAVs, with an average wing loading of  $1,177\text{ N/m}^2$  as shown in Table 11.1. In combination with the aircraft weight of  $2,448\text{ kg}$ , as computed in Chapter 10, the wing area was calculated to be  $20.8\text{ m}^2$ .

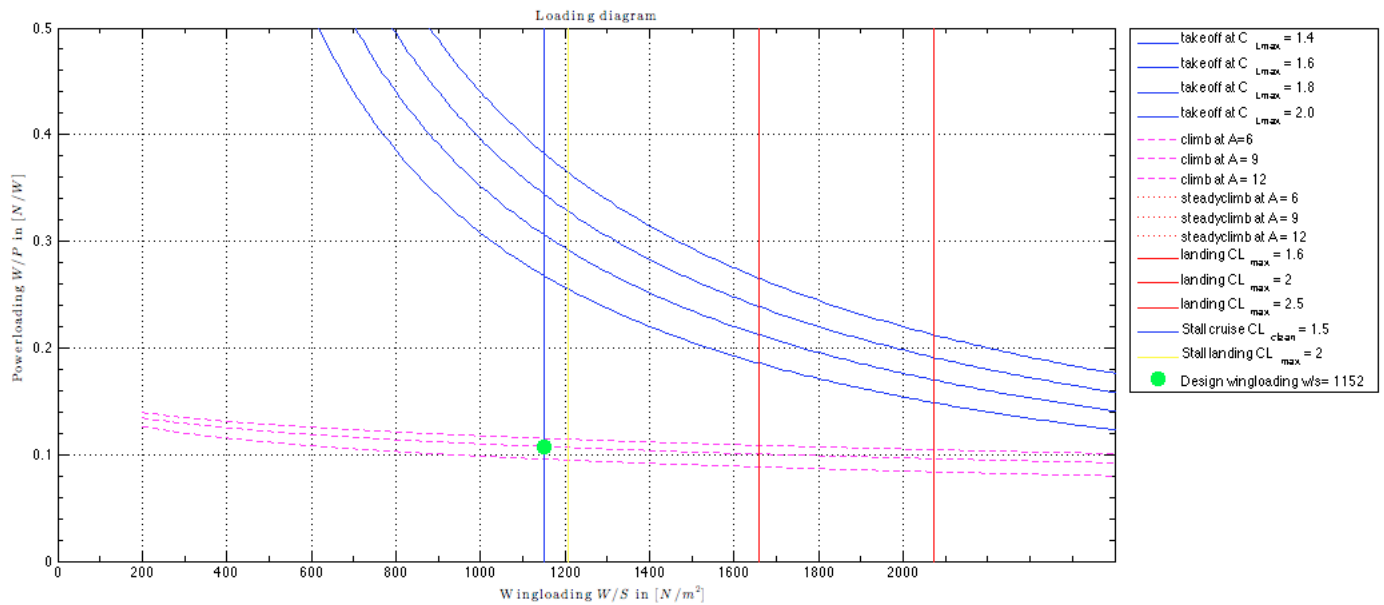


Figure 11.1: Wing loading diagram

Similar to the wing loading, the aspect ratio (AR) was also based on reference aircraft as shown in Table 11.1 and estimated to be  $AR = 9$ . As it can be seen from the data in the table, the aspect ratio was based on manned aeroplanes rather than UAVs, since the mission in terms of range and payload is more similar to the reference manned aeroplanes' missions. The reference UAVs in the table are mostly designed for a high endurance mission and not for fast cargo delivery.

Table 11.1: Wing loading comparison with reference aircraft

Propeller aircraft (single engine):	MTOW [kg]	Wing loading [ $N/m^2$ ]	Span [m]	AR [-]
Cessna caravan	3,629	1,369.2	15.9	9.7
Cessna grand caravan ex	3,995	1,507.3	15.9	9.7
Cessna turbo stationair	1,633	1,001.2	11.0	7.6
Beechcraft Queen Air	3,992	1,434.5	15.3	8.6
Pilatus PC-12 NG	4,740	1,801.6	16.3	10.3
Pilatus PC-6	2,800	911.0	15.9	8.4
Singular	3,800	1,331.4	14	7.0
<b>Average AR manned aeroplanes:</b>				<b>8.8</b>
<b>UAVs:</b>				
Darkstar	3,900	725.9	21	15
Predator B	4,500	814.2	20	17.5
Predator	1,020	873.1	14.8	19
<b>Average</b>	---	<b>1,177.0</b>	<b>16.0</b>	<b>11.3</b>
<b>Chosen design range (point)</b>	---	<b>approx. 1,152</b>	<b>13.6 - 15.6</b>	<b>9 - 12</b>

Since the design was done according to a cruise speed of  $400 \text{ km/h}$  at an altitude of  $6,100 \text{ m}$  as will be discussed in Chapter 12.1.3), the design Mach was calculated to be 0.35. Below a Mach of 0.4, there is no aerodynamic reason for wing sweep, as mentioned in the lecture slides of the TU Delft course AE2101 [81]). This is because sweep is mainly used at transonic and supersonic speeds, to reduce the adverse effects of the flow. Therefore, it was decided to not use sweep on the main wing.

Wings with none to little sweep normally have a taper ratio of 0.4 – 0.5. Taper has an effect on the lift distribution along the span. According to the Prandtl wing theory, minimum induced drag- the drag due to lift- is generated when the lift is distributed elliptically over the span. For an unswept wing, a taper of 0.4 gives an almost elliptical lift distribution. Therefore, a taper of 0.4 was chosen on the main wing.

For the chosen aerofoil, see Section 11.3, the lift coefficient at zero angle of attack was higher than the design lift coefficient. To optimise the cruise for horizontal flight, the aircraft should fly preferably at an angle of attack of  $0^\circ$ . In order to reduce the lift coefficient to the design lift coefficient during cruise, the aeroplane could either fly at a small negative angle of attack or a wing incidence angle could be set. This angle is the pitch angle of the wing with respect to the fuselage. For an untwisted wing, the wing incidence angle corresponds to the angle between the fuselage axis and the wing's aerofoil chordline. No twist is used on the wing, since the aerofoil on the main wing stalls from the root chord and a twist angle is mainly used to prevent wing tip stall. Therefore, a small negative wing incidence angle of  $-0.5^\circ$  is used so that the aircraft can fly horizontally during cruise.

Due to the engine mounted at the nose of the aircraft, it was decided to use a high-wing configuration in order to prevent the airflow from being disturbed by the propeller before reaching the wing. The angle of the wing with respect to the horizontal plane is called the dihedral angle. The wing dihedral is composed of the geometrical dihedral and the effective dihedral which results from wing sweep. Positive dihedral tends to generate a moment which tends to roll the aeroplane level whenever it is banked, and is thus a stabilising feature. For high-mounted wings, there is a stabilising dihedral effect, since air pushed over the top of the fuselage pushes up against the forward wing. Therefore, for unswept, high-mounted wings, no geometric dihedral is required.

From the selected main wing parameters, the wing geometry was determined. The root chord and the tip chord were calculated using trigonometry, which resulted in a root chord of  $2.17\text{ m}$  and a tip chord of  $0.870\text{ m}$ .

### 11.1.1 Unconventional design considerations

For the design of the UAV multiple configurations can be thought of, amongst others the canard configuration. One of the major advantages of the use of this system is that no negative lift is created by the tail, that would need to be compensated by the wing, as is the case for the traditional configuration (tail located behind the wing). As a consequence, this generally decreases the induced drag created by the aeroplane.

However, in the case of the cargo UAV to be designed, a canard configuration would pose some significant downsides. For the drop of the cargo unit a large stability is required to handle the shift in centre of gravity (cg) This range is rather limited for canard designs.

It has been decided that in order to serve as a counteracting weight, the propeller engine should be placed in the front of the UAV. Placing the horizontal stabilisers of a canard configuration directly behind this engine would result in a disturbed flow over the stabilisers. A canard configuration is chosen because the stabilisers have undisturbed flow. This is not the case with a front mounted propeller though.

Furthermore, it was decided that a part of the fuel required for the journey would be stored inside the wings to reduce the bending moment created when the UAV instantly loses weight after the drop and an upwards resultant force acts on the wing. For a canard the fuel cg would lie further behind the total aeroplane cg than in conventional designs. This would have a negative effect on the stability during the drop, since the distance between the aircraft cg and fuel cg would then be larger. All the information provided in this section was based on information provided by Dr.ir. Gianfranco La Rocca in the 'Systems Engineering and Aerospace Design course' [82].

Based on this it has been decided that the canard configuration is not a suitable option in order to perform this mission in the best possible way.

## 11.2 Tail design

The required surface area needed to allow for effective use of the tail is determined by the stability analysis, as is the optimal tail configuration. Both are discussed in Chapter 14. Based on these required surface areas for the horizontal and vertical tail, the actual design has been generated. This design process will be discussed in this section.

### 11.2.1 Horizontal tailplane

The surface area for the horizontal tailplane was determined to be  $4.2\text{ m}^2$ . From the many tails that have been designed for aeroplane over the years, a number of ground rules have been established, which are the following for the horizontal tailplane: an aspect ratio (AR) of approximately five and a taper ratio between 0.3 and 0.5. Since cruise is the longest phase in which the UAV will be operating, a minimal lift contribution of the tail is required, since the tail creates negative lift in this instant. Based on this, the most optimal aerofoil would be one with zero camber that produces approximately zero lift at a zero degree angle of attack.

In the same analogy as the design of the wing, experimental data of aerofoils has been collected and compared with the results of XFLR5 for applicable aerofoils [83]. Based on these data the next aerofoils were found to be suitable:

NACA 64<sub>1</sub> – 012, NACA 65<sub>2</sub> – 015, NACA 66<sub>2</sub> – 015 and the NACA 66<sub>4</sub> – 021. All of these showed stall characteristics at high angles of attack between 15 and 20°. When including the effect of downwash the effective angle of attack as seen by the tail is even less, meaning that the flow over the horizontal tailplane of these aerofoils will not stall before the stall of the wing.

The other major requirement of the horizontal tailplane is to have it create a minimal amount of drag. The NACA 66<sub>2</sub> – 015 creates the least amount of drag with a drag coefficient ( $C_d$ ) of 0.0034 at an angle of attack of zero degrees. The rest of the aerofoils had  $C_d$  values around 0.0040 or higher, resulting in the use of the NACA66<sub>2</sub> – 015 for the horizontal tailplane. A representation of this aerofoil can be found in Figure 11.2a.

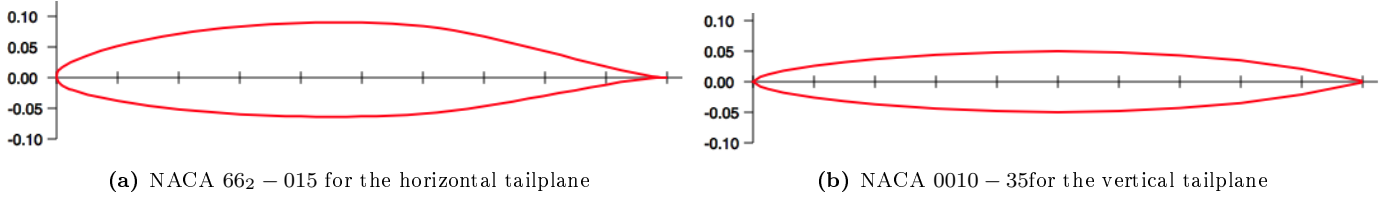


**Figure 11.2:** The aerofoils used for the horizontal and vertical tailplane of the UAV [2]

The following formulae were used for the sizing:

$$AR = \frac{b^2}{S} \quad (11.1) \quad S = \frac{b}{2}(c_r + c_t) \quad (11.2)$$

In Equation 11.1 AR is the aspect ratio of 5, b is the span of 4.58 m, based on surface area S of 4.2 m<sup>2</sup>. Combined with a taper ratio of 0.4 this results in a root chord ( $c_r$ ) of 1.31 m and a tip chord of 0.524 m when rewriting Equation 11.2. Since the UAV will be operating below a Mach number of 0.4 no sweep angle is required.

### 11.2.2 Vertical tailplane

For a vertical tail a symmetric aerofoil is required, since the UAV should not yaw into a certain direction when no control forces are applied on the rudder. The aerofoils have been compared, using the same method as for the horizontal tailplane: NACA 0009, NACA 0010 – 34 and the NACA 0010 – 35. The latter creates the least amount of drag ( $C_d$  of 0.0035) and was therefore chosen as the aerofoil to be used for the vertical tailplane. A visualisation of the NACA 0010 – 35 aerofoil can be found in Figure 11.2b.

Just as for the design of the horizontal tailplane some guidelines are available for the design of a vertical tail: AR should be in the range of 1.2 to 1.8 for conventional tail layout, taper ratios vary from 0.4 to 0.6 and the sweep angle is in the order of 35° to 40° [84], [85].

From the stability analysis it was determined that a surface area of 1.59 m<sup>2</sup> was required for the vertical tailplane. In combination with the guidelines and Equations 11.1 and 11.2 a vertical tailplane has been designed that has an AR of 1.5, taper ratio of 0.4, resulting in a span (b) of 1.54 m, a root chord length ( $c_r$ ) of 1.47 m and a tip chord length ( $c_t$ ) of 0.588 m. The sweep angle has been set to 40°.

## 11.3 Aerofoil selection

The selection of the aerofoil is primarily based on cruise conditions. The most important parameter for the aerofoil is the design lift coefficient  $C_{L_{des}}$  during cruise which can be estimated from Equation 11.3. The lift coefficient can then be converted to the 2D design lift coefficient  $C_{l_{des}}$  using Equation 11.4.

$$C_{L,des} = 1.1 \frac{1}{q} \left\{ \frac{1}{2} \left[ \left( \frac{W}{S} \right)_{start\ cruise} + \left( \frac{W}{S} \right)_{end\ cruise} \right] \right\} \quad (11.3) \quad C_{l_{des}} = \frac{C_{L_{des}}}{\cos^2 \lambda} \quad (11.4)$$

where q is the dynamic pressure at cruise altitude, W is the aircraft weight and S is the wing reference area.  $\lambda$  is the sweep angle. Since the wing is unswept,  $C_{l_{des}} = C_{L_{des}}$ . The design lift coefficient was calculated to be 0.27.

### 11.3.1 Lift distribution

Unswept wings with a taper of 0.4 have an almost-elliptical lift distribution [81]. From the elliptical lift distribution given in ‘Fundamentals of Aerodynamics’ by Anderson [86], the lift distribution over the wings of the UAV can be approximated. Equation 11.5 gives the elliptical lift distribution per unit span.

$$L' = \rho_\infty V_\infty \Gamma_0 \sqrt{1 - \left( \frac{2y}{b} \right)^2} \quad (11.5) \quad \Gamma_0 = \frac{4L}{\rho_\infty V_\infty b \pi} \quad (11.6)$$

where  $L'$  is the lift distribution per unit length,  $\rho_\infty$  is the freestream air density and  $V_\infty$  is the freestream velocity.  $\Gamma_0$  is the circulation at the origin,  $y$  is the distance along the span,  $b$  is the wing span and  $L$  is the total lift. The lift distribution can therefore be expressed as shown in Equation 11.7.

$$L' = \frac{L}{b\pi} \sqrt{1 - \left(\frac{2y}{b}\right)^2} \quad \text{for} \quad -\frac{b}{2} \leq y \leq \frac{b}{2} \quad (11.7)$$

This relation is used as an approximation for the loading of the wing as an input to the structural analysis presented in Chapter 13.

To select an appropriate program to analyse the aerofoil, XFLR5 (based on XFOIL) and JavaFoil were compared. Initially, two aerofoils were analysed from the NACA 6-digit series (NACA 63<sub>3</sub>-418 and NACA 64<sub>2</sub>-415) with design lift coefficients of 0.4. The design Reynolds number during cruise can be calculated from Equation 11.8.

$$Re = \frac{\rho V c}{\mu} \quad (11.8)$$

where  $\rho$  is the air density,  $V$  is the airspeed,  $c$  is the average chord length and  $\mu$  is the dynamic viscosity of air.

The Reynolds number during cruise is calculated as 6.8 million. To validate the programs, the two aerofoils were analysed for Reynolds numbers of 6 and 9 million, since experimental data was provided at those Reynolds numbers in [83]. From comparing the lift coefficients as simulated by XFLR5 and JavaFoil to experimental windtunnel data, it was concluded that XFLR5 produces more accurate results. Consequently, this program was chosen for further analysis. Although producing results closer to reality than JavaFoil, XFLR5 overpredicted the aerofoil design lift coefficient by approximately 11 – 14% whilst underpredicting the maximum lift coefficient by 3 – 5%.

After the program selection, two aerofoils with zero-lift coefficients close to the design lift coefficient were chosen for further analysis: the NACA 64<sub>3</sub>-418 and the natural laminar flow (NLF) aerofoil NLF(1) – 0416, developed by NASA. Both aerofoils were designed for  $C_l = 0.4$  with maximum thicknesses of 18% and 16% of the chord length, respectively. The NLF aerofoil was selected, since there was a closer fit between experimental data provided by Somers in his paper in [87]) and the results generated by XFLR5. The NLF aerofoil can be visualised in Figure 11.3.

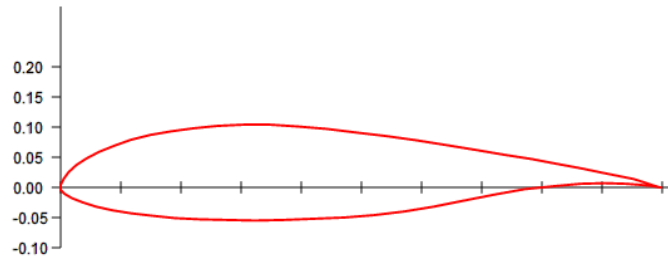


**Figure 11.3:** Visualisation of the NLF(1) – 0416 aerofoil used for the wing [2]

Figure 11.4 displays the overall layout of the main wing in combination with its horizontal and vertical tail wings. This image was generated with XFLR5 and displays the approximate lift and drag distribution in cruise.

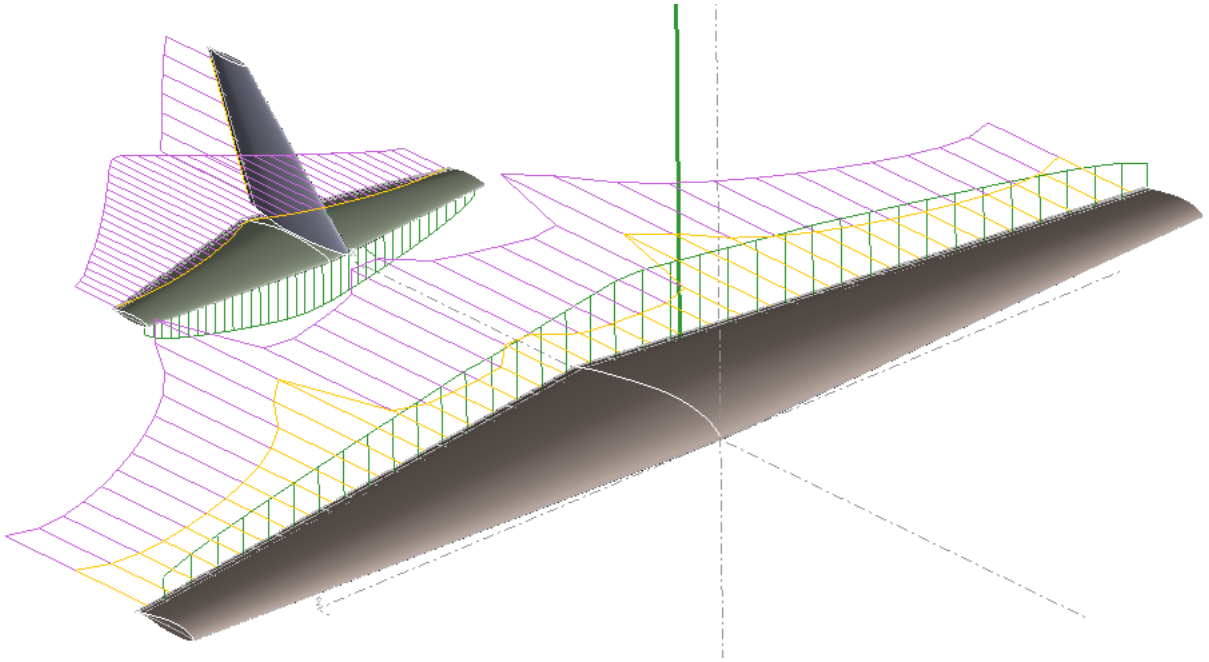


Figure 11.4: Overall wing layout with lift and drag distributions generated by XFLR5

## 11.4 High lift devices

Regulatory aviation organisations such as the Federal Aviation Regulations (FAR) and European Aviation Safety Agency (EASA) have determined the minimum speed requirements that aircraft need to be able to fulfil. For general aviation type aircraft these regulations are combined in FAR23 [88] and CS-23 [89]. These organisations stipulate that the stall speed at maximum weight ( $V_{stall}$ ) should not exceed  $113 \text{ km/h}$ , the take-off speed is  $1.2V_{stall}$  and the landing speed is  $1.3V_{stall}$ . Without the use of high lift devices (HLDs) the stall speed requirement for the UAV would be violated.

The most commonly used type of HLDs on small aircraft are either plain flaps or single slotted flaps due to limited space available in the wing. The program used for modelling the wing (XFLR5) does not allow to model different types of flaps, nor was there any experimental data available for the NLF(1) – 0416 aerofoil with flap combination. This would make it impossible to validate the increase in  $C_L$  provided by the program. As a result, an analytical approach was used to size the required flaps. This approach was based on the following formulae from Raymer’s aircraft design book [80]:

$$\Delta C_{L_{max}} = 0.9 \Delta C_{l_{max}} \frac{S_{wf}}{S} \cos(\Lambda_{H.L.}) \quad (11.9) \quad \Delta \alpha_{0L} = (\Delta \alpha_{0L})_{airfoil} \frac{S_{wf}}{S} \cos(\Lambda_{H.L.}) \quad (11.10)$$

Where in Equation 11.9  $\Delta C_{l_{max}}$  is the change in the 2D lift coefficient when flaps are included. For the landing case this is 0.9 for the plain flap and 1.3 for the single slotted flap. In Equation 11.10  $\Delta \alpha_{0L}$  is the change in zero lift angle of attack due to the use of HLDs. In both Equation 11.9 and 11.10  $S_{wf}/S$  is the ratio indicating the wing surface area that is flapped over the complete wing surface area and  $\Lambda_{H.L.}$  is the hinge line sweep angle (equal to zero since no sweep required).

### Worst case landing scenario and cargo drop scenario

The flap sizing for this UAV has been based on the requirements for dropping the cargo unit and for the worst case landing scenario. During the drop procedure it is most beneficial to fly as level as possible, which is explained in Chapter 18. This can be achieved when the  $C_{L_{max}}$  value is increased to 2.2, which is a reasonable value for aircraft with flaps extended [90]. For the worst case landing scenario it is assumed that the UAV will have to land as fast as possible after take-off, for instance after a technical malfunction. This means that it will have to be able to land with nearly its take-off weight.

With the increase of the  $C_{L_{max}}$  value to 2.2 it is possible to land the UAV safely with its full weight. This  $C_{L_{max}}$  value will therefore be used for the flap sizing.  $C_{L_{max}}$  of the wing during landing was computed to be 1.57, which leads to a change in  $C_L$  ( $\Delta C_L$ ) of 0.63. Correspondingly, using Equation 11.9 this leads to a  $S_{wf}/S$  ratio of 0.540. Combined with the surface area of  $20.8 \text{ m}^2$  and using trigonometry the length of the flaps can be computed, which turns out to be  $3.25 \text{ m}$  on each side of the wing. The wing length from fuselage to tip is  $6.15 \text{ m}$ . This corresponds to around 53%

of the wing length being covered with flaps when the single slotted flaps are used, which leaves enough space on the wing for the ailerons. From reference aircraft it has been estimated that most of the time the part of the wing covered with flaps varies from 40% to 60% [91] [92] [93]. The space needed in the wing for single slotted flaps is around 25% of the wing's chord length. This space is available since the rear spar of the wing box is located at 57.1% as explained in Section 13.3 in Chapter 13. of the wing chord length.

For the drop-off part of the mission the required  $C_L$  and correspondingly the angle of attack have been computed based on the approximate weight at the moment just before the drop, which was found to be around 2,025 kg to 2,050 kg

Turning to the change in zero lift angle of attack, Equation 11.10 can be used. Based on the aircraft design book by Raymer [80] it is assumed that the aerofoil change in zero lift angle of attack during landing is equal to  $15^\circ$ . In turn this leads to a change in the wing's zero lift angle of attack of  $8.1^\circ$ .

The visualisation of the change in maximum lift coefficient and zero lift angle of attack for the two cases described here can be found in Figure 11.5a. In the same figure the angles of attack have been indicated.

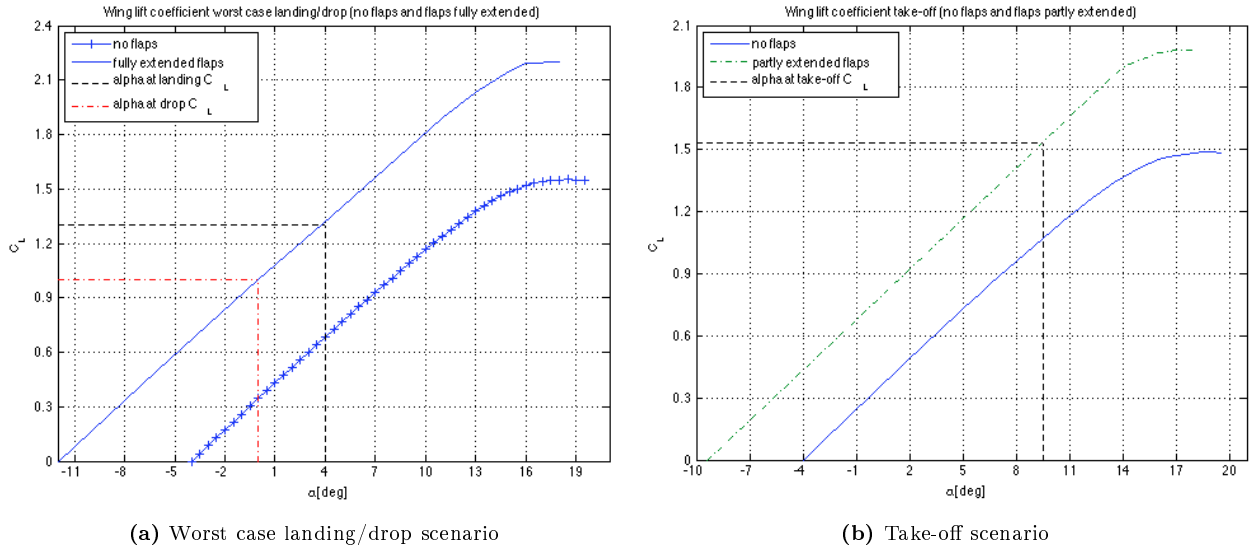


Figure 11.5: Change in lift coefficient and angle of attack for the drop/worst case landing and the take-off scenario

### Take-off scenario

For take-off, the flaps are usually extended to a lesser extent, which can be accounted for by taking a lower value for the 2D lift coefficient of approximately 60 to 80% of the 1.3 value used for landing sizing [80]. In order to limit the angle of attack at which the UAV would have to take off, this value has been set to 75%, leading to a  $\Delta C_{l,max}$  of 0.975 and a  $\Delta C_{L,max}$  of 0.473. Doing so allows the UAV to take off at an angle of attack of  $9.5^\circ$ . The take-off angle of attack for general aviation aircraft is on average between  $8^\circ$  and  $12^\circ$  [94].

For the change in zero lift angle of attack of the aerofoil, as needed in Equation 11.10, a value of  $10^\circ$  should be used for take-off according to Raymer. This leads to a change in the zero lift angle of attack of  $5.40^\circ$ .

The change in the lift coefficient during take-off can be seen in Figure 11.5b.

## 11.5 Aerodynamic simulation

Having selected an aerofoil on the main wing, the wing was modeled in XFLR5 with an aspect ratio of 9, zero sweep and a taper of 0.4. 2D and 3D analyses were then carried out under cruise conditions where  $Re_{avg} = 6.8$  million. An important assumption that was made was that the accuracy of XFLR5 in predicting the lift and drag coefficients was the same for the 3D analysis as for the 2D analysis. From comparison between experimental data given in ‘Theory of wing sections’ by Abbott and von Doenhoff [83] for the aerofoil at a Reynolds number of 6 million (the experimental data available closest to cruise conditions) and the program, the following conclusions could be drawn:  $C_{l,des}$  was over-predicted by 11% whilst  $C_{l,max}$  was underpredicted by 3%. The results from the 3D analysis during cruise condition were corrected accordingly which resulted in a  $C_{L,des}$  of 0.37 and a  $C_{L,max}$  of 1.8.

Throughout the entire analysis of the wing, the assumption was made that the wing has to generate 110% times the lift required to carry the total weight of the aircraft ( $L = 1.1L_{tot}$ ). This is a valid assumption made for conventional aircraft design to compensate for the negative lift contribution generated by the tail to trim the aeroplane. Taking this assumption into account, the effective  $C_L$  of the aeroplane was determined to be 0.33 and the effective

$C_{L_{max}}$  was 1.6.

The aeroplane drag coefficient during cruise can be estimated with the relation given in Equations 11.11 and Equation 11.12.

$$C_D = C_{D_0} + C_{D_i} \quad (11.11) \quad C_{D_i} = \frac{C_L^2}{\pi AR e} \quad (11.12)$$

where  $C_D$  is the total aircraft drag coefficient,  $C_{D_0}$  is the zero-lift drag coefficient,  $C_{D_i}$  is the induced drag,  $C_L$  is the cruise lift coefficient,  $AR$  is the wing aspect ratio and  $e$  is the Oswald factor.

The zero-lift drag can be estimated from the different components of the aeroplane according to methods given by Roskam [95]. During cruise the following aeroplane components contribute to the overall drag: the main wing, the fuselage, the nacelles, the horizontal tail and the vertical tail. Table 11.2 displays the individual zero lift drag components (denoted  $C_{D_\pi}$ ) as estimated. Although, the window-less UAV will generally have lower fuselage drag, it was assumed that the effect of placing a camera at the bottom of the fuselage would in turn lead to a drag increase. Hence, the conventional drag estimation methods by Roskam were assumed to be applicable.

**Table 11.2:**  $C_{D_0}$  components for different parts of the UAV

Aircraft components	$C_{D_\pi}$	$S_{ref} [m^2]$	$C_{D_\pi} S_{ref} [m^2]$
Wing	0.01	20.82	0.14
Fuselage	0.11	1.54	0.17
Nacelles	0.06	3.14	0.19
Horizontal tail	0.01	4.00	0.03
Vertical tail	0.01	2.00	0.02
<b>Total</b>			<b>0.54</b>

The overall zero-lift drag coefficient can be approximated by summing up all the individual drag components times their reference areas and dividing by the wing reference area. This results in an overall  $C_{D,0}$  of 0.026 during cruise.  $C_D$  for the entire aircraft based on  $C_L = 0.33$  results in a total  $C_D$  of 0.035. According to [96], for  $C_L = 0.3$  a typical value for  $C_D$  is 0.02, which is of the same order of magnitude.

Additional drag is produced by the landing gear and the high lift devices during take-off and landing (during the cargo drop-off additional drag is produced only by the high lift devices). This increase in drag can also be estimated using the methods given by Roskam. For the landing gear, Equation 11.13 can be used for estimating the drag increase.

$$\Delta C_{D,gear} = \frac{S_G}{S_{ref}} (C_{D_{G_{C_L=0}}} + p C_L) \quad (11.13)$$

where  $S_G$  is the reference area used for landing gear drag coefficients,  $S_{ref}$  is the aeroplane reference area,  $C_{D_{G_{C_L=0}}}$  is the zero-lift drag coefficient of the landing gear based on  $S_G$ . For the main landing gear  $S_G$  is  $a \cdot b$  where  $b$  is the vertical distance from the top of the strut to the bottom of the wheel and  $a$  is the horizontal distance from the wheel to the strut; for the nose landing gear  $S_G$  is  $B \cdot D$ , where  $B$  is the tire width and  $D$  is the tire diameter. The same tires are used on both the main landing gear and on the nose gear. The factor  $p$  accounts for the variation of  $\Delta C_D$  with lift. From the nose and main landing gear geometry, the increase in drag due to the main landing gear is  $\Delta C_{D,main} = 0.0035$  and  $\Delta C_{D,nose} = 0.0004$  during take-off and 0.0007 during landing; The overall drag coefficient of the aircraft in take-off configuration is  $C_D = 0.166$ , during drop-off  $C_D = 0.162$  and during landing  $C_D = 0.166$ .

## 11.6 Take-off and landing distances

Based on the total aeroplane drag during take-off and landing, the take-off and landing distance can be estimated. For take-off the ground distance can be calculated using Equation 11.14 and 11.15 and for landing Equations 11.16 and 11.17 can be used. These equations have been provided with the lecture material of the course AE2104, Flight and Orbital Mechanics [97].

$$s_{ground} = \frac{WV_{LOF}^2}{2g(\bar{T} - \bar{D} - \bar{D}_g)} \quad (11.14)$$

$$s_{scr} = \left( \frac{V_{scr}^2 - V_{LOF}^2}{2g} + h_{scr} \right) \frac{1}{\sin(\gamma_{scr})} + s_{LOF} \quad (11.15)$$

where  $W$  is the aircraft weight,  $V_{LOF}$  is  $1.1V_{stall}$  is the speed at lift-off,  $g$  is the acceleration due to gravity.  $\bar{T}$ ,  $\bar{D}$  and  $\bar{D}_g$  are the average thrust, drag and ground drag due to the tires, respectively. The ground drag is calculated by the product of the normal force  $N = W - L$  and the surface friction coefficient of the runway  $\mu$ . For  $\mu$  a value of 0.03 was used for take-off from dry concrete/asphalt (applicable to the runways at Punta Cana international airport) and a value of 0.4 for brakes on during landing, according to Table 17.1 in [80]. The runway was assumed to be dry, since effects of a wet runway are accounted for with the safety factors used later on. The average values in Equation 11.14 occur at a speed of  $V$  is equal to  $V_{LOF}/\sqrt{2}$ .  $V_{scr}$  is the screen velocity which is approximately  $V_{scr}$  equals  $1.2V_{stall}$ ,  $h_{scr}$  is the screen height (10.7 m according to the CS-23 regulations for small utility aircraft by EASA [89]).  $\gamma_{scr}$  is the flight path angle at screen height which is taken to be  $4^\circ$  according to the airworthiness regulations set by EASA. Solving for  $s_{scr}$  results in the total take-off distance.

$$s_{airborne} = \frac{\frac{V_A^2}{2g} - \frac{V_T^2}{2g} + h_{scr}}{\frac{1}{2}[\sin\gamma_A + (\frac{C_D}{C_L})_T]} \quad (11.16)$$

$$s_{ground} = \frac{W}{2g} \frac{V_T^2}{[T_{rev} + \bar{D} + \bar{D}_g]} \quad (11.17)$$

where  $V_A$  is the approach speed,  $V_T$  is the speed at touch-down,  $\gamma_A$  is the approach angle (which is set at  $4^\circ$  by EASA) and  $(C_D/C_L)_T$  is the inverse of the aerodynamic ratio during approach.  $T_{rev}$  is the average reverse thrust to slow down the aircraft.

It should be noted that according to airworthiness regulations for the take-off and landing distances safety factors of 1.15 (to account for a wet runway) and 1.15 (10/6) are applied, respectively.

From Equations 11.14, 11.15, 11.16 and 11.17 the distance required during take-off is 1,097 m and the distance for landing is 877 m. Both calculated at maximum take-off weight to make sure that the aircraft is able to land safely in case of an emergency straight after take-off. Punta Cana International Airport has two runways with a length of 3.1 km each [98]. In Equation 11.17 the approximation has been made that the average reverse thrust is equal to 50% of the maximum thrust available. It should be noticed that the required take-off and landing distances thus fall well below the available runway length.

Take-off and landing distances for comparable aircraft are displayed in Table 11.3.

**Table 11.3:** Take-off distance for a few aeroplanes of comparable size as the UAV designed

Reference aircraft	MTOW [kg]	Take-off distance [m]
Cessna Citation Mustang	3,960	948
Pilatus PC-6	2,800	440
Predator B	4,763	610

## 11.7 Sensitivity study

The aim of this section is to indicate the effect of a 25% increase in the velocity required to perform the mission and consecutively indicate the effects of a 25% increase in weight.

### 11.7.1 Increase in velocity

The current Mach number of the UAV during cruise is 0.352 where the velocity is 400 km/h. An increment of 25% would result in a velocity of 500 km/h (Mach number of 0.439). For wings operating at a Mach number below 0.4 there is no aerodynamic reason to use swept wings. Since the Mach number has increased, an entirely different analysis of the aerofoil would be needed to determine whether sweep would be required and to what extent. In the worst case scenario this would mean that due to the sweep, the lift capabilities will be diminished (or heavier structure is needed for same lift), the lift over drag ratio would decrease, resulting in a larger fuel consumption. Furthermore, there would be an increase in the tip loading and a possible reduction in the effectiveness of the use of high lift devices.

### 11.7.2 Increase in weight

One of the problems often encountered in the design of aircraft is staying within the weight constraints imposed on the project. Therefore this subsection will discuss the effects of a 25% increase in weight. If this increment in weight does not include, or only partially includes the increase in surface area there will be an increase in the wing loading. The value of this wing loading determines the design lift coefficient of the wing. In the worst case scenario, where the increase in the weight is not counteracted by an increase in the surface area, the wing loading at the start of the cruise (on the way to Haiti) will increase from 1,153 N/m<sup>2</sup> to 1,406 N/m<sup>2</sup>. The same happens at the end of cruise (at drop

location), where the wing loading would increase from  $983 \text{ N/m}^2$  to  $1,228 \text{ N/m}^2$ . As a result, using Equation 11.18 indicated that the design lift coefficient ( $C_{l_{des}}$ ) would increase from 0.27 to 0.36.

$$C_{l_{des}} = 1.1 \frac{1}{\frac{1}{2}\rho V^2} \left\{ \frac{1}{2} \left[ \left( \frac{W}{S} \right)_{start\ cruise} + \left( \frac{W}{S} \right)_{end\ cruise} \right] \right\} \quad (11.18)$$

Looking just at the wing this would mean that its contribution to the drag would increase from a  $C_D$  value that used to be 0.0085 to a  $C_D$  value of 0.0095. This would mean that the same aerofoil could still be used, however as a compromise it will create more drag that will in turn require more fuel consumption, which again add to the weight.

## 11.8 Recommendations

With regard to the aerodynamic analysis the following recommendations can be given for future analysis:

- Find a way to validate the results that were generated by converting the 2D aerofoil to the 3D wing. It was assumed that the deviations of the 2D analytical results from the experimental aerofoil data were the same for the 3D simulation results.
- Look into more sophisticated aerofoil analytical software that allows for the numerical analysis of a wing in the take-off and landing situation with different types of flaps extended. Another very useful software feature would be to be able to accurately analyse the complete wing-tail configuration. For XFLR5 it was not known if the analytical results for the wing-tail combination was validated.
- Construct a small-scale model of the aircraft and run windtunnel tests to obtain experimental lift and drag data. This model could also be used to optimise the shape of the fuselage for minimum drag.

# 12 | Propulsion analysis

This chapter discusses the propulsion system of the UAV. In Section 12.1, the type of engine will be selected. Section 12.2 explores the possibilities of different fuel types. The engine will be selected in Section 12.3. After that, Section 12.4 looks at propeller design options. A verification study will be performed in Section 18.5. / Lastly, a conclusion on the propulsion analysis will be made in Section 12.6

## 12.1 Engines

The required amount of thrust which was derived from both the mission requirements and the mission profile, has been calculated in Chapter 11. This thrust has to be generated by an engine, where various engines employ different methods of thrust generation. The purpose of this section is to determine the most suitable method to generate the required thrust. From this, the appropriate engine type will be selected in a brief trade-off. In the concept trade-off, the selection has been narrowed down to propellers. Therefore, the different types of jet engine are not considered.

### 12.1.1 Piston engine

Light aircraft are usually powered by a piston engine, which converts the reciprocating motion of a number of pistons into a rotating motion. The piston engine has a relatively low power-to-weight ratio. With power-to-weight values of between 0.5 and 1.0, it is outclassed by turboprops on performance by a factor of four [99]. Figure 12.1 shows a cross section of a typical piston engine.

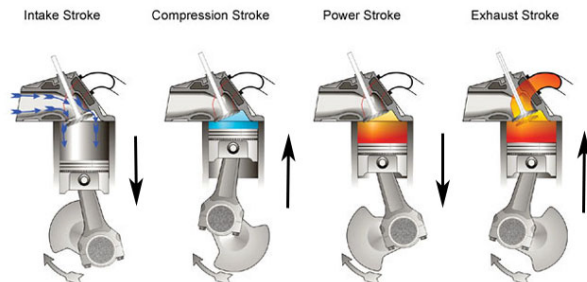


**Figure 12.1:** Graphical representation of the longitudinal cross section and workings of a piston engine

Being the engine of choice in the automotive industry, the piston engine costs less than a typical gas turbine engine. The working principle of a piston engine is more complex than that of turbine powered engines, which is why they have

a relatively low time between overhaul (TBO). The TBO gives an indication on the overall reliability of the engine and lies in the range of 1,200 to 2,000 hours for a piston engine. For efficiency considerations, piston engines are not flown at altitudes above 9,000 *m* and Mach numbers higher than 0.4. Typical ranges for piston powered aircraft are less than 2,000 *km*, as found in 'All the world's aircraft' by Janes [100].

### 12.1.2 Gas turbines

Gas turbines are a class of engines which use principles of the Brayton cycle in order to convert internal energy into mechanical energy. There are four main categories of gas turbines; turbojets, turboprops, turboshafts and turbofans. Gas turbines suitable for aviation-propeller configurations are the turboprop and the propfan. The propfan is a combination of turbofan- and turboprop technology. These engines will be considered as gas turbine options for the propulsion of the UAV.

#### Turboprop

With a turboprop configuration, most of the thrust is provided by the propeller. Figure 12.2 shows a graphical representation of a longitudinal cross section of a turboprop engine.

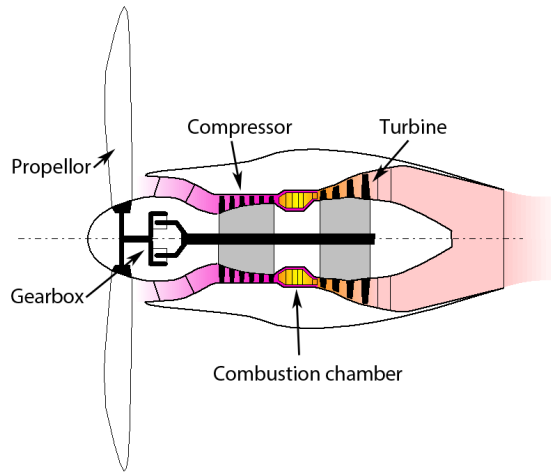


**Figure 12.2:** Graphical representation of the longitudinal cross section of a double spool turboprop engine [3]

The engine is designed to use about 90% of the generated power to drive the propeller. The other 10% is mostly used to drive the compressor, leaving only a small percentage of energy leaving the engine in the form of exhaust gases. The propeller is coupled with the turbine through a gearbox that converts the high revolutions per minute (RPM) at low torque input to low RPM and high torque. This is necessary due to the nature of propellers. If they spin too fast, the tips of the propeller will reach supersonic conditions which leads to a large increase in drag. Turboprops conventionally fly in airspeed ranges from Mach 0.2 to Mach 0.7.

A turboprop engine is not complex since it has few moving parts. The only moving parts are the compressor, turbine and the drive train. The high complexity of the manufacturing of gas turbines however, does command large initial cost. Turboprops are best suited for altitudes of up to 6,100 *km* [101]. The average TBO for turboprop engines ranges from 3,000 *hrs* to 5,000*hrs* [102]. This is an important design parameter of the design since the engine has to be taken apart during overhaul. Turboprops have few moving parts compared to piston and propfan counterparts which explains the long TBO. An example of a possible turboprop engine is the Pratt & Whitney PT6A-34AG.

#### Propfan

With a propfan configuration, the thrust is provided by the propeller. Figure 12.3 shows a graphical representation of a longitudinal cross section of a propfan engine [3].

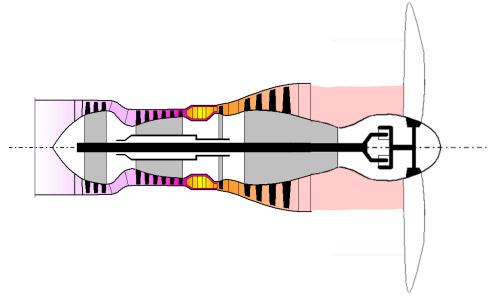


**Figure 12.3:** Graphical representation of the longitudinal cross section of a single spool propfan engine [3]

An evolution in turboprop design resulted in the propfan concept. A propfan is a crossover between a turbofan and a turboprop. The propfan uses the same mechanism as a turboprop to generate power. However, the gas turbine drives a rear propeller instead of one on the front-end. The propeller is designed with highly twisted blades which resemble turbofan compressor blades. The design was made to offer the speed of a turbofan with the efficiency of a turboprop. The propfan was designed for transonic airspeeds which ranges from Mach 0.7 to Mach 0.9. At sea level this corresponds to a minimum airspeed of  $238\text{ m/s}$  or  $857\text{ km/h}$ . At sea-level this corresponds to a maximum airspeed of  $306\text{ m/s}$  or  $1,102\text{ km/h}$ .

Operating at these higher speeds commands a large disk loading to keep the diameter of the propeller small, in order to prevent supersonic tip speeds. This design choice results in the use of more blades than a conventional turboprop in order to maximise the absorbed power of the propellers. A propfan has between six and twelve blades, compared to the typical two to six for a turboprop [99]. In order to reduce wave drag, the blades are scimitar-shaped and swept. The propfan engine is quite similar to the turboprop in both terms of complexity and manufacturing. The manufacturing of the scimitar-shaped blades is more complex.

Propfans are best suited for altitudes of up to  $6,100\text{ km}$  since they rely on the same principles as conventional propellers. The TBO for propfan engines is estimated to be similar to those of turboprop engines. The estimated TBO is thus  $3,000\text{ hrs}$ . The propfan is a concept which has never been employed on commercial aircraft. Unfortunately, this creates a lack of statistical data from which the TBO can accurately be derived. The TBO is thus estimated in the more conservative side of the turboprop TBO range. An example of a possible propfan engine is the Pratt & Whitney R-2800 Double Wasp.

### 12.1.3 Engine trade-off

The choice of engine greatly determines the flight envelope since it fixes the amount of power that is available at every altitude. This has strong repercussions on the maximum angle of attack, maximum speed, stall speed and manoeuvrability of the aeroplane. From the characteristics of the suitable engines a trade-off has been made. The specifications of the engines are given side-by-side in Table 12.1.

**Table 12.1:** Engine specification

Specifications	Piston engine	Turboprop engine	Propfan engine
Mach range	0.1-0.4	0.2-0.7	0.4-0.8
Relative complexity	3	1	2
TBO [hrs]	<2,000	3,000-5,000	3,000
Operation altitude [m]	3,700	6,100	6,100
Average power-to-weight ratio	0.8	2.4	2.4

From Table 12.1 the differences in the engine types can be seen. The piston engines disadvantages of heavy weight and high complexity coupled with a low operational altitude lead to it being discarded as the optimal engine for the mission. The main advantage of the piston engine is that it is initially cheaper than gas turbines and more efficient at speeds below Mach 0.3. The propfan and turbofan rely on the same working principle yet use different configurations. The propfans main advantage is that it can reach speeds which turboprops cannot due to wave drag. The mission does not require speed which enter the transonic zone. The blades for propfan configurations are very complex and weight more due to higher disk loading. The advantage of higher TBO and a more reliable concept make the turboprop the best choice for the design. The turboprop is chosen as the engine type for the design.

By choosing the turboprop, the optimum cruise conditions should be used by the UAV. The optimum cruise velocity should lie between 400 *km/h* for the greatest efficiency [103]. The corresponding altitude for a small turboprop lies around 20,000 *ft*, or 6,100 *km*.

## 12.2 Fuel type

Aircraft engines require higher quality fuel than generally used in the automotive industry. Furthermore, aviation fuel often contains additives to reduce the chance of freezing or igniting at extreme temperatures.

The typical fuel used in turboprop engines is jet fuel. There are a number of qualities to which jet fuel must comply. For instance, it is important that there is no water contamination in jet fuel. Due to the low temperatures at high altitudes, the water might form droplets which can supercool to below freezing points and potentially block pipe inlets. Fuel containing unacceptable amounts of water is usually heated to prevent ice forming. Antistatic agents should also be added to dissipate any static electricity which may cause sparks.

Based on the current aviation fuel market, the typical fuel used commercially is Jet-A1 fuel. The United States military uses JP-8 fuel, which has the same characteristics as Jet-A1 apart from a few minor additives. While these fuel types are widely available, a promising option for a sustainable future is the use of biofuel.

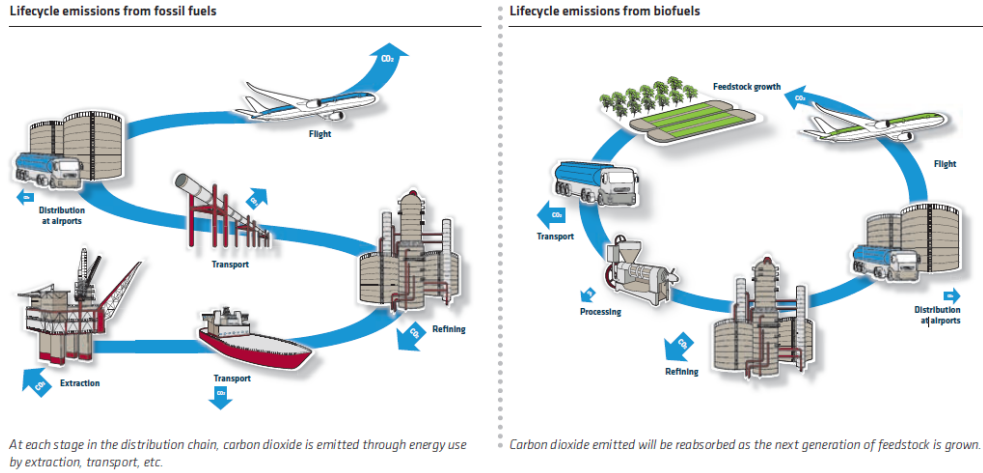


Figure 12.4: Lifecycle emissions from fossil fuels and biofuels [4]

Biomass which is grown sustainably and does not compete for land or water with food crops, also known as second generation biofuel, is the only option for biofuel in the aviation industry. Currently, several aircraft have flown with biofuel made from algae [104] [105]. The amount of carbon dioxide absorbed by plants during growth of biomass is roughly equivalent to the amount of carbon produced when the fuel is burned in an engine, as can be seen in Figure 12.5 Taking the emissions which are produced during production of biofuel into account, the total emission is anticipated to be 80% lower than for fossil fuels. Second generation biofuel has the same characteristics as fuel currently in use. This allows for its use without any modifications to existing engines. Therefore the UAV should use pure biofuel as much as possible or alternatively, blended with normal aviation fuels. ATAG has written a 'Beginners guide on aviation biofuel' [4], which contains further studies on the use of aviation biofuel, and is backed by both Airbus and Boeing.

## 12.3 Engine selection

To select the engine which is best suited for the UAV, a Matlab script which analyses general engine performance was written. The script uses gas turbine theory to calculate properties at every station in the engine. These stages comprise of the inlet, the compressor, the combustion chamber, the turbine, and the nozzle. The script strongly relies on both the isentropic relations for an ideal gas found in Equation 12.1, as well as a simplified heat balance formula as seen in Equation 12.2.

$$\left(\frac{T_2}{T_1}\right) = \left(\frac{p_2}{p_1}\right)^{\frac{\gamma-1}{\gamma}} = \left(\frac{V_1}{V_2}\right)^{(\gamma-1)} = \left(\frac{\rho_2}{\rho_1}\right)^{(\gamma-1)} \quad (12.1)$$

$$\dot{m}_{air} \cdot c_{pg} \cdot \Delta T_{cc} = \eta_{cc} \cdot \dot{m}_{fuel} \cdot LHV_{fuel} \quad (12.2)$$

The inputs of the script are based on a number of factors. First of all, properties of the international standard atmosphere (ISA) at cruise altitude are used [106]. Secondly, all engine specific values are taken from the Rolls Royce RR300 prior to the first iteration [107]. Lastly, all efficiency factors at every gas turbine station are assumed. However, these assumptions are in the same ballpark compared to typical values as found in various literature such as 'U.S. Standard atmosphere 1976 by NASA, and 'Gas Turbine Theory' by Cohen and Rogers [108] [101].

The program uses all the inputs to generate a plot of the total thrust produced by the engine for a range of powers. Since the largest contributor to this total thrust is the propeller, the program also plots the propeller thrust in the same figure. Because the only variable is the power output consumed by the propeller, the plot reaches a point where all the energy addition of the air is extracted by the propeller. In practice however, propellers are designed to produce between 80 – 90% of the total thrust.

Taking this fact in mind, the engine specific values can be tweaked to get desired values. Together with data from existing engines, several iterations were performed to get to a desired engine. Taking cruise drag from Chapter 11 as the desired total thrust, the output shaft horse power (SHP) can be read from Figure 12.6. After several iterations, the engine power found can be used to select an engine. The power is found to be approximately 290 kW, or 389 hp, as can be seen in Figure 12.6. At the selected point, the propeller produces around 85% of the total thrust.

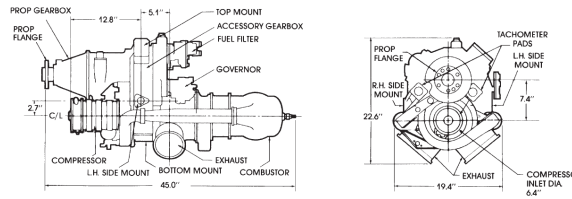


Figure 12.5: Front- and side-view of the selected M250-B17F model

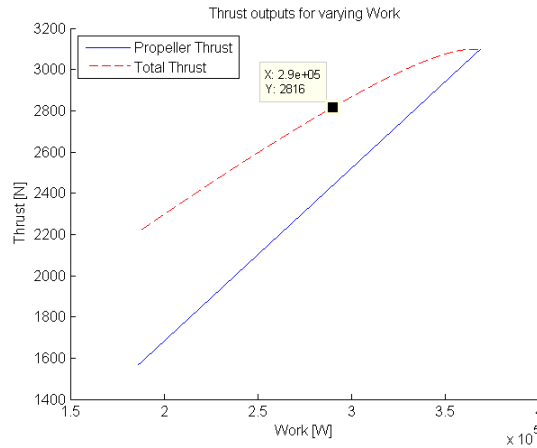


Figure 12.6: Plot of the total engine thrust and accompanying propeller thrust of the final engine

Knowing the required amount of engine power allows for the final selection of the engine. Unfortunately, there are very few turboprops in the 375 – 389 hp range. One of the most popular and trusted engines in this range is the Rolls Royce M250 family. Originally designed to be a 250 hp engine in the 1960s, its different models and applications have made it one of the best selling engines in its range. The most suitable type for the UAV is the M250-B17F [109], with an operational range of 377 – 450 hp, the engine is more than capable of providing the required power during cruise and take-off. Table 12.2 shows the selected engine compared to other similar engines. Although these engines have higher power outputs, choosing an engine which outperforms the ideal conditions will have a negative impact on fuel consumption. Therefore the Rolls Royce M250-B17F will be used in the UAV.

### 12.3.1 Fuel system characteristics

Having selected an engine, it is a good idea to look at its fuel consumption. This is because fuel pumps have to be installed close to the engine to deliver a constant supply of fuel. Equation 12.3 shows how the required massflow of fuel can be found.

**Table 12.2:** Selected engine versus similar engines

Engine model	SHP [hp]	Dry weight [kg]
RR250-B17F	380	93
P&W PT6A	576	150
T-Arrius 2F	504	103
Honeywell TPE331	640	150

$$\dot{m}_{fuel} = \frac{\dot{m}C_{p_g}(T_{0_4} - T_{0_3})}{LHV\eta_{comb}} \quad (12.3)$$

Where the massflow  $\dot{m}$  is  $1.73 \text{ kg/s}$ ,  $C_{p_g}$  is  $1,150$ , combustion chamber temperature  $T_{0,3}$  is  $494.13 \text{ K}$ , turbine inlet temperature  $T_{0,4}$  is  $1,083 \text{ K}$ , combustion efficiency  $\eta_c$  is  $0.995$ , and the lower heating value LHV is  $42.8 \text{ MJ/kg}$ .

This gives a final fuel massflow of  $0.0275 \text{ kg/s}$ . Fuel pumps capable of delivering the fuel constantly at this rate should be installed. These values are all calculated with the help of the written Matlab script.

It should be noted that the engine uses its own bleed exhaust air to heat up all the fuel lines of the UAV. This is necessary as a safety precaution due to the possibility of water presence in the fuel as stated in Section 12.2.

## 12.4 Propeller design

To select an appropriate propeller to fit onto the engine, the M250 characteristics are inserted into the Matlab script. The results are found in Table 12.4 To design the most efficient propeller for the cruise conditions of the UAV, JavaProp software is used. This software takes the input of said conditions and models the most efficient propeller as output.

For given velocity and power settings, there are three factors which influence the design of the propeller. These factors are the number of revolutions per minute (rpm), propeller diameter, and number of blades. Because propellers are more efficient with increasing size, the diameter should be maximised. This is discussed in 'Propeller Efficiency' by D. Rogers [110]. However, since the fuselage has a height of  $1.2 \text{ m}$ , it is impractical to have a propeller diameter larger than  $2 \text{ m}$ . This is due to ground clearance regulations set by the FAA [111]. The M250 engine has a set  $2,013 \text{ rpm}$  shaft output, produced by the reduction gearbox, which leaves the number of blades as the only variable input.

Three different propellers will be designed, after which the best suitable option is chosen based on efficiency and weight. Propeller weight is estimated using the NASA Propeller Performance and Weight Prediction guide [112]. The weight formula of a double-acting propeller can be found in Equation 12.4.

$$Wt_{prop} = k_w \left[ \left( \frac{D}{10} \right)^2 \left( \frac{B}{4} \right)^{0.7} \left( \frac{AF}{100} \right)^{0.75} \left( \frac{ND}{20000} \right)^{0.5} (M + 1)^{0.5} \left( \frac{SHP}{10D^2} \right)^{0.12} \right] \quad (12.4)$$

Where  $k_w$  is a constant depending on the material selection, and has a value of  $355$  for aluminum propeller blades.  $D$  represents the propeller diameter,  $B$  the number of blades,  $N$  the speed in rpm,  $M$  the Mach number, and  $AF$  the activity factor of the blades.

The activity factor is defined as in Equation 12.5, with  $\sigma$  being the solidity factor [113].

$$AF = \frac{100000\pi\sigma}{128B} \quad (12.5)$$

Combining the results of the JavaProp program and the weight estimation formula in Table 12.3, it can be seen that a six-bladed propeller is the most suitable option for the needs of the UAV. Propellers with fixed diameter have higher efficiency and thrust levels when using multiple blades. Due to the lower activity factor on propellers with more blades, the structural weight also happens to be lower in this particular case.

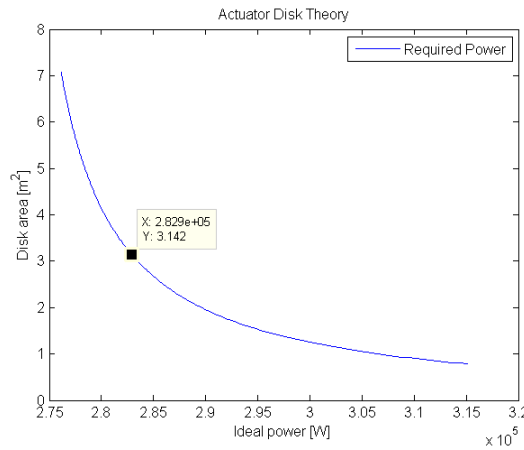
**Table 12.3:** Results of Javaprop and Equation 12.4 combined

Number of Blades B	2	3	6
Solidity sigma	0.1069	0.1064	0.104
Efficiency $\eta$	0.81	0.82	0.84
Net Thrust T [N]	2,108	2,148	2,196
Ideal Thrust [N]	2,613	2,613	2,612
Power P [kW]	290	290	290
Activity Factor	131	87	43
$W_{prop}$ [kg]	106	103	98

## 12.5 Verification

To verify the results obtained from the propeller design, it is compared to actuator disk theory. This theory helps understand the performance of a propeller and is described in Chapter 10.10 of Aircraft Design by Kundu [103]. To get the ideal performance of a disk, some assumptions were made. The rotation of the flow is neglected, and the flow is deemed incompressible. Furthermore, the flow is steady, and the velocity changes continuously over the disk. The minimum ideal required power can be found with Equation 12.6. Figure 12.7 shows the required power for different disk areas. It also shows that the minimum ideal required power for a propeller of two meters in diameter is about 283 kW, which is less than the calculated 325 kW from the Matlab script. Due to the various inefficiencies in the engine, the actual power should lie higher by a small margin. Therefore, it can be assumed that the Matlab script performs correctly.

$$P_{ideal} = \frac{1}{2}Tu_0 \left[ \left( \frac{T}{A_{disk}u_0^2 \frac{\rho}{2}} + 1 \right)^{0.5} + 1 \right] \quad (12.6)$$

**Figure 12.7:** Plot of the ideal disk power for varying surface area

## 12.6 Conclusion

The final results of all the engine calculations can be found in Table 12.4. It features the values that resulted from the various iterations of the Matlab script, as well as the final values which resulted from inserting the final engine and propeller into Matlab. The difference is also represented in the last column.

Overall, the choice of engine type is arguably the biggest decision in the propulsion analysis. On one hand there is the piston engine, which is considerably cheaper than the turboprop engine. On the other, the turboprop engine offers the best solution from a technological point of view. Since the UAV project is aiming at the best solution compared to the cheapest, this major design decision is deemed valid.

As for fuel type, there is no question as to whether or not to make use of biofuels. Not only is this good for the environment, the media publicity will work towards a more sustainable future.

Based on the self-generated Matlab script, the engine analysis proved to be of sufficient quality to provide representable thrust and power values. Further investigation should try to look into the use of professional software like GasTurb12, to either verify self made programs or to act as primary software.

**Table 12.4:** Engine values before and after final engine and propeller choice

	Matlab	Final	Difference
Thrust [N]	2,816	2,816	0 %
Propeller thrust [N]	2,437	2,671	9.6 %
Diameter [m]	2	2	0 %
Required power [kW]	290	325	12 %
Required power [hp]	389	436	12 %
Mass fuel flow [kg/s]	0.0275	0.0275	0 %

## 13 | Structural and material analysis

This chapter describes the structural and material analysis. After discussing general aspects needed for a structural analysis together with the assumptions, the applied theory will be discussed. The results of the analytical analysis (dimensions) will be used to perform a Finite Element Method (FEM)-analysis in Abaqus.

### 13.1 Reference frames

The reference frames for the cross-sections and 3D models of both the wingbox and fuselage can be found in Figures 13.1 and 13.2.

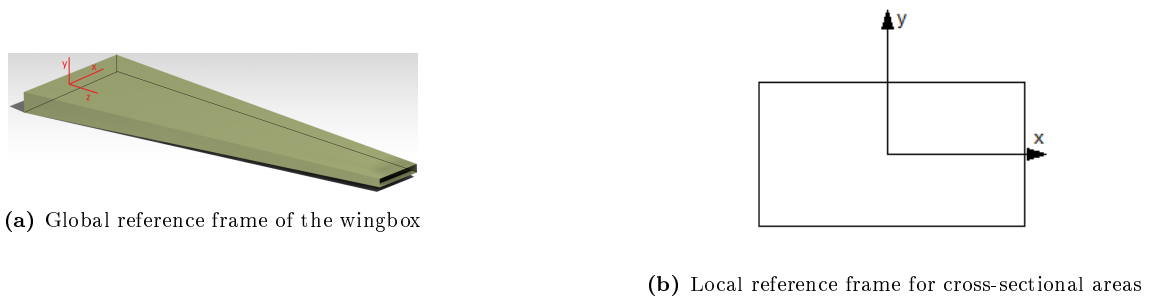


**Figure 13.1:** Reference frames wing

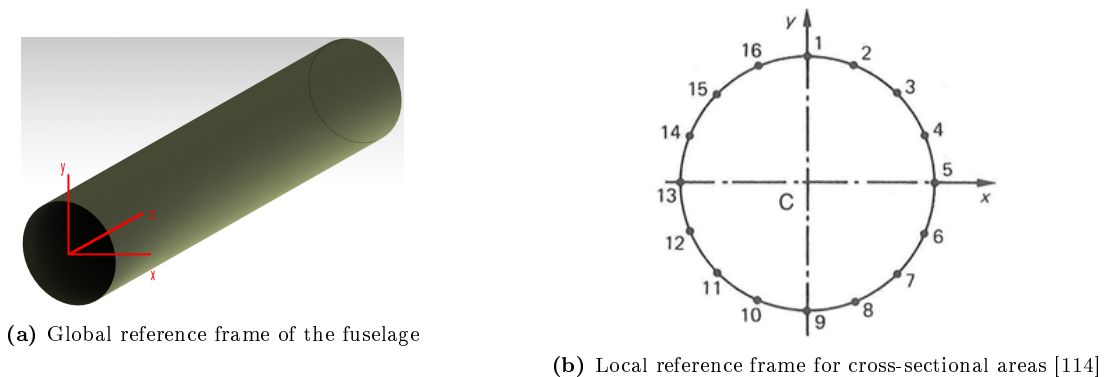


**Figure 13.2:** Reference frames fuselage

### 13.2 Assumptions

To be able to perform an analytical analysis using Matlab, some assumptions need to be considered. Below one can find general assumptions together with assumptions related only to the wing and to the fuselage.

**General assumptions:**

- **Structures are homogeneous (one material)** - Taking this assumption gives that all cross-section have similar traits except geometry. The calculations will be performed assuming aluminium 7075-T6 as the material used.

- **Thin walled structures** - This assumptions means that a plate cannot take any shear stress in its thickness direction. This results in a different stress distribution, but in a total stress which is the same as for the real case.
- **Plane sections remain plane after deformation** - This assumption states that in a cross-section the skins, spars et cetera are always straight, meaning that no new created curvature (deflection) needs to be taken into account in further calculations.
- **Constant shear stress** - Shear stress will be assumed as being constant throughout skin.
- **Von Mises stress criteria** - The stress analysis can be performed by using the von Mises stress criteria or the Tresca yield criteria. Based on literature, the von Mises criteria turned out to be more accurate and veracious [115].

### Assumptions wing

- **Boundary condition** - The wing box is ideally clamped at the wing root (this is not in the middle of the fuselage, but just outside the fuselage).
- **Simplified wingbox** - No flaps, control surfaces et cetera will be assumed.
- **Massless wing box & zero drag** - Assuming this results in lift and fuel weight as being the only forces acting on the wing (in y-direction).
- **Linear taper (no curvature)** - This assumption makes the cross section shape fixed, which is an advantage for the extensive calculations.
- **Lift acts at quarter chord line** - By not considering the lift as a distribution over the chord length, it makes life easier since only an integral over the wingspan is required.
- **Buckling at flanges does not occur** - Since the buckling coefficient for the flanges is much higher than for the top- and bottom sheet, it will be assumed not to occur.
- **Spacing booms** - Booms are equally spaced over plates and spars.
- **Only booms carry normal loads** - The skins between booms do not carry these loads.

### Assumptions fuselage

- **Simplified fuselage** - The fuselage will be assumed as being a straight, hollow tube with a constant diameter.
- **16 stringers assumed** - To make the Matlab program less extensive as for the wing, it is assumed to have 16 stringers equally separated over the cross-sectional skin.
- **Forces acting on fuselage** - The forces and moments acting on the fuselage are considered to be the lift force, weight, tail-lift force and the pitching moment.
- **Cruise flight conditions** - In order to treat the fuselage as a (simple) static problem, only calculations are performed according to cruise flight conditions.
- **Forces acting in plane of symmetry** - Other forces are assumed to act in the plane of symmetry, as a result no torsion will occur.

## 13.3 Dimensions

From the aerodynamic analysis the dimensions of the wing are known; chord at root will be around  $2.17\text{ m}$ , chord at the tip will be  $0.87\text{ m}$  and the wingspan  $13.7\text{ m}$ . Based on this in combination with the chosen aerofoil, the dimensions of the wingbox can be determined, as can be seen in Figure 13.3. These dimensions turned out to be  $0.929\text{ m} \times 0.244\text{ m}$  ( $w \times h$ ) at the root to  $0.396\text{ m} \times 0.104\text{ m}$  at the tip over a length of  $6.15\text{ m}$ .

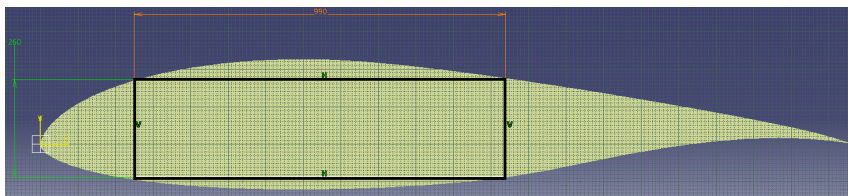


**Figure 13.3:** Derivation of wingbox dimensions from aerofoil dimensions

The fuselage will be analysed as being a constant diameter tube, its length is  $6.5\text{ m}$  and the diameter is  $1.4\text{ m}$ .

## 13.4 Load cases

In this section the load cases considered during the analysis of the wing will be shown, these values are determined in Chapter 10. The maximum load factors for every load case will be used, in the determination of the load factors is already a safety factor implemented. The following load cases will be discussed: cruise flight, turns, drop-off and ground operation.

- **Cruise flight** - In cruise flight the forces acting on the aeroplane are in equilibrium. The total lift is equal to the weight, this gives a load factor of 1.
- **Turn** - The maximum load factor for a steep turn will according to above mentioned section be equal to 1.66.
- **Drop-off** - The drop-off is a drastic change in weight, this causes also an increase in load factor. In the worst case, the drop-off during a turn will give a load factor of 2.16.
- **Ground operation** - The stresses in the wing due to the fuel can be determined by considering a situation in which no lift is generated by the wings. This is the case for an aeroplane standing on the ground.

For the first three load cases, the analysis will be performed for both empty and filled fuel tanks.

## 13.5 Failure modes

For structures in general the following failure modes can be distinguished: *buckling, fracture, yielding, fatigue and impact*. For the structural analysis in this report, the first three failure modes will be taken into account.

## 13.6 Material properties

As mentioned in Section 13.2, the chosen material is aluminium 7075-T6. This was chosen since this particular material is widely used in the industry, besides doing calculations with this material is accurate and gives proper results. If it turns out to be the wrong material, composites will be considered.

Aluminium 7075-T6 has the following properties, see Table 13.1:

**Table 13.1:** Material properties aluminium 7075-T6 [32]

Material:	E-modulus [GPa]	Ultimate Tensile Strength [MPa]	Fatigue strength [MPa]	Elongation at break [%]
Aluminium 7075-T6	72	572	159	11

## 13.7 Applied theory

This section describes the theory applied to get the stresses for both the wingbox and fuselage. The wingbox will be the main focus of this section, however the same theory can also be applied to the fuselage.

### 13.7.1 Centroid position

The wingbox and fuselage are assumed to be two axis symmetric, this yields that  $x_c$  and  $y_c$  are equal to zero.

### 13.7.2 Chord length

Due to the fact that the wing(box) is tapered, the chord length varies along the  $z$ -axis. Given a taper ratio of 0.4, Equation 13.1 shows how to calculate the chord length at every segment.

$$c_i = c_r - \frac{c_r - c_t}{l} \cdot z \quad (13.1)$$

Where  $c_i$  is the chord length at a certain segment  $i$ ,  $c_r$  and  $c_t$  are the chord length at the root and tip,  $l$  is the total length of the wingbox and  $z$  is the position of the particular segment on the  $z$ -axis.

### 13.7.3 Boom area

For this analytical analysis, the structure is idealised with booms. The wingbox is split into 'n' segments, each segment is idealised with booms, as can be seen in Figure 13.4 (the figure shows four booms, in theory it can be 'n' booms).

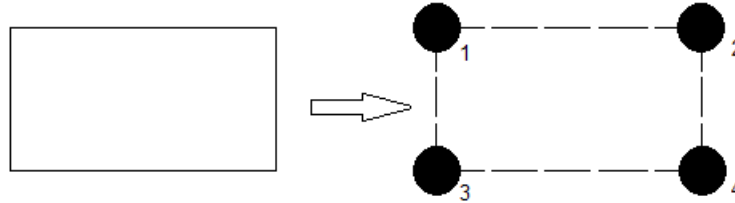


**Figure 13.4:** Non-idealised and idealised cross-section

To calculate the moments of Inertia, the areas of the booms are needed. The boom-area can be calculated with Equation 13.2 [114]. In this equation,  $b$  is the distance between two booms,  $t_d$  is the thickness of the plate between those two booms.  $\sigma_{n-1}/\sigma_n$  is equal to the ratio of the y-positions of the two adjacent booms. Since all the booms are connected to each other, the boom area includes two contributions (summation) from adjacent booms.

$$B(n) = \frac{t_d \cdot b}{6} \cdot \left(2 + \frac{\sigma_{n-1}}{\sigma_n}\right) + \frac{t_d \cdot b}{6} \cdot \left(2 + \frac{\sigma_{n+1}}{\sigma_n}\right) \quad (13.2)$$

### 13.7.4 Moments of Inertia

If the area of the booms is known, the moment of inertia can be calculated. To do so, the center of gravity point [ $x_{c.g.}$ ] must be determined first. Because of symmetry in the x-axis  $y_{cg}$  is zero, so the y-position can be defined according to the reference frame and dimensions. Since  $I_{yy}$  will not be used, also  $x_{cg}$  is not needed. For the moment of inertia only the parallel axes contribution is needed, see Equation 13.3. In this equation  $A_{boom}$  is the boom-area and  $y_{boom}$  is the corresponding position on the y-axis.

$$I_{xx} = \sum_{i=1}^n A_{boom} \cdot y_{boom}^2 \quad (13.3)$$

### 13.7.5 Shear and bending moments

In Figure 13.5 the actual shear forces acting on the wing (with fully filled fuel tanks) can be seen.

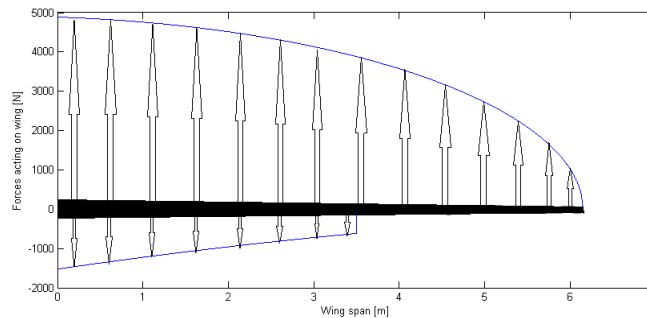


**Figure 13.5:** The lift distribution along the wing span and the (negative) shear force distribution caused by the weight of the fuel

Equations 13.4 and 13.5 show the formulae for the lift distribution and fuel weight distribution over the wingspan ( $z$ ). The latter equation only yields for the first 3.5 m of the wingspan, as explained in Chapter 10.

$$V(z)_{lift} = \frac{4 \cdot L}{b \cdot \pi} \sqrt{1 - \left(\frac{2 \cdot z}{b}\right)^2} \quad (13.4)$$

$$V(z)_{fuel} = 16 \cdot z^2 - 3.2 \cdot 10^2 \cdot z + 1.5 \cdot 10^3 \quad (13.5)$$

Where  $L$  is the total lift,  $b$  is the wingspan and  $z$  is the location of the segment along the z-axis. Since the shear forces are vectors (function of wingspan), the moment acting on every segment  $n$  can be determined using Equation 13.6.

$$M = -\frac{l}{n} \cdot \sum_{i=1}^n L(i+1) \cdot \sum_{i=1}^n z(i+1) - z(i) \quad (13.6)$$

Based on the information, with regard to forces and moments acting on the fuselage (lift of wing and tail, weight, pitching moment) from other departments, the following shear and moment diagrams can be drawn, see Figure 13.6.

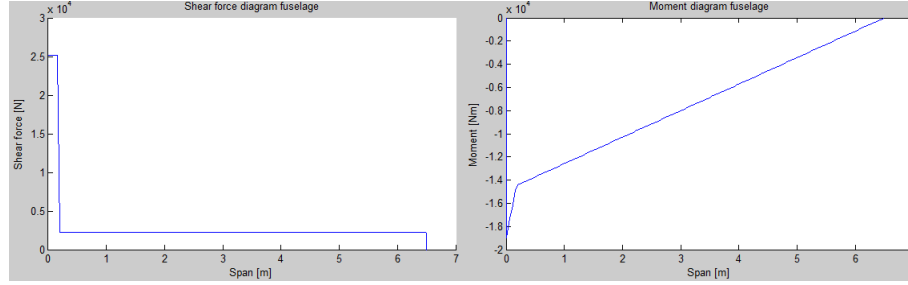


**Figure 13.6:** Shear and moment diagram for fuselage

### 13.7.6 Bending stress distribution

Now the bending moment, moment of inertia and the vertical distances from booms to centroid are known for every cross-section, the normal stresses in every boom for each segment can be calculated. Since there is no moment around the y-axis ( $M_y$ ) and  $I_{xy}$  is zero due to symmetry, the general equation for bending stress can be simplified to Equation 13.7 (see section 16.2 [114]).

$$\sigma_{z,boom} = \left( \frac{M_x}{I_{xx}} \right) y_{boom} \quad (13.7)$$

Where  $\sigma_{z,boom}$  and  $y_{boom}$  are the bending stress and y-coordinate of the booms relative to the local reference frame.

### 13.7.7 Shear stress distribution

As for the bending stress distribution, the equation for the shear flow can also be simplified. Since  $I_{xy}$  is zero, the horizontal shear force  $S_x$  is not present and  $t_D$  is also zero due to the fact that the skin only carries shear stresses. The general equation can be simplified to Equation 13.8 (see section 20.3 [114]).

$$q_{bs} = -\frac{S_y}{I_{xx}} \left[ + \sum_{r=1}^n B_r \cdot y_r \right] + q_{s0} \quad (13.8)$$

Where  $B_r$  is the boom area [ $m^2$ ] and  $y_r$  is the y-coordinate of the local reference frame.

$q_{s0}$  can be calculated by taking moments around the center of symmetry and solving for  $q_{s0}$ , Equation 13.9 shows the general approach.

$$S_y \cdot dist = \sum q \cdot length \cdot dist + A \cdot q_{s0} \quad (13.9)$$

Where  $q$  is the shear flow in each skin between two booms,  $length$  is the length of the particular skin and  $dist$  is the distance between the skin and the center of symmetry.

The resulting shear stress  $\tau$  in each cross-section can now be found by divide the shear flow by the thickness of the skin, see Equation 13.10.

$$\tau = \frac{q_{bs}}{t} \quad (13.10)$$

### 13.7.8 Von Mises stress

When all the stresses are known, they can be combined into a Von Mises stress. This von Mises stress can be used to analyse and verify the design choices of the wingbox. Equation 13.11 shows a simplified version of the general equation for von Mises stresses. In this equation the stresses gained in earlier subsections can be implemented.

$$\sigma_{vm} = \sqrt{\frac{1}{2}(\sigma_z^2 + 6(\tau_s^2 + \tau_t^2))} \quad (13.11)$$

Where  $\sigma_z$  is the bending stress,  $\tau_s$  is the shear stress and  $\tau_t$  is the stress due to torsion.

### 13.7.9 Buckling failure

One of the failure modes of a wingbox which greatly influences the design is buckling. Using Equations 13.12 and 13.13, the critical stresses according to buckling can be determined.

$$\sigma_{cr} = K_c \cdot E \cdot \left(\frac{t}{b}\right)^2 \quad (13.12)$$

$$\tau_{cr} = K_s \cdot E \cdot \left(\frac{t}{b}\right)^2 \quad (13.13)$$

Where  $K$  is the buckling coefficient for bending (c) and shear (s), these coefficients can be determined based on dimensions and boundary conditions of the wingbox [116]. It can be found that  $K_c$  is 8 and  $K_s$  is 6. The  $E$  is the E-modulus of the used material,  $t$  is the skin thickness and  $b$  is the short side of the plate.

## 13.8 Analytical tool

A Matlab code is written to do the analysis, all based on the theory described in Section 13.7. In Appendix B, the input and output constants and variables for both the wing and fuselage analysis can be found. The italic ones are the variables, the rest is a constant or is fixed by other departments.

## 13.9 Analytical results

This section shows and discusses the results for the analytical analysis. The results for the wingbox and fuselage will be treated separately. The whole design process using the Matlab tool is based on iterations, knowing how the stresses change when changing input parameters is an important aspect in these iteration processes.

### 13.9.1 Wingbox analytical results

The structural analysis started with only a wingbox made of aluminium 7075-T6, no stringer or ribs were included. It became clear that the skins would be very thick in order to carry all the stresses. That is why adding stringers and ribs was required. The amount of ribs and stringers were influencing the results a lot. The amount of ribs was chosen based on getting the highest buckling coefficient values. After selecting a certain amount of stringers it was only possible to iterate on the stringer area and stringer length. In the end a certain stringer area was chosen, with this particular stringer area it was possible to decrease the stringer length since this was less influencing the design stresses. The whole iteration process ended up with the dimensions shown in Table 13.2. The results related to these dimensions, together with the ratios of the results and the critical stresses for different load cases can be found in Table 13.3. When compared to similar problem results in for example Megson's book [114], running the program with the same values gives the corresponding results. Later on in this chapter, there will also be a comparison between these results and the Abaqus results.

**Table 13.2:** Final design considerations wingbox

<b>Subject</b>	<b>Result</b>	<b>Unit</b>
Stringers in top & bottom plate:	8	
Stringers left and right spar (incl. corners):	4	
Area stringers:	500	mm <sup>2</sup>
Length stringers:	3.7	m
Thickness all skins:	8	mm
Rib spacing (along wing span):	1	m
Material:	Aluminium 7075-T6	

**Table 13.3:** Analytical results wingbox

Load case:	Load factor:	Fuel tank:	Critical bending stress [MPa]	Max. bending stress [MPa]	Ratio:
<i>Turn</i>	1,66	<i>Full</i>	83,952	59,674	1,41
		<i>Empty</i>	83,952	62,597	1,34
<i>Drop-off</i>	2,23	<i>Full</i>	83,952	77,804	1,08
		<i>Empty</i>	83,952	81,452	<b>1,03</b>
<i>Cruise</i>	1	<i>Full</i>	83,952	35,743	2,35
		<i>Empty</i>	83,952	37,709	2,23
<i>On ground</i>	-	<i>Full</i>	83,952	7,220	11,63
Critical shear stress [MPa]	Max. shear stress [MPa]	Ratio:	Ult. Tensile stress (alu 7075-T6) [MPa]	Max. von Mises stress [Mpa]	Ratio:
62,964	15,608	4,03	572	47,670	12,00
62,964	19,508	3,23	572	56,094	10,20
62,964	21,484	2,93	572	66,911	8,55
62,964	24,679	2,55	572	64,547	8,86
62,964	7,852	8,02	572	27,282	20,97
62,964	11,752	5,36	572	33,792	16,93
62,964	3,275	19,23	572	8,885	64,38

For the highest load case, plots of the results are shown in Figures 13.7 and 13.8.

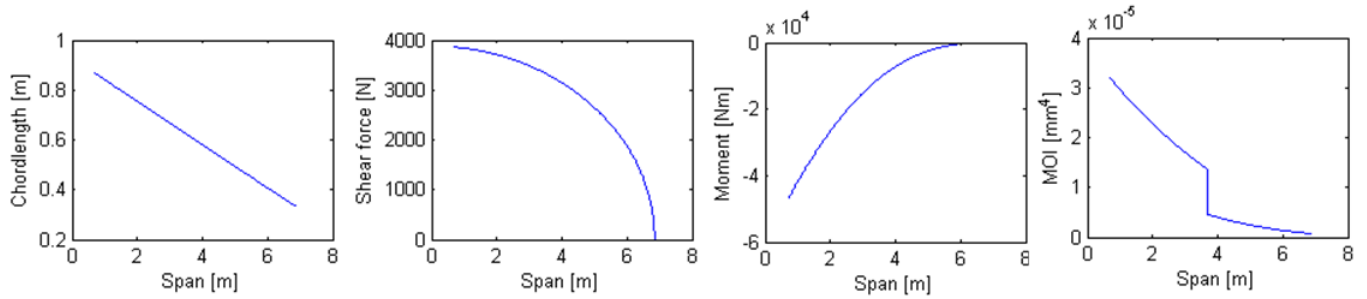


**Figure 13.7:** Plots on chord length, force distribution, moments and moment of inertia along span length

The force distribution only shows the lift distribution, since adding the fuel weight decreases the bending moment and stress. The plot showing the moments of inertia indicates clearly the length of the stringers, where the moment of inertia drops the stringers end. The other two plots show the taper in spanwise direction and the moments related to the force distribution.

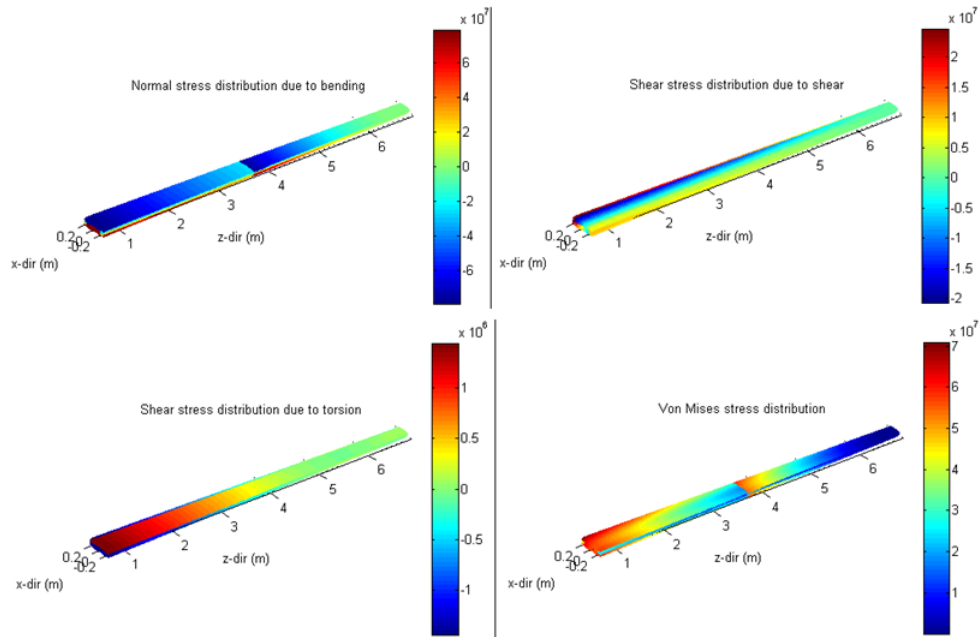


**Figure 13.8:** Bending-, shear-, torsion and von Mises stress of the wingbox for the highest load case

Especially in the plots for bending- and the von Mises stresses also the placement of the stringers is visible. All the plots are representative for their type of stresses and can be used to check where the highest stresses will occur.

### 13.9.2 Fuselage analytical results

For the fuselage it was a similar but less extensive job to get the stresses. This is mainly due to the assumptions made for the fuselage, this part of the structural analysis was only meant to compare results from some basic calculations with the FEM-analysis in Abaqus. However, it was not managed to get data from a FEM-analysis for the fuselage. The final dimensions of the simplified fuselage can be found in Table 13.4, these dimensions are based on commonly used dimensions for wall thickness and stringer area [114]. With these dimensions the highest von Mises stress becomes  $11.27 \text{ MPa}$ , this is a factor 50 lower than the ultimate tensile stress of the used material.

**Table 13.4:** Final design considerations fuselage

Subject	Result	Unit
Length fuselage	6.5	m
Amount of booms	16	
Skin thickness	1	mm
Stringer area	100	$\text{mm}^2$
Fuselage diameter	1.4	m
Material	Aluminium 7075-T6	

Figure 13.9 shows a plot of the von Mises stress for the fuselage.

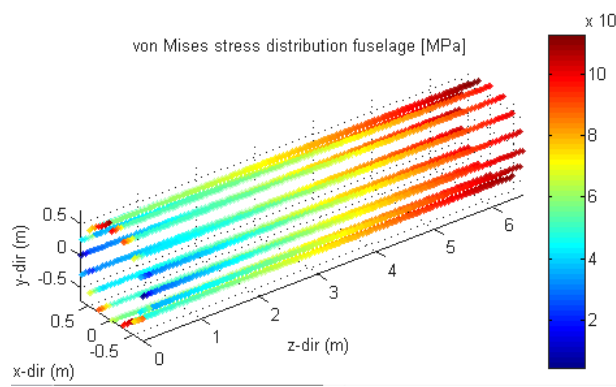


**Figure 13.9:** Von Mises stress for fuselage during cruise conditions

## 13.10 Sensitivity study

This is a short section which describes the behaviour of the model when one of the input parameters is changed. An increase in weight and velocity will be considered. Since the structural model does not take sweep into account, the result is the same: an increase in lift. See also Subsection 11.7.1. When looking only at the critical load case, an increase of 25 % will cause the following changes in the bending and shear stress ratios, see Table 13.5.

**Table 13.5:** Results comparison for sensitivity study

	<b>Bending stress ratio:</b>	<b>Shear stress ratio:</b>	<b>Von Mises ult. Tensile stress ratio:</b>
<b>Lift = 25172 N</b>	1.03	2.55	8.86
<b>Lift = 31465 N</b>	0.8868	2.33	7.13

## 13.11 Structural analysis - finite element analysis

In this section the numerical analysis conducted on the wing will be detailed. A numerical analysis has been done in order to be able to verify whether the analytical results obtained in the Section 13.9 are correct. The section will start with a rudimentary introduction into what numerical method has been used. This will be followed by the analysis parameters and the verification of the chosen approach. The assumptions associated with this model of the geometry will be listed and their implications briefly discussed.

### 13.11.1 Finite element method

The finite element method (FEM) is a method which is conventionally employed in order to analyse structures which are too complex to be solved efficiently analytically. The method was originally developed as a tool for stress analysis but has branched out to also encompass heat, magnetic, electric and fluid flow analysis. Only the stress analysis functionality was used in the current analysis.

The finite element method is based on discretisation. Discretisation is here defined as the process of transferring continuous models and equations into discrete counterparts. To illustrate, a circle can be modelled as a finite number of straight lines connected thus that they form an approximation of a circle. This illustration also shows that the finite element method rarely produces exact results since each discrete element is an approximation of the true continuous representation. The error involved with discretisation can be minimised by using more finite elements to approximate the structure. The more points that are positioned along the circle and connected with lines, the more accurate the curve approximating the circle becomes.

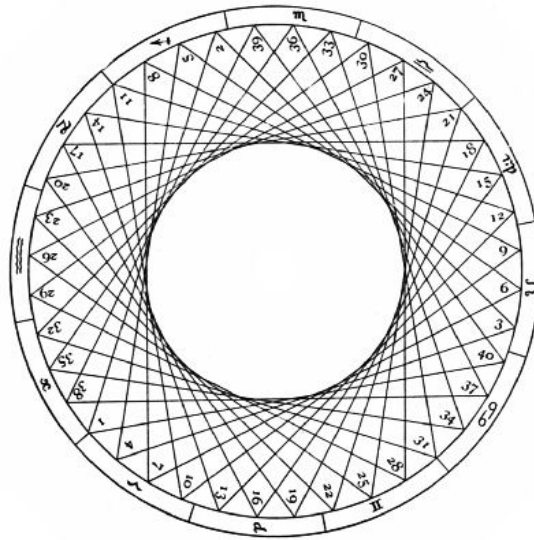


**Figure 13.10:** Discretisation of a circle

Once the body has been divided into a finite amount of discrete segments these segments need to be assigned geometry and properties. The segments are assigned element types which dictate the shape, number of nodes, number of integration points, and stiffness. The nodes vary in number depending on the order of the element type which is assigned. For example, first solid order elements have four nodes, where their second order counterpart has eight. The properties of the elements are defined, which translates into the deformation states and degrees of freedom which are allowed by the model. By doing this correctly the compatibility condition is met, no breaking or cracks are initiated in the body. The loads at each node has to be determined due to the applied forces. This is done numerically by solving the boundary value problem differential equations for each element. In order to be able to solve the differential equations the last property has to be defined, how the body is supported. This is achieved by applying boundary conditions to the model. These boundary specify the degrees of freedom of a single node, a group of nodes, and edge or a surface. With the compatibility of the model defined these conditions propagate through the model and assign the relevant degrees of freedom for each node accordingly. At this point the differential equations are solved to calculate the nodal displacements in the loaded step. Using strain displacement relations the calculated displacement can be used to calculate the strains and stresses in each element of the model. Using this output a stress distribution and a displacement distribution is generated of the model.

### 13.11.2 Software - Dassault systems abaqus CAE

Finite element analysis is done by software since solving all the differential equations by hand is inefficient. The software environment selected for the analysis is Dassault System Abaqus CAE V6.13 (Abaqus). Abaqus CAE is graphic interface driven finite element analysis tool. Abaqus is an industry standard software package which specialises in stress analysis of 3D bodies using FEM. Abaqus has a graphical workbench interface which allows for graphical manipulation of 3D bodies. The required 3D bodies were designed in Dassault Systems Catia V5 (Catia). The process of conducting the analysis included in this report will be concisely described in order to ensure reproducibility of the results of the analysis.

### 13.11.3 Problem analysis and element choice

A wing of an aeroplane contains different geometrical components. These components differ in dimension and shape which gives reason to assign these components different properties and behavioural constraints in the analysis. The loading of the model and the required output also influence the element choice. In order to ensure accuracy the problem has to be analysed. The loaded wingbox has two distributed loads acting on it, the lift distribution and the fuel weight distribution. The wingbox is assumed to be weightless. The result of this assumption is that there is no uniform gravity load working on the model. These loads both cause large bending moments at the root of the wingbox. The desired field output is the stress distribution and the displacement. The stress distribution will be dominated by the bending stress distribution. This problem is classified as a bending problem. From this classification suitable elements can be chosen. The elements assigned will be discussed.

An element is defined as a single discrete volume of the 3D model. The amount of nodes that an element has define the degrees of freedom (DOF) that can be integrated over the entire surface. The stiffness and mass of an element are calculated numerically at integration points within the element. The numerical algorithm used to integrate these variables influences how an element behaves. The stiffness and mass of an element are directly proportionate to the stiffness matrix generated to analyse the shape. They are thus directly proportionate to the displacement and strains calculated in the analysis. The choice of the correct algorithm and the element type is essential for producing

representative results. The modelled wingbox consists of four main components. These are the skin, the webs, the spars, and the stringers. The wing itself also includes the aerofoil shaped skin which surrounds the wingbox. For this analysis the wingbox is assumed to be load bearing and therefore the thin airfoil shaped geometry is neglected.

The components are all dimensioned in a way that one dimension of the geometry is considerably smaller than the others. For all the components the thickness is very small compared to the in-plane dimensions. The maximum ratio thickness to the smallest in-plane dimension is found on the smallest rib. The value of this ratio is 0.05, which is never exceeded throughout the rest of the structure. This defines the structure as a shell-like structure. The element choice has to mirror this classification which leaves three element types available for the analysis. These are 3D-stress solid elements, continuum shell elements and shell elements. 3D-stress solid elements and continuum shell elements require the model to be constructed as a solid whereas shell elements required a surface defined model. The pros and cons of each model type will be briefly discussed.

### Solid elements

Solid elements are divided into first order and second order elements. First order elements have fewer integration points and fewer nodes than their second order counterparts. Using full integration (using four Gauss integration points throughout the element), a first order solid element has four nodes and four integration points, a second order element has eight nodes and nine integration points. First order solid elements in bending problems can give inaccurate results due to shear locking. This phenomenon is that bending energy goes into shearing an element rather than bending it, an artificial shear stress is created. As a result the model becomes overly stiff. This yields inaccurate displacements thus stresses in the simulation of the model. Fully integrated first order elements are thus discarded.

First order elements under reduced integration (one Gauss integration point) solve the shear locking issue due to the fact that a single integration point cannot record energy into shearing. However this results in the element being overly flexible. This has as a downside that these elements suffer from hour-glassing. Hour-glassing is visualised in Figure 13.11C. Notice that the horizontal and vertical dotted lines do not change in length. Hour-glassing is that the distance through the integration point is zero while the outer edges deform to an hourglass shape. This commands that the normal and shear stresses at the integration point are zero. This occurs because each element edge only has nodes at the vertices which limit the DOF. The only motion two nodes can describe is a linear one. The element portrayed has straight edges even under deformation. This zero-energy mode can propagate over the model, causing an overly flexible model with unusable results. Hour-glassing can be solved by adding more elements through the thickness of the geometry with a minimum of four elements. Each pair of elements then records either tension or compression in the deformed shape. Due to the thin nature of the modelled wingbox the aspect ratio of the elements becomes very high when this is done leading to inaccurate results. 1st order reduced integration solid elements are discarded.

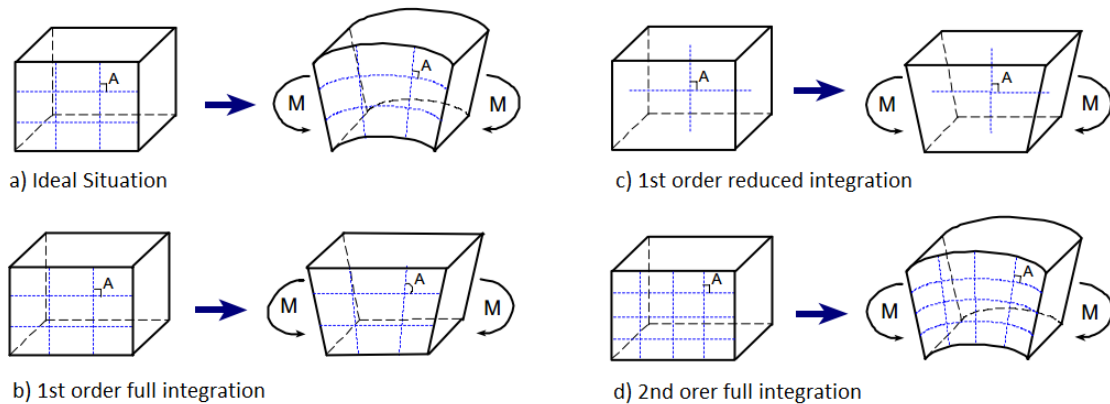


**Figure 13.11:** Shape deformation of elements under an applied bending moment with visible shear locking in (B) and hour-glassing in (C)

First order solid elements with incompatible integration prevent hour-glassing and shear locking and are the most suitable first order 3D-stress solid elements for bending problems. These elements suffer from distortions however. Element distortions make these elements overly stiff. These elements can thus only be used when the overall mesh shape retains their original rectangular shape. Multiple incompatible elements through the thickness improves accuracy but is not mandatory to prevent shear locking.

2nd order solid elements do not suffer from hour-glassing or shear locking because the extra nodes in the edges of the element allow for curved deformation. Second order solid elements are poor for modelling contact between geometries however. They are overly responsive due to the full range of freedom that the nodes afford. Since no contact is

modelled for the simulation of the wingbox structure second order solid elements are the best option to model the wingbox in the 3D-stress element family.

Continuum shell elements are 3D-stress and displacement elements for use in modelling structures with a shell-like response but continuum element topology. Continuum shell elements are first order elements which employ reduced integration to prevent shear locking. They do not suffer from hour-glassing. The elements allow for thick and thin shell applications, linear, and non-linear behaviour, a high aspect ratio between in-plane dimensions and the thickness. Continuum shell elements are less accurate than second order solid elements in bending and are therefore discarded.

#### Shell elements

Shell elements are elements which can be assigned to extruded surfaces which have no thickness. Shell elements are 2D elements which assign a thickness to the part through section definition. The advantage of shell elements is that the modelling of surfaces is relatively fast and efficient due to the simplification of the surfaces. Shell elements can suffer from shear and membrane locking and hour-glassing. Reduced integration solves both locking modes and is uniformly applied to shell elements. No indication of hour-glassing is given however. Due to complexity of the model and the need for tie constraints to model contact shell modelling is considered inferior to solid modelling. Shell elements are thus discarded for the wingbox.

#### Element choice

Second order 3D-stress elements are the most suitable elements for solid modelled shells and are thus chosen to model the ribs, spars and webs. The skin has such a low thickness to in-plane dimension ratio that shell elements are used to model the skin. These choices require the model to be generated using solid elements which thickness defined in the topology. Assigning continuum shell sections to parts requires a choice between Gaussian or Simpson thickness integration. Thickness integration of models concerns quadrature. It is a approximation of the definite integral of the face. Interpolation with polynomials evaluated at equally spaced points is applied in the Simpson rule. Allowing for varying distance between the interpolation points results in a Gaussian integral. Using rectangular or trapezoidal elements allows for the Simpson rule but Gaussian expression are usually more accurate. Due to the complex nature of the geometry Gaussian thickness integration will be used in order to maximise accuracy of the results.

### 13.11.4 Meshing

Meshing assigns a grid to the part on which the elements are applied. The higher the number of seeds that the part has the finer the grid and the greater the amount of elements. Increasing the amount of seeds increases the accuracy up to a certain point. The results of finer meshes converge to a asymptote and this phenomenon is called mesh convergence. Increasing the number of seeds also greatly increases computational time. To this end coarse meshes have been used to evaluate the model globally while mesh refinement was used to achieve mesh convergence. Mesh convergence has been defined when the results from mesh to mesh deviate less than 5 %.

Mesh controls define the manner in which the mesh is laid over the model. Due to the elongated shape of most model parts the most commonly employed mesh control was sweep control. Sweep meshing creates a source side mesh and propagates it through the depth of the region to the target side. This method is best used when the two faces are of similar geometry and is thus very suitable for the wingbox model. The meshes were applied part dependently to achieve optimal meshes. Some parts lend themselves for structured meshes. When possible this mesh control was used as the mesh then fits perfectly into the geometry in structured rectangular elements which are the most accurate.

### 13.11.5 Loads and boundary conditions

The wingbox model is loaded with two distributed analytical field loads. These are the span wise lift distribution and the span wise fuel weight distribution. Both loads act on the bottom surface of the wingbox in opposite directions. The loads counter-act each other from the tip to 3,500 mm from the root of the wingbox. Stringers have been applied over this area in order to increase the stiffness of the wingbox. The model has been analysed for two loaded cases, one with no fuel mass and one with full fuel. These load cases have been evaluated and the case with no fuel mass evaluated as the critical loading case. This load step occurs toward the end of the flight once the cargo has been dropped and the fuel mass is at the lowest possible value. For the model the payload and original lift distribution at cruise flight have been taken to ensure structural integrity. The loads are described by functions determined from the aerodynamic analysis. The lift distribution is elliptical and is defined by Equation 13.14. The load for the fuel weight distribution is parabolic and defined by Equation 13.15.

$$2,339.23 \cdot \sqrt{1 - \left(\frac{X}{6,150}\right)^2} \quad (13.14)$$

$$16 \cdot \left(\frac{X}{1,000}\right)^2 - 0.32X - 1,500 \quad (13.15)$$

#### Method Verification

To verify that the approach chosen for the analysis was sound, the approach was verified in small steps in order to minimise waste in accordance with lean design principles. To this end a clamped homogeneous cantilever beam was

modelled in Catia and imported into Abaqus. The simulation results are shown in Figure 13.12a. This was also done for a thin plate. These results are shown in Figure 13.14b.

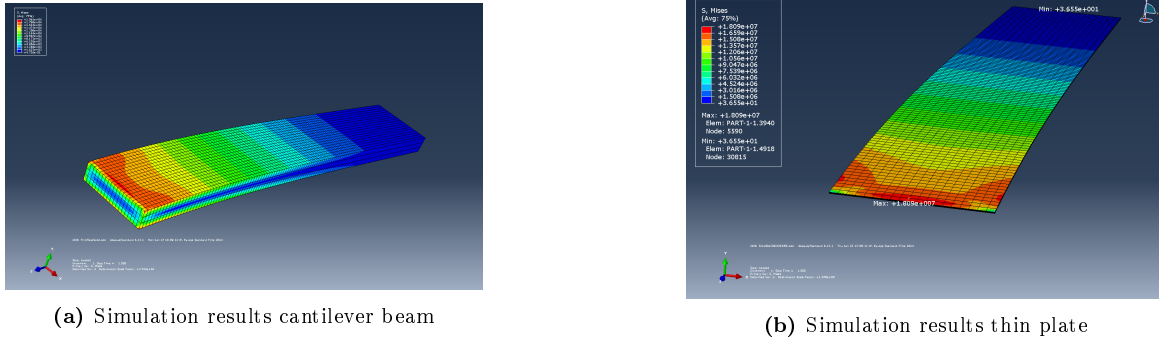


**Figure 13.12:** FEM model of a loaded beam and thin plate

To verify the results from Abaqus analytical hand calculations were used. Using the defined material properties for aluminium 7075-T6 the deflection and Von Mises stress distribution can be calculated. Due to symmetric loading about the  $yz$  cross-sections the nodes at the top surface of the beam have no shear stress. Using these simplifications the Von Mises equivalent stress is equal to the stress in  $x$  direction, Equation 13.16.

$$\sigma_x = -\frac{Mc}{I} \quad (13.16)$$

The displacement of the cantilever beam at the tip when a uniform distributed load of  $100 \text{ N/m}$  is applied can be calculated using Equation 13.17.

$$\delta_{max} = \frac{qL^4}{8EI} \quad (13.17)$$

Using the equations, the maximum stress of the cantilever beam is  $2.05 \text{ MPa}$  and the maximum deflection at the tip of the beam is  $12.9 \text{ mm}$ . Of the plate in bending the maximum stress is  $19.1 \text{ MPa}$  and the maximum displacement is  $0.6292 \text{ m}$ . These results are compared to the finite element simulations in the tables below.

**Table 13.6:** Solid wingbox model stress evaluation

Solid wingbox	Beam Theory	Solid 1 <sup>st</sup> order incompatible	Solid 1 <sup>st</sup> order reduced	Solid 1 <sup>st</sup> order full	Solid 2 <sup>nd</sup> order	Continuum Shell
Max Stress [Pa]	2.05E+05	1.96E+05	1.48E+05	1.79E+05	1.94E+05	1.55E+05
Ratio		1.05	1.39	1.15	1.06	1.32
Error		-4.51%	-38.52%	-14.55%	-5.86%	-32.10%

**Table 13.7:** Solid wingbox displacement evaluation

Solid wingbox	Beam Theory	Solid 1 <sup>st</sup> order incompatible	Solid 1 <sup>st</sup> order reduced	Solid 1 <sup>st</sup> order full	Solid 2 <sup>nd</sup> order	Continuum Shell
Displacement [mm]	2.22E-04	2.04E-04	2.13E-04	2.04E-04	2.05E-04	2.03E-04
Ratio		1.09	1.04	1.09	1.08	1.09
Error		-8.61%	-4.11%	-8.92%	-8.43%	-9.03%

**Table 13.8:** Thin plate stress evaluation

Thin Plate	Beam Theory	Solid 1 <sup>st</sup> order incompatible	Solid 1 <sup>st</sup> order reduced	Solid 1 <sup>st</sup> order full	Solid 2 <sup>nd</sup> order	Continuum Shell	Shell 1 <sup>st</sup> order	Shell 2 <sup>nd</sup> order
Max Stress Pascal	1.91E07	1.80E07	1.33E04	5.05E06	1.87E07	1.30E04	1.41E07	1.45E07
Error		1.06 -5.96%	1439.24 -14.38E04%	3.78 -277.76%	1.02 -2.16%	1470.28 -14.70E04%	1.36 -35.64%	1.32 -31.53%

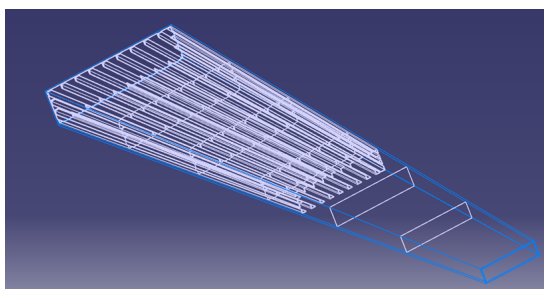
**Table 13.9:** Thin plate displacement evaluation

Thin Plate	Beam Theory	Solid 1 <sup>st</sup> order incompatible	Solid 1 <sup>st</sup> order reduced	Solid 1 <sup>st</sup> order full	Solid 2 <sup>nd</sup> order	Continuum Shell	Shell 1 <sup>st</sup> order	Shell 2 <sup>nd</sup> order
Displ. mm	0.62919	5.70E - 01	5.497	3.85E - 02	5.70E - 01	0.2804	5.71E - 01	5.71E - 01
Ratio		1.10	0.11	16.34	1.10	2.24	1.10	1.10
Error		-10.35%	88.55%	-1534.26%	-10.31%	-124.39%	-10.23%	-10.21%

From these comparisons the second order solid elements perform adequately with low error percentages. These results are in accordance with [117].

### 13.11.6 Model Improvement

The simplification of the wing as a cantilever beam is considered inaccurate. In order to get better results the 3D-model of the wing had to be improved. To this end a 3D double-tapered wing box was modelled in Catia and imported into Abaqus. The geometry of the wingbox is identical to the geometry used in the analytical analysis model. This allows for one on one comparison between both models. The model is built up of twenty stringers and six ribs and an outer thick shell. All the parts have been individually modelled as solids and given the corresponding element types.

**Figure 13.13:** Skeleton view of the final model

Further refinement of the model is possible in Abaqus but left outside of the scope of this design. Recommendations for further development would be to include the skin of the wing as a load carrying element. This would further increase the accuracy of the model. As a last refinement the wingbox representation of the load carrying structure of the wing could be abandoned in favour of the exact geometry of the wing were it taken into production.

### 13.11.7 Results

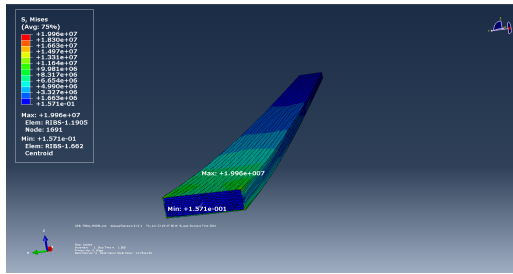
The results from the numerical analysis in Abaqus were used to verify the analytical calculations. From the field output the locations and magnitude of the maximum stresses and displacements have been determined. The results from both methods are presented in Table 13.10.

**Table 13.10:** Analytical and FEM simulation end result comparison

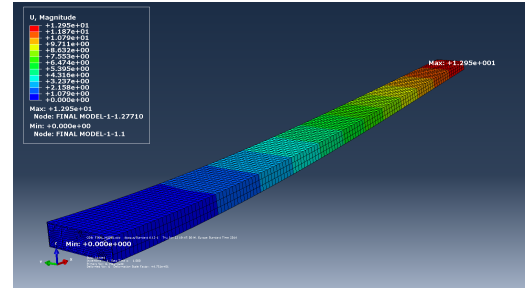
	Analytical model	FEM analysis	error
Maximum Von Mises stress [Mpa]	2.7	2.0	-35.68%
Maximum displacement [mm]	0	13	N.A

The error between the models is 36 %. Though this error is considerable it shows that the stresses are in the right region and it verifies the analysis. The difference in results can be attributed to a number of factors. The analytical

simplifies the model using booms to represent the stiffness matrix of the structure. This simplification is not shared in the numerical analysis causing some error. The numerical analysis also considers membrane strain in the skin of the wingbox which is left out of the analytical model. The location of the maximum stress differs because of interpretation of the boundary conditions. The analytical model assumes that the elements right next to the boundary conditions are deformable whereas the numerical model more realistically represents the propagation of the boundary conditions throughout the structure. Numerical analysis rarely gives exact answers since finite elements cannot exactly model continuous geometry. The main difference between the models is that the analytical model assumes that there is no displacement which increases the stresses. The finite element simulation includes displacement which causes the difference in stress. The analytical model is more conservative so the structure can be concluded to be structurally sound.



(a) FEM model displaying the final stress of the wingbox



(b) FEM model displaying the final displacement of the wingbox

**Figure 13.14:** FEM models with the final results

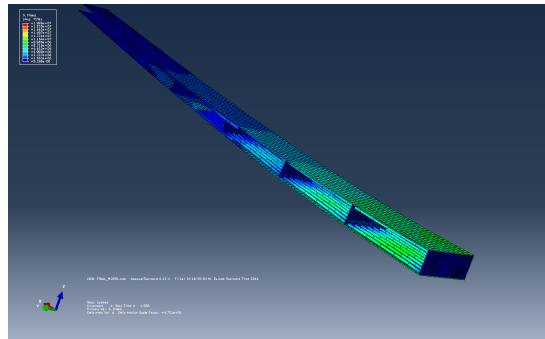


**Figure 13.15:** FEM model displaying the cross sectional view of the final stress in the wingbox

### 13.11.8 Recommendations

In further analysis the structural analysis could be extended to the level that fasteners and manufacture are taken into account. Stress concentrations at necessary holes in the structure should be analysed and the repercussions on the total design taken into account. The lift distribution now acts in the centre of the wingbox. This is because the chordwise distribution of the lift is unknown. CFD or windtunnel analysis should yield the formula for the chordwise distribution to further improve the analysis. The stringers should be tapered towards the tip of the wingbox to decrease stress concentrations due to the drop in moment of inertia.

The most critical component, the wing, has now been simulated. The next step would be to verify the fuselage calculations using the same approach. Modelling the structure the analytical model is based on and comparing the results will ensure a structurally sound fuselage.

Further material choices could be experimented with. The structure will now be constructed out of Aluminium 7075-T6. If the concept moves into the production phase this choice should be critically analysed for each individual component. In order to assemble the components fasteners will have to be taken into account. This along with possible manufacturing limitations could still alter the geometry of the structure. These changes are assumed to be so small that the final conclusions drawn at this moment will still be valid.

### 13.12 Landing gear

During taxi, take-off, and landing, the landing gear will protect the UAV from touching the ground. Therefore it should have the following functions: absorb landing shocks and taxiing shocks, provide ability for ground manoeuvring, provide braking capability, and protect the ground surface. The landing gear must be able to withstand three

types of load: vertical loads due to touchdown, longitudinal loads due to braking, and lateral loads due to cross-wind for example. Due to time constraints the critical load will be analysed. The vertical load and the positioning has been evaluated. The design method of Torenbeek has been used [79].

For the landing gear type, a retractable tricycle has been chosen. This was done because of its good steering capabilities, stability characteristics, and aerodynamics during cruise flight. The static load on the struts can be calculated using Equation 13.18.

$$P_n = \frac{W_{to}l_m}{l_m + l_n}, \text{ and } P_m = \frac{W_{to}l_n}{n_s(l_m + l_n)} \quad (13.18)$$

Where  $P$  is the strut load,  $l$  is the distance between the landing gear and the centre of gravity and  $n_s$  is the number of struts used in the main landing gear. The subscript  $n$  denotes the nose gear and  $m$  denotes the main gear. The wheel base, the distance between the nose and main landing gear, is approximately 25% of the wingspan. It is calculated to be 3.3 m, resulting in a  $l_m$  and  $l_n$  of 0.9 m and 2.4 m respectively. Since the UAV is a small aeroplane with a relatively low MTOW, two struts will be used. The static load must be multiplied with 1.25 to account for weight growth. Solving Equation 13.18 leads to a strut load of 1,200 kg for both the main and nose landing gears.

Since the airport of the Dominican Republic is international, the ground surface may be assumed to be at least tarmac with good foundation. Therefore the maximum allowable tire pressure is 70-90 psi. Using the tables presented by Roskam a tire is selected [118]. The 15x6-6 type III tire from B.F. Goodrich was selected for its small dimensions. The dimensions are 15x6 inch (0.38 m x 0.15 m) and the maximum loading is 1590 kg.

To absorb the landing shocks, a oleo-pneumatic, liquid or air shock breaker will be used for the nose gear and a cantilever spring for the main gear. Due to the limited resources available in the project, only the cantilever spring will be designed in this phase of the design. Figure 13.16 shows the cantilever beam before touchdown and in the static phase. The stroke  $s$  is calculated using Equation 13.19.

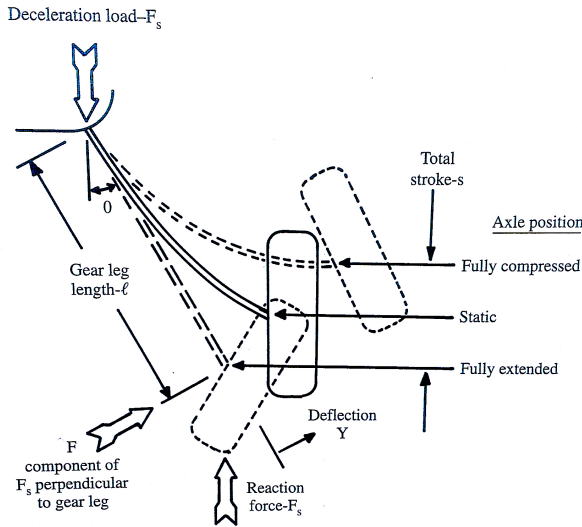


**Figure 13.16:** Top view of the UAV with the cg. locations of all the components

$$S = F_s \sin^2(\theta) \frac{l^3}{3EI} \quad (13.19)$$

Where  $F_s$  is the reaction force,  $\theta$  the angle which the fully extended landing gear makes with the vertical line from the attachment point,  $l$  the gear-leg length,  $E$  the young's modulus, and  $I$  the moment of inertia of the gear leg. The shape of the leg is chosen to be circular so the moment of inertia is the same in all directions. Also the circular shape contributes to the aerodynamic performance. To meet the tip over and roll requirements, the length of the strut must be 1.2 m with an angle  $\theta$  of 45°. Since the landing gear has to be designed according to the safe-life criteria, it is chosen to use titanium as material. The titanium leg has a Young's modulus of 110 GPa and a diameter of 3 cm. The maximum deflection for a load three times higher than the static load is 18 cm.

### 13.13 Wing mounting

For the wing mounting a proven system is chosen. According to the cargo hold dimensions of the Hercules, both the wings should be detachable. In Figure 13.17 a rendering of the concept is shown. For the tail of the UAV, a similar concept will be used.

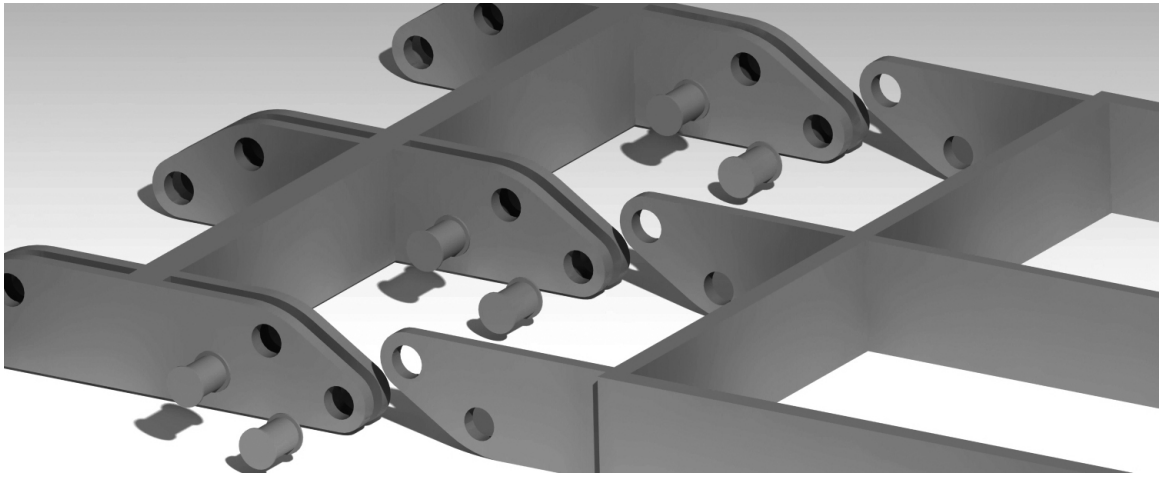


Figure 13.17: Illustration of the wing mounting principle

From the analytical model of the wingbox it is known that the maximum moment at the root will be around  $68.9 \text{ kNm}$ , when having a distance of  $0.2 \text{ m}$  between the two bolts, a maximum force of  $344.6 \text{ kN}$  will act on the bolt. Equation 13.20 can be used to calculate the diameter of the bolt, in this equation a safety factor of 1.5 is already taken into account [119].

$$D = \sqrt{\frac{F}{0.5 \cdot \pi \cdot \tau}} \quad (13.20)$$

Where  $D$  is the diameter,  $F$  is the force applied to the bolt and  $\tau$  is the critical shear stress of the bolt. Filling in numbers,  $F = 344.6 \text{ kN}$  and  $\tau = 331 \text{ MPa}$  gives a required diameter of  $31.532 \text{ mm}$ .

### 13.14 Cargo drop system

It was important to think of a way to release the cargo from the aeroplane and drop it. In Chapter 18 the parachute system is widely described. This section focuses on the structure inside the aeroplane. Figure 13.18 shows the concept. It consists of a cage with a 22 rollers on the bottom and 12 on both sides. Just after the parachute is released, after approximately 0.3 seconds, the cargo will be released and slides out of the aeroplane.



Figure 13.18: Rail system for the cargo drop system

## 14 | Stability and control

The stability of an aircraft is an important aspect of its ability to fly and be controlled. The more stable an aircraft is, the more quickly its eigenmotions damp out and the quicker it recovers from disturbances. Disturbances could be sudden gusts or a shift in center of gravity. A very stable aircraft however, can be difficult to control, because it tends

to go back to its equilibrium fast. In this chapter the controllability and longitudinal stability of the aircraft will be discussed. First, the tail is designed to meet the stability and controllability requirements. Then the control surfaces are designed, and lastly the flight dynamics is analysed. Only the longitudinal stability is calculated, this is because the coefficients needed for lateral stability have not yet been determined, there will be some comments on this in the recommendations section of this chapter. All the steps for calculating the lateral stability have been taken however. In this way, the stability can be determined, once the coefficients are known.

## 14.1 Tail sizing

A tailplane, also known as the horizontal stabiliser, is a small lifting surface located behind the main wing. The main function of a tailplane is to provide stability and control. The design of a tailplane has to meet three main requirements: ensure equilibrium of moments in steady flight (trim condition), ensure stability around this state of equilibrium, and generate forces for manoeuvring, hence to change on demand the aeroplane equilibrium state. (rotate at takeoff, initiate a climb, roll, ect.). The first two requirements will be elaborated in Section 14.1.1, the third requirement will be elaborated in Section 14.1.2

### 14.1.1 Sizing for stability

The basic modes of static stability are shown in Figure 14.1. The tail should be designed in such a way that the aeroplane is statically stable, meaning that it should converge to the initial state of equilibrium after a small disturbance. This state is shown in the most left drawing. Methods to calculate this stability have been presented during the systems engineering & aerospace design course of the bachelor aerospace engineering [85]. The lecture slides of this course have been used to perform most of the calculations.

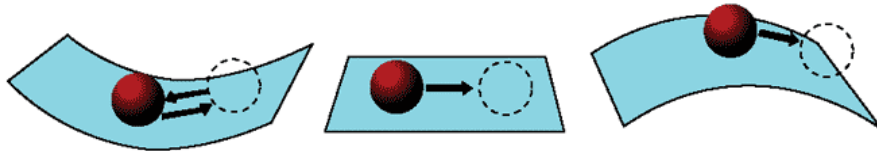


Figure 14.1: Three different types of stability

The functional requirements must be guaranteed for different possible configurations of the aeroplane. The most important are:

1. Centre of gravity travel, especially after the cargo drop.
2. Different settings of high-lift devices
3. Changes in landing gear

If for example the angle of attack suddenly changes due to a perturbation, both the wing and tail will generate more lift. When only considering the change in lift, it can be shown that there is a point where the resultant force applies. This is called the neutral point. The starting point of the stability calculations is shown in Figure 14.2.

When solving the equations accordingly, one arrives at an equation of the neutral point, which is shown in Equation 14.1.

$$\bar{x}_{np} = \bar{x}_{ac} + \frac{C_{L_{\alpha_h}}}{C_{L_{\alpha}}} \left(1 - \frac{d\epsilon}{d\alpha}\right) \frac{S_h l_h}{S \bar{c}} \left(\frac{V_h}{V}\right)^2 \quad (14.1)$$

A high tail lift rate coefficient ( $C_{L_{\alpha_h}}$ ) contributes to the stability since it moves the neutral point more backwards. Also the larger the distance between the main wing and the tail ( $l_h$ ), the better the stability becomes. A high downwash ( $d\epsilon/d\alpha$ ) is destabilising. Also the ratio between the airspeed of the tail and the main wing ( $V_h/V$ ) is important. The closer this ratio is to one, the more stable the aeroplane is. The tail over wing speed ratio is determined using statistics. For fuselage-mounted stabilisers this is 0.85, for fin-mounted stabilisers 0.95 and for a T-tail 1. The lift-rate coefficients have been computed using the DATCOM method presented during the course Aerospace Design and Systems Engineering Elements II [81].

#### Downwash

The wing downwash gradient is a function of wing geometry, placement of the tail and propeller influences. It is calculated using the methods presented in Systems Engineering & Aerospace Design [85]. Without the presence of the propeller, it is beneficial to have a T-tail since the effect of downwash is lower using this type of tail compared to a conventional tail. Due to the presence of the propeller, however, the advantage of having a T-tail is only achieved when installing it more than 2.5 m above the fuselage. This would result in more structural complexity and thus weight, hence a conventional tail is chosen.

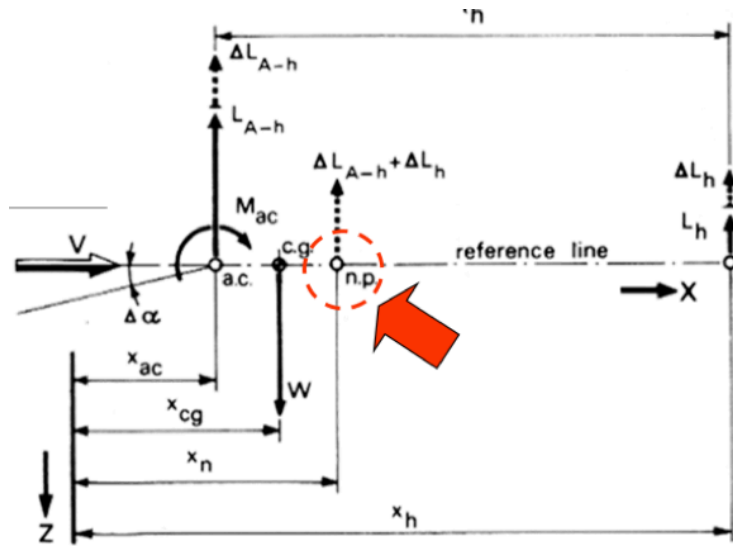


Figure 14.2: Free body diagram of UAV including neutral point

### 14.1.2 Sizing for controllability

Given a certain aeroplane configuration and flight modus, a combination of settings should exist such that the total moment coefficient is zero. This is referred to as the trim condition or configuration. For different locations of centre of gravity, different settings of the high lift devices and for different airspeeds, the tail should be able to generate enough lift. In Section 14.2 the required elevator deflection is calculated. In this section the general formulas are presented to size the surface area of the horizontal stabiliser. In the trimmed condition, Equation 14.2 is true.

$$C_{m_{ac}} + C_{L_{A-h}} (\bar{x}_{cg} - \bar{x}_{ac}) = \frac{C_{L_h} S_h l_h}{S \bar{c}} \left( \frac{V_h}{V} \right)^2 \quad (14.2)$$

Where the right side of the equation is the tail contribution,  $C_{L_h}$  is the lift coefficient of the tail which is  $-0.6$  for a fixed tail according to literature. The zero lift pitching moment of the UAV without tail ( $C_{m_{ac}}$ ) consists of the pitching moment of the main wing and contributions of the flaps, fuselage, and engine nacelles. Methods to calculate the zero lift pitching moment are not presented here, since they are described in detail in the used literature. All the calculations have been performed for stall speed at sea altitude for that is the most difficult phase to control.

### 14.1.3 Results of tail sizing

Equation 14.1 and 14.2 can be rewritten in such a way that  $S_h/S$  is a function of the c.g. location expressed in terms of the mean aerodynamic chord. The result is shown in Figure 14.3.

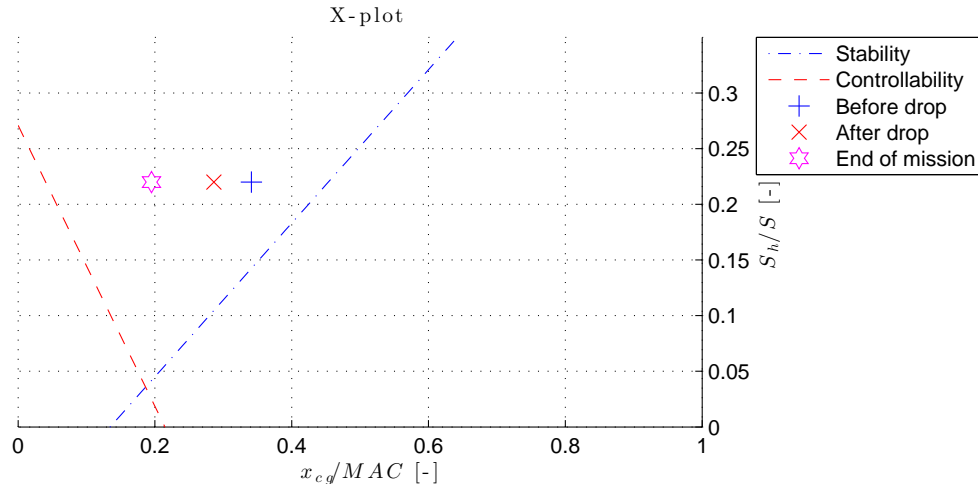


Figure 14.3: X-plot, indicating the stability and controllability lines

To ensure stability, it is required that the c.g. lies on the left side of the stability line. For controllability it is required that the c.g. lies on the right side of the controllability line. During the design iterations, this x-plot was used to keep track of the location of the c.g. and check whether the stability requirements were met. After a few iterations, the surface area of the tail was found to be  $4.2 \text{ m}^2$  for the horizontal stabiliser and  $1.6 \text{ m}^2$  for the vertical stabiliser. The distance between the aerodynamic centre of the main wing and the tail plane was determined to be  $6.3 \text{ m}$ . As can be seen, this is the case for the most extreme cases, hence the UAV will be both stable and controllable.

A commonly used term to compare tails of different aeroplanes is the tail volume coefficient, defined by:  $S_h l_h / S \bar{c}$ . With a tail volume coefficient of 0.7, the UAV has a comparable tail to reference aeroplanes with an average value of around 0.67.

The loads on the tail vary with different flying conditions. To design the fuselage structure, it is required to know the loading conditions on the tail. Using Equation 14.3 the tail loading is calculated. The results are shown in Figure 14.4.

$$N_h \approx \frac{1}{l_h} \left\{ C_{m_{ac}} \frac{1}{2} \rho V^2 S \bar{c} + W (x_{cg} - x_w) \right\} \quad (14.3)$$

Where the first part of the equation depends on the airspeed and the second part on the c.g. location.

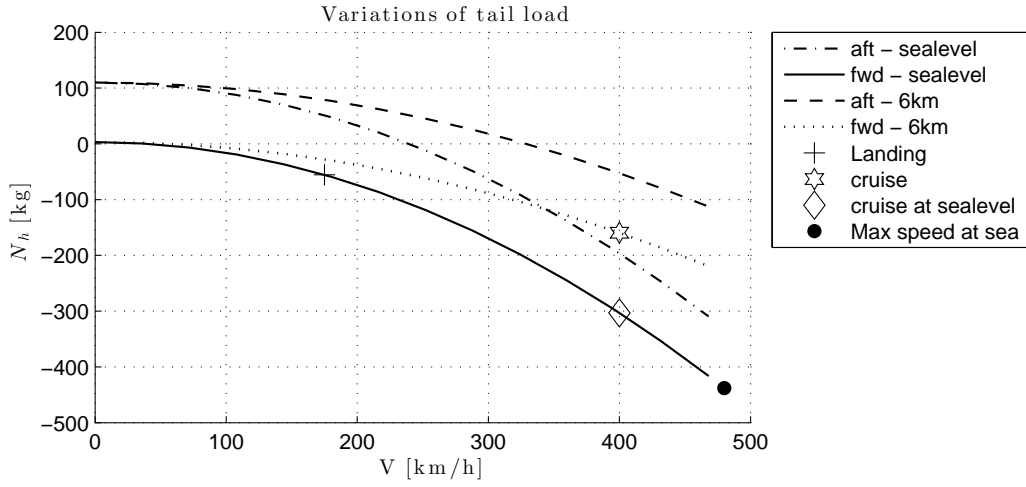


**Figure 14.4:** Tail loads during various conditions

The ultimate loading case is when flying with maximum speed at sea-altitude. Therefore the structure must be designed for a loading of  $400 \text{ N}$ .

## 14.2 Elevator sizing

Elevators are flight control surfaces which control the aircraft longitudinal attitude by changing the pitch balance. For every location of the centre of gravity and angle of attack, the elevators must balance the pitch moment of the UAV to ensure steady flight. The moment coefficient is shown in Equation 14.4.

$$C_m = C_{m_0} + C_{m_\alpha} (\alpha - \alpha_0) + C_{m_{\delta_e}} \delta_e = 0 \quad (14.4)$$

It consists of three parts;  $C_{m_0}$  which is independent of angle of attack ( $\alpha$ ) or the elevator deflection ( $\delta_e$ ),  $C_{m_\alpha}$  which influence varies with  $\alpha$  and  $C_{m_{\delta_e}}$  which influence varies with  $\delta_e$ . They are shown in Equation 14.5a, 14.5b and 14.5c.

$$C_{m_0} = C_{m_{ac}} - C_{N_{h\alpha}} (\alpha_0 + i_h) \left( \frac{V_h}{V} \right)^2 \frac{S_h l_h}{S \bar{c}} \quad (14.5a)$$

$$C_{m_\alpha} = C_{N_{w\alpha}} \frac{x_{cg} - x_w}{\bar{c}} - C_{N_{h\alpha}} \left( 1 - \frac{d\epsilon}{d\alpha} \right) \left( \frac{V_h}{V} \right)^2 \frac{S_h l_h}{S \bar{c}} \quad (14.5b)$$

$$C_{m_{\delta_e}} = -C_{N_{h\delta}} \left( \frac{V_h}{V} \right)^2 \frac{S_h l_h}{S \bar{c}} \quad (14.5c)$$

Where  $C_{m_{ac}}$  is the moment coefficient around the aerodynamic centre of the wing,  $C_{N_{h\alpha}}$  is the lift gradient of the horizontal tailplane,  $C_{N_{w\alpha}}$  is the lift gradient of the main wing and  $C_{N_{h\delta}}$  is the lift gradient of the horizontal tailplane

due to elevator deflection. Figure 14.5 shows the different contributions of the UAV without tail, the tail, and the elevator to the pitch moment coefficient.

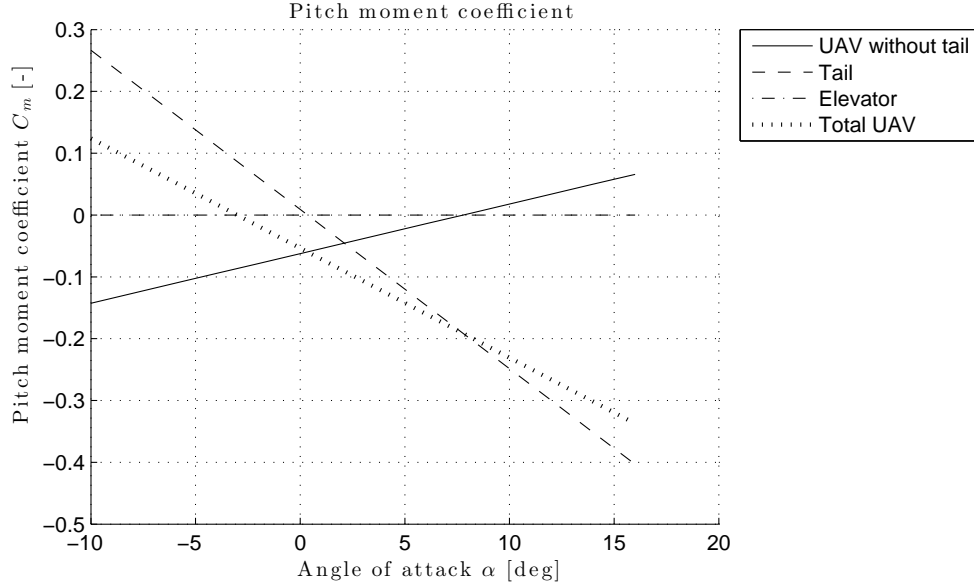


**Figure 14.5:** Pitch moment coefficients for different groups of the UAV, elevator deflection is zero here

The slope of the total UAV is negative, which is required for longitudinal stability. The pitch moment is zero at an angle of attack of -3, hence the UAV is trimmed in that condition. By changing the deflection of the elevator, the trim condition is manipulated. Equation 14.6 shows a rewritten form of Equation 14.4 which is used to calculate the required elevator deflection for trim condition.

$$\delta_e = -\frac{1}{C_{m\delta_e}} [C_{m_o} + C_{m\alpha} (\alpha - \alpha_0)] \quad (14.6)$$

To change the trim condition to an angle of attack of zero, an elevator deflection of -3 degrees is required. The required elevator deflection is calculated for different angles of attack. For an angle of attack of 16 degrees, the required elevator deflection is the largest: -20 degrees.

For the sizing of the actuators of the elevator, the design hinge moment must be calculated. This is done by assuming a maximum lift coefficient of 1.2 for the elevator. The elevator chord length is 25% of the local chord, resulting in a surface area of 0.42  $m^2$ . Furthermore, the aerodynamic centre of the elevator is at quarter chord. The hinge moment required when flying at maximum airspeed at sea level is 480  $Nm$ .

### 14.3 Aileron sizing

Ailerons are flight control surfaces attached to the trailing edge of each wing, which control the roll motion of the UAV. They deflect in opposite direction, creating a difference in lift of each wing, hence the UAV will roll. The short design approach from the aircraft preliminary design handbook, written by Gudmundsson, is used to design the ailerons [120].

The ailerons are according to the following criteria: responsiveness at slow speeds with large deflection and responsiveness at high speeds with low deflection. Another term for responsiveness is roll authority. For comparison, the roll authority is expressed in terms of the helix angle  $pb/2V$  shown in Equation 14.7.

$$\frac{pb}{2V} = -\frac{C_{l\delta_a}}{C_{l_p}} \delta_a \quad (14.7)$$

The roll authority  $C_{l\delta_a}$  is shown in Equation 14.8 and the roll damping  $C_{l_p}$  is shown in Equation 14.9. Deflection  $\delta_a$  is the aileron deflection during flight, which is approximately 75% of the maximum deflection angle on ground, which is assumed to be 20°. The helix angle describes the responsiveness of the aeroplane to an aileron deflection. It does not depend on the airspeed, making it a suitable for comparison. For cargo aircraft the helix angle should be equal or larger than 0.07  $rad$ .

$$C_{l_{\delta_a}} = \frac{c_{l_{\delta_a}} C_r}{Sb} \left[ (b_2^2 - b_1^2) + \frac{4(\lambda - 1)}{3b} (b_2^3 - b_1^3) \right] \quad (14.8)$$

Where  $c_{l_{\delta_a}}$  is the change in lift coefficient of the airfoil with respect to a change in aileron deflection. According to the Gudmundsson's handbook, values around 3 per radian are in the right ballpark, hence 3 per radian is chosen for the initial design.  $C_r$  is the root chord, the y-location of the root of the aileron is  $b_1 = 4m$ , and the y-location of the tip of the aileron is  $b_2 = 6m$ .

$$C_{l_p} = -\frac{(c_{l_\alpha} + c_{d_0} C_r b)}{24S} [1 + 3\lambda] \quad (14.9)$$

Where  $c_{l_\alpha}$  is the lift gradient of the airfoil which is calculated to be 5.7 per radian and  $c_{d_0}$  is the section drag coefficient which is calculated to be 0.007. Using Equation 14.7 it can be shown that the helix angle is 0.09, hence the UAV has sufficient roll authority according to regulations. Gudmundsson stressed that poorly designed ailerons may only deflect 25% of the on-ground deflection, a fact that has to be taken into account.

Before the aileron actuators can be sized, the aileron hinge moment has to be calculated. The chord length of the ailerons will be 25% of the local chord. The largest forces on the aileron, hence the largest hinge moment, are exerted when flying at sea level with maximum airspeed and maximum aileron deflection. To approximate the hinge moment, the maximum lift coefficient ( $C_{L_{\alpha_{max}}}$ ) of the aileron is assumed to be 1.2. The hinge force can be calculated using the basic lift equation. The force is assumed to act at quarter-chord of the aileron. The maximum hinge moment to design for is 487 Nm.

## 14.4 Determining the coefficients of the state-space system

Every aircraft has eigenmotions, motions that are induced by disturbances acting on the aircraft. These eigenmotions and their damping factor can be simulated using mathematical models. These mathematical representations exist for longitudinal and lateral motions of the aircraft. The set of equations describing these motion are called the equations of motion (EOM) and can be found in the reader of the Flight Dynamics course (AE3202) [121]. The EOM for longitudinal and lateral motions and are given by Equation 14.10 and 14.13, respectively.

Matlab can model dynamic systems, the function `SYS = ss(A,B,C,D)` creates an object `SYS` representing the continuous-time state-space model. Using this model, the behaviour of the aircraft can be predicted. The EOM need to be rewritten to a space-state system for this task. Equations 14.10 to 14.15 show how the space-state system is derived.

$$\begin{bmatrix} C_{X_u} - 2\mu_c D_c & C_{X_\alpha} & C_{Z_0} & C_{X_q} \\ C_{Z_u} & C_{Z_\alpha} + (C_{Z_{\dot{\alpha}}} - 2\mu_c) D_c & -C_{X_0} & C_{Z_q} + 2\mu_c \\ 0 & 0 & -D_c & 1 \\ C_{m_u} & C_{m_\alpha} + C_{m_{\dot{\alpha}}} D_c & 0 & C_{m_q} - 2\mu_c K_Y^2 D_c \end{bmatrix} \begin{bmatrix} \hat{u} \\ \alpha \\ \theta \\ \frac{q\bar{c}}{V} \end{bmatrix} = \begin{bmatrix} -C_{X_{\delta_e}} \\ -C_{Z_{\delta_e}} \\ 0 \\ -C_{m_{\delta_e}} \end{bmatrix} \delta_e \quad (14.10)$$

$$\begin{bmatrix} -2\mu_c \frac{\bar{c}}{V^2} & 0 & 0 & 0 \\ 0 & (C_{Z_{\dot{\alpha}}} + 2\mu_c) \frac{\bar{c}}{V} & 0 & 0 \\ 0 & 0 & -\frac{\bar{c}}{V} & 0 \\ 0 & C_{m_{\dot{\alpha}}} \frac{\bar{c}}{V} & 0 & -2\mu_c K_Y^2 \left(\frac{\bar{c}}{V}\right)^2 \end{bmatrix} \begin{bmatrix} \dot{u} \\ \dot{\alpha} \\ \dot{\theta} \\ \dot{q} \end{bmatrix} + \begin{bmatrix} C_{X_u} \frac{1}{V} & C_{X_\alpha} & C_{Z_0} & C_{X_q} \frac{\bar{c}}{V} \\ C_{Z_u} \frac{1}{V} & C_{Z_\alpha} & -C_{X_0} & (C_{Z_q} + 2\mu_c) \frac{\bar{c}}{V} \\ 0 & 0 & 0 & \frac{\bar{c}}{V} \\ C_{m_u} \frac{1}{V} & C_{m_\alpha} & 0 & C_{m_q} \frac{\bar{c}}{V} \end{bmatrix} \begin{bmatrix} u \\ \alpha \\ \theta \\ q \end{bmatrix} + \begin{bmatrix} C_{X_{\delta_e}} \\ C_{Z_{\delta_e}} \\ 0 \\ C_{m_{\delta_e}} \end{bmatrix} \delta_e = 0 \quad (14.11)$$

Which is in the form of:

$$C_{1_s} \dot{\bar{x}} + C_{2_s} \bar{x} + C_{3_s} \bar{u} = \bar{0} \quad (14.12)$$

The EOM for lateral motions are also derived to the space-state system. This is shown below in Equation 14.13 to 14.15.

$$\begin{bmatrix} C_{Y_\beta} + (C_{Y_\beta} - 2\mu_b) D_b & C_L & C_{Y_p} & C_{Y_r} - 4\mu_b \\ 0 & -\frac{1}{2}D_b & 1 & 0 \\ C_{l_\beta} & 0 & C_{l_p} - 4\mu_b K_X^2 D_b & C_{l_r} + 4\mu_b K_{XY} D_b \\ C_{n_\beta} + C_{n_\beta} D_b & 0 & C_{n_p} + 4\mu_b K_{XZ} D_b & C_{n_r} - 4\mu_b K_Z^2 D_b \end{bmatrix} \begin{bmatrix} \beta \\ \varphi \\ \frac{pb}{2V} \\ \frac{rb}{2V} \end{bmatrix} = \begin{bmatrix} -C_{Y_{\delta\alpha}} \\ 0 \\ -C_{l_{\delta\alpha}} \\ -C_{n_{\delta\alpha}} \end{bmatrix} \delta_\alpha + \begin{bmatrix} -C_{Y_{\delta r}} \\ 0 \\ -C_{l_{\delta r}} \\ -C_{n_{\delta r}} \end{bmatrix} \delta_r \quad (14.13)$$

$$\begin{bmatrix} (C_{Y_\beta} - 2\mu_b) \frac{b}{V} & 0 & 0 & 0 \\ 0 & -\frac{1}{2} \frac{b}{V} & 1 & 0 \\ 0 & 0 & -4\mu_b K_X^2 \frac{b^2}{V^2} & 4\mu_b K_{XY} \frac{b^2}{V^2} \\ C_{n_\beta} \frac{b}{V} & 0 & 4\mu_b K_{XZ} \frac{b^2}{V^2} & -4\mu_b K_Z^2 \frac{b^2}{V^2} \end{bmatrix} \begin{bmatrix} \dot{\beta} \\ \dot{\varphi} \\ \dot{p} \\ \dot{r} \end{bmatrix} + \begin{bmatrix} C_{Y_\beta} & C_L & C_{Y_p} \frac{b}{2V} & (C_{Y_r} - 4\mu_b) \frac{b}{2V} \\ 0 & 0 & 0 & 0 \\ C_{l_\beta} & 0 & C_{l_p} \frac{b}{2V} & C_{l_r} \frac{b}{2V} \\ C_{n_\beta} & 0 & C_{n_p} \frac{b}{2V} & C_{n_r} \frac{b}{2V} \end{bmatrix} \begin{bmatrix} \beta \\ \varphi \\ p \\ r \end{bmatrix} + \begin{bmatrix} C_{Y_{\delta\alpha}} & C_{Y_{\delta r}} \\ 0 & 0 \\ C_{l_{\delta\alpha}} & C_{l_{\delta r}} \\ C_{n_{\delta\alpha}} & C_{n_{\delta r}} \end{bmatrix} \begin{bmatrix} \delta_\alpha \\ \delta_r \end{bmatrix} = 0 \quad (14.14)$$

Which is again in the form of:

$$C_{1_a} \dot{\bar{x}} + C_{2_a} \bar{x} + C_{3_a} \bar{u} = \bar{0} \quad (14.15)$$

In Equations 14.10 to 14.15,  $\bar{x}$  is the state vector, representing the states of the aircraft. For the longitudinal case, these states are: horizontal airspeed ( $u$ ), angle of attack ( $\alpha$ ), pitch angle ( $\theta$ ) and pitch rate ( $q$ ). For the lateral case, these are: sideslip angle ( $\beta$ ), bank angle ( $\varphi$ ), angle of roll ( $p$ ) and angle of yaw ( $r$ ).  $\dot{\bar{x}}$  is the output vector, which includes the first derivatives of the states represented by  $\bar{x}$ . The input of control vector is  $\bar{u}$ , in the EOM for the longitudinal this represents the elevator deflection ( $\delta_e$ ) wherein the lateral case  $\bar{u}$  represents the aileron ( $\delta_\alpha$ ) and rudder deflection ( $\delta_r$ ). Together with all the stability and control derivatives, they form the EOM for the UAV.

The variables starting with a C are stability and control variables, the values of which are given in Appendix F. The  $\mu_c$  and  $\mu_b$  are the relative density for the symmetric and asymmetric motions, respectively.

Equations 14.11 and 14.14 are put into the Matlab program as the state-space system.

## 14.5 Longitudinal stability during cruise

By creating a state-space system, the stability of a multiple input, multiple output system can be calculated. In order to do so, the eigenvalues ( $\lambda$ ) of the system are to be determined. Using these eigenvalues, the undamped natural frequency ( $\omega_0$ ), damping ratio ( $\zeta$ ) and half time ( $T_{\frac{1}{2}}$ ) can be determined. The relations between these stability characteristics are obtained from Cook [122]. To find the different values aforementioned, the eigenvalues are written in the form:

$$\lambda_c = \xi_c \pm \eta_c j \quad (14.16)$$

Where  $\xi_c$  is the real part and  $\eta_c$  the imaginary part of the eigenvalue. Using the real and imaginary part of the eigenvalue, the undamped natural frequency can be determined using Equation 14.17.

$$\omega_0 = \sqrt{\xi_c^2 + \eta_c^2} \quad (14.17)$$

When the undamped natural frequency is determined, the damping coefficient can be calculated using Equation 14.18.

$$\zeta = -\frac{\xi_c}{\omega_0} \quad (14.18)$$

From Equation 14.18 follows that the real part of the eigenvalue should be negative in order to have a positive damping factor and thus be stable. This is also clear when looking at Equation 14.19, here a negative real part of the eigenvalue will result in a positive half time.

$$T_{\frac{1}{2}} = \frac{\ln(\frac{1}{2})}{\xi_c} \quad (14.19)$$

The results of the numerical program and Equation 14.16 to 14.19 for steady cruise are displayed in Table 14.1. The last three rows indicate the level of flying quality according to Cook [122].

**Table 14.1:** Longitudinal stability characteristics of the UAV for the phugoid and short period motion

	Phugoid	Short period motion
Eigenvalues	$-0.0095 \pm 0.11j$	$-2.52 \pm 3.78j$
Undamped natural frequency	0.11	4.54
Damping ratio	0.09	0.55
Time to damp to half the amplitude	72.69 s	0.28 s
Damping ratio level 1 flying quality	> 0.04	0.35 – 1.30
Damping ratio level 2 flying quality	0	0.25 – 2.00
Damping ratio level 3 flying quality	Unstable, $T > 55$ s	> 0.10

The short period motion is a highly damped motion and the long period motion (or phugoid) damps out slowly. This is the case with most conventional aircraft. Cook differentiates three different levels of flying quality for manned flight. These levels indicate the comfort for passengers and the ease of manoeuvring for pilots. Level 1 being comfortable and level 3 needing constant attention of the pilot. For a UAV it is of course no problem to pay constant attention, but for level 1 flight conditions the loads are smaller and the UAV also require less corrections. Therefore it is still profitable to stay in this area if possible. As can be seen, the designed UAV is within the limits for level 1 flying quality stability.

All the calculated values indicate that the aircraft is stable for longitudinal motions during cruise. In order to check if this is true, the response of the UAV to a disturbance in the longitudinal direction can be simulated. In Figure 14.6 the response of the aircraft to such a step input is given. This is done for the horizontal airspeed, angle of attack, pitch and pitch rate respectively. Note that the scale of the plot for the angle of attack is only ten seconds, where the others are 200 seconds. Looking at the response of the aircraft one can conclude that it is stable during cruise. One can also differentiate between the effect of the short period motion and the phugoid. The short period motion only creates a peak in the first second, while the phugoid is still visible in the aircraft response after 200 seconds.

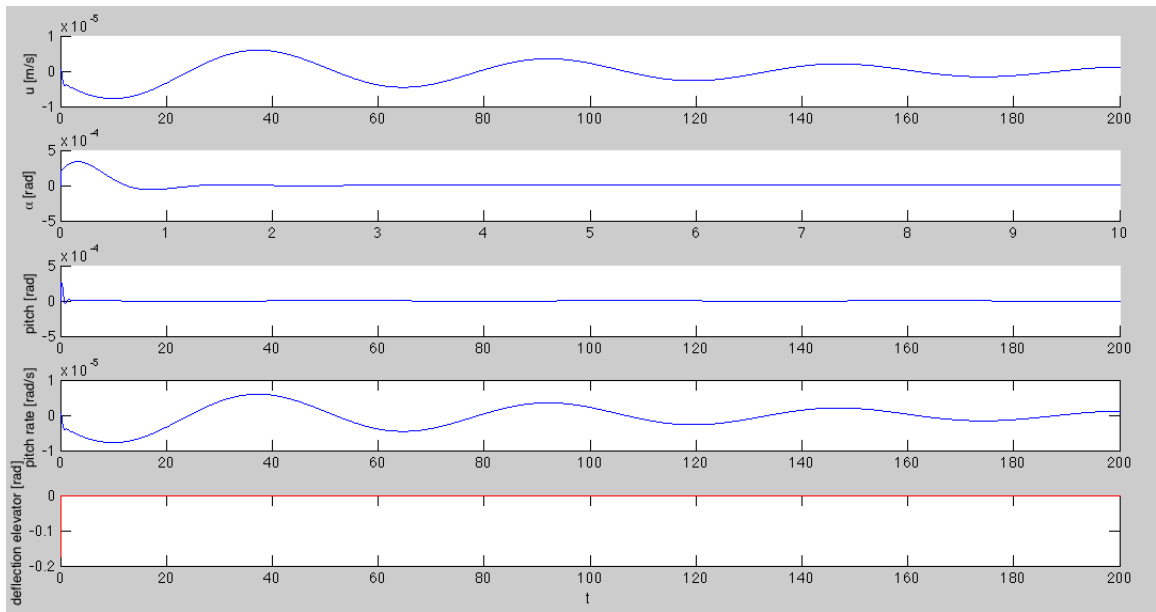


**Figure 14.6:** Reponse of the aircraft to a  $10^\circ$  step input to the elevator

## 14.6 Longitudinal stability during cargo drop

During the cargo drop several input parameters will differ from those in cruise flight. The UAV will fly slower and at a lower altitude for example. But the most important aspect of the cargo drop considering stability will be the shift in CG. To see what happens to the aircraft's stability when the cargo is being dropped, a sensitivity study is performed. The shift in CG will cause the eigenvalues of the aircraft to change and will give the aircraft a sudden impulse comparable to a step input from the elevator. As mentioned before, the ultimate CG during cargo drop will be  $0.48\bar{c}$ . In the ideal case the aircraft is still stable at that moment. Figure 14.7 and 14.8 show the eigenvalues for the phugoid and short period motion on the S-plane, respectively. Just like before, the eigenvalues should have a negative real value for a stable aircraft.

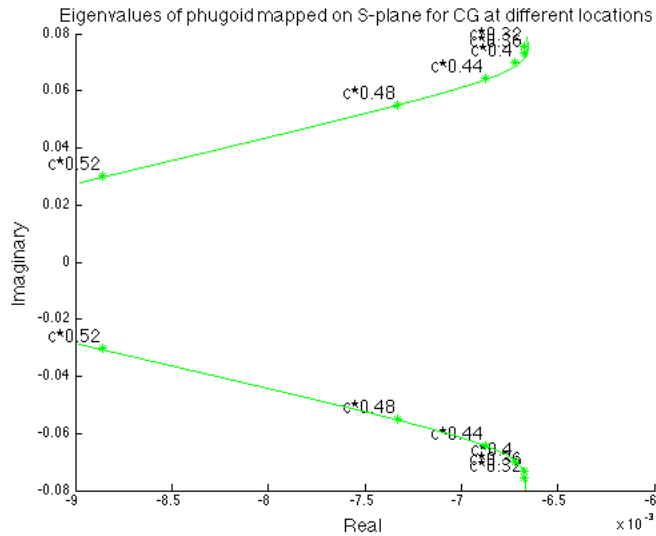


Figure 14.7: Eigenvalues of the phugoid during the drop

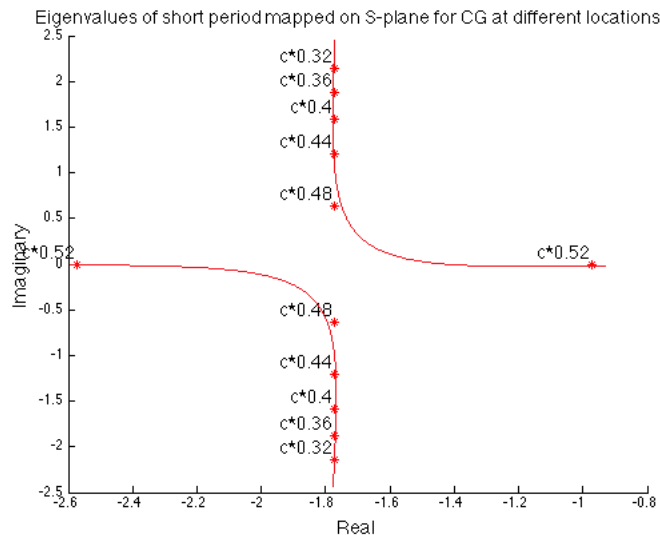


Figure 14.8: Eigenvalues of the short period motion during the drop

As can be seen, the CG shift does not cause the aircraft to be unstable. Up until a CG of  $0.48\bar{c}$  the phugoid becomes slightly more stable while its undamped natural frequency decreases. Since the phugoid is a very slow motion and the difference in damping ratio and undamped natural frequency only moves slightly (scale on x-axis is  $10^{-3}$ ) this is of no significance for the drop.

The undamped natural frequency of the short period motion decreases more and also becomes a little more stable up until a CG of  $0.48\bar{c}$ . This means there won't be any problem during the drop.

**Table 14.2:** Damping factors calculated analytically and numerically

	Phugoid	Short period motion
Damping factor (analytical)	0.0824	0.5539
Damping factor (numerical)	0.0853	0.5541

When increasing the CG even more to  $0.52\bar{c}$  for example, it can be seen that the eigenmotions of the aircraft will change. Both the poles of the short period motion for example are on the real axis, this means that the motion will not be oscillatory for that position of the CG. Since both those values are still negative, the aircraft will still be stable. If in the future, design parameters change, this graph should be reconsidered to check for stability.

## 14.7 Verification of the program

Using Matlab to numerically solve the EOM of the UAV that is designed for this mission is a powerful tool for determining the stability of the aircraft. The problem when using programs that solve problems numerically, is that the results can be difficult to verify. Two ways of verification can be distinguished: using a simplified model that can be solved analytically or using input parameters of which the outputs are already determined.

### 14.7.1 Simplification of equations of motion

To be able to determine the eigenvalues for the stability, the equations of motion need to be simplified. This section first discusses symmetric motions and after that the asymmetric motions. The two symmetric motions that can be identified are the short period and the phugoid. The asymmetric eigenmotions are the aperiodic roll, the Dutch roll and the spiral. The results presented in this section are obtained with help of the lecture slides of the Flight Dynamics course (AE3202) [121].

For the short period the EOM are simplified using the assumption that  $V = \text{constant}$ . This implies that the forces in the  $X_b$  direction remain constant. It is also assumed that the initial state is steady so  $\gamma_0$  and  $C_{X_0}$  are zero. With these assumptions Equation 14.20 is determined.

$$\begin{bmatrix} C_{Z_\alpha} + (C_{Z_{\dot{\alpha}}} - 2\mu_c)D_c & C_{Z_q} + 2\mu_c \\ C_{m_\alpha} + C_{m_{\dot{\alpha}}}D_c & C_{m_q} - 2\mu_c K_Y^2 D_c \end{bmatrix} \begin{bmatrix} \alpha \\ \frac{q\bar{c}}{V} \end{bmatrix} = \bar{0} \quad (14.20)$$

Using Equation 14.20 the eigenvalues of the aircraft for the short period motion can be determined. Using these eigenvalues it can be said if the aircraft is stable or not.

The EOM for the phugoid are determined using the assumptions that  $\alpha$  and  $\dot{q}$  are zero, with this the Equation 14.21 can be obtained from the general EOM.

$$\begin{bmatrix} C_{X_u} - 2\mu_c D_c & C_{Z_0} & 0 \\ C_{Z_u} & 0 & 2\mu_c \\ 0 & -D_c & 1 \end{bmatrix} \begin{bmatrix} \hat{u} \\ \theta \\ \frac{q\bar{c}}{V} \end{bmatrix} = \bar{0} \quad (14.21)$$

Using these simplifications the eigenvalues of the UAV can be determined analytically. The results of both the numerical and analytical solution can be found in Table 14.2. The results of both methods are comparable and indicate that the program gives correct results. The difference between the numbers can be explained due to assumptions made in the analytical solution.

### 14.7.2 Using known inputs and outputs

For the second method, the stability and control derivatives for the Cessna Citation are used. The eigenvalues of its symmetric and asymmetric motions have already been computed and can therefore be used to verify the written Matlab program. The eigenvalues for the Citation's longitudinal and lateral eigenmotions calculated by the program written for this project can be found in Table 14.3. The damping ratios of the Cessna can be found in the reader for the Flight Dynamics course [121] and are also given in Table 14.3.

**Table 14.3:** Damping ratios calculated using Matlab and those in the reader for the Flight Dynamics course (AE3202)

	Phugoid	Short period motion	Dutch roll
Damping ratio Matlab program	0.0441	0.7182	0.1397
Damping ratio Flight Dynamics reader	0.0441	0.7182	0.0940

When comparing the values, it can be seen that the program gives the exact same results for the longitudinal eigenmotions. This indicates that the written program is working correctly and the EOM are properly rewritten to a space-state system. For the lateral eigenmotion (Dutch roll) this is not the case. The values are within the same order of magnitude, but are not exactly the same. This can be explained by the fact that the coefficients  $C_{Y_{\dot{\beta}}}$  and  $C_{n_{\dot{\beta}}}$  are not stated in the reader a that the assumption of those being zero is incorrect.

## 14.8 Recommendations

When looking at the eigenvalues of the longitudinal eigenmotions of the UAV, it can be said that the aircraft is inherently stable in for symmetric motions and that it will recover nicely from disturbances in the longitudinal direction during cruise. For the lateral case, this still has to be determined using lateral stability coefficients. It is recommended that these coefficients are determined using computational fluid dynamics (CFD) or wind tunnel testing as a next step. The written program can compute the lateral stability once these coefficients are known.

In this chapter only the stability of the aircraft during cruise and cargo drop-off is determined. It is recommended to look into the settings controllers on the Lisa/L board. There are several proportional integral derivative (PID) controllers that need to be tweaked in a way that the UAV is stable during its entire flight envelope. This can be done by adding controllers are tweaking their gain.  
analysis

# 15 | Performance analysis

## 15.1 Maximum load factor

To check if the structural integrity of the fuselage, wings and support structures are not in jeopardy, the maximum load factor which can be achieved in normal flight is determined. This maximum load factor is reached in a horizontal sustained turn. This is because the lift vector is under an angle during turns, inducing a centrifugal force on the body which contributes to the resultant body force vector. Using chapter 12 of the book Elements of Airplane Performance by Ruijgrok, the maximum load factor can be determined with Equations 15.1 through 15.4. It should be noted that Equation 15.2 is the lift coefficient where the ratio between  $C_L$  and  $C_D$  is maxed. Table 15.1 shows all the inputs into the equations, and the acquired outputs.

The maximum load factor is evaluated in two different phases of flight. The first being with cargo, the second being after the drop has been made, so without cargo. The load factors are then used to calculate the associated roll angles, as load factor is the inverse of the cosine of the roll angle.

$$n_{max} = \frac{T_{max}}{W} \left( \frac{C_L}{C_D} \right)_{max} \quad (15.1)$$

$$C_L = \sqrt{C_{D_0}} \pi A e \quad (15.2)$$

$$C_D = C_{D_0} + \frac{C_L^2}{\pi A e} \quad (15.3)$$

$$V_{nmax} = \sqrt{\frac{n_{max} W}{S} \frac{2}{\rho} \frac{1}{C_L}} \quad (15.4)$$

## 15.2 Standard rate turns

When approaching airports, it is convenient for the air traffic controller to know an aircrafts turning radius during standardised turns. The UAV should be able to perform these standardised turns. The standardised rate one turn implies a rate of turn of  $3^\circ/s$  or  $\pi/60 \text{ rad/s}$ . Filling in Equation 15.6 leads to a rate one turn radius of 2613.45 m. The results can be found in Table 15.2. The radius is used in Equation 15.5 to find corresponding load factors and roll angles.

$$R = \frac{V^2}{g\sqrt{n^2 - 1}} \quad (15.5)$$

$$\Omega = \frac{V}{R} \quad (15.6)$$

**Table 15.1:** Variables used in determining the maximum load factor

	Variable	Value	Unit
<i>inputs</i>			
	$\rho$	0.6547	$[\frac{kg}{m^3}]$
	Maximum Thrust $T_{max}$	2816	[N]
	Zero lift drag $C_{D_0}$	0.03	[-]
	Aspect ratio A	9	[-]
	Oswald factor e	0.783	[-]
	Weight before drop $W_1$	23024	[N]
	Weight after drop $W_2$	17138	[N]
	Surface S	19.9	$[m^2]$
<i>outputs</i>			
	Load factor $n_{max_1}$	1.59	[-]
	Roll angle $\phi_1$	51	[deg]
	Velocity $V_{nmax_1}$	83.03	$[m/s]$
	Load factor $n_{max_2}$	2.11	[-]
	Roll angle $\phi_2$	61.71	[deg]
	Velocity $V_{nmax_2}$	83.03	$[m/s]$

**Table 15.2:** Variables used in determining the maximum load factor

	Variable	Value	Unit
<i>inputs</i>			
	$V_{approach}$	38.01	$[m/s]$
	Turn rate $\omega$	0.0523	$[rad/s]$
	Gravitational constant g	9.81	$[\frac{m}{s^2}]$
<i>outputs</i>			
	Turn radius R	726	[m]
	Load factor n	1.0203	[-]
	Roll angle $\phi$	11.5	[deg]

### 15.3 Climbing performance

Another value which indicates performance, is the rate of climb (RC) of the aircraft. Ideally, climb is performed under the lowest power requirement setting. This means that drag should be minimised as well as velocity. This is because required power is drag times velocity. When flying at  $C_{L_{max}}$ , the velocity is at its minimum. Using a drag coefficient of 0.033, and an approach velocity of 38.01  $[m/s]$ , the drag can be determined at 607.4  $[N]$ , and required power at 23087.5  $[W]$ . These conditions give the maximum RC. Using Equation 15.7, the RC at ground level is determined to be 12.57  $[m/s]$ . At cruise level, the velocity is 111  $[m/s]$ , and air density  $\rho$  is 0.6547  $[kg/m^3]$ . Cruise drag has a value of 2816  $[N]$  as calculated in the aerodynamics chapter. RC at cruise level is then 0.517  $[m/s]$ . Table 15.3 shows the results.

$$RC = \frac{P_a - DV}{W} \quad (15.7)$$

analysis

## 16 | Avionics

The term avionics is a portmanteau of *avionics* and *electronics* and covers all the electrical systems used in an aeroplane. The intention of this chapter is to describe the complete electronic system configuration of the UAV to provide functionality that meets the requirements.

**Table 15.3:** Variables used in determining the maximum load factor

	Variable	Value	Unit
<i>inputs</i>			
	$V_{approach}$	38.01	[m/s]
	$D_{approach}$	607.4	[N]
	$V_{cruise}$	111	[m/s]
	$D_{cruise}$	2816	[N]
	$P_a$	325000	[W]
<i>outputs</i>			
	$RC_{max}$	12.57	[m/s]
	$RC_{cruise}$	0.517	[m/s]

## 16.1 Requirements analysis

The requirements of the avionics are listed below. The first order requirements may seem obvious and are essential for the UAV to fulfill its mission. The second order requirements are not essential but are set to produce an innovative design with unique capabilities.

First order requirements:

1. Ability to fly the UAV
2. Navigate the UAV according to the mission plan
3. Allow the cargo drop-off according to the drop
4. Allow take-off and landing of the UAV
5. Allow the UAV to collect visual data

Second order requirements:

6. Allow seamless integration into the civil aviation system:
  - (a) Perform automatic collision avoidance
  - (b) Communicate the aeroplane's position to ATC
  - (c) Allow human intervention at all times
7. Allow continuous monitoring of the UAV

Each of the requirements is numbered and will be referred to in the rest of the section.

## 16.2 System selection & overview

This section describes the avionic subsystems of the UAV and whether they are flight critical or not. A subsystem is flight-critical if its failure results in a crash. The identification of the flight-critical systems is key to the determination of reliability measures. The flight-critical systems are tagged with an \* in the following list:

The following systems are required to fly the UAV (requirement 1).

- **Autopilot\***
- **Inertial measurement unit (IMU)\***
- **Static pressure sensor\*** For standard atmosphere based altitude indications.
- **Differential pressure sensor\*** For indicated airspeed indication.
- **Control surface actuators & transducers\***
- **Engine control actuators & transducers\***

The following systems are required to navigate the UAV according to the mission plan (requirement 2):

- **GPS receiver\***
- **Computer memory\*** This allows the autopilot to read the mission plan.

The following systems are required to perform an accurate cargo drop-off (requirement 3):

- **GPS receiver** To release the cargo at an exact location.
- **Line of sight (LOS) communications transceiver** To transmit a message to the crew at drop-off location that the UAV is inbound, and to receive clearance for drop-off.
- **Radio altimeter** This system uses radar signals to report the height of the UAV above the ground to the autopilot.
- **Cargo release actuator**

Although these systems are not flight-critical, they are critical for the mission of the UAV. The systems that allow take-off and landing of the UAV are:

- **LOS communications transceiver\*** This allows a controller to take control over the UAV.
- **A camera** This provides a live video feed during landing and taxiing. The landing speed of the UAV and the distance at which it needs to be controlled makes distance observed landing unfeasible, though not impossible.
- **Radio altimeter** This is an aid for landing the UAV.

The following systems allow the UAV to gather visual data (requirement 4):

- **A camera**
- **A gimbal**

The systems required for integration into the civil avionic system (requirement 5) are:

- **TCAS** For requirement 5a [123] .
- **ADS-B** For requirement 5b. This allows the ATC to monitor the position of the UAV.
- **Satellite communication link (SATCOM)** For requirement 5c. This allows human intervention at all times.

The SATCOM system also allows for continuous monitoring of the UAV, so requirement 6 is also met.

### 16.2.1 Choice of satellite link

There are two main requirements for the satellite link:

- The satellite link is available at all times in the operating area.
- The required equipment fits inside the UAV.

A company called Inmarsat owns a satellite network with a service designed for aviation with global coverage, except for polar regions, called Swiftbroadband. The data-rate capabilities of Swiftbroadband are sufficient for video links (up-to 432 kbps per channel, depending on antenna) [124]. The commercial costs of an Inmarsat Swiftbroadband satellite link is shown on page 28 of the mid-term report. Inmarsat claims to have provided free satellite communication services to aid organisations in the Haiti earthquake aftermath [125] .

## 16.3 Component selection

An overview with all avionic subsystems, their most relevant technical characteristics, references to their datasheets, and the most important reasons for their selection is shown in Appendix G. The following subsections provide an elaboration on the selection of some systems.

### 16.3.1 General guidelines for avionic component selection

Aviation grade components were usually preferred in the selection of the avionic subsystems, especially if they are flight-critical. Aviation grade means that the components were especially designed for professional aviation purposes, and subjected to tests that prove a high level of reliability and the ability to cope with the environmental conditions that the UAV meets. Examples are vibration and temperature variation tests. Some components are open-source technology, which is preferred by the client. However, none of these components are aviation grade. Recommendations about these components are made in section 16.13.

### 16.3.2 Telemetry

The system contains several subsystems that require the sending and receiving of radio signals for their functioning. Table 16.1 provides an overview of these systems and the frequencies at which they operate. This is relevant information for antenna selection and placement, and for the assessment of the chance of frequency interference. The reason for the operating frequency of the LOS link is with the evaluation of the link budget.

**Table 16.1:** UAV radio transmission and reception systems

<b>System:</b>	<b>Frequency</b>	<b>No of Antennas</b>	<b>Position</b>
SATCOM	1.5 – 1.7 GHz	1	Top
LOS-link	900 MHz	2	Top, bottom, distanced from SATCOM
GPS	1575.42 MHz	1	Top
ADS-B	1090 MHz	1	Top
TCAS	1030 MHz send, 1090 MHz receive	2	Top, bottom
Radio altimeter	24.0 – 24.5 GHz	1	Bottom

### Antenna selection and placement

Aviation grade antennas were preferred in antenna selection, as well as an aerodynamic shape that results in a low amount of drag while being able to meet the radio system requirements. The antenna of the LOS link was selected based on its link budget as described below.

Care should be taken with the placement of antennas. They are preferably spaced 1 *m* or more from each other, have unobstructed line-of-sight views and are not placed near an engine exhaust. Furthermore, antennas for radio systems that operate at frequencies which are integer multiples of each other should not be placed near one another to avoid frequency interference [126].

### LOS link budget

This section analyses the link budget of the LOS communication system. The goal is to select an appropriate transceiver with matching antennae. This method is proposed in the book Space Mission Analysis and Design [127], which will be referred to as SMAD from now on.

The signal gains and losses in each of the system components are calculated or taken from datasheets. These values are converted to a logarithmic scale which allows for easy manipulation. Design iterations in a spreadsheet allow the extraction of component requirements. The downlink budget is shown in Table 16.2. The source column contains references to SMAD, and references to comments and equations shown below.

**Table 16.2:** LOS link budget

<b>DOWNLINK</b>					
<b>Item</b>	<b>Symbol</b>	<b>Unit</b>	<b>Source</b>	<b>900 Mhz</b>	<b>2400 Mhz</b>
Horizontal distance	$d$	km	Comment 1	50	50
UAV altitude	$h$	m	Comment 2	6000	6000
Frequency	$f$	MHz	Comment 3	900	2400
Transmitter power	$P_t$	Watts	Comment 4	1	1
Transmitter power	$P_t$	dBW	10log(P)	0	0
Transmitter Line Loss	$L_{lt}$	dB	Comment 5	-1	-1
Avg Transmit Antenna Gain	$G_{ta}$	dBi	Comment 6	2.4	4.5
Transmit Total Gain	$G_t$	dB	$G_{ta} + L_{lt}$	1.4	3.5
Eq. Isotropic Radiated Power	$EIRP$	dBW	$P_t + G_{ta} + L_{lt}$	1.4	3.5
Propagation Path Length	$r$	km	From h and d	50.36	50.36
Space Loss	$L_s$	dB	Eq 16.2	-125.56	-134.08
Propagation and Polarization Loss	$L_a$	dB	[128]	-0.5	-0.5
Peak Receive Antenna Gain	$G_r$	dBi	Comment 7	13	15
System Noise Temperature	$T$	K	SMAD Tbl 13-10	1000	1000
Data Rate	$R$	bps	Comment 8	384000	384000
Eb/No	$SNR$	dB	Eq. 16.4	31.08	24.66
Bit Error Rate	$BER$		SMAD fig 13-9	1.00E-004	1.00E-004
Required Eb/No	$SNR_r$	dB-Hz	SMAD fig 13-9	11	11
Implementation Loss	$L_i$	dB	SMAD pg. 568	-2	-2
<b>Margin</b>		<b>dB</b>		<b>18.08</b>	<b>11.66</b>

**Comment 1:** Distance within LOS range at which it would be convenient to start communications to prepare for landing.

**Comment 2:** Cruise altitude of the UAV.

**Comment 3:** Evaluation at 900 and 2400 Mhz because these frequencies are ISM (Industrial, Scientific, Medical) bands [129]. These bands require no license and versatile commercial off the shelf (COTS) wireless equipment is offered for these frequencies [130].

**Comment 4:** Sending equipment is usually limited to a power  $P$  of 1 W for these frequencies, which is a legal constraint in some countries for unlicensed transmission.

**Comment 5:** A  $L_{lt}$  of  $-1$  [dBW] was found as a typical value for several meters of transmission line [131].

**Comment 6:** Research into suitable aeroplane antennae revealed that an omni-directional  $G_{ta}$  of 2.4 and 4.5 [dBi] is obtainable [132] for these frequencies.

**Comment 7:** Typical antenna gain for omni-directional receiver antenna [133].

**Comment 8:** Requirement for medium quality video streaming [134].

The following paragraph explains the most important formulas in the derivation of the link budget.  $L_s$  refers to the free space loss (SMAD eq. 13 – 8):

$$L_s = \left(\frac{\lambda}{4\pi r}\right)^2 \quad (16.1)$$

where  $\lambda$  is the wavelength in  $m$  and  $r$  is the transmission distance in  $m$ .

Conversion of this formula to decibels and using frequency instead of wavelength results in:

$$L_s = 32.4 + 20 \log(f) + 20 \log(r) \quad (16.2)$$

$L_s$  is now given in  $dB$ , the unit of  $f$  is  $MHz$  and the unit of  $r$  is  $km$ .

$E_b/E_0$  is the signal to noise ratio of the LOS link configuration. It is defined as the ratio of received energy-per-bit to noise-density, and is an indication of the quality of the link. The formula is:

$$\frac{E_b}{E_0} = \frac{PL_l G_t L_s L_a G_r}{kT_s R} \quad (16.3)$$

where  $P$  is the transmitter power in  $W$ ,  $L_l$  is the line loss between the antenna's and transceivers,  $G_t$  is the transmit antenna gain,  $L_s$  is the space loss,  $L_a$  is transmission path loss,  $G_r$  is the receive antenna gain,  $k$  is the Boltzmann's constant =  $1.38 \cdot 10^{-23}$  [J/K],  $T_s$  is the system noise temperature in  $K$  and  $R$  is the range in  $m$ .  $L_a$  is a function of factors such as rainfall density and atmosphere attenuation. The frequencies at which the link is evaluated are insensitive to these factors as reference [128] shows.

After conversion to decibels equation 16.3 changes to:

$$\frac{E_b}{E_0} = P + L_l + G_t + L_s + L_a + G_r + 228.6 - 10 \log T_s - 10 \log R \quad (16.4)$$

where  $E_b/E_0$ ,  $L_l$ ,  $G_t$ ,  $L_s$ ,  $L_a$  and  $G_r$  are in  $dB$ ,  $P$  is in  $dBW$ ,  $T_s$  is in  $K$ ,  $R$  is in  $bps$  and  $10 \log k = -228.60$  [dBW/(Hz · K)].

Table 16.2 shows that at both frequencies the signal-to-noise ratio requirements are met by a large margin. The LOS downlink will work using a 900 MHz system with 1 W transmitter power, a transmit antenna gain of 2.4 dB and receive antenna gain of 15 dB.

The uplink was evaluated in the same way with the same components. The required uplink datarate is smaller which results in a larger margin.

### 16.3.3 Control surface actuators

The control surfaces are controlled by actuators. Three types of actuators are found in fly-by-wire control systems: electromechanical (EMA), electrohydrostatic (EHA), and electrohydraulic (EH) actuators. Table 16.3 provides a general comparison of these actuators.

The working principle of an EHA is shown in figure 16.1 from paper [135]. EHA and EMA are favored over EH in modern aeroplanes such as the Lockheed Martin F35 [136], because they remove the need for a central hydraulic system. For the same reason this UAV will use either EHA or EMA on the flight control surfaces. Despite its drawbacks, EMA is a potentially more suitable solution than EHA because of the relatively low control forces of this UAV compared to the usual EHA-applied aeroplane [137].

Manufacturers of aeroplane grade EMA and EHA such as Moog do not offer enough information to non-customers about their products to be able to select control surface actuators for this UAV. However, it is possible to derive the

**Table 16.3:** Comparison of three different actuation systems

	<b>EH</b>	<b>EHA</b>	<b>EMA</b>
<b>Working principle</b>	Central hydraulic power controlled by electrical servovalves	Local hydraulic system powered by electric motor	Brushless DC motor power converted by gearbox
<b>Advantages</b>	Mature technology, reliable	Applied on modern aeroplane primary control surfaces	Lowest cost, lowest complexity
<b>Disadvantages</b>	Highest weight, complex central hydraulic system	High component complexity	Unpredictable jamming behavior, unpredictable wear life

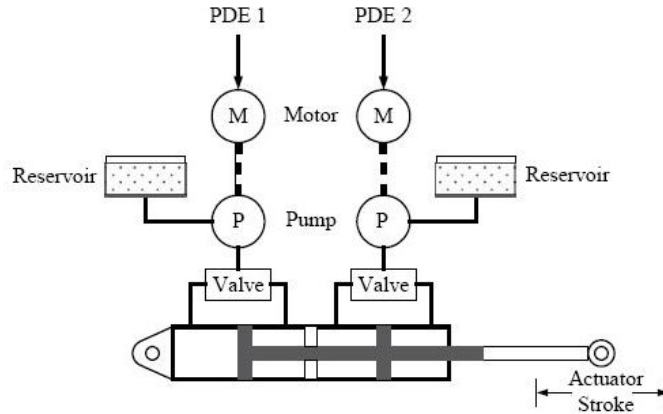


**Figure 16.1:** The working principle of a dual-redundant EHA

power requirements from the control surface hinge moments. This is required to estimate the power budget of the avionic system in section 16.9, and the weight of the actuators based on statistical data [135].

The power  $P$  in  $W$  required to exert a torque  $T$  in  $Nm$  at an angular velocity  $\omega$  in  $rad/s$  is:

$$P = T \cdot \omega \quad (16.5)$$

This formula is converted to:

$$P_{out} = T \cdot \frac{2 \cdot \pi \cdot \alpha}{360} \cdot \frac{1}{t} \cdot 2 \cdot 1.1 \cdot 0.7 \quad (16.6)$$

where  $\alpha$  is the control surface deflection in  $^\circ$ , the maximum deflection angle is multiplied by 2 for a full stroke, the factor 1.1 is a safety factor, and  $t$  is the time required for a full stroke in  $s$ .

Reference [135] advises that the maximum allowable time  $t$  spent on full elevator and rudder strokes is 1.0  $s$  and for full aileron stroke 0.5  $s$ . These rates are defined at 70 % of stall load, which explains the factor of 0.7. See page 48 of paper [135].

To derive the consumption power, the equation above is multiplied by the inverse of the typical efficiencies of an electric motor ( $\lambda = 0.9$ ) and a converter (gearbox or electro-hydraulic pump,  $\lambda = 0.85$  for both). See page 48 of [135], and website [138]. This yields the results shown in table 16.4.

The hinge moments for the ailerons and the elevator were obtained by the stability group. Those of the rudder were not available, so the power estimate of the rudder was done by averaging the power requirements of the other control surfaces, which is assumed to be possible. The validity of this assumption is based on the control surface hinge moments of other aeroplanes. See page 42 and 117 of [135] page 42.

**Table 16.4:** Control surface actuators power estimation

Control surface	Deflection ( $\alpha$ ) in $[\circ]$	T, in $Nm$	$P_{out}$ in $W$	$P_c$ in $W$
Aileron	20	426	458	598
Elevator	20	500	537	701

The weight of the actuator is estimated from Figure E-1 in [135]. The power to weight ratio is predicted at  $0.13 Kw/kg$  at this power requirement. The results for the weight estimations are found in the component list.

## 16.4 Landing gear actuator

The method to estimate the power and the weight of the landing gear actuator is the same as the estimation of the control surface actuator power.

The weight  $w$  of the landing gear is estimated to be  $123 kg$  in total from the second class weight estimation. The length  $l$  is estimated to be  $1 m$  at the time of actuator sizing. The weight is conservatively guessed to be concentrated at 80 % of the total landing gear length. The actuator is assumed to move into the fuselage as a stiff system, so it does not fold and thereby reduce the required moment. The power and weight of the actuator are estimated as if one actuator controls the entire weight of the landing gear. In reality, the total weight of the landing gear is divided over three actuators, one for each strut. However, for the numbers derived this does not make a difference because all the relations are linear.

The peak torque is obtained from the moment exerted by the weight of the landing gear about the hinge when the landing gear is parallel to the ground:

$$T_{peak} = 0.8 [m] \cdot 123 [kg] \cdot 9.81 [N/m^2] = 965.3 [Nm] \quad (16.7)$$

Based on aviation experience, the landing gear will likely move over an angle  $\alpha = 110^\circ$  in about 8 s. This provides the average angular velocity at which the landing gear will move at  $T_{peak}$ :

$$P_{out} = T_{peak} \cdot \frac{2 \cdot \pi \cdot \alpha}{360} \cdot \frac{1}{t} \cdot SF \quad (16.8)$$

This results in a  $P_{out}$  of  $254 W$  if a SF of 1.1 is used. With an efficiency of 0.9 for the electric motor and 0.85 for the converter as in the previous section,  $P_c = 322 W$

## 16.5 Fuel pump

Unfortunately, little information about the fuel pump of the selected powerplant (Rolls Royce M250F) is provided. The fuel pump is powered electrically which requires the following fuel pump power estimation. The equation for ideal pump power is derived from basic fluid dynamics. Omitting the derivations and simply providing the formula gives [139]:

$$P_{ideal} = \dot{m} \frac{p_1 - p_2}{\rho} \quad (16.9)$$

where  $P_{ideal}$  is the ideal pump power in  $W$ ,  $\dot{m}$  is the mass flow rate, estimated by the propulsion group to be  $0.0275 kg/s$  at takeoff,  $\rho$  is the fluid density of  $800 kg/m^3$  for kerosene and  $p_1$  and  $p_2$  are the pressures that the pump works between in  $N/m^2$ . For this fuel pump  $p_1 - p_2 = 41.38 \cdot 10^5 N/m^2$  [140]. Inserting these numbers into the equation yields a  $P_{ideal} = 0.14 kW$

Multiplication with a conservative efficiency factor of  $1/0.6$  to convert to shaft power, and a factor of  $1/0.9$  to convert to electric power results in an electric power consumption of  $0.27 kW$ . The efficiency factor to convert to shaft power seems very low (especially considering the efficiency factor of 0.85 of the EHA pumps in Subsection 16.3.3. However, this efficiency factor checked with the efficiency of the fuel pump of a Beechcraft Bonanza.

## 16.6 Reliability

The system was designed for reliability in an intuitive way. See section 16.13 on recommendations for a suggestion of a more scientific method. The system is designed such that the failure of one of the flight critical systems, as pointed out in Section 16.2, does not result in loss of the aeroplane. Table 16.5 yields the reliability measures for the flight critical systems:

The autopilot and IMU are triple redundant because they are not aviation-grade products.

**Table 16.5:** Avionic system reliability measures

System	Reliability measures:
Autopilot + Gumstix Overo	3x redundant
Static & dynamic pressure	3x redundant (onboard autopilot)
IMU	3x redundant
GPS	2x redundant
GPS antenna	2x redundant
LOS link	Backed up by SATCOM
Flight critical actuators	2x redundant
Engine monitor	Obtain reliability information from manufacturer
Power system	Backup battery

The work-around in case of engine failure is to combine the information of a number of other sensors (angle of attack, airspeed, configuration) to determine the most important engine parameters based on system knowledge of the aerop. This could be done by autopilot software. The flight critical actuators will have integrated redundancy of all actuator subsystems [141].

## 16.7 Interfaces and system layout

Appendix J shows the avionic system layout. The flight critical systems are shown in red. Each subsystem has an ID which is also found in the component list in Appendix G.

The interfaces and protocols used to control the subsystems are mainly selected by matching the available interfaces and protocols supported by the autopilot to those supported by its peripherals. The CAN databus is used to control all actuators and some other subsystems. The main reasons are the fault tolerant design of the CAN databus [142] and its ability to support a large number of nodes compared to the other available interfaces [143].

The camera (ID: 5) sends its video signals by DVI to the Flight Data Recorder for storage, and to the SATCOM and LOS link for transmission. It is controlled by the autopilot using CAN.

The SATCOM connection layout is requires attention. The satellite transceiver controls the directional antenna through ARINC 429. The transmission and receiver signals are forwarded to the antenna through a combined high power amplifier and diplexer/low noise amplifier, as shown in the diagram. Some subsystems are controlled by the autopilot through General Purpose Input/Output (GPIO). This is usually done to turn a device on or off.

### 16.7.1 Connectors and cabling

The table below the diagram in Appendix J provides the recommended connectors for the most common interfaces. These were provided in the specifications for RS-232 and CAN [144] [145]. The exact type of cabling depends on the application and setting of the datalink. The connector recommendations for UART-TTL and USB were done by the author of this chapter. The main requirement is a robust connection. Figure 16.2 shows the selected type of USB connector.



**Figure 16.2:** The recommended type of USB connector

## 16.8 Triple redundant autopilot layout

The layout of the triple redundant autopilot is shown in Appendix I. Three autopilots are shown in the middle of the page, each attached to its own additional computer through SPI. The interfaces on all autopilots are interconnected, and share one external connection. In that way, each autopilot has the ability to receive and transmit messages to all peripherals.

The I<sup>2</sup>C1 interface is connected to an I<sup>2</sup>C GPIO expander (an integrated circuit such as MCP23017) to accommodate more GPIO than the autopilot and additional computer offers (four in total). This was done because the entire avionic system will probably require many more GPIO than is predicted at this design stage. A USB-hub creates extra USB ports for more peripherals. Unfortunately, the autopilot does not possess an RS-232 interface. The MAX232 IC converts the UART-TTL signals to the RS-232 protocol and back.

### 16.8.1 Software level implementations

Implementations on a software level are required for this triple redundant system to work. A possible solution is to designate a first, second and third autopilot. Under normal circumstances the first autopilot controls the UAV, and the second autopilot periodically tests the first autopilot for failure through one of their interconnected interfaces such as I<sup>2</sup>C. The third autopilot is asleep. Should autopilot one fail, the second autopilot takes over control and the third autopilot wakes up to test the second autopilot.

## 16.9 Power budget

The purpose of determining the power budget is to find the requirements for the electrical power system. It is found by summing the power requirements of all individual subsystems of which simultaneous operation is a possibility. This in itself is an improbable situation: it would mean maximum power requirement for all control surfaces while extending the landing gear and flaps at the same time.

Two cases are considered:

1. Maximum power requirement during normal operation.
2. Maximum power requirement for all flight critical subsystems in case of power shortage.

The results are shown in Table 16.6

**Table 16.6:** Power budget estimations

	Power $W$
Total power budget:	4481
Total power budget with 15% margin:	5249
Flight critical power budget:	1694
Flight critical power budget with 15% margin:	1948

The 15% margin was chosen in agreement with a satellite electronics engineer. The information about the generator that is usually delivered with the Rolls Royce M250F engine is too limited to assess whether it meets the power budget requirements. However, the maximum electrical power requirement is 1.6 % of the shaft horse power delivered by the engine during cruise.

The energy requirement for an emergency descent from the cruise altitude of 6096  $m$  to ground level at a descent rate of 5  $m/s$  was calculated to size the batteries for an engine failure. The goal is to be able to control the aeroplane with the satellite link to perform an emergency landing. Five meters per second is a typical zero-thrust descent rate for similar aeroplanes according to an experienced pilot. This descent takes 1,219  $s$ .

The emergency descent energy requirement was based on the following main assumptions:

The total flight critical energy requirement for an emergency descent due to engine failure including a 15 % margin is: 1.16  $MJ$ . A NiCd battery was selected with a total energy capacity of 1.98  $MJ$ .

The choice between aviation grade NiCd and lead-acid batteries is difficult and there is no definitive argument for either type of battery. Both can do the job and each has its own advantages and disadvantages [146].

**Table 16.7:** Emergency descent power requirement assumptions

System	Assumption
SATCOM	Operates at 200 W, full time
Camera	Operates at full power, full time
Control surface actuators	Operate at 50% power, 40% of the time
Landing gear brake actuators	Operate at 100% power, 20 seconds
Landing gear actuators	Operate at 100% power, 8 seconds
Flap actuators	Operate at 100% power, 8 seconds

## 16.10 Electrical circuit

The electrical circuit is shown in Appendix H. The circuitry on the left delivers electrical power to the three main buses: The actuators bus, the high power avionics bus and the low power avionics bus. This configuration was chosen because it is a convenient method of power distribution.

The following walk-through describes the steps involved in powering up the electrical system and explains the working principle of the electrical circuit:

1. sw1 is manually closed by the ground controller.
2. The autopilot is powered up.
3. The autopilot turns on the MODEM by controlling its switch through the power drive.
4. The MODEM receives a wireless command to start the engine and sends it to the autopilot.
5. asw1 is closed until the Starter/Generator started the engine.
6. The Starter/Generator starts generating electricity, the battery is being charged and the system is powered by the generator
7. The Ammeter tells the autopilot that electricity is being generated.
8. The autopilot opens asw1 to protect the DC/DC converter.

In case of a power failure:

1. The autopilot is protected from power failure by its parallel capacitor for a short period.
2. The autopilot opens asw1 to provide emergency electrical power.
3. The most flight critical systems are started and the UAV goes into safe flight mode.
4. The GCS is alerted and the autopilot attempts to restart the electrical power generation.

The sizing of the power bus circuit breakers was based on a 30 % margin on top of the maximum possible current consumption of that power bus.

Only the main circuit breakers are shown in the electrical circuit. In reality, every subsystem is equipped with its own circuit breaker.

The diodes d1, d2, and d3 prevent the current from flowing in the wrong direction.

## 16.11 System placement

The placement of the avionic systems inside the aeroplane is described in Section 17.2. Note the space available for the avionics cabinet. A suitable cabinet needs to be developed that allows for easy maintenance of the avionic systems, system flexibility, isolation from vibrations and EMI and sufficient cooling of the avionic systems.

## 16.12 Conclusions

The UAV avionic system proposed in this chapter is unique in its capability to integrate with the existing civil aviation system. This is achieved by a combination of ADS-B, TCAS and a satellite communication link allowing ATC position monitoring, collision avoidance and human intervention.

The UAV achieves a precision cargo delivery by timing the drop based on the measurement of its position, ground speed, and absolute height. It does this using a combination of GPS and a radio altimeter. An on-board camera enables the UAV to capture images and video during night and day. Landing and take-off of the UAV are ground-controlled through a LOS link.

The avionic system is designed around the open-source Lisa/L autopilot. System reliability is achieved by redundancy measures for flight-critical systems or proposing workarounds in case of critical subsystem failure. The CAN interface of Lisa/L is used to communicate with the motion actuators. This interface was selected for its fault tolerant design, multiple-node capabilities, and relative immunity to noise.

The power requirement of the avionic system is met by the DC generator delivered with the engine. The electrical power system was designed to be able to cope with sustained generator failure, allowing a human controlled emergency landing. The cumulative system weight of this system is predicted at 177 kg and a rough estimation of the system cost is \$ 46,000.

## 16.13 Recommendations

The following recommendations are made for the next stage of avionic system design and to verify the presented results:

- The methodology to design for reliability in Section 16.6. A more in-depth analysis is required in the next stage of design. Guidelines and methods for conducting the safety assessment are described in SAE ARP 4761. This document proposes a number of techniques to capture the failure modes of a complex system such as this, and offers design guidelines which have been adopted by the main aviation certification agencies.
- Some flight critical components, such as the autopilot and the IMU, have not been tested under the environmental conditions they will meet during their lifetime. Before the avionic system is built, these systems need to be tested and if necessary redesigned for physical effects due to: EMI, lightning, vibration, temperature, altitude, humidity, dust, shock and contaminants. This list is by no means exhaustive. MIL-STD-461 and MIL-STD-462 are useful documents.
- A more elegant method to assess the link budget could be proposed which makes use of probability theory to evaluate the likelihood of systems functioning simultaneously. In this way, the power budget is evaluated more realistically which could lead to a lighter power system design.

# 17 | Final configuration

This chapter shows the final internal and external configuration.

## 17.1 External configuration

In Chapters 10 and 14 information about the external configuration can be found. The result of these elaborations are illustrated in Figure 17.1.

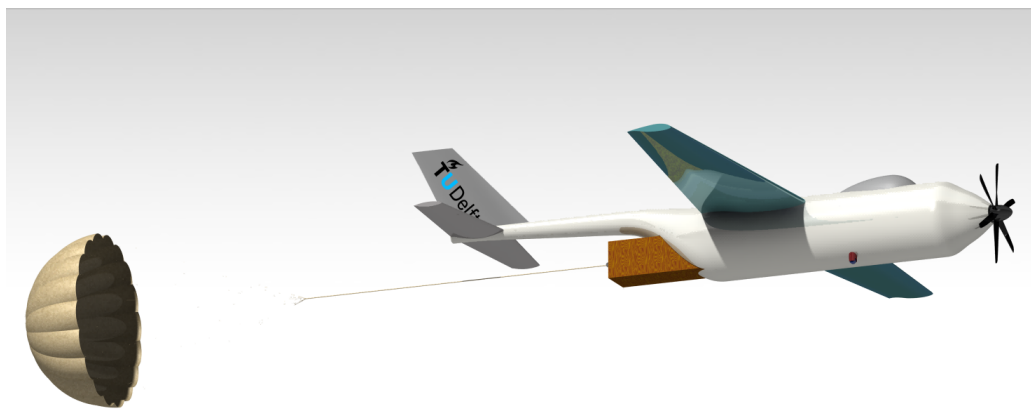


**Figure 17.1:** Illustration of the external configuration

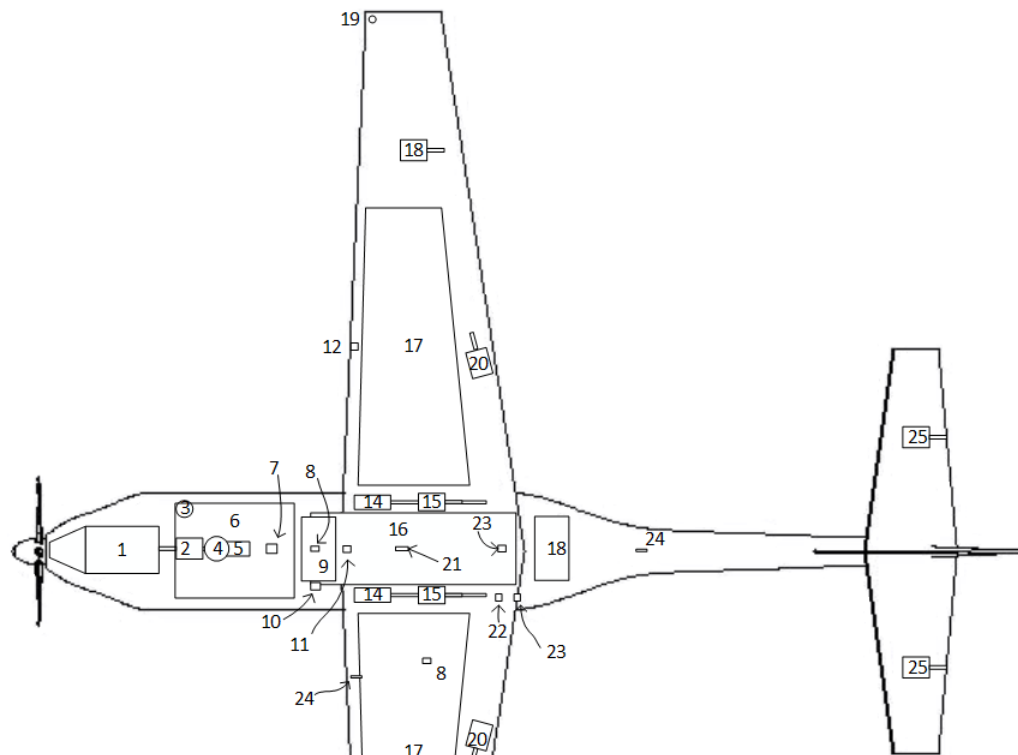
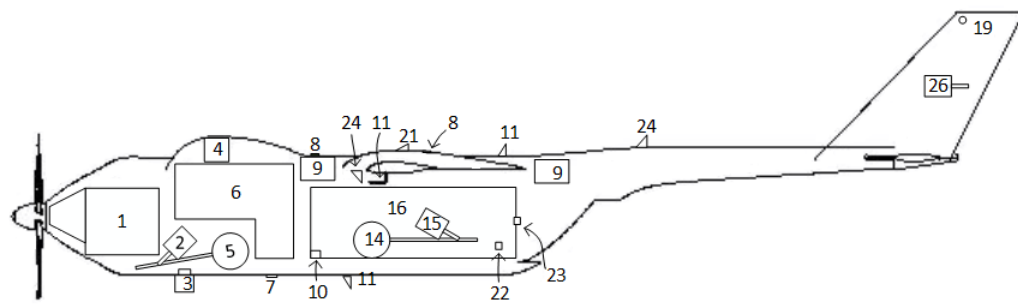
## 17.2 Internal configuration

Apart from all the avionics, as explained in Chapter 16, also the fuel tanks are part of the internal configuration. The fuel will be stored mainly in the wings to counteract the wing loading, a small amount of fuel will be stored in the fuselage. Kerosine will be used as fuel, hence the density is  $0.81 \text{ kg/L}$  and the required volume  $V_{fuel}$  is  $1,010 \text{ L}$ . To be able to store all the fuel, a fuel tank with a length of  $3.5 \text{ m}$  is needed in the wingbox.

In Figure 17.2 an illustration of the internal configuration of the UAV can be found. To get a complete overview of the UAV, a specification sheet is shown in Table 17.1

**Table 17.1:** Specification and description "Aidplane"

<b>Dimensions</b>		<b>Powerplant</b>	
Maximum take-off weight	2,448 <i>kg</i>	Engine	Rolls Royce Model 250-B17F
Operational empty weight	1,021 <i>kg</i>	Power/weight ratio	2,2
Fuel weight	828 <i>kg</i>	Shaft output	2,000 <i>rpm</i>
Wing surface area	20.8 <i>m</i> <sup>2</sup>	Cruise power	425 <i>shp</i>
Wing span	13,7 <i>m</i>	Take-off power	450 <i>shp</i>
Chord length at root	2.17 <i>m</i>	Fuel	Jet-A1, JP-8, Biofuel
Chord length at tip	0.8697 <i>m</i>	Propeller	Variable pitch, double acting, 6 bladed, aluminium
Aspect Ratio	9	<b>Avionics equipment list</b>	
Taper ratio	0,4	<i>Primary flight systems</i>	
Overall length	11.75 <i>m</i>	Autopilot	Lisa/L
Overall height	4 <i>m</i>	Computer	Gumstix Overo
<b>Performance</b>		IMU	Aspirin
Cruise speed	400 <i>km/h</i>	GPS	NexNav MAX
Service ceiling	6,096 <i>m</i> (20,000 <i>ft</i> )	<i>Telecommunications</i>	
Takeoff distance	1,097 <i>m</i>	LOS link	Microhard lpn920 UHF MODEM
Landing distance	877 <i>m</i>	Sattelite communications	SCOTY UAV SATCOM unit
Range	2,000 <i>km</i>	<i>Aviation system integration</i>	
Stall speed	105 <i>km/h</i>	TCAS	Avidyne TAS 605
		ADS-B out	Sagatech XPS-TRB
		<i>Flight control system</i>	
		Actuators	Electro-hydrostatic actuators
		<i>Others</i>	
		Pitot probe heating	Dynon Avionics Heated AOA/Pitot Probe
		Wing ice detector	UTC Model 0871LH1



1	Engine	15	Main landing gear
2	Front landing gear actuator	15	Main landing gear actuator
3	Camera	16	Cargo
4	Satellite communications antenna	17	Fuel tank
5	Front landing gear	18	Aileron actuator
6	Avionics cabinet	19	Navigation/strobe lights
7	Radio altimeter	20	Flap actuator
8	GPS antenna	21	ADS-B antenna
9	Secondary fuel tank	22	Cargo release sensor
10	Cargo release solenoid	23	Parachute release solenoid
11	TCAS antenna	24	UHF link antenna
12	Ice detector	25	Elevator actuator
13	Pitot probe	26	Rudder actuator

Figure 17.2: Illustration of the internal configuration

## Part IV

# Detailed design cargo delivery system

# 18 | Cargo delivery system

Based on the results of the conceptual design in Chapter 8, the use of a parachute to deliver the cargo was found to be the best solution. In this chapter, the parachute and other components of the delivery system are designed in detail. The most efficient method of dropping with a parachute will be chosen first, after which the trajectory of the delivery system can be determined. To reduce the impact on the cargo during landing, an impact attenuator is designed. With this information, the parachute can be sized, and the drop-off precision determined. In the end, the design process will be concluded and recommendations will be given.

## 18.1 Drop-off method

The main challenge for the cargo delivery system is the requirement of a high precision drop accuracy of within 50 m. When dropping the system from a high altitude, unpredictable factors such as wind have a large effect on the precision. Guided parachutes are available, but these are highly expensive at a price of approximately \$64,000, and can ensure an accurate precision of only 150 m [147]. To avoid having to use a guided parachute, the system should be dropped from a low altitude so that unpredictable factors only have a small effect on the precision. Flying close to the ground at an altitude of around 5 – 10 m using a low altitude parachute extraction system (LAPES) is a commonly used method. However, this requires a large area, cleared from obstructions such as buildings and trees. Since this is not available, an alternative is to fly at an altitude of around 50 m, avoiding obstructions and minimising effects from unpredictable factors. This method, the parachute low-altitude delivery system (PLADS), is being used by the US Army. With a comparable cargo weight and airspeed, and a parachute area of approximately 35 m<sup>2</sup>, a precision of within 20 m can be achieved [34]. A lower altitude results in a higher precision. However, the buildings in Haiti are approximately 40 m high. A drop-off altitude of 45 m was therefore chosen as the lowest, safe altitude.

To release the cargo from the aeroplane, it is possible to fly at a certain angle so the cargo will be pushed out by gravity, or to have an extraction parachute pulling the cargo from the cargo hold. Since the cargo will be dropped at a low altitude, and has little time to slow down, the extraction method is most efficient in this case. The parachute will be reefed for extraction, since the aeroplane will otherwise experience a large shock during inflation. This reefed parachute is deployed, for example by using a spring mechanism, into the aeroplane’s slipstream and will inflate. When the cargo is detached from the aeroplane, the parachute is disreefed and will fully inflate. This method is commonly used by the US Army [148].

## 18.2 Trajectory determination

To determine the precision of the airdrop, the behaviour of the cargo throughout the drop has to be analysed. In order to do so, the motion is divided into two parts: the swinging motion (1), and the falling motion (2). These two motions can be seen in Figure 18.1. The swinging motion is assumed to be critically damped because of the high vertical velocity, which means the cargo will fall like a pendulum with respect to the parachute until the parachute-cargo system is in a vertical position. During this motion, the entire system will also be falling. During both motions the system will have a horizontal velocity due to the velocity of the aeroplane. Furthermore, to simplify the calculations, it is assumed that the parachute is disreefed from the start of the motion.

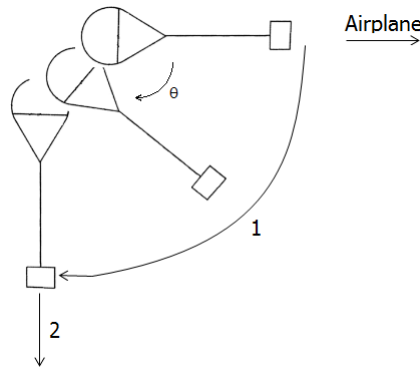


**Figure 18.1:** The two motions of the delivery system: the swinging motion (1), and the falling motion (2)

The time to complete the swing is calculated with basic pendulum physics, using Equation 18.1.

$$t_1(\theta) = \frac{s(\theta)}{V(\theta)} = \frac{\theta/360 \cdot 2\pi \cdot l}{\sqrt{2gl \sin(\theta)}} \quad (18.1)$$

Where  $\theta$  is the angle in degrees between the horizontal and the body axis of the system, as seen in Figure 18.1,  $l$  the length of the line between the parachute and the cargo in meters, and  $g$  is the gravitational acceleration which is  $9.81 \text{ m/s}^2$ .

### 18.2.1 Vertical movement

The result from Equation 18.1 can then be used to calculate the vertical velocity of the system, with the equation for the vertical velocity of a falling object with drag [149]. To simplify the model, it is assumed that at the end of motion (1), the total vertical drag caused by the parachute will be equal to the total horizontal drag. This results in Equation 18.2.

$$V_{y,1}(t_1) = \sqrt{\frac{2mg}{\rho(S_c C_{d_c} + \frac{1}{2} S_p C_{d_p})}} \tanh \left( t_1 \sqrt{\frac{g\rho(S_c C_{d_c} + \frac{1}{2} S_p C_{d_p})}{2m}} \right) \quad (18.2)$$

Where  $m$  is the mass of the total system for which a value of  $600 \text{ kg}$  is used.  $S_p$  is the area of the parachute,  $C_{d_p}$  is the drag coefficient of the parachute which is  $0.75$  for a circular shape, and  $\rho$  is the air density in Port-au-Prince which is  $1.221 \text{ kg/m}^3$ .  $S_c$  is the area of the cargo container, for which the dimensions  $0.7 \text{ m} \times 2 \text{ m}$  are used. For the drag coefficient of the cargo,  $C_{d_c}$ , a value of  $2.1$  is used which is normal for a rectangular box [150]. With this, the vertical velocity at the end of motion (1) can be determined, and used to calculate the vertical velocity of motion (2) in Equation 18.3.

$$V_{y,2}(t) = V_{y,1}(t_{1(\theta=90)}) + \sqrt{\frac{2mg}{\rho(S_c C_{d_c} + S_p C_{d_p})}} \left( \tanh \left( t \sqrt{\frac{g\rho(S_c C_{d_c} + S_p C_{d_p})}{2m}} \right) - \tanh \left( t_{1(\theta=90)} \sqrt{\frac{g\rho(S_c C_{d_c} + S_p C_{d_p})}{2m}} \right) \right) \quad (18.3)$$

Where  $t_{1(\theta=90)}$  is the time after which the system is in a vertical position, and thus at the end of motion (1). Now that the velocity is known, the covered distance with respect to time can be determined. This is done with Equation 18.4.

$$s_y = V_{y,average} \cdot t = V_{y,1,average} \cdot t_{1(\theta=90)} + V_{y,2,average} \cdot (t - t_{1(\theta=90)}) \quad (18.4)$$

In which  $s_y$  is the vertical distance,  $V_{y,1,average}$  is the average vertical velocity for motion (1), and  $V_{y,2,average}$  the average vertical velocity for motion (2). Since the cargo is going to be dropped from  $45 \text{ m}$ , the time can be determined after which this distance is covered.

### 18.2.2 Horizontal movement

During motion (1) the horizontal drag is caused by both the cargo and the parachute. This results in Equation 18.5 as a relation for the horizontal velocity.

$$V_{x,1}(t_1) = V_{min} - \frac{\frac{1}{2}\rho(\frac{1}{2}S_p C_{d_p} + S_c C_{d_c})V_x^2}{m} \cdot t_1 \quad (18.5)$$

Where  $V_{min}$  is the minimum velocity of the UAV and  $V_x$  the horizontal velocity of the delivery system. For motion (2) it is assumed that only the cargo causes horizontal drag, as can be seen in Equation 18.6.

$$V_{x,2} = V_{x,1}(t_{1(\theta=90)}) - \frac{\frac{1}{2}\rho(S_c C_{d_c})V_x^2}{m} \cdot t \quad (18.6)$$

With the horizontal velocity with respect to time known, the horizontal distance that the delivery system travels from the drop-off point can be determined. This is done with Equation 18.7.

$$s_x = V_{x,average} \cdot t = V_{x,1,average} \cdot t_{1(\theta=90)} + V_{x,2,average} \cdot (t - t_{1(\theta=90)}) \quad (18.7)$$

In which  $s_x$  is the horizontal distance from the drop-off point,  $V_{x,1,average}$  is the average horizontal velocity for motion (1), and  $V_{x,2,average}$  the average horizontal velocity for motion (2). The time  $t$  depends on the drop-off altitude, and can be determined by Equation 18.4.

## 18.3 Impact attenuation design

Since the cargo that has to be dropped carries sensitive and breakable materials, the impact at landing will have to be reduced. This is partly done by the parachute, but also by an impact attenuator.

To determine the size of this impact attenuator, the allowable impact on the cargo content has to be known. This impact deceleration factor is given in multiples  $n$  of the acceleration of gravity for different materials in Table 6-11 in the Parachute Recovery System Design Manual of the U.S. Navy [151]. For sensitive electronic equipment, such

as solar panels, this factor  $n$  is 10. For the rest of the content, mostly the housing materials,  $n = 20$ . If the impact attenuator would be designed for the solar panels, it would be largely over-designed. Therefore, the main impact attenuator will be designed for the gross of the content, and the solar equipment will have to be extra cushioned, for example with foam, within the cargo box.

This same study of the U.S. Navy states in Figure 6-68, that for an allowable impact factor of 20, and expected velocities not lower than 10  $m/s$ , an airbag is the most suitable impact attenuator [151]. A great advantage of airbags over other shock attenuators like honeycomb materials is that they are reusable and light-weighted. The required deceleration stroke, or the height of the airbag, can be calculated with Equation 18.8.

$$s_{airbag} = \frac{V_y^2}{2 \cdot n \cdot g \cdot \eta_{airbag}} \quad (18.8)$$

Where  $s_{airbag}$  is the required deceleration stroke,  $V_y$  the vertical velocity at impact with the ground in,  $n$  the allowable impact factor,  $g$  the gravitational acceleration, and  $\eta_{airbag}$  the efficiency of an airbag which is usually 0.65 according to the U.S. Navy [151]. The deceleration stroke should not be larger than 1.25 times the diameter of the airbag. Since the airbag will cover the bottom of the cargo box, with a minimum width of 0.8  $m$ , the deceleration stroke should not exceed 1  $m$ . With this known, the maximum  $V_y$  can be calculated with the use of Equation 18.8 and results in a value of 15.97  $m/s$ . To be sure the cargo content will not be damaged, even if terminal velocity is reached, this value is used as the terminal velocity in Equation 18.9.

$$V_{terminal} = \sqrt{\frac{2mg}{\rho(S_c C_{d_c} + S_p C_{d_p})}} \quad (18.9)$$

From this equation, the minimum parachute area  $S_p$  was determined to be 46  $m^2$  for a circular parachute with a drag coefficient  $C_{d_p}$  of 0.75. The line length  $l$  in relation with the diameter  $d_p$  of the parachute slightly influences the drag coefficient. When the ratio  $l/d_p$  is larger than 1,  $C_{d_p}$  will increase. For this first design a ratio of 1 will be used and so the initial drag coefficient of 0.75 for a circular parachute will be maintained. This results in a line length of 7.7  $m$ .

Commonly used materials for parachutes are nylon and Kevlar. Kevlar is stronger than nylon and more durable, but also three times as expensive [152]. Looking at Figure 1 from 'The degradation of parachutes' by the US Army it was found that many nylon parachutes exist that have a lifetime of over 10 years [153]. After that time period, the nylon can be recycled. Bio-degradable materials were also looked into, but since the airbags are reusable and will have to be returned, the parachutes can also be reused. This is more sustainable than dropping bio-degradable parachutes. Therefore, nylon was found to be a cost-efficient and durable material that is well-suited for this delivery system.

According to John H. Oswald (CEO of Mills Manufacturing, a company that provides military parachutes for the U.S. government), a parachute of this size and material, having to carry a 600  $kg$  cargo, will cost between \$2,000 and \$3,000.

## 18.4 Landing precision

With the size of the parachute, the minimum airspeed of the aeroplane at drop-off ( $V_{min} = 40.81 m/s$ ), and the drop-off altitude ( $h = 45 m$ ) known, the equations from Section 18.2 can be used to calculate the horizontal distance travelled from the drop-off point until landing. It is assumed that when the cargo meets the ground, it will not slide any further. The precision of the drop-off can be determined by analysing this distance for any possible input error. When looking at Equation 18.7 and Equation 18.6, the horizontal distance mainly depends on the velocity the aeroplane is flying at and the time the delivery system is in the air, which depends on the drop-off altitude. Errors in these values may be:

- The aeroplane is flying at a velocity with an error of 5  $km/h$ , which also results in an error in the parachute inflation time
- The aeroplane is flying at an altitude with an error of 2  $m$
- The predicted, continuous wind has an error of 10  $m/s$  (3 Beaufort)
- The release time has an error of 25%

The standard release time is 0.3  $s$ , as mentioned in Section 13.14. The parachute inflation time can be calculated with Equation 18.10.

$$t_f = \frac{n \cdot D}{V} \quad (18.10)$$

Where  $n$  is the filling constant which is 8 for a circular parachute as described in the Parachute Design Handbook by the US Army [154].  $D$  is the parachute diameter. Since the parachute is reefed during extraction,  $D$  will be the reefed parachute diameter, which is usually 1/5 of the disreefed parachute diameter [154].  $D$  is therefore 1.54  $m$ .  $V$  is the

velocity, which in this case is the velocity the aeroplane is flying at. It can be observed that for a higher velocity of the aeroplane, the inflation time decreases and thus the cargo will be extracted from the aeroplane faster.

The effects of these errors on the horizontal distance can be found in Table D.1 in Appendix D. It can be seen that the highest error in horizontal distance is for the case when flying at a higher altitude, a higher airspeed in combination with wind in the same direction, and having a release time error. This results in an error in the horizontal distance of 42  $m$  with respect to the expected landing point. This is within the required precision of 50  $m$ .

## 18.5 Verification & validation

To verify the model from Section 18.2, the vertical velocity is analysed. When the time  $t$  goes to infinity, the vertical velocity will diverge to the terminal velocity as described in Equation 18.9. Comparing the terminal velocity of the model with the analytical terminal velocity for different values for the parachute area  $S_p$  results in the values shown in Table 18.1.

**Table 18.1:** Errors in the modelled terminal velocities with respect to the numerical values

$S_p$ [ $m^2$ ]	$V_t$ numerical	$V_t$ model	error [%]
30	19.30	19.53	1.2
35	18.04	18.33	1.6
40	17.00	17.35	2.0
45	16.11	16.53	2.5
50	15.63	15.85	1.4
55	14.70	15.26	3.7
60	14.12	14.75	4.3
65	13.60	14.30	4.9

It can be seen that the error in the model increases with an increasing  $S_p$ . However, the modelled  $V_t$  is higher than the numerical value. This will cause an over-designed parachute and airbag in Section 18.3 and will thus not have catastrophic effects. Also, for the expected range of parachute areas (30 – 50  $m^2$ ) the errors are reasonable values, lower than 2 %. For this range of parachute areas, a 2 % change in velocity results in a change between 1 and 2  $m^2$ . Since the horizontal velocity is calculated by using the same model, it can be assumed that it will have the same errors. Since the modelled horizontal distance will, therefore, be larger than the actual distance, the precision is still within the 50  $m$ .

The designed parachute can be validated by comparing it to reference PLADS missions. These values can be found in Table 18.2. It can be seen that the designed parachute is a bit larger than the reference parachutes, which might be because of a difference in allowable impact. The reference missions have a much higher precision, which is probably because it was assumed that changes in wind do not have any impact on the precision.

**Table 18.2:** Characteristics of reference PLADS missions [33] [34], the designed mission of this project is displayed in bold numbers

Cargo weight [kg]	Diameter [m]	Altitude [m]	Vmin [m/s]	Precision [m]
<b>600</b>	<b>7.7</b>	<b>45</b>	<b>41</b>	<b>42</b>
700	6.7	61	67	5
225-900	7.3	69	62	10

## 18.6 Conclusion & recommendations

From this chapter, it can be concluded that the cargo will have to be dropped from an altitude of 45  $m$ . In combination with a 50  $m^2$  nylon parachute and a 1  $m$  high airbag covering the bottom of the cargo box, the impact at landing is reduced to protect most of the cargo content. The sensitive solar panels will have to be cushioned within the cargo box. For the worst case scenario, when all input errors for the travelled horizontal distance occur and affect the distance in the same direction, the landing position differs 42  $m$  from the expected position.

However, the model as described in Section 18.2 is a simplified model where many assumptions have been made. For instance, the oscillation is assumed to be critically damped because of the high velocities. In reality this oscillation is often highly damped, but will oscillate beyond  $\theta = 90$   $deg$ . An alternative model, such as described in Appendix C, could give more accurate results. This model uses the equations of motion (EOMs) for any kind of motion of the

cargo-parachute system. During this project the EOMs were solved using an explicit Euler method. This resulted in unstable values for the tension  $T$ , which lead to an unrealistic trajectory. It was found that the wrong numerical method was used, and that an implicit method could solve the problem. Unfortunately, due to time constraints it was not possible to apply this method, and thus a simplified model was used. For further design it is advised to use the EOMs in combination with an implicit numerical method.

Another assumption made in the simplified model was that when the cargo is extracted from the aeroplane and motion (1) starts, the parachute is already fully inflated. The inflation time of the parachute can be calculated with Equation 18.10 from Section 18.4. For a parachute area of  $46 \text{ m}^2$ , flying at the minimum drop-off airspeed, this time is  $1.5 \text{ s}$ , which is significant with respect to the total time the system is in the air. The drag the parachute causes will therefore be lower. This effect would have to be taken into account for a further design to accurately determine the precision and impact.

The impact attenuators, both airbag and parachute, are designed for an allowable deceleration of  $20 \text{ g}$ , assuming the sensitive solar equipment can be cushioned sufficiently within the cargo box. To prove that this is correct, tests will have to be performed to measure the forces on the equipment.

To determine the drop-off precision, it was assumed that the cargo will not slide after impact. This might not be true for surfaces with low sliding friction coefficients, such as wet grass. Therefore, the total travelled horizontal distance might increase because of the addition of a horizontal distance on ground. This distance depends on the sliding friction coefficients of both the ground surface and the airbag underneath the cargo box, and the velocity at landing. The precision will thus also depend on the possible errors in the sliding friction coefficients because of weather conditions causing wet or dry surfaces for example.

## Part V

# Detailed design cargo

# 19 | Wind loading

The purpose of this mission is to provide permanent housing in the 2010 earthquake disaster zone in Haiti. Wind is the most important parameter in the design of the house. Over the past ten years, Haiti was hit by at least one tropical storm or hurricane with wind speeds up to 150 *mph* per year. The permanent house must be designed to withstand these wind loadings.

## 19.1 Frictional effects

The input for the design is the maximum wind speed of 150 *mph*. However, this is the free wind speed which should be corrected for frictional effects near the ground surface. The height at which the movement of air is no longer affected by ground obstructions is called the gradient height ( $Z_G$ ). This height varies for different terrains. For Haiti, terrain category 2 is assumed, which stands for an open country with low scrub or scattered trees. The near ground wind speed can be calculated with Equation 19.1 [155].

$$\frac{V_Z}{V_{Z_G}} = \left(\frac{Z}{Z_G}\right)^\alpha \quad (19.1)$$

Where  $V_Z$  is the real wind speed [m/s] at height  $Z$  [m].  $V_{Z_G}$  is the unobstructed wind speed and  $\alpha$  is the mean speed component. For terrain category 2,  $Z_G = 300 \text{ m}$  and  $\alpha = 0.15$ . The real wind speed from 0 to 2 *m* height can be seen in Figure 19.1 [155]. [For further calculations an average wind speed from 0 to 2 *m* height of 27.5 *m/s* is assumed.]

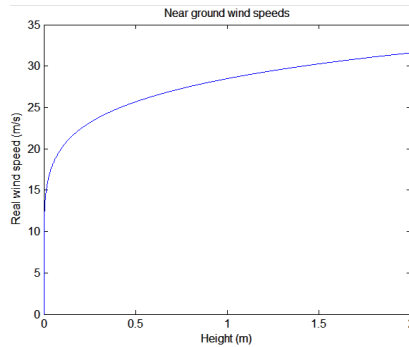


Figure 19.1: Near ground surface frictional effects on the wind speed

## 19.2 Design wind speed and design pressure

The average wind speed from the previous section shall be modified to obtain the design wind speed  $V_D$ . Four effects influence the design wind speed: risk level, terrain roughness, local topography, and importance factor for the cyclonic region. The design wind speed can be calculated with Equation 19.2 [5].

$$V_D = V_Z * K_1 * K_2 * K_3 * K_4 \quad (19.2)$$

$K_1$  is the risk coefficient which depends on the suggested life span of the design. For a mean probable design life of the structure between 5 and 25 years the risk coefficient equals 0.94.  $K_2$  is the terrain and height factor. For a category 2 terrain this factor equals 1.0.  $K_3$  is the topography factor. Topographic features such as hills, valleys, cliffs, or ridges can affect the wind speed. The terrain is assumed to be flat. When the upwind slope is smaller than  $3^\circ$ ,  $K_3$  can be assumed to be 1.0. The final factor  $K_4$ , is the importance factor for cyclonic regions. For structures of post-cyclone importance this factor is 1.3. With Equation 19.2 the design wind speed is determined to be 33.6 *m/s*.

The next step for the wind loading analysis is the calculation of the wind pressures. The wind pressure at any height can be obtained by Equation 19.3 [5].

$$p_Z = 0.6 * V_D^2 \quad (19.3)$$

Where  $p_Z$  is the wind pressure at height  $Z$  [ $N/m^2$ ]. Here the air density is assumed to be 1.20  $kg/m^3$  and constant. To obtain the design wind pressure, this wind pressure should be modified with Equation 19.4 [5].

$$p_D = K_d * K_a * K_c * p_Z \quad (19.4)$$

Where  $p_D$  is the design wind pressure [ $N/m^2$ ].  $K_d$  is the wind directionality factor, which for cyclone affected regions is taken as 1.0.  $K_a$  is the area averaging factor. Large areas decrease the correlation of measured pressures. However, for side areas smaller than  $10 m^2$  the effect can be neglected [ $K_a$  equals 1.0].  $K_c$  is the combination factor for wind pressure contributed from two or more building surfaces. The under pressures or overpressure will not be fully correlated and can be assumed to be 0.8 for this design [5]. With Equation 19.4 the design wind pressure is calculated to be  $541 N/m^2$ .

### 19.3 Wind loading

Wind loading is calculated for individual structural elements and the building as a whole. For wind loading on individual structural elements it is important to take account of the pressure difference between opposite faces of the element. The wind load  $F_n$  acting in a direction normal to the structural element can be calculated with Equation 19.5 [5].

$$F_n = (C_{pe} - C_{pi}) * A * p_D \tag{19.5}$$

Where  $C_{pe}$  is the external pressure coefficient,  $C_{pi}$  is the internal pressure coefficient, and  $A$  is the surface area of the structural element. Due to the direction of airflow in relation to openings in the building, the internal air pressure may be positive or negative. From design standards, in case of buildings where the claddings permit the flow of air with openings not more than about 5 percent of the wall area, wind loading should be examined with an internal pressure coefficient of +0.2 and -0.2 as extreme values [5]. The average external pressure coefficients are given in Figure 19.2.

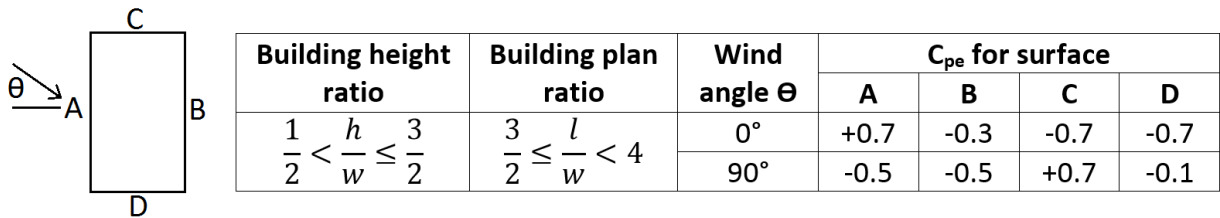


**Figure 19.2:** External pressure coefficients for walls of rectangular buildings.  $h$  is the height,  $l$  is the greater horizontal dimension and  $w$  is the lesser horizontal dimension of the building [5]

The total wind load  $F_{tot}$  on a building or structure can be calculated with Equation 19.6 [5].

$$F_{tot} = C_f * A_e * p_d \tag{19.6}$$

Where  $C_f$  is the force coefficient for the building and  $A_e$  is the effective frontal area of the building. The value of the force coefficient differs for the direction of the wind loading. To analyse the critical load, the total wind load should be calculated for each wind direction. In general, frictional drag between the surface and the wind flow should be taken into account. However, for rectangular clad buildings this can be neglected when the ratio  $w/h$  and  $w/l$  is smaller than four. The overall force coefficient for rectangular clad buildings of uniform section with flat roofs in uniform flow can be determined from Figure 19.3 [5].

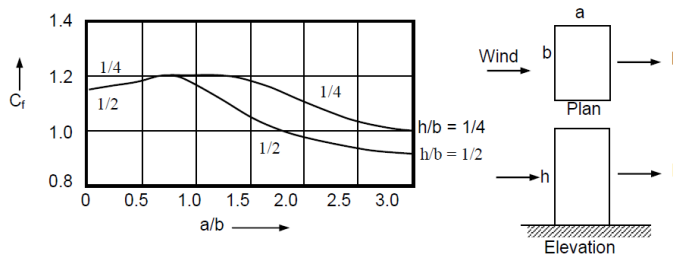


**Figure 19.3:** Values of the force coefficient versus  $a/b$  for  $h/b < 1$

## 20 | Housing - Structural analysis

The equations from Chapter 19 can be used to calculate the general wind loading on the building. However, for a realistic structural analysis, dynamic wind loading and flow separation should also be included. The computation of

airflow around buildings is complicated, and cannot be done analytically. Just as for airfoils, software is available to model the airflow. Here, Visual Analysis 11.0 is used to analyse the wind loads on the building.

## 20.1 Model

The first weight estimation in the conceptual design phase showed a total weight of 269 *kg* for the modular cabin design. Because this is only half of the maximum package weight of 500 *kg*, it was decided to increase the conceptual design of 4 by 3 panels to a model of 6 by 3 panels.

The members in the model are made of rectangular 6 x 4 *cm* wooden beams. The story height is 2 *m* and the horizontal bay spacing in X and Y direction is 0.6 *m*. To complete the model, some assumptions are made:

- The ground supports are fixed.
- The roof connections are free supports.
- The supporting framework is load bearing.

## 20.2 Modeled wind loading

The analytical equations to calculate wind loading from Chapter 19 are all included within the Visual Analysis software tool. Only inputs are needed to model the wind loading. The wind speed is set to the extreme case of 150 *mph*. To account for the dynamic interaction between the flowing air and the structure, a gust factor  $G$  is included within the model. The gust factor is defined as the ratio of the peak gust to the mean wind speed. From engineering standards of wind loading analysis, the gust factor is set to 0.85 [156].

As explained in Section 19.3 of Chapter 19, wind loading should be examined for positive and negative internal pressure. The two wind directions are 0 and 90 degrees wind angle as shown in Figure 19.2. In the maximum load case, dead load should also be included. Dead loads are constant static forces including the weight of the structure itself. From engineering standards, a building should withstand maximum wind loading plus 1.2 times the dead load [156].

## 20.3 Design optimisation

The results of the first wind model show that the building cannot withstand the wind loading. The stresses in the columns are larger than the material strength. To optimise the model triangular elements are created to strengthen the framework. Eight steel cables with a diameter of 5 *mm* are added from the lower left corners to the top corner of the first panel, as can be seen in Figure 20.1. With this change the member dimensions can be decreased to a solid 4 *cm* squared shape. This beam dimension is chosen, because this is a standard off-the-shelf wooden beam size. The final model of the house can be seen in Figure 20.1. Spruce-pine-fir is used as wooden material for the beams, because this is the most common used wooden material for supporting frameworks and can be bought in every hardware store. As for the steel cables, the standard A36 steel is used as material.

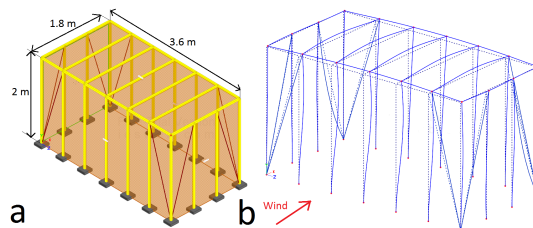


**Figure 20.1:** a: Model of the modular cabin design created in Visual Analysis 11; b: Result view of the critical 0 degrees wind, negative internal pressure loading case. The dotted lines indicate the unloaded model

## 20.4 Wind loading results

The results from the wind loading model are shown in Table 20.1. Here all the forces, moments, and stresses are summarised by the extreme values for the four load cases. Where  $F_x$  is the axial force,  $V$  is the local shear force in  $y$  and  $z$  direction,  $M$  is the moment in  $x$ ,  $y$ , and  $z$  direction,  $f_a$  is the axial stress,  $f_b$  is the axis bending stress in  $y$  and  $z$  direction,  $F_{xc}$  is the axial force for all cables, and  $f_{ac}$  is the axial stress for all cables. The critical loading case from these results is the 0° wind with negative internal pressure. The result view of the critical loading case can be seen in

Figure 20.1. The maximum bending stress of  $47 \text{ MPa}$  is achieved in the 2 middle columns on the windward side of the building. The ultimate bending strength of spruce-pine-fir, the so called modulus of rupture, is  $71.7 \text{ MPa}$  [157]. The maximum bending stress in the framework is well within the ultimate bending strength of the material. The maximum axial stress for all cables is  $301 \text{ MPa}$ . Steel A36 has an ultimate tensile strength of 400 to  $550 \text{ MPa}$  [158]. Therefore, the framework will withstand the extreme wind loading during a hurricane.

**Table 20.1:** Extreme force, moment and stress results for the four wind loading cases: 0 and 90 degrees wind and positive [+] and negative [-] internal pressure

Symbol	Units	0° [-]		0° [+]		90° [-]		90° [+]	
		Min.	Max.	Min.	Max.	Min.	Max.	Min.	Max.
Fx	N	-5,029	1,238	-4,953	1,568	-1,967	801	-1,831	884
Vy	N	-691	1,035	-949	951	-540	851	-708	708
Vz	N	-891	891	-1,032	1,032	-537	537	-628	628
Mx	Nm	-63	61	-63	59	-44	44	-24	24
My	Nm	-321	293	-392	369	-181	172	-211	211
Mz	Nm	-502	268	-392	278	-358	162	-211	214
fa	MPa	-3.14	0.77	-3.10	0.98	-1.23	5.00	-1.14	0.55
fby	MPa	-30.11	30.11	-36.72	36.72	-16.93	16.93	-19.75	19.75
fbz	MPa	-47.08	47.08	-36.77	36.77	-33.54	33.54	-20.07	20.07
Fxc	N	3	5,913	3	5,874	5	2,854	5	2,844
fac	MPa	0.15	301.17	0.16	299.14	0.26	145.37	0.26	144.83

## 20.5 Wind loading verification

To guarantee the strength of the housing design, the created model in Visual Analysis should be verified. However, wind loading is a complex loading case, which cannot be analysed analytically for the entire model. The only possibility is to validate the model with real test results, but within the scope of this project there is no possibility to test the model. To still verify the software tool, simple loading cases on cantilever beams and 2D truss constructions were modeled. The stress results of these models were within one percent of the results from analytical stress calculations [159]. Therefore, the stress calculations for a specific loading case in Visual Analysis are assumed to be realistic.

The assumptions made in Section 20.1 can influence the stress results and therefore the strength of the building. To guarantee the wind resistance of the design, the influence of the assumptions on the stress results should be investigated. The first assumption: the ground supports are fixed, depends on the anchoring method of the building. The anchor design as fixed points can be seen in the next chapter. The second assumption: the roof connections are free supports, is verified by looking at different connection options. The roof connections were also modeled as fixed, pinned, and rotation fixed supports. However, the maximum stress results are achieved when the connections are modeled as free supports. Therefore, the strength of the building is always guaranteed by making the second assumption. The last assumption: the supporting frame work is load bearing, includes also a safety margin for the strength of the design. In real life, the loading is more evenly distributed along the entire structure. The wall and roof panels will strengthen the framework, while these make more internal connections between the different beams. Therefore, the maximum stresses in the supporting framework will be lower in reality.

## 20.6 Conclusion

The building is modeled for the most extreme wind case of  $150 \text{ mph}$ . Combining this load case with safety margins generated by the assumptions made in Section 20.1 will guarantee the strength of the housing design. While the stress results are well within the ultimate material strengths, the design could be optimised. However, decreasing the beam dimensions will increase the cost of the design, while smaller beam dimensions are not commonly used off-the-shelf products. To also guarantee the strength of the building when holes and grooves are cut in the beams to construct the building, the design is not further optimised.

# 21 | Housing - Detailed design

This chapter summarises the detailed design of the housing solution. The sections follow the steps to construct the house in a chronological order. Due to page restrictions, not every detail can be shown in the pictures.

## 21.1 Floor panels

The floor consists of three different panels, the standard  $2000 \times 620 \text{ mm}$  panels and two different  $2000 \times 380 \text{ mm}$  end panels. The panels are made from  $15 \text{ mm}$  thick High-Density Polyethylene (HDPE). This is a common used plastic for floor panels [160]. Therefore, the production of the floor panels can be fitted into existing production lines, which will decrease the costs. The panels are connected with tongue and groove connections. To protect the building from rising damp, the panels have  $50 \text{ mm}$  high HDPE studs. Different pictures of the floor panels can be seen in Figure 21.1.

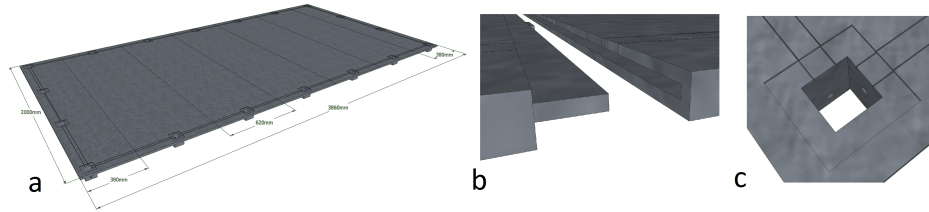


**Figure 21.1:** a: The entire floor made out of 7 panels. b: The tongue and groove connection between different floor panels. c: Grooves and holes in the floor panels for the anchors, columns and wall panels to slide into

## 21.2 Anchors

In Chapter 20, the ground connections are assumed to be fixed supports. To withstand the wind loading, ground anchors should be used. Common used ground anchors for small constructions, are  $2 \text{ mm}$  thick galvanised steel pole holders [161]. These anchors should be modified to fit within the floor panels. From engineering standards, the anchor depth for fixed supports should be  $1/3$  of the construction height [162]. The design of the ground anchors can be seen in Figure 21.2.

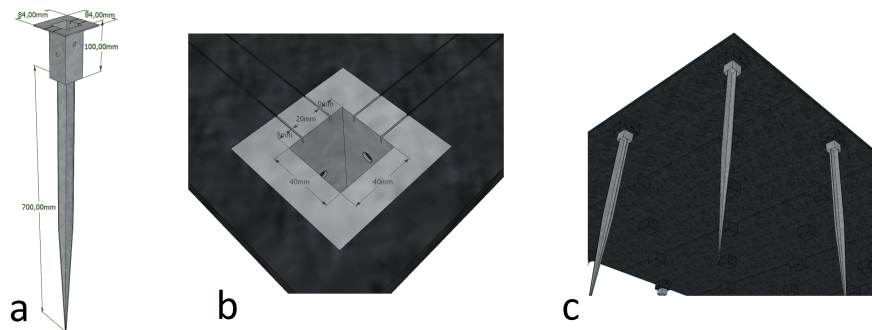


**Figure 21.2:** a: Anchor with general dimensions. b: Anchor precisely fitted into the hole in the floor panel. c: The 70 cm pins will ensure a fixed connection to the ground

## 21.3 Wooden columns

The house design consists of four different wooden columns. The columns are made of the common used  $40 \times 40 \text{ mm}$  spruce-pine-fir construction wood [163]. The columns have grooves where the wall panels can slide into. The different columns can be seen in Figure 21.3. To strengthen the building during storms, the door is designed as a sliding door, instead of a hinged door. Therefore, to slide the door, a slit is made in the left door column.

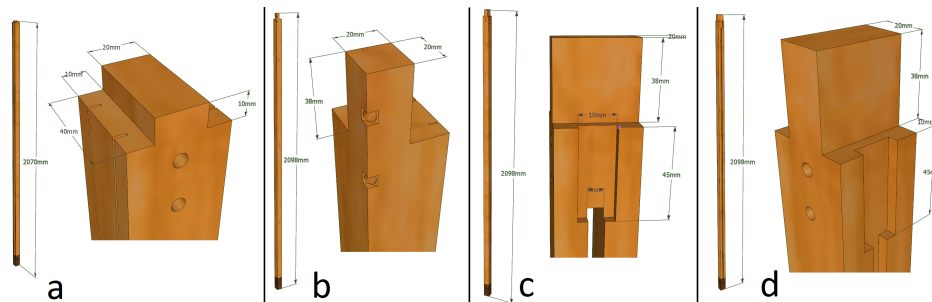


**Figure 21.3:** a: Standard column. b: Corner column. c: Door column left. d: Door column right

## 21.4 Bolting

The columns, floor panels, and anchors are bolted together as shown in Figure 21.4. To ensure the strength of the bolted connection, the shear stress in the different components should be calculated for the maximum loading. The results from the wind loading model from Chapter 20 show a maximum axial force of  $6286\text{ N}$  at the corner connections. Two stainless steel bolts in a row are used to transfer the loads as shown in Figure 21.4. Because of the two bolts, the load transferred by one bolt is reduced by a factor 2 [164]. The average shear stress  $\tau_{avg}$  in one bolt, an anchor sheet and the beam can be calculated with Equations 21.1, 21.2, and 21.3 respectively [159].

$$\tau_{avg_{bolt}} = \frac{V}{A_{sec}} = \frac{\frac{F}{2}}{\pi(R_{bolt})^2} = 62.5\text{MPa} \quad (21.1)$$

$$\tau_{avg_{anchor}} = \frac{V}{A_{sec}} = \frac{\frac{F}{4}}{0.03\text{m} * 0.002\text{m}} = 26.2\text{MPa} \quad (21.2)$$

$$\tau_{avg_{column}} = \frac{V}{A_{sec}} = \frac{\frac{F}{2}}{0.05\text{m} * 0.04\text{m}} = 0.786\text{MPa} \quad (21.3)$$

Where  $V$  is the internal resultant shear force at the section,  $A_{sec}$  is the area at the section,  $R_{bolt}$  is the radius of the bolt, and  $F$  is the axial force. The ultimate stress for steel is  $375\text{ MPa}$  and for spruce-pine-fir is  $10\text{ MPa}$ . Therefore the bolted connection will not fail during extreme wind loading.

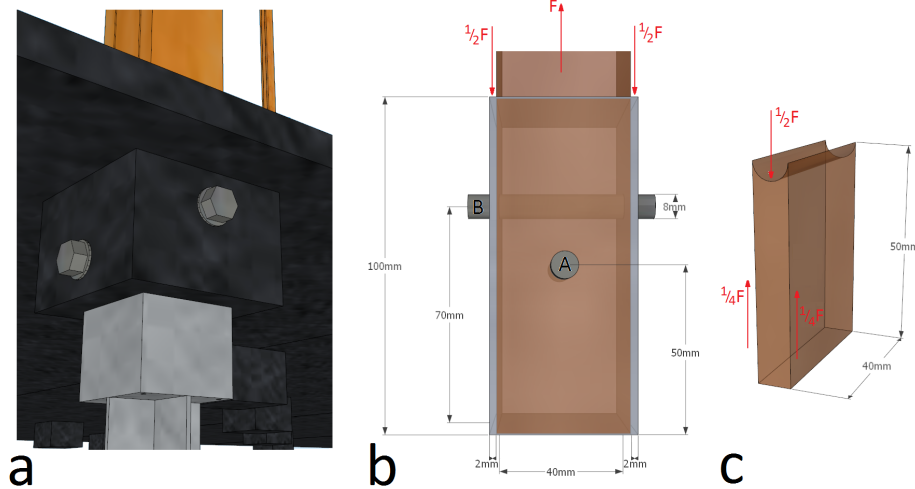


**Figure 21.4:** a: Bolted connection between the column, floor panel and anchor. b: Load distribution in the bolted connection. c: Shear flow in wooden column due to bolting

## 21.5 Wall panels

Haiti has a warm climate with an average temperature of 30 degrees Celsius in the daytime (Chapter 5). Therefore heat insulation is an important factor in the wall panel design. To make a lightweight building and a small package, off-the-shelf  $1\text{ mm}$  thick aluminium wall panels were chosen in the conceptual design phase [165]. The best solution to insulate the building is to make a double walled structure, with air as insulator. The space in between the panels can also be used for wiring and hoses. Insulative paint can be used to further optimise the building for heat insulation [166]. While the house needs to be dropped, it is not convenient to use glass for the windows. Alternatively, lightweight and shock proof plexiglass is used as window material [167]. The sliding door is made of single walled  $2\text{ mm}$  thick aluminium. The dimensions of the three different wall panels can be seen in Figure 21.5.

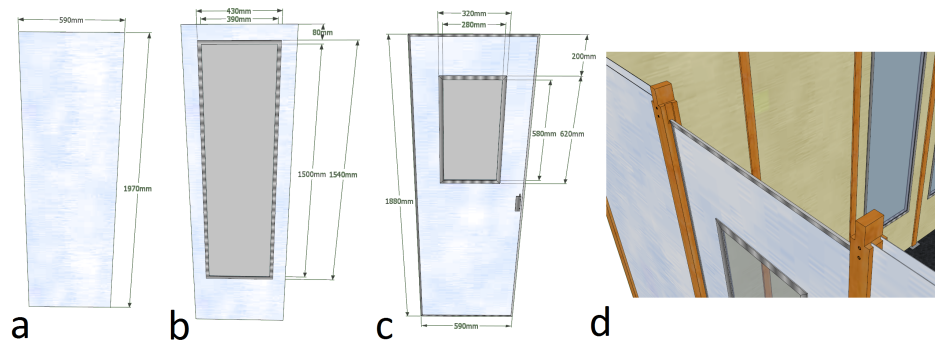


**Figure 21.5:** a: Standard wall panel. b: Window panel. c: Door panel. d: Wall panels fitted into the grooves in the columns

## 21.6 Wooden beams

The house design consists of seven different wooden beams. The different beams can be seen in Figure 21.6. A strong connection between the columns and the different beams is needed to transfer the loads. Three different 2 mm thick galvanised steel connections are designed, based on off-the-shelf beam carriers [168]. It is hard to ensure the strength of the connections, while the stress distribution in the connections is complicated. However, beam carriers are designed to carry the weight of entire floors. These weights can be thousands of kilograms. Therefore, the connections in this design are assumed to be strong enough to carry the loads. In a further design phase, the connection should be tested in real life to ensure their strength. The three connection designs are shown in Figure 21.7.

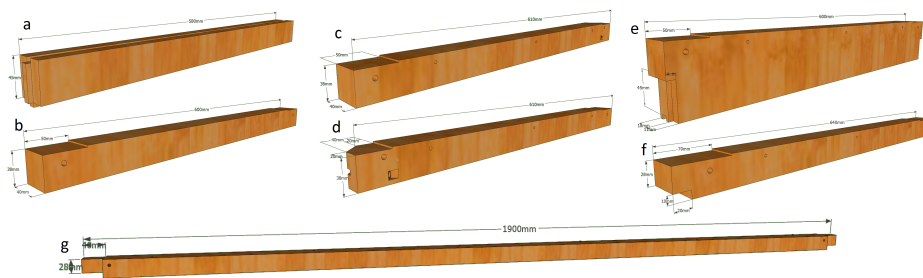


**Figure 21.6:** a: Bottom door beam. b: Standard beam. c: Corner beam 1. d: Corner beam 2. e: Top door beam. f: Top window beam. g: Roof beam

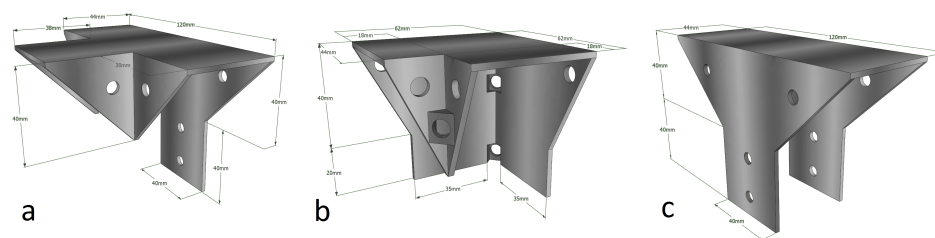


**Figure 21.7:** a: Steel connection at the long side of the building. b: Steel corner connection. c: Steel connection at the small side of the building

## 21.7 Roof panels

To fix the roof panels, two different aluminum profiles are designed. These profiles provide a watertight roof as shown in Figure 21.8. Despite of the flat roof, the terrain can be prepared with a small angle to allow for water drainage. From a construction point of view, the roof panels are single walled 1 mm thick aluminium panels. Insulative paint is used to insulate the roof.

To complete the design, the steel cables with a diameter of 5 mm are bolted to the structure. These provide the strong ‘triangular’ elements as discussed in Chapter 20. The final empty design of the house can be seen in Figure 21.9. In order to construct the house the first drops should include a toolbox. These tools can later be reused to construct other houses. The toolbox should include the wright size wrenches and a maul hammer.

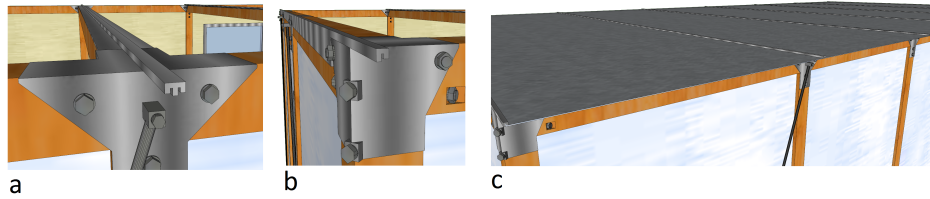


**Figure 21.8:** a: Watertight aluminium roof profile. b: Watertight aluminium roof end profile. c: Roof panels slid into the profiles



**Figure 21.9:** Final empty design of the permanent house

## 22 | Subsystems

In this chapter, the solar system and the biosand water filter are designed in detail. Also, a simple interior is designed for a more permanent solution. The last components to be chosen are the emergency supplies required for every drop.

### 22.1 Power supply

A solar home system consists of several components. The solar panel collects energy from the sun, this energy can be stored in a battery. The flow of the current to the solar panel is regulated by a charge controller, preferably with a maximum power point tracker (MPPT). MPPT controllers are able to follow on the changes of irradiation, obtaining the maximum possible output in all weather conditions [169]. For large systems that have to provide energy for appliances that run on alternating current (AC), an inverter has to be used. This solar home system however will not have to provide for such appliances, and thus no inverter is needed. Later on, when the modular houses are being extended and more appliances are added, an inverter could be added to the solar home system as well.

#### 22.1.1 Energy required

Before the solar home system can be sized, the required energy has to be determined. This is done in Table 22.1.

**Table 22.1:** Required energy for different appliances

Item	Power [W]	Time of use [h]	Energy [Wh]
Lights (2x)	20	5	200
Radio	10	4	40
Small refrigerator	40	5	200
Cooking plate	1,500	0.5	750
<b>Total</b>	<b>1,570</b>		<b>1,190</b>

The required energy depends on the appliances that have to be powered. Their required power, multiplied by the time of use, results in the required energy. The total required energy for one house is 1,190 Wh.

### 22.1.2 Solar panels

To calculate the solar panel surface that is needed to provide the required energy, the incoming energy has to be determined first. With the use of the solar irradiance (the rate of energy that is being delivered to a surface area at any given time), and solar insolation (the total amount of energy that is collected on a surface area within a given time), the amount of peak sun hours can be calculated. The solar irradiance is approximately  $1,000 \text{ W/m}^2$  at the equator. Since Haiti lies on  $18^\circ$  latitude, its solar irradiance equals  $950 \text{ W/m}^2$ . The average annual insolation in Haiti, determined with the use of the Solar Electricity Handbook [170], is  $5.3 \text{ kWh/m}^2/\text{day}$ . This is calculated for a flat surface, assuming the solar panels will be placed flat on the roof to increase the simplicity of installation. Of course, when they would be placed under an angle pointing South, they would receive more energy. However, they will then have to be precisely mounted on the houses. Figure 22.1 shows a schematic view of the solar home system.

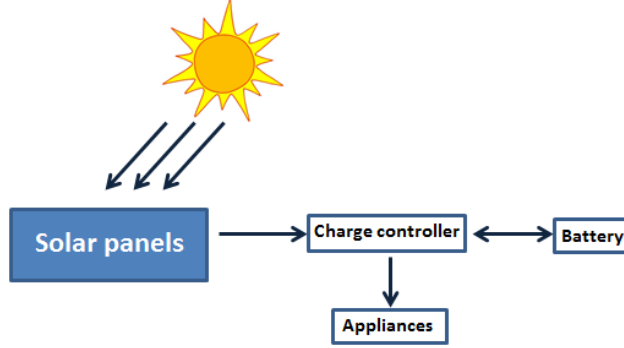


Figure 22.1: Schematic view of the solar home system

$$\text{Peak sun hours} = \frac{\text{Insolation}}{\text{Irradiance}} \quad (22.1)$$

With Equation 22.1, the amount of peak sun hours can be calculated which resulted in  $5.6 \text{ h/day}$ .

$$\text{Daily demand} = \frac{\text{Required energy}}{\text{System voltage}} \cdot 1.1 \quad (22.2)$$

The daily electric current demand can be calculated with Equation 22.2. The system voltage is usually  $12 \text{ V}$  or  $24 \text{ V}$ , depending on the size of the system and the voltages the appliances will run on. Since this will be a small system and all the appliances run on a low voltage, a system voltage of  $12 \text{ V}$  is used. To account for system losses (for example through wiring) a safety factor of 1.1 is used. This equation results in a daily demand of  $109 \text{ Ah}$ .

$$\text{Charging current} = \frac{\text{Daily demand}}{\text{Peak sun hours}} \quad (22.3)$$

The charging current of the system can then be calculated with Equation 22.3. This was calculated to be  $19.5 \text{ A}$ .

$$\text{Minimum power output} = \text{Charging current} \cdot \text{System voltage} \quad (22.4)$$

With both the system voltage and the charging current known, the minimum power output of the system can be calculated using Equation 22.4. The minimum power that the system has to provide was found to be  $234 \text{ W}$ . This can be met by using three panels with a power output of  $80 \text{ W}$  each. An example of this panel has an area of  $1.2 \text{ m} \times 0.55 \text{ m}$ , weighs  $8.2 \text{ kg}$ , and costs  $\$120$  [171]. The panel has a lifetime of over fifteen years, and is thus a permanent option.

### 22.1.3 Battery

The required battery capacity  $C$  depends on the daily electric current demand, the amount of days the system has to be able to provide energy if there is no incoming energy (for example during the night), and the depth of discharge (DoD). The amount of days of autonomy  $n_{\text{days}}$  was decided to be 1, so that if there is one day with less sun than usual there is still enough energy available. A too high DoD is not good for the quality of the battery, a standard value for this is 80 %.

$$C = \frac{\text{Daily demand}}{\text{DoD}} \cdot n_{\text{days}} \quad (22.5)$$

With the use of Equation 22.5 the required capacity was calculated to be  $136 \text{ Ah}$ . Different types of batteries can be chosen, but the most permanent and maintenance-free batteries are the absorbed glass matt (AGM) types [172].

An example of an AGM battery, with a power of 140 W, and a voltage of 12 V battery weighs 45 kg and costs approximately \$150 [173].

### 22.1.4 Charge controller

The size of the charge controller is determined with Equation 22.6.

$$Size\ charge\ controller = Number\ of\ panels \cdot \frac{Power\ output}{Maximum\ power\ voltage} \cdot \frac{1}{\eta_{charge\ controller}} \quad (22.6)$$

where the number of panels is three, the power output of one panel is 80 W, the maximum power voltage of the panels is 18 V, and the efficiency of the charge controller  $\eta_{charge\ controller}$  is 90 %. This results in a size of 14.7 A. An example of a 15 A charge controller with MPPT weighs 0.5 kg and costs approximately \$15 [174].

## 22.2 Water treatment

The biosand water filter comes in different sizes and materials. The most commonly used type is the concrete container which has an empty weight of 70 kg and lasts a lifetime. A lighter alternative is an off-the-shelf plastic container from Hydrad, that weighs 3.6 kg and still has a lifetime of over ten years [175]. The container has a height of 0.77 m and a diameter of 0.42 m, producing 47 L/h which is enough for a family of three. More than 55,000 of these filters have already been distributed in many developing countries, and have proven to be successful and durable products. This filter costs \$ 34 and can be seen in Figure 22.2.

The filtered water from the biosand filter is collected in a water tank. A simple water pump provides running water [176].



Figure 22.2: The Hydrad biosand water filter [6]

## 22.3 Interior

For a more permanent housing solution an interior is designed. The design of the interior is based on caravans of the same size [177]. The interior includes: a single bed, a double bed, two seats, a table, a small kitchen, a shower, and a chemical toilet [178]. Figure 22.3 shows a pictures of the interior. The biosand filter is included within the kitchen cabinet. The battery and the charge controller can be stored underneath the double bed.



Figure 22.3: Interior design of the housing unit

## 22.4 Emergency supplies

From the requirements, each cargo drop should be equipped with food, blankets, emergency equipment, and medicine kits. The content of these kits is highly dependent on the specific needs of the people in the disaster zone. The IFRC has a large variety of off-the-shelf emergency items [179]. Cooperation with the IFRC will provide the necessary emergency kits for every dropped package.

# 23 | Weight and cost estimation

In this chapter, the weight and cost of the total housing design are estimated. In addition, the final package dimensions are determined.

## 23.1 Weight estimation

The initial requirement for the package weight was set at  $500\text{ kg}$ . To obtain the weight of the different components of the housing design, the material densities are used. Combining these densities with the exact part dimensions obtained in Chapter 21 gives the weight results as shown in Table 23.1. The total weight of the house, including the interior, is estimated to be  $453\text{ kg}$ .

## 23.2 Cost estimation

To make a realistic cost estimation, prices of off-the-shelf comparable products are used [160] [161] [163] [180] [165] [167] [178]. The production of the different parts can easily be fitted into existing production lines, while all the parts are based on existing products. It is likely that the products can be bought cheaper at wholesalers and importers. The difference between the two prices is assumed to cover the modification costs of some of the parts. Therefore, the off-the-shelf prices are assumed to be realistic. The cost results for the different parts can be found in Table 23.1. The total cost of the house including the interior is estimated to be  $\text{€}4,071$

## 23.3 Packaging

The house is designed to be transported by a UAV. Therefore, a small package including all the parts is preferable. The smallest pile dimensions are found by analysing the parts in a 3D drawing to be  $694 \times 2098 \times 712\text{ mm}$ . The resulting view can be seen in Figure 23.1. To bundle all the parts, the pile is packed in a wooden crate. Wooden transport crates are commonly made out of  $1.5\text{ mm}$  thick multiplex [181]. Summing up the weight and the cost of the package material will give a total weight of  $489\text{ kg}$  and  $\text{€}4,215$ . The final package dimensions including the wooden crate will be  $740 \times 2150 \times 750\text{ mm}$ .

**Table 23.1:** Weight and cost of different parts of the housing design

Part	Weight [kg]	Price [€]
Floor panels	120.24	481
Anchors	19.44	214
Columns	24.10	95
Wall panels	108.51	1,700
Beams	13.77	55
Connections	3.78	54
Bolts and nuts	3.82	36
Profiles	3.23	21
Roof panels	20.39	300
Cables	10.78	44
Power system	64.71	382
Water system	4.18	70
Interior	56.04	619
<b>Total</b>	<b>452.99</b>	<b>4,071</b>

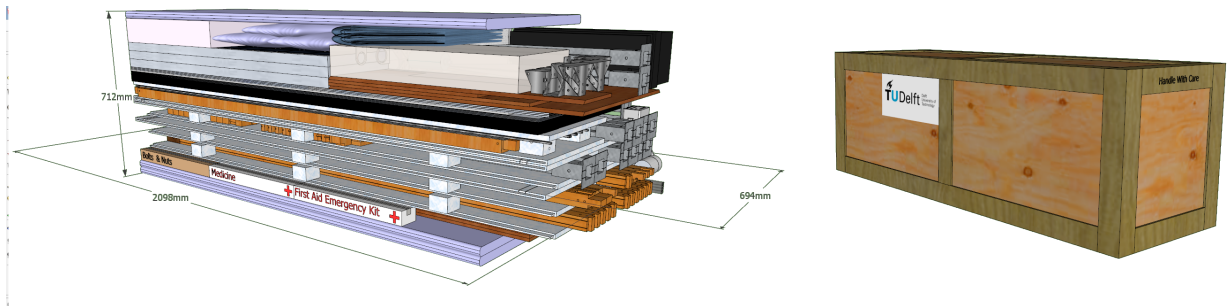


**Figure 23.1:** a: Smallest pile of all the housing parts. b: The final transport package

## Part VI

# Final design considerations

## 24 | Technical risk assessment

In this chapter, an assessment will be made of the technical risks involved in the UAV cargo delivery system. The purpose of this risk assessment is to identify the most critical aspects, which have to be prioritised during further design phases. The risks defined in the mid-term report have been taken into account during the detailed design phase.

### 24.1 Categories of risk

The different risks can be classified into different categories. For every category, it is described how the risk is minimised.

#### **Structures**

One of the failures with severe consequences is structures related. The wing is one of the most important components of the UAV due to its lift-generating capabilities. When the main wing breaks off, the UAV will lose its ability to produce lift and will be uncontrollable. The same applies for the tail. Therefore, during the analysis the worst case scenarios have been taken into account. On the ultimate load, a conservative safety factor has been applied.

#### **Electronics**

The UAV carries a lot of electronic subsystems to perform different tasks. A subsystem is flight-critical if its failure results in a crash. In Chapter 16, the flight critical subsystems has been determined. When a subsystem is determined to be flight-critical, reliability measures in the form of redundancy have been implemented. The autopilot for example, have been determined to be a flight critical subsystem since it controls the UAV. Also the means of communication is critical, since communication is required to land with approval of the flight managers.

#### **Delivery system**

During the concept generation, one of the risks identified was a failure in the soft- or hardware of the parachute's operating system. After research on the different delivery systems and flight characteristics, it has been chosen to use the PLADS-method. In terms of technical risk and safety, this method shows some advantages. First of all, the system does not utilise an operating system, resulting in a more robust dropping system. The flight precision is obtained by the drop altitude and flight speed instead of active controls. Therefore, there are no risks associated with the parachute controls. In contrast to a high altitude dropping system, the PLADS-method is safe when it comes to deployment failure. When there is a error with the parachute deployment mechanism after drop-off, the cargo will be damaged at arrival but nobody will be injured.

### 24.2 Events

The different technical risks have been identified and presented in Table 24.1. Only the severe and major risks are presented here due to limited space.

**Table 24.1:** Identified technical risks

Event	Description
Control surfaces breaking off	Without an elevator or rudder, it is not possible to control the attitude of the UAV, this may result in a crash.
Wing failure	Due to structural failure the wing breaks off. Cause can be overloading or fatigue.
Engine	Propeller blades get severely damaged and fall off, turbine blades getting damaged. Since the UAV has only one engine, the loss of it can be considered as severe.
Inertial measurement unit failure	This unit consists of gyroscopes providing the flight control computer with attitude information. For some reason an unreliable or null reading is done.
Autopilot Failure	The UAV autopilot computer fails, this can be due to hardware or software. The UAV becomes uncontrollable, a crash is inevitable.
Communications link failure	The communication used by the operator to control the UAV at the international airport and the drop zone. GPS-link should be designed as a redundancy.
Parachute deploy	Due to wrong package, corrupt control software, or damaged hardware the parachute may fail to deploy.
Airbag	Airbag fails to deploy in time, therefore the impact on the cargo is too high. When the deceleration is higher than 20 <i>g</i> components may be damaged.
Differential pressure sensor	The sensor to measure the difference between the static and dynamic pressure, thereby determining the speed, fails. It gives an unrealistic reading or no reading at all. Therefore the UAV should deduce the speed from the GPS readings.
Static pressure sensor	No information of the altitude is available due to a error in the static pressure sensor. Without altitude information it is difficult to safely operate the UAV, avoid mountains, and land. The last option is deduce the altitude from the GPS information which is less accurate.
Control tab getting stuck	One of the control tabs getting stuck in a certain position. If both of the control tabs for the same motion are stuck at the same time the situation is worse. Can be due to deformation in the tab itself, or signal loss from the flight control computer.
Disruption in fuel flow	Fuel supply is disrupted for a short moment. When this happens during cruise the risk of a critical failure is low, but in the landing phase it can be more of a problem.

### 24.3 Conclusions and design guidelines

From the risk assessment a number of conclusions have been drawn which have to be taken into account for the further phases of the design and manufacturing process. The risks presented are the most severe events, therefore it is important to perform intensive quality checks. Furthermore, the maintenance and inspections must be performed in such a way that safety is assured.

## 25 | Project design & development logic

The purpose of this chapter is to discuss the logical order of activities to be performed during the whole project, from design to full scale testing and in the end the test flights. In Figure 25.1 a schematic representation of the project design and development logic from the detailed design phase on is given. The first set of blocks shows the activities performed during the detailed design phase of the DSE. The second set of blocks shows the outcomes of this design phase. The aeroplane's lay-out is determined for example by combining the results of all the previous blocks. This could not be done before all input parameters were determined by the first set of blocks. The computational fluid dynamics (CFD) and finite element method (FEM) analysis are to be done in the next design phase, in order to get more accurate results. A FEM analysis on the wing was already done in the previous stage, but a FEM analysis on the other parts of the UAV still need to be performed.

After the numerical analysis (FEM and CFD), parts of the structure need to be tested for things like fatigue, impact loading and electrical failure. When these tests have been conducted, a scale model can be made to get more insight in

the aerodynamic behaviour of the aeroplane. Next to this, the propeller can be tested for its aerodynamic performance. If all is well, materials and products can be ordered in order to manufacture and test a full scale model.

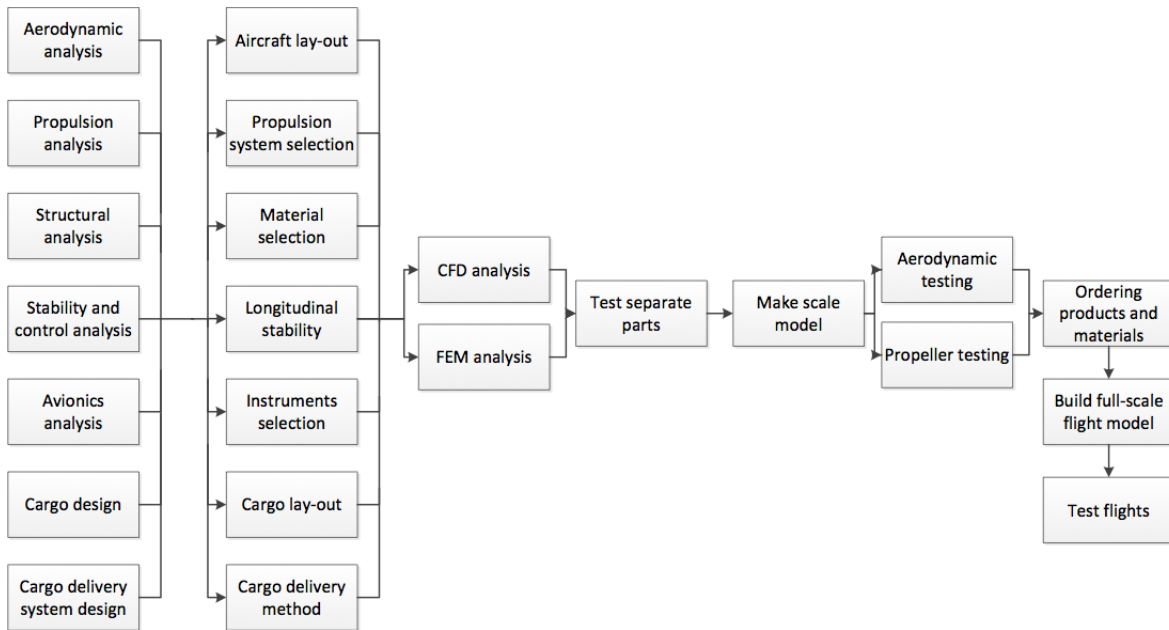


Figure 25.1: Schematic representation of the project design and development logic

## 26 | Production plan

The purpose of this chapter is to provide a production plan for the manufacturing of the UAVs. This will allow for efficient production and assembly processes. The following sections will discuss the production of the individual parts, the assembly into the complete UAV and how this can be done using a lean manufacturing approach.

### 26.1 Production

The production of all main parts of the UAV (e.g. the fuselage, wings, tail) is performed as a line production process, meaning that product parts are passed on to the next station at specific time slots [182].

Using this allows for simple planning, a good indication of occurring delays, maximal amount of equal shaped products, minimal transportation costs and an optimal crew routine forming. This last one means that crews will experience a ‘learning curve’, since more experience means a continuous decrease in the working hours needed to perform a work package until a minimum is reached. In this labour extensive industry this approach provides the option to achieve significant cost reductions, especially when taking into account that at least 200 units will be produced [182] [183].

The smaller elements of these large components will need to be manufactured in batches, which will take place in workshops. Finished parts will be stored in local warehouses and will serve as stock for the production line. The number of parts needed in stock is determined by the time needed to produce a new batch and the number of parts that will be used in the mean time. Using this approach, the critical number of parts needed in stock can be identified so that no parts will remain in stock longer than absolutely necessary [182].

When using external suppliers it should be noted that, as a form of build in redundancy, at least two suppliers will be used for the critical components. In this way, if one supplier fails to deliver on time, there will be a backup plan such that possible delays can be minimised.

### 26.2 Integration and assembly

The main components that need to be manufactured or ordered from third party companies have been identified and structured. These components have been divided into processes that can be performed instantaneously and processes that can start during later phases of the production. Based on this analysis the following six phases can be identified:

- Phase one: production of essential parts that require the longest time to manufacture and that can be produced independently of each other.
- Phase two: production of the tail components
- Phase three: assembly of the wing and the tail
- Phase four: assembly of the aircraft structure
- Phase five: order the off-the-shelf components
- Phase six: final assembly into UAVs

All these different phases, and their corresponding subcomponents, can be found in Figure 26.1. In this chart the colours (symbols) represent the different phases of the production.

According to this figure, assembly of the wing and the tail (phase three) will need to be finished around the same time. The finishing of the other components of phase one should also be around the same time as the end of phase three so that all components can easily go into phase four of the production without any delay or components having to be stored for too long. This means that if the production of one of the components is not very time consuming, it should start later. Depending on the time needed to receive the off-the-shelf components (phase five), they should be ordered just in time for a smooth transition to phase six. The reason that these off-the-shelf components should be ordered in a later stage is because it generally is better to have the expensive parts (such as the engines) built and delivered as late as possible in order to avoid high interest costs. For the same reason it was indicated that the less time consuming components in phase one should start later than the time consuming parts.

## 26.3 Lean manufacturing

Production will be done according to the lean manufacturing principle, taking sustainability into account. Using this principle, the main emphasis is placed on the elimination of waste as much as possible in the entire production line and everything associated to it. Waste is in this case defined as the resources used that do not add value to the end product. Examples of this are: waiting, inventory, transportation, processing, defects and motion [184].

Inventory waste can be limited, for example by identifying the critical number of parts needed in stock (as explained in Section 26.1) and by streamlining the supply chain for these parts as much as possible in order to reduce this critical number. Transportation time can be minimised by locating the different manufacturing halls at strategic locations that allow for fast and reliable transportation to the main assembly hall.

Since the crew get more experience working through routine forming, the chances of defects in the end product are minimised. Based on the stations in the production line the crew do not need to be relocated, reducing the unnecessary motion.

Successful implementation of this way of thinking will minimise production time and environmental impact, and therefore maximise stakeholder value.

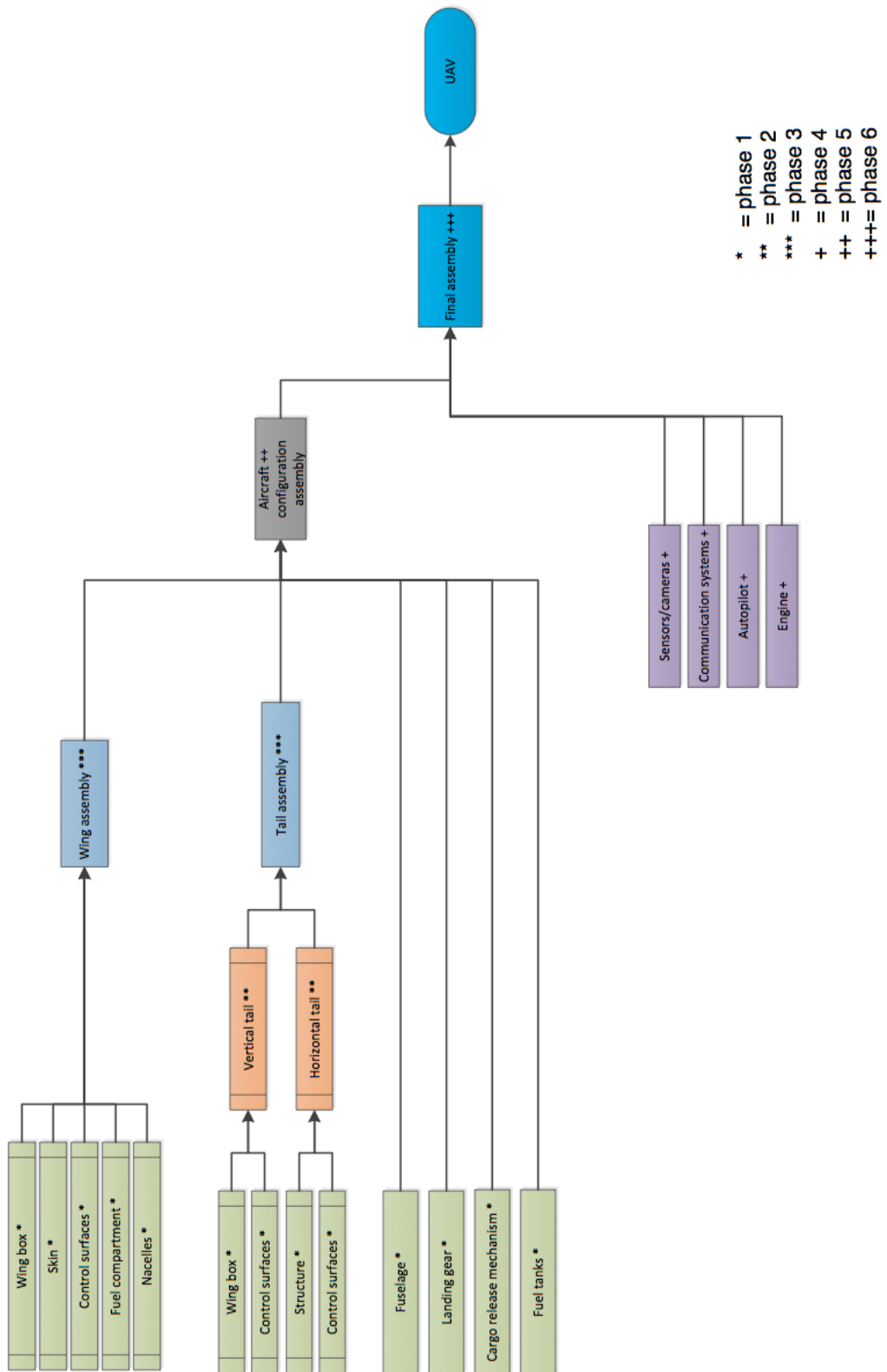


Figure 26.1: Production plan for the assembly of the UAV.

## 27 | Costs

This chapter shows the cost breakdown structure of both the housing unit and the UAV. In this case the return on investment will not be considered since the IFRC, the organisation expected to operate the system, is a non-profit organisation.

The costs of the parachute system are based on the assumption that a parachute can be used over a period of 10 years, as mentioned in Section 18.3. Assuming that parachutes will be returned one week after usage, one UAV requires 14 parachutes for two drops per day. Adding 10 % for airbags and 10 % for maintenance, based on a price per parachute of \$3,000 the total costs for the parachutes over a period of 10 years will be around \$50,500.

The cost breakdown structure is based on real data for the avionics (see right side in Table 27.1) and engine [185], these values are provided by the corresponding departments. Based on reference data, the cost division over separate elements could be determined [186] [187]. This division can also be found in Table 27.1 and forms the basis for the cost breakdown structure created.

For the cargo an extensive cost breakdown has been created. This can be found on the left side in Table 27.1. These are the costs for only one housing unit. Since these costs are quite accurately determined, no safety factor will be included. When increasing the amount of units to be built, the constant costs per unit will definitely decrease due to economies of scale.

**Table 27.1:** Cost breakdown structure for the housing unit and UAV

Component	Cost [\$]	Division of costs	Percentage [%]	Cost [\$]
Floor panels	649	Avionics	3.3	46,000
Anchors	289	- <i>Actuators:</i>		<i>15,000</i>
Columns	128	- <i>Sensors:</i>		<i>9,200</i>
Wall panels	2,295	- <i>Computers:</i>		<i>3,800</i>
Beams	75	- <i>Receivers, transceivers, converters</i>		<i>9,600</i>
Connections	73	- <i>Camera, lights, battery (charger)</i>		<i>8,700</i>
Bolts and nuts	48	Engine	19	265,000
Profiles	28	Engineering	12	167,400
Roof panels	59	Manufacturing	28	391,000
Cables	516	Tooling	12	167,000
Power system	94	Quality Control	8	112,000
Water system	836	Development	3.3	46,000
Interior	<b>5,496</b>	Flight test	3.3	46,000
<b>Total housing unit</b>	405	Materials	10.1	141,000
		Profit	1	14,000
		<b>Total UAV:</b>	<b>100</b>	<b>1,427,700</b>

## 28 | Conclusion

Following up from the generation and preliminary design of three UAV concepts, a detailed design of the concept best suited for the cargo delivery mission was made. This was the fixed wing aircraft which was able to perform the cargo delivery mission with the highest efficiency in terms of the set requirements. Cruising at  $400\text{ km/h}$ , the aeroplane easily meets the requirement of delivering two cargo units per day over a mission range of  $2,000\text{ km}$ . With a total weight of less than  $2,500\text{ kg}$ , the aircraft was optimised to carry a  $500\text{ kg}$ -cargo payload. A powerful Rolls Royce engine was selected which provides a maximum power of  $450\text{ hp}$  and generates the required thrust for take-off and cruise with a 6-bladed propeller.

A double-tapered wing box made of aluminium is incorporated in a Natural Laminar Flow aerofoil on the main wing which has a lift coefficient that suits the design lift coefficient of the aeroplane well. To optimise the wing for cruise and to not overdesign it, single slotted flaps- high lift devices of low complexity- were incorporated along the trailing edge of the wing to be able to generate sufficient lift at low velocities such as during take-off, cargo drop, and landing.

The cargo delivery system achieves its precision drop with a maximal deviation of less than the  $50\text{ m}$  set by the mission requirements. The cargo is extracted from the back of the fuselage with sufficient space for the extraction parachute to safely deploy. An airbag mounted to the bottom of the cargo package in combination with a parachute of a diameter of  $46\text{ m}$  will ensure the smooth descent of the cargo package to the delivery zone.

A unique avionics system has been designed which seamlessly integrates with the existing civil aviation system. Equipped with highly accurate instruments, the UAV is able to perform a precise cargo drop. Images and video can be used to record valuable data that can both provide additional information on the disaster zone and closely monitor the cargo delivery process. The core of the avionics system is the triple redundant Lisa/L autopilot which provides the interface to communicate with the motion actuators in the aircraft. The DC generator as part of the engine provides sufficient power for the entire avionic system. In case of failure, a human controlled emergency landing can be performed.

Upon delivery, the modular housing unit will provide a comfortable, flexible, and expandable environment for the victims of a natural disaster. Equipped with all major components to ensure a permanent and pleasant life in one of the modular houses, each unit can cover its own power needs using a sustainable source of energy. Due to its ability to withstand the harshest environmental impacts, the design of a set of units can be easily adjusted to any environment where a natural disaster might strike.

In conclusion, the cargo UAV meets all its mission requirements with additional contingencies on the major ones. In combination with its cargo delivery system and compact cargo package, its design proved to be a many-sided engineering challenge. Keeping the design complexity as low as possible and yet meeting all the complex design goals was an interesting task which the team managed to fulfil to the best of its abilities.

Part VII  
Appendices

# A | Functional flow diagrams and functional breakdown structure

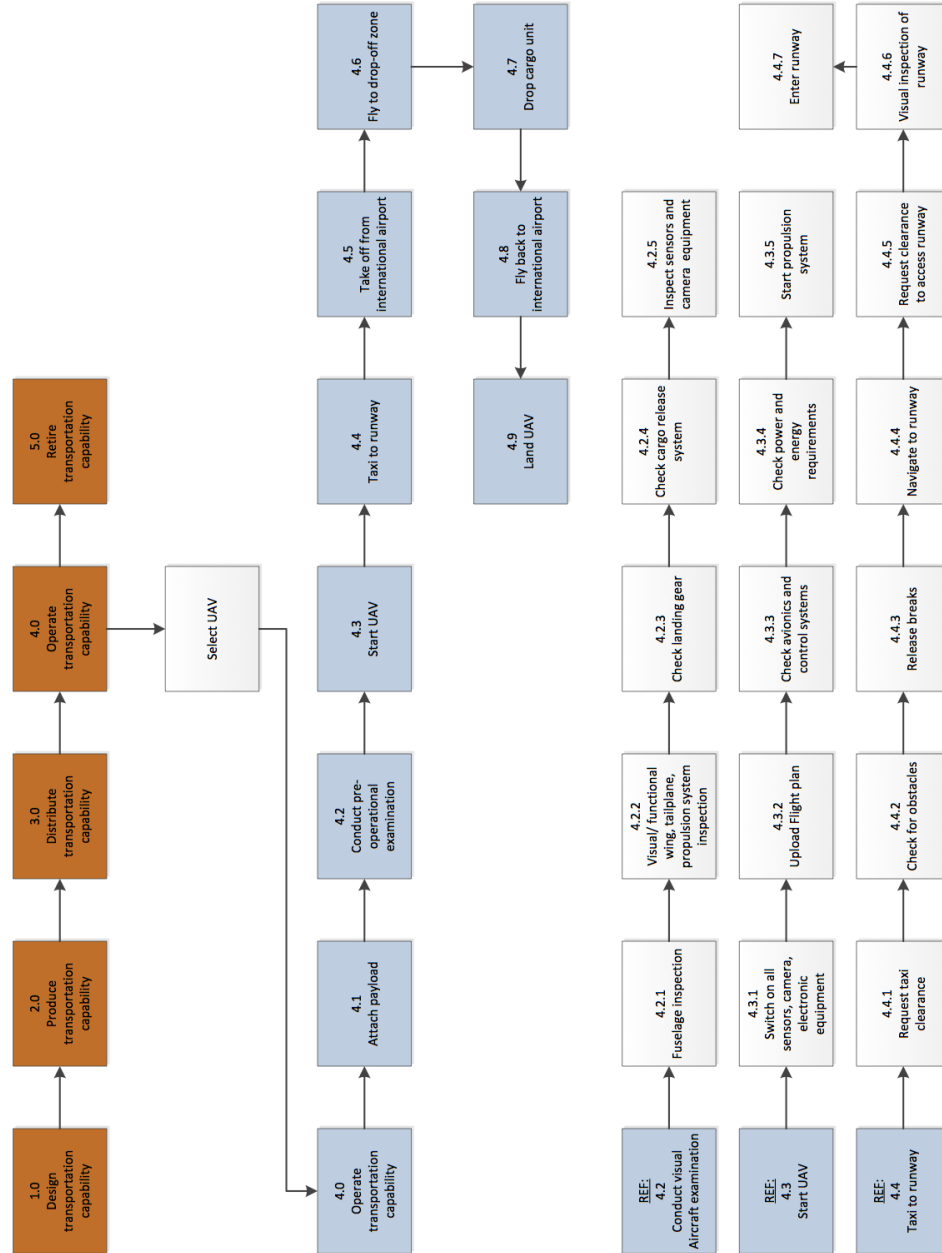


Figure A.1: Functional flow diagram for the complete operation of the UAV, part 1

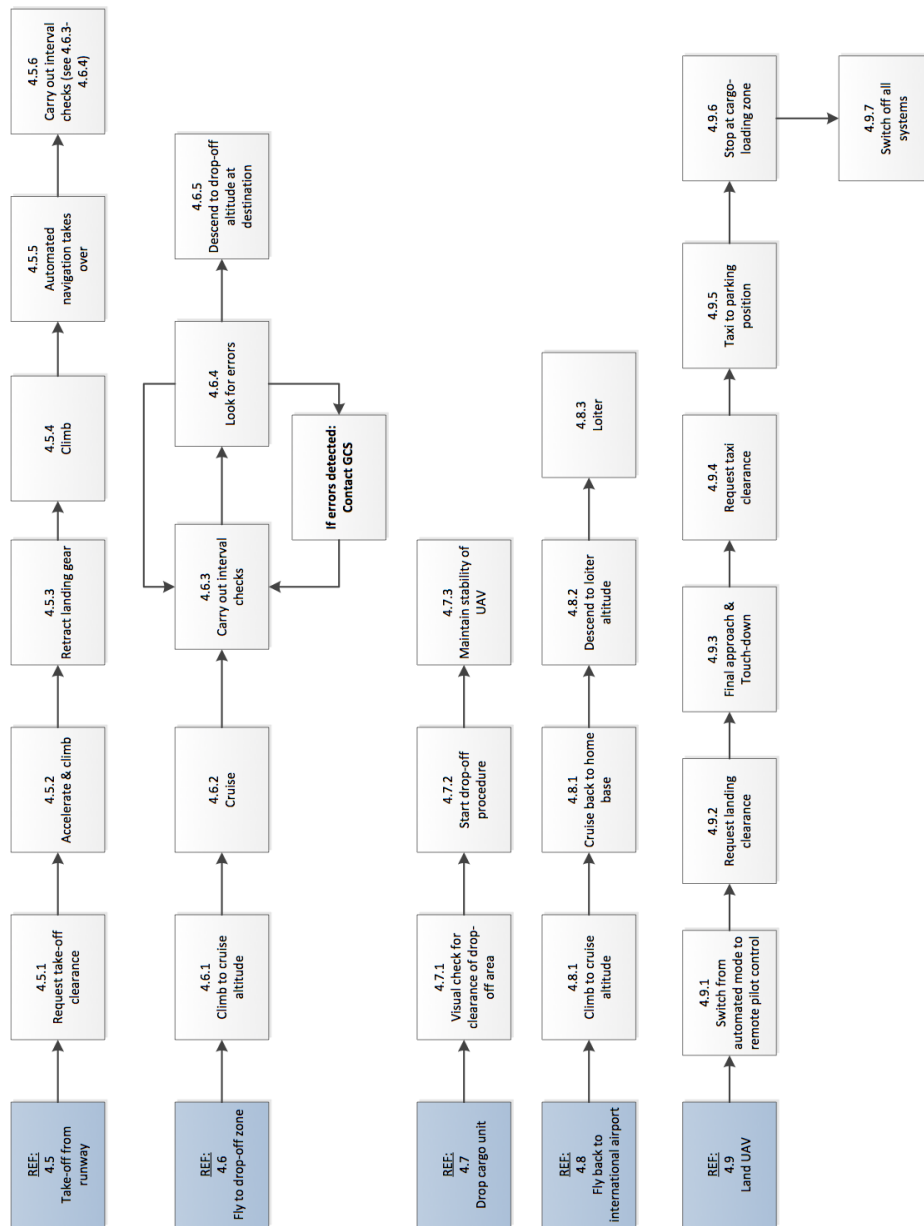


Figure A.2: Functional flow diagram for the complete operation of the UAV, part 2

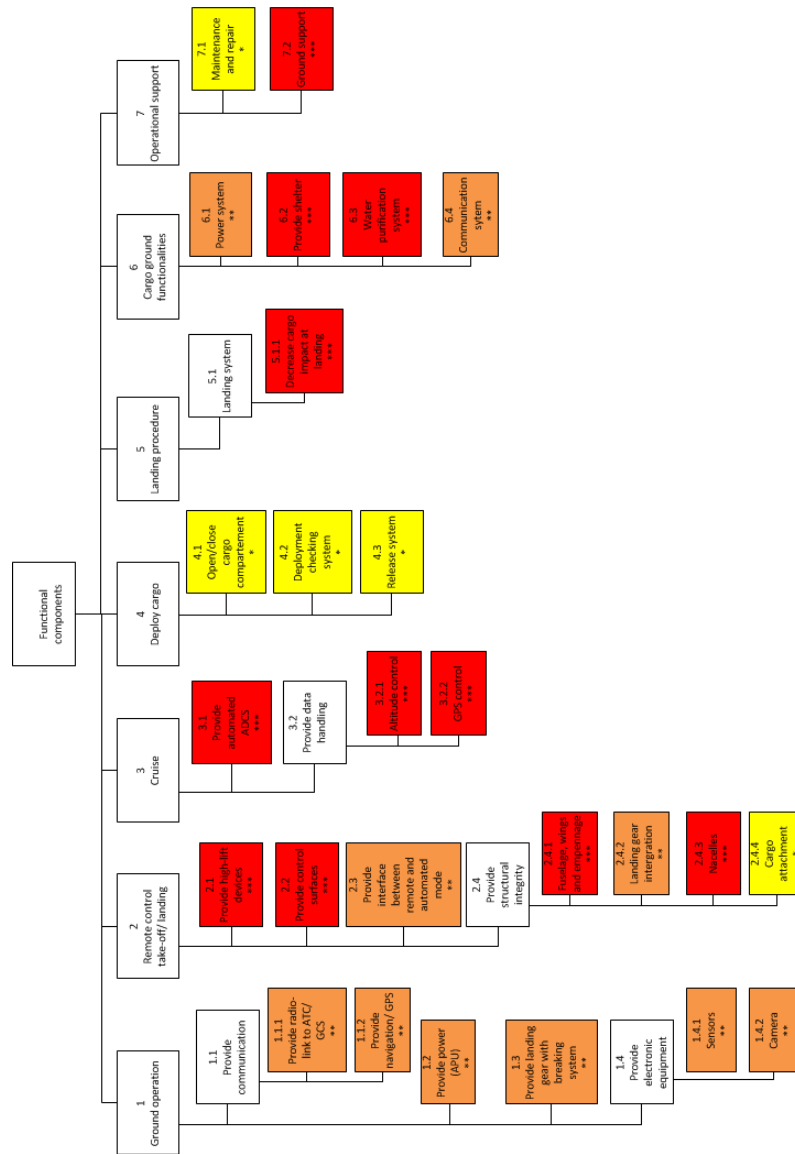


Figure A.4: Functional breakdown structure for the essential parts of the UAV operation

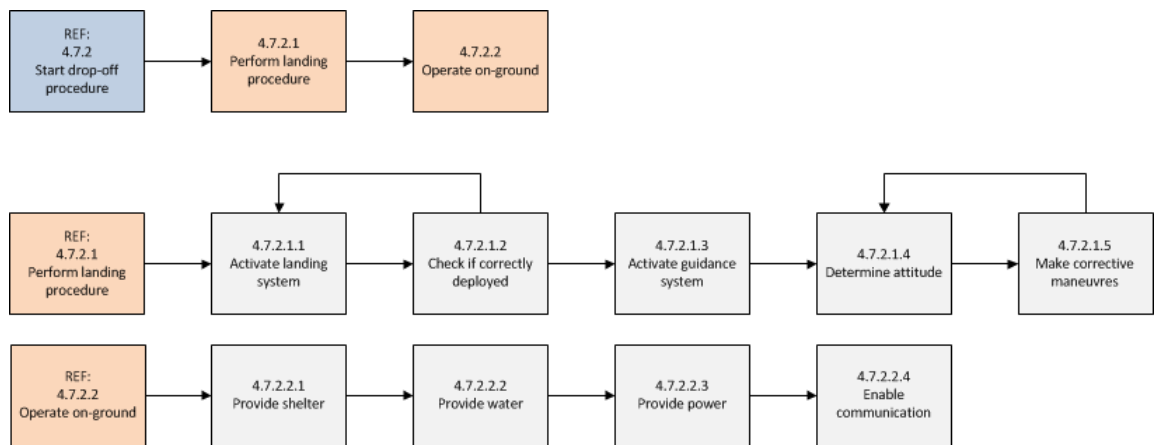


Figure A.3: Functional flow diagram for the operation of the cargo unit

# B | Structural analysis input and output

## Structural analysis tool input and output:

### WINGBOX INPUT:

- Dimensions wingbox
- *Amount of stringers in top & bottom plate*
- *Amount of stringers in left & right spar*
- *Stringer area*
- *Stringer length*
- *Amount of ribs*
- Load factor n
- Lift (function of span length, elliptical distribution)
- Fuel weight (function of span length)
- *Thickness of top and bottom plate*
- *Thickness of left and right spar*
- *E-modulus material*
- *Kc and Ks (buckling coefficients)*
- Fuselage diameter
- *Ultimate tensile strength material*
- *Number of segments of wing box*

### WINGBOX OUTPUT:

- Final dimensions and configuration wingbox
- Several plots (next slide)
- Critical bending stress
- Critical shear stress
- Bending stresses
- Shear stresses
- Torsional stresses
- Von Mises stresses
- Ratios between critical and maximum stresses

## Structural analysis tool input and output:

### FUSELAGE INPUT:

- *Number of stringers*
- *Stringer area*
- Distance from a.c. to c.g.
- Distance a.c. to position of tail lift vector
- Total amount of lift generated by lift
- Total weight
- Total amount of lift generated by tail
- *Thickness skin*
- Fuselage diameter
- *Ultimate tensile strength*
- *Number of segments*

### FUSELAGE OUTPUT:

- Thickness skin and stringer area
- Several plots (next slide)
- Bending stresses
- Shear stresses
- Von Mises stresses
- Ratios between critical and maximum stresses

Figure B.1: Structural analysis tool input and output

# C | Equations of motion parachute

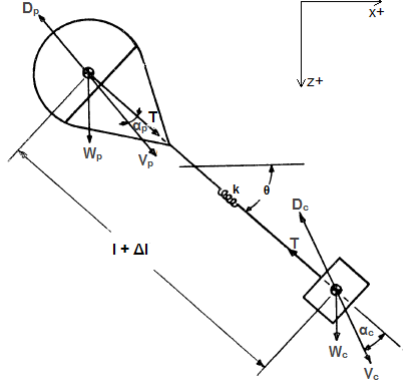


**Figure C.1:** The free-body diagram for the combined cargo-parachute system

Equations of motion:

$$\frac{d}{dt} \begin{bmatrix} V_c \\ \theta + \alpha_c \\ V_p \\ \theta + \alpha_p \end{bmatrix} = \begin{bmatrix} -V_c^2 \cdot \frac{\rho}{2m_c} \cdot C_{D_c} \cdot S_c - \frac{T}{m_c} \cdot \cos(\alpha_c) + g \cdot \sin(\theta + \alpha_c) \\ \frac{T}{V_c \cdot m_c} \cdot \sin(\alpha_c) + \frac{g}{V_c} \cdot \cos(\theta + \alpha_c) \\ -V_p^2 \cdot \frac{\rho}{2m_p} \cdot C_{D_p} \cdot S_p - \frac{T}{m_p} \cdot \cos(\alpha_p) + g \cdot \sin(\theta + \alpha_p) \\ -\frac{T}{V_p \cdot m_p} \cdot \sin(\alpha_p) + \frac{g}{V_p} \cdot \cos(\theta + \alpha_p) \end{bmatrix} \quad (\text{C.1})$$

Where  $V_c$  is the velocity of the cargo,  $V_p$  the velocity of the parachute,  $m_c$  the mass of the cargo,  $m_p$  the mass of the parachute,  $C_{D_c}$  the drag coefficient of the cargo,  $S_c$  the area of the cargo,  $T$  the tension in the cord,  $\alpha_c$  the angle between the body axis of the system and the velocity of the cargo,  $\alpha_p$  the angle between the body axis of the system and the velocity of the parachute,  $\theta$  the angle between the horizontal axis and the body axis of the system, and  $g$  the gravitational acceleration.

Equations for the tension in the cord, the angle  $\theta$ , and the positions are:

$$T = k(\sqrt{(x_c - x_p)^2 + (z_c - z_p)^2} - l) \quad (\text{C.2})$$

and

$$\frac{d\theta}{dt} = \frac{1}{l + \Delta l} \cdot (V_c \cdot \sin(\alpha_c) - V_p \cdot \sin(\alpha_p)) \quad (\text{C.3})$$

Where  $l$  is the original length of the cord and  $\Delta l$  is the elongation.

$$\begin{aligned} \frac{dx_c}{dt} &= V_c \cdot \cos(\theta + \alpha_c) \\ \frac{dx_p}{dt} &= V_p \cdot \cos(\theta + \alpha_p) \\ \frac{dz_c}{dt} &= V_c \cdot \sin(\theta + \alpha_c) \\ \frac{dz_p}{dt} &= V_p \cdot \sin(\theta + \alpha_p) \end{aligned} \quad (\text{C.4})$$

Where  $\frac{dx_c}{dt}$  is the difference in horizontal position of the cargo over time,  $\frac{dx_p}{dt}$  is the difference in horizontal position of the parachute over time,  $\frac{dz_c}{dt}$  is the difference in vertical position of the cargo over time,  $\frac{dz_p}{dt}$  is the difference in vertical position of the parachute over time.

# D | Landing precision

Table D.1: Change in horizontal distance travelled due to errors

Wrong $V_{min}$ 5 km/h	Canopy opening time				Release time error + 0.3 * 25%				
	$t_f$ [s]	$dt_f$ [s]	$sx$ [m]	$dsx$ [m]	$t_r$ [s]	$sx$ [m]	$dsx$ [m]	$sx$ [m]	$dsx$ [m]
$V_{min}$	0.30	0.00	93.28		0.08	96.34	3.06	90.22	-3.06
$V_{min} - error$	0.31	0.01	91.26	-1.59	0.08	94.22	0.94	88.73	-4.55
$V_{min} + error$	0.29	-0.01	95.18	1.48	0.08	98.34	5.06	91.59	-1.68
$V_{min}$	0.30	0.00	69.07	-24.20	0.08	72.13	-21.14	66.01	-27.26
$V_{min} - error$	0.31	0.01	67.59	-25.27	0.08	70.54	-22.73	65.05	-28.23
$V_{min} + error$	0.29	-0.01	70.46	-23.24	0.08	73.62	-19.65	66.88	-26.40
$V_{min}$	0.30	0.00	75.79	-17.48	0.08	78.86	-14.42	72.73	-20.54
$V_{min} - error$	0.31	0.01	74.16	-18.69	0.08	77.12	-16.16	71.62	-21.65
$V_{min} + error$	0.29	-0.01	77.32	-16.37	0.08	80.49	-12.79	73.74	-19.54
+Wind 10 m/s	Canopy opening time				Release time error + 0.3 * 25%				
	$t_f$ [s]	$dt_f$ [s]	$sx$ [m]	$dsx$ [m]	$t_r$ [s]	$sx$ [m]	$dsx$ [m]	$sx$ [m]	$dsx$ [m]
$V_{min} - error - V_{wind}$	0.42	0.12	61.90	-31.38	0.075	64.10	-29.17	59.69	-33.58
$V_{min} + error + V_{wind}$	0.24	-0.07	106.46	13.18	0.075	110.37	19.11	102.54	11.28
$V_{min} - error - V_{wind}$	0.42	0.12	59.20	-34.07	0.075	61.407	-7.67	56.99	-12.08
$V_{min} + error + V_{wind}$	0.24	-0.07	100.52	7.25	0.075	104.44	36.85	96.61	29.02
$V_{min} - error - V_{wind}$	0.42	0.12	64.63	-28.65	0.075	66.84	-8.96	62.42	-13.37
$V_{min} + error + V_{wind}$	0.24	-0.07	112.47	19.19	0.075	116.38	42.22	108.55	34.39

# E Numerical values used for the areodynamic analysis

Table E.1: Numerical values used for the areodynamic analysis

Symbol	Value	Units	Symbol	Value	Units
<b>General aeroplane:</b>					
$W/S$	1,152	$N/m^2$	$C_{D_{G_{C_L=0,MLG}}}$	0.32	—
$AR$	9	—	$C_{D_{G_{C_L=0,nose\ gear}}}$	0.8	—
$M_{des}$	0.3516	—	$p_{nose}$	-0.4	—
$\lambda$	0.4	—	$\Delta C_{D,MLG}$	0.0035	—
$i_w$	-0.5	$^\circ$	$\Delta C_{D,nose\ gear\ (TO)}$	0.0004383	—
$c_r$	2.174	$m$	$\Delta C_{D,nose\ gear\ (land)}$	0.0006527	—
$c_t$	0.8697	$m$	$V_{LOF}$	115.79	$km/h$
$C_{L_{des}}$	0.2674	—	$V_{scr}$	126.32	$km/h$
$\rho$	0.6528	$kg/m^3$	$V_{avg}$	81.88	$km/h$
$L$	22462	$N$	$h_{scr}$	10.67	$m$
$C_L$	0.3317	—	$\gamma_{scr}$	3	$^\circ$
$\mu$	$1.59 * 10^{-5}$	$kg/(ms)$	$s_{scr}$	1,097.2	$m$
$Re_{avg}$	$6.8 * 10^6$	—	$s_{ground\ (TO)}$	800.56	$m$
$C_{L_{max}}$	1.8	—	$V_A$	136.84	$km/h$
$a$	0.23	$m$	$V_T$	121.05	$km/h$
$b$	1	$m$	$T_{rev}$	929.1	—
$B$	0.126	$m$	$\gamma_A$	4	$^\circ$
$D$	0.36	$m$	$s_{ground\ (land)}$	160.9	$m$
$S_{ref_{MLG}}$	0.23	$m^2$	$s_{airborne\ (land)}$	296.55	$m$
$S_{ref_{nose\ gear}}$	0.0454	$m^2$	$\mu_{take-off}$	0.03	—
$\mu_{landing}$	0.4	—			
<b>Horizontal tailplane:</b>			<b>Vertical tailplane:</b>		
$S$	4.2	$m^2$	$S$	1.59	$m^2$
$C_{L_{des}}$	0	—	$C_{L_{des}}$	0	—
$AR$	5	$m$	$AR$	1.5	—
$b$	4.58	$m$	$b$	1.54	$m$
$\lambda$	0.4	—	$\lambda$	0.4	—
$c_r$	1.31	$m$	$c_r$	1.47	$m$
$c_t$	0.524	$m$	$c_t$	0.588	$m$
$\Lambda$	40	$^\circ$	$\Lambda$	0	$^\circ$
<b>High lift devices:</b>					
$C_{L_{max}}$	2.2	—	$\Delta\alpha_{0L_{TO}}$	5.40	$^\circ$
$\Delta C_{l_{max,TO}}$	0.975	—	$\Delta\alpha_{0L_{landing}}$	8.10	$^\circ$
$\Delta C_{l_{max,landing}}$	1.3	—	$\alpha_{drop}$	0	$^\circ$
$\frac{S_{wf}}{S}$	0.540	—	$\alpha_{TO}$	9.5	$^\circ$
$\Delta C_{L_{max,TO}}$	0.473	—	$\alpha_{landing}$	4	$^\circ$
$\Delta C_{L_{max,landing}}$	0.630	—			

# F | Values of stability and control coefficients

In this appendix the formulas and values of the used stability and control coefficients are given in Table F.1. Coefficients 1 to 6 say something about the relation between the force in X-direction and the flight characteristics, horizontal speed, angle of attack, pitch angle, change in angle of attack and elevator deflection, respectively. Coefficient 7 to 18 do this for the forces in Z-direction and the moment around the Y-axis. The control coefficients can be found in row 6, 12 and 18. Most of the formulas used are obtained using the reader of the Flight Dynamics course [121]. When not the case, the reference is labeled after the formula.

**Table F.1:** Values of stability and control coefficients influencing the resulting force in X-direction during cruise

No.	Coefficient	Formula	Value
1	$C_{X_0}$	$\frac{W \sin(\gamma_0)}{\frac{1}{2} \rho V^2 S}$	0
2	$C_{X_u}$	$-2C_D$ [122]	-0.22
3	$C_{X_\alpha}$	$C_L(1 - \frac{2C_{L\alpha}}{\pi A e})$	0.47
4	$C_{X_q}$	0	0
5	$C_{X_{\dot{\alpha}}}$	0	0
6	$C_{X_{\delta_e}}$	0	0
7	$C_{Z_0}$	$-\frac{W \cos(\gamma_0)}{\frac{1}{2} \rho V^2 S}$	-1.14
8	$C_{Z_u}$	$-2C_L$ [122]	-2.27
9	$C_{Z_\alpha}$	$-C_{N_{w\alpha}} - C_{N_{h\alpha}}(1 - \frac{d\epsilon}{d\alpha})(\frac{V_h}{V})^2 \frac{S_h}{S}$	-5.16
10	$C_{Z_q}$	$-2C_{N_{h\alpha}}(\frac{V_h}{V})^2 \frac{S_h l_h}{S c}$	-3.86
11	$C_{Z_{\dot{\alpha}}}$	$-C_{N_{h\alpha}}(\frac{V_h}{V})^2 \frac{d\epsilon}{d\alpha} \frac{S_h l_h}{S c}$	-1.43
12	$C_{Z_{\delta_e}}$	$-C_{N_{h\delta_e}}(\frac{V_h}{V})^2 \frac{S_h}{S}$	-0.62
13	$C_{m_0}$	0	0
14	$C_{m_u}$	0	0
15	$C_{m_\alpha}$	$C_{N_{w\alpha}} \frac{x_{cg} - x_w}{c} - C_{N_{h\alpha}}(1 - \frac{d\epsilon}{d\alpha})(\frac{V_h}{V})^2 \frac{S_h l_h}{S c}$	-0.43
16	$C_{m_q}$	$-1.15 C_{N_{h\alpha}}(\frac{V_h}{V})^2 \frac{S_h l_h^2}{S c^2}$	-7.04
17	$C_{m_{\dot{\alpha}}}$	$-C_{N_{h\alpha}} * (\frac{V_h}{V})^2 \frac{d\epsilon}{d\alpha} \frac{S_h l_h^2}{S c^2}$	-3.7
18	$C_{m_{\delta_e}}$	$-C_{N_{h\delta_e}}(\frac{V_h}{V})^2 \frac{S_h l_h}{S c}$	-1.554

# G | Avionics system components

ID	Component	Model	Flight Critical system	Suggested redundancy	I/O bus	Supply voltage (V)	Max power consumption (W)	Cost	Total weight (g)
1	Autopilot	Lisa/L	yes		CAN UART -TTL I <sup>2</sup> C SPI 3A/D	6 – 18 V	0.1683	690	490
2	Additional computer	Gumstix Overo	yes		I <sup>2</sup> C SPI GPIO A/D UART-TTL USB host		1	450	127.8
3	Differential pressure		yes		3 USB OTG				0
4	Barometer		yes						0
5	Camera	Cloudcaptech TASE400	no		RS-232 CAN 1 Ethernet	10 – 30V	125	8000	3400
6	DVI to USB converter	Epiphan DVI2USB 3.0	no		DVI 1 USB			700	
7	IMU	Aspirin IMU	yes		I <sup>2</sup> C 3 SPI		0.05	315	225
8	Nav & strobe lights	NavStrobe Sextant Aircraft Navigation System	no		1	14-28VDC	15	150	50
9	Flight data recorder	Curtiss-wright S3DR-S	no		Ethernet ARINC 429 1 RS-232	14/28 VDC	6	300	3000
10	GPS	NexNav MAX	yes		UART-TTL RS-232		5	800	1020
11	GPS antenna	PCTEL 12700	yes		2 Customized 2 TNC Male	10-32VDC 4.5 – 9 VDC	0.36	200	204
12	ADS-B	Sagatech XPS-TRB	no		1 RS 232	10 – 32	11	500	100
13	ADS-B antenna	Sensor systems S85-5366-895L	no		1			100	2670
14	TCAS	Avidyne TAS 605	no		1 ARINC-429	14/28 VDC	42	5000	3100
15	TCAS antenna	Avidyne TAS 605 antenna's	no		2 included				640
16	Satellite transeiver	SCOTTY UAV SATCOM Unit	no		1 ARINC429	28VDC	350	8000	6100
17	Satcom antenna	Cobham HGA-6000	no		1 ARINC429	28VDC	22.4		1800
18	Satellite amplifier	Cobham HLD7260	no		1	28VDC	10	0	2400
19	UHF link MODEM	Microhard Ipn920	yes		RS -232 RS-485 RS-422				
20	UHF link antenna	Pharad UHF to C-band UAV antenna	yes		1 USB 2	7 – 30 VDC	6	400	250 150
21	Radio altimeter	Smartmicro UMR-0Ax70x-22070x-05070x	no		CAN 1 RS485	7 – 32 VDC	3.7	2500	350
22	Aileron 1 actuator	EHA or EMA	yes		CAN 2 RS485	28 VDC	598	2000	7360
23	Aileron 2 actuator	EHA or EMA	yes		CAN 2 RS485	28 VDC	598	2000	7360
24	Elevator actuator	EHA or EMA	yes		CAN 2 RS485	28 VDC	701	2000	8,628
25	Rudder actuator	EHA EMA	yes		CAN 2 RS485	28 VDC	600	2000	7,385
26	Flap 1 actuator	Electric motor	yes		CAN 2 RS485	28 VDC	300	1000	3,692
27	Flap 2 actuator	Electric motor	yes		CAN 2 RS485	28 VDC	300	1000	3,692
28	Landing gear brake actuators	EHA	yes		CAN 1 RS485	28 VDC	100	600	1,231
29	Landing gear actuators	EHA or EMA	yes		CAN 2 RS485	28 VDC	332	2000	4,086
30	Cargo release actuator	Solenoid	no		1 GPIO	28 VDC	2	200	0
31	Cargo release sensor	Laser sensor	no		1 GPIO		0.2	30	110
32	Engine monitor	JAV Navigation EM02	yes		1 RS-232	7 – 14 VDC	2.1	2000	260
33	Engine activators	Stepper motors	yes		CAN 1 RS485		30	1200	2000
34	Fuel pump		yes		CAN 2 RS485	28 VDC	270		0
35	Battery	SAFT 2758	yes		1	24 VDC		5000	25000
36	Pitot probe heat controller	Dynon Avionics Heated AOA/Pitot probe	no		1	13.8V	100	400	140
37	USB to ARINC429	MBS Electronics ARINC 429 + CAN USB	no		1		1		150
38	Starter motor/generator					28 VDC			0
39	Ice Detector	JTC Model 0871LH1	no		CAN	24 VDC	24	150	150

**Figure G.1:** List of all avionics system components. The datasheets corresponding to the components are found in the bibliography. They are linked to the component id in the following list: 1: [7], 2: [8], 5: [9], 6: [10], 7: [11], 8: [12], 9: [13], 10: [14], 11: [15], 12: [16], 13: [17], 14 [18], 16 [19], 17 [20], 18 [21], 19 [22], 20 [23], 21 [24], 22, 23, 24, 25: [25], 26 [26], 33 [27], 35 [28], 36 [29], 37 [30], 39 [31].

# H | Layout of the electrical power system

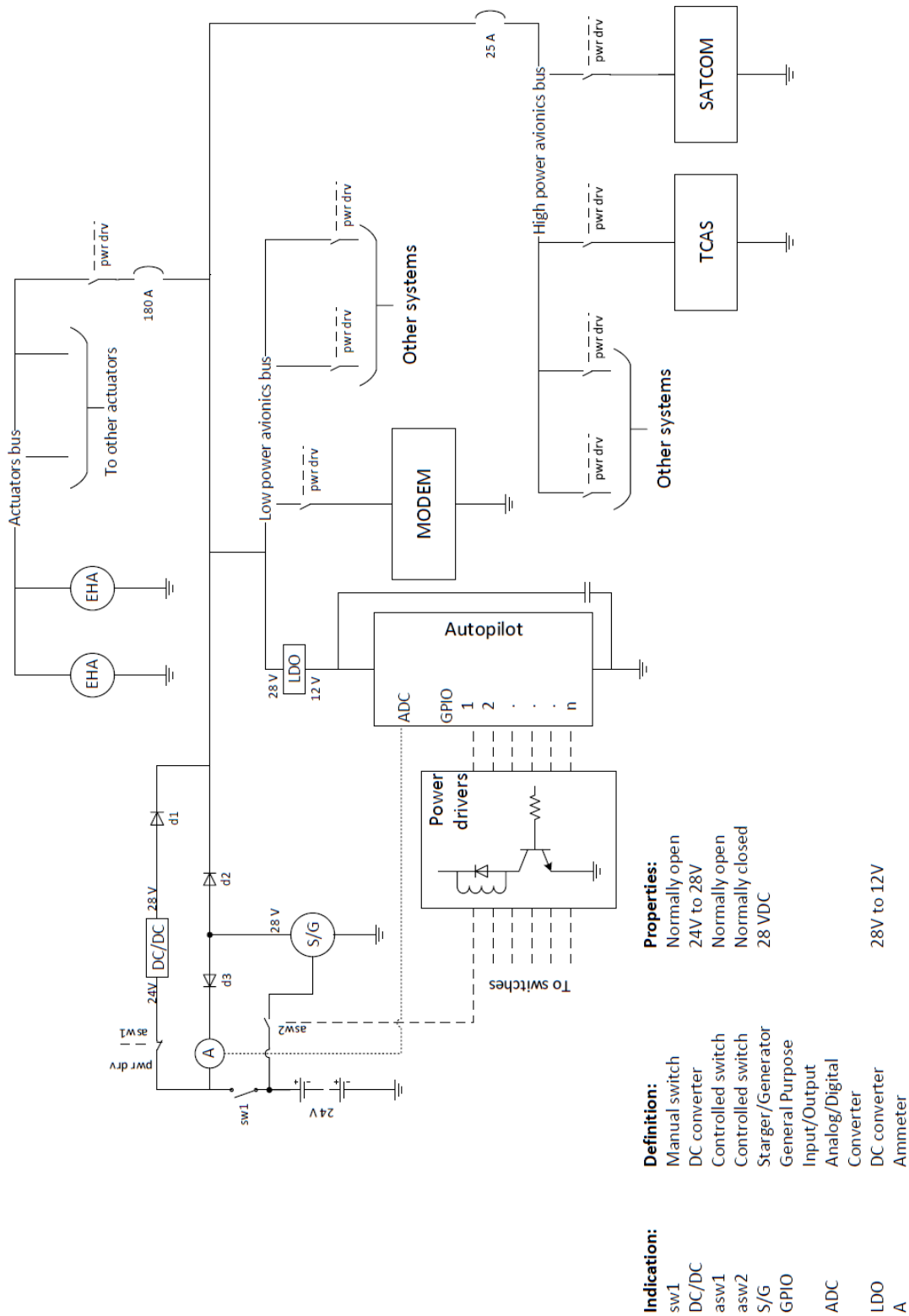


Figure H.1: The layout of the electrical power system

# I | Layout of the triple redundant autopilot

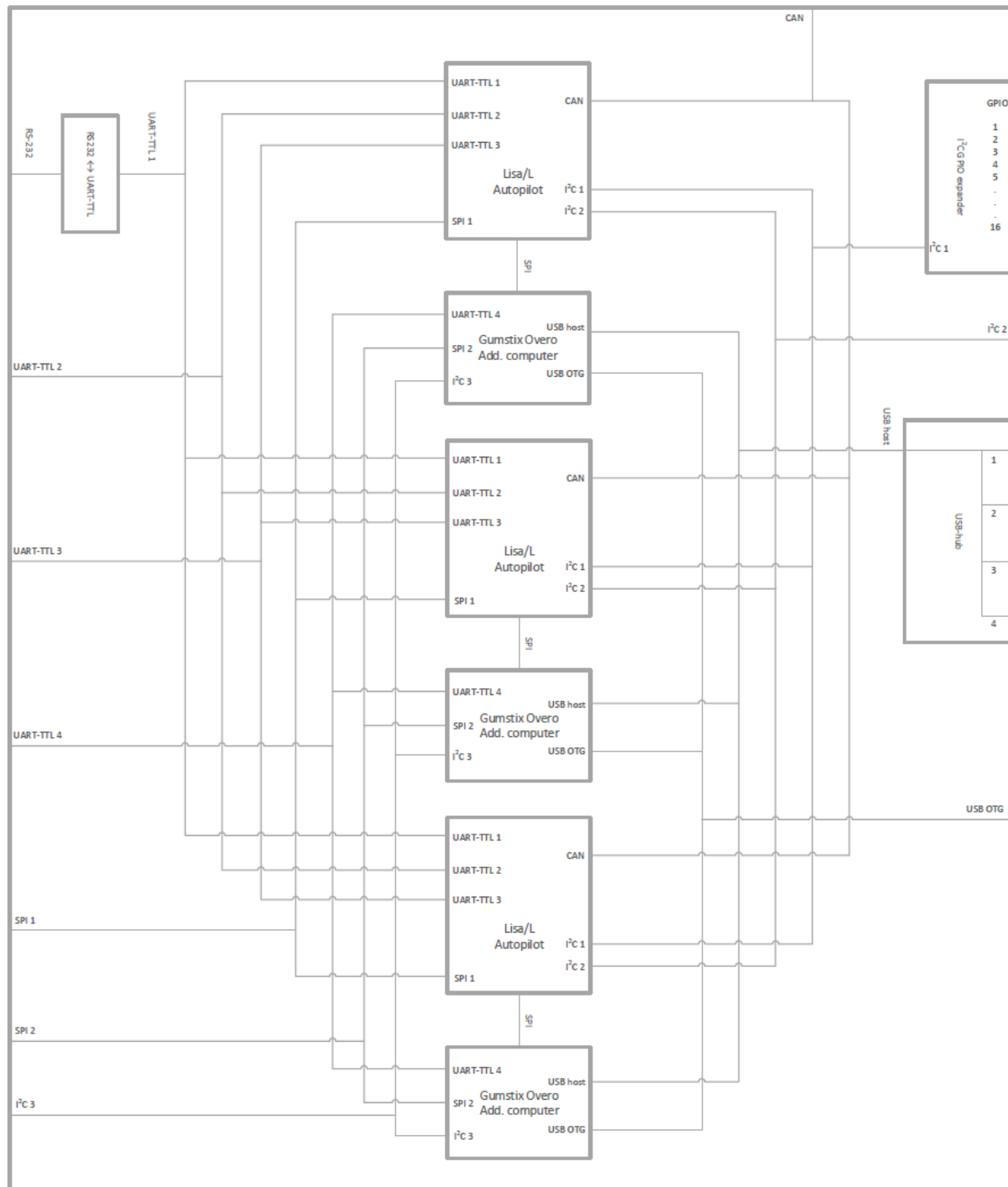
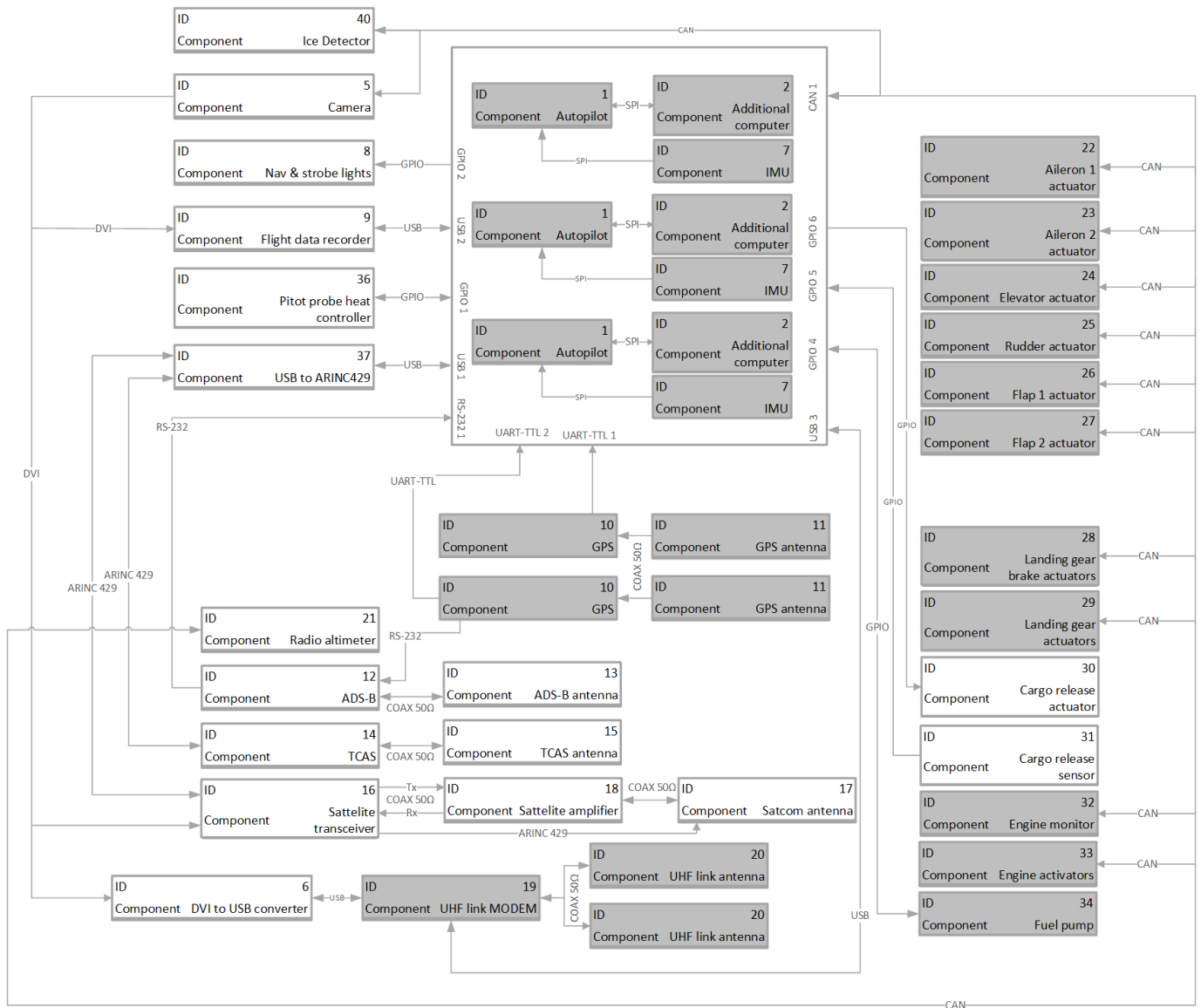


Figure I.1: The layout of the triple redundant autopilot

# J | Layout of the entire avionics system



Interface	Connector recommendation	Cable recommendation	Source
RS-232	DE-9, DA-15 or DB-25	Shielded twisted pair	Specification recommendation
UART-TTL	DE-9	Shielded twisted pair	Author recommendation
CAN	DE-9 5 pin mini style 5 pin micro style	Shielded twisted pair	Specification recommendation
USB	IP67/IP20 grade	Shielded twisted pair	Author recommendation

Figure J.1: The layout of the entire avionics system

# K | Flowcharts operations & logistics

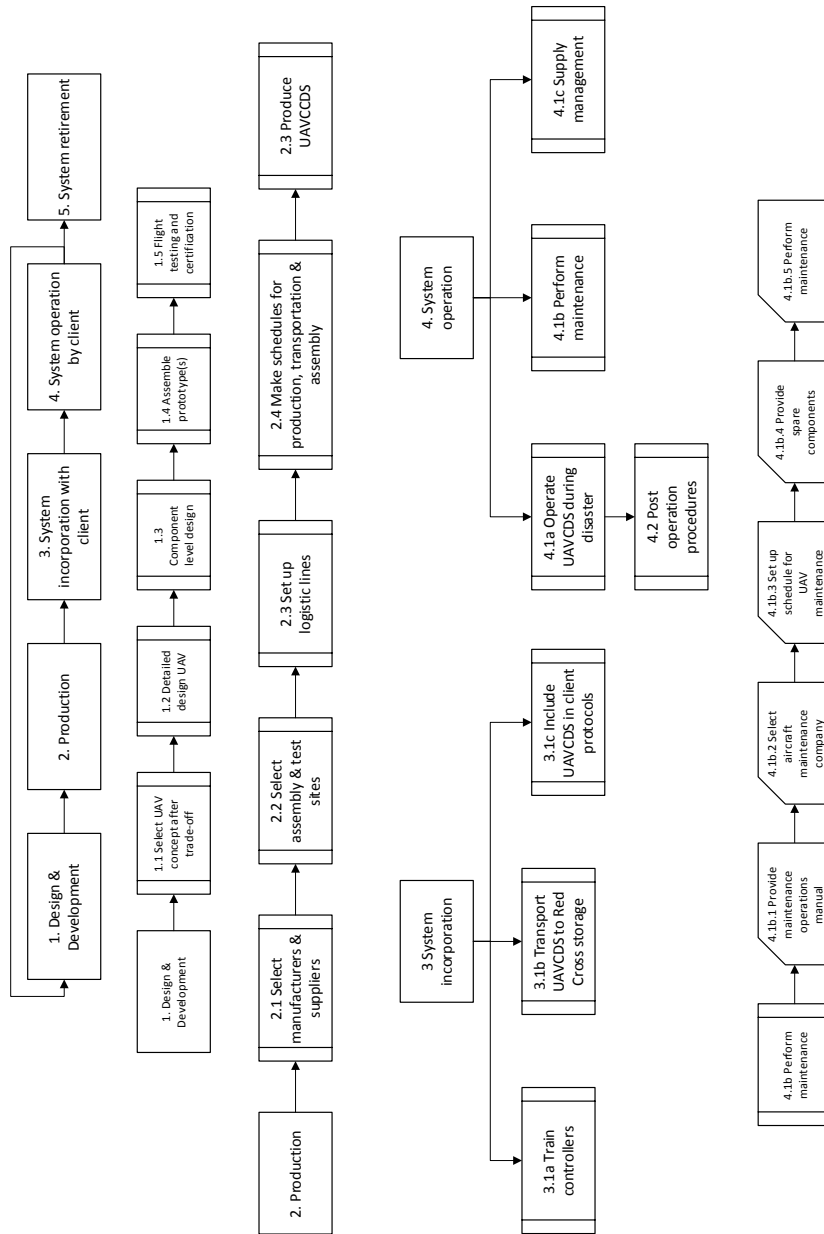


Figure K.1: Operations & logistics flowcharts

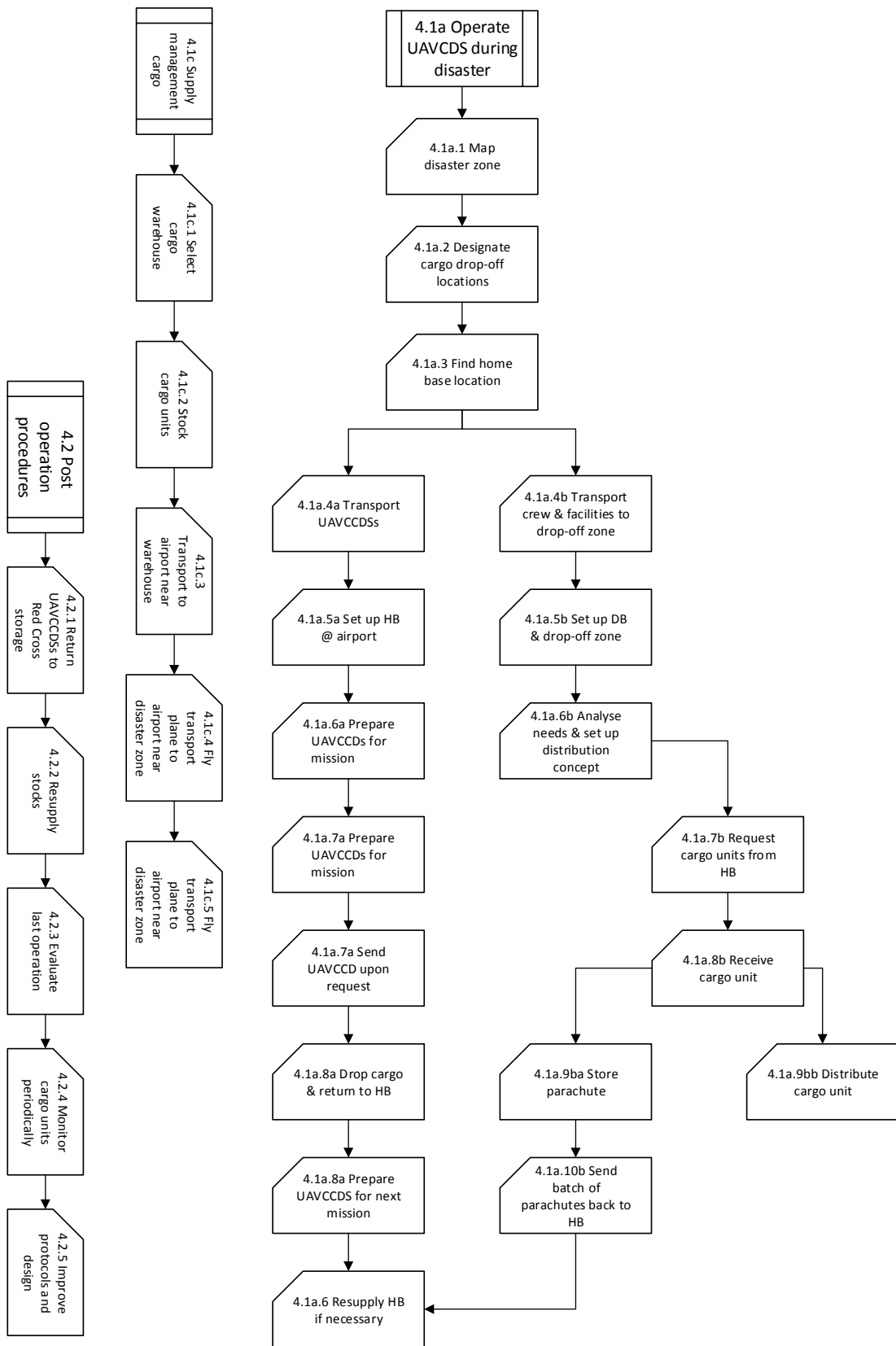


Figure K.2: Operations & logistics flowcharts

# L | Gantt charts

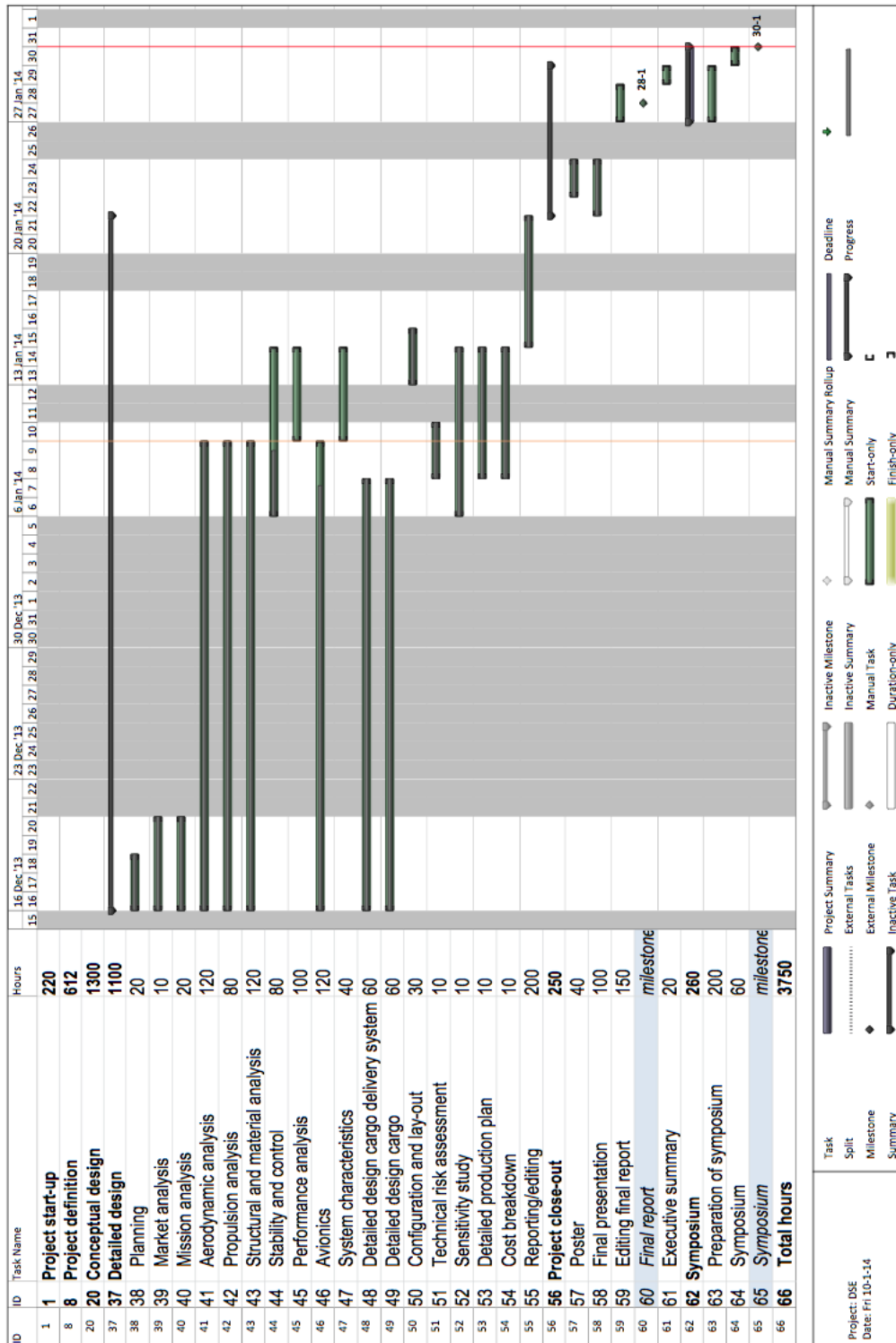


Figure L.1: Gantt chart of the DSE project from the mid-term report up until the symposium

# Bibliography

- [1] A. Moloney, "Haitians still homeless, suffering in despair 4 years after quake - amnesty." <http://www.trust.org/item/20140113063728-6lwyr/>, 2014.
- [2] AID, "Aid: Airfoil investigation database." <http://www.airfoildb.com>, 2013.
- [3] Institute of Jet Propulsion and Turbomachinery, "Gasturb 12." <http://www.gasturb.de/impressum.html>, 2013.
- [4] Air Transport Action Group, "Beginner's guide to aviation biofuels." [www.enviro.aero](http://www.enviro.aero), 2009.
- [5] D. K. K. Dr. Prem Krishna and D. N. Bhandari, "Wind loads on buildings and structures." Department of Civil Engineering.
- [6] HYDRAID, "Hydrad efficacy." <http://hydrad.org/efficacy>, 2012.
- [7] Various contributors, "Lisa/l." <http://wiki.paparazziuav.org/wiki/Lisa/L>, Accessed 2014.
- [8] Gumstix, "Gumstix overo." <https://store.gumstix.com/index.php/category/33/>, Accessed 2014.
- [9] Cloudcaptech, "Cloudcaptech tase400." <http://www.cloudcaptech.com/Sales%20and%20Marketing%20Documents/TASE400%20Data%20Sheet.pdf>, Accessed 2014.
- [10] Epiphan, "Dvi 2 usb 3.0." <http://www.epiphan.com/products/frame-grabbers/dvi2usb-3-0/>, Accessed 2014.
- [11] Contributors, "Aspirin." <http://wiki.paparazziuav.org/wiki/AspirinIMU>, Accessed 2014.
- [12] Navstrobe lighting, "Navstrobe sextant aircraft navigation system." <http://www.navstrobelight.com/products/NavStrobe-Sextant-Aircraft-Navigation-System-with-constant-%26-fast-strobes,-30w.html>, Accessed 2014.
- [13] CWC, "S3dr rugged flight data recorder." <http://www.cwc-ae.com/product/s3dr-s>, Accessed 2014.
- [14] Accord Technology, "Nexnav max." [http://www.accord-technology.com/nexnav\\_max.html](http://www.accord-technology.com/nexnav_max.html), Accessed 2014.
- [15] Antenna.com, "12700 series, airborne antennas." <http://www.antenna.com/artifacts/201010112700SERIESAIRBORNE.pdf>, Accessed 2014.
- [16] Sagatech, "Uav ads-b solutions." [http://www.sagattechcorp.com/unmanned-solutions/#.UrAqD0J\\_vyc](http://www.sagattechcorp.com/unmanned-solutions/#.UrAqD0J_vyc), Accessed 2014.
- [17] Sensor systems, "Sensor systems s65-5366-895l." [http://www.sensorantennas.com/antenna\\_pdf/LBAND/S65-5366-895L.pdf](http://www.sensorantennas.com/antenna_pdf/LBAND/S65-5366-895L.pdf), Accessed 2014.
- [18] Avidyne, "Avidyne tas 605." [http://www.completeavionics.com/assets/av633-tas600\\_lr.pdf](http://www.completeavionics.com/assets/av633-tas600_lr.pdf), Accessed 2014.
- [19] SCOTTY, "Scott uav satcom unit." [http://www.scottygroup.com/images/content/pdfs/a4\\_scotty\\_uav\\_prelim1.pdf](http://www.scottygroup.com/images/content/pdfs/a4_scotty_uav_prelim1.pdf), Accessed 2014.
- [20] Cobham, "Cobham aviator hga-6000." <http://www.cobhamswiftbroadband.com/UserFiles/File/HGA-6000.pdf>, Accessed 2014.
- [21] Cobham, "Cobham aviator hld-7260." <http://www.cobham.com/media/632985/hld-7260.pdf>, Accessed 2014.
- [22] Microhard, "Microhard lpn 920." <http://www.microhardcorp.com/brochures/Nano%20IP%20Series.IPn920.Brochure.Rev.1.3.pdf>, Accessed 2014.
- [23] Pharad, "Pharad uhf to c-band uav antenna." <http://www.pharad.com/uhf-to-c-band-uav-antenna.html>, Accessed 2014.
- [24] Smartmicro, "Smartmicro umrr-0ax70x-22070x-05070x." [http://www.smartmicro.de/images/smartmicro/airborne/micro\\_radar\\_altimeter/Micro\\_Radar\\_Altimeter\\_Data\\_Sheet.pdf](http://www.smartmicro.de/images/smartmicro/airborne/micro_radar_altimeter/Micro_Radar_Altimeter_Data_Sheet.pdf), Accessed 2014.
- [25] Meng Fanliang, "Actuation system design with electrically powered actuators." [https://dspace.lib.cranfield.ac.uk/bitstream/1826/6282/1/Meng\\_Fanliang\\_Thesis\\_2010.pdf](https://dspace.lib.cranfield.ac.uk/bitstream/1826/6282/1/Meng_Fanliang_Thesis_2010.pdf), 2011.
- [26] QAA, "Flap motor." <http://www.qaa.com/products/aircraft-motors/aircraft-flap-motors/cessna-flap-motor-1>, Accessed 2014.
- [27] UAVnavigation.com, "Engine monitor." <http://www.uavnavigation.com/sites/default/files/ds/EM02.pdf>, Accessed 2014.
- [28] SAFT, "Saft battery 2758." <http://www.saftbatteries.com/battery-search/2758>, Accessed 2014.
- [29] Dynon, "Dynon avionics heated aoa/pitot probe." <http://www.aircraftspruce.com/catalog/pdf/dynonheatedaoamanual.pdf>, Accessed 2014.
- [30] MBS Electronics, "Arinc 429 + can usb." <http://www.mbs-electronics.com/products/arinc-429/arinc-429-can-usb.html>, Accessed 2014.
- [31] UTC Aerospace Systems, "Ice detector model 0871lh1." <http://utcaerospacesystems.com/cap/systems/sisdocuments/Ice%20Detection%20and%20Protection%20Systems/Ice%20Detector%20Model%200871LH.pdf>, Accessed 2014.
- [32] A. S. M. Inc, "Aluminum 7075-t6; 7075-t651." <http://asm.matweb.com/search/SpecificMaterial.asp?bassnum=MA7075T6>, January 2014.
- [33] M. A. Rohrlick, "Parachute low altitude delivery system," tech. rep., 1968.
- [34] C. D. A. L. Captain Lowell W. Jones, "Air university review: Tactical airlift." <http://www.airpower.maxwell.af.mil/airchronicles/aureview/1967/oct/lindbo.html>, 1967.
- [35] Chris Huber, World Vision U.S., "Five of the worst natural disasters in 2013." <http://www.worldvision.org/news-stories-videos/2013-top-natural-disasters>, 2013.
- [36] United Nations Office for the Coordination of Humanitarian Affairs, "Typhoon haiyan." <http://www.unocha.org/crisis/typhoonhaiyan>, 2013.
- [37] Daniella Silva, NBC News, "Typhoon haiyan: A crisis by the numbers." [http://worldnews.nbcnews.com/\\_news/2013/11/17/21496134-typhoon-haiyan-a-crisis-by-the-numbers?lite](http://worldnews.nbcnews.com/_news/2013/11/17/21496134-typhoon-haiyan-a-crisis-by-the-numbers?lite), 2013.
- [38] The Associated Press, "Military drone crashes into lake ontario." <http://www.cbc.ca/news/world/military-drone-crashes-into-lake-ontario-1.2424330>, 2013.

- [39] The Associated Press, "Teal group predicts worldwide uav market will total \$89 billion in its 2013 uav market profile and forecast." <http://tealgroup.com/index.php/about-teal-group-corporation/press-releases/94-2013-uav-press-release>, 2013.
- [40] Lucintel, "Growth opportunity in global uav market." <http://www.lucintel.com/LucintelBrief/UAVMarketOpportunity.pdf>, 2011.
- [41] E. Group, "Uav market to top \$13 billion by 2014," *Aircraft Engineering and Aerospace Technology*, vol. 78, no. 2, 2006.
- [42] Matthew H. Jones, Stephen D. Patek, and Barbara E. Tawney, eds., "Unmanned aerial vehicle (uav) cargo system: senior design capstone project." <http://ieeexplore.ieee.org/stamp/stamp.jsp?tp=&arnumber=1314671>, 2004.
- [43] Claire Provost, "A decade of disasters - get the key data." <https://docs.google.com/spreadsheet/ccc?key=0AonYZs4Mz1ZbdExJc3FUakhELVhFZ2JJVUNZnBuU1E&hl=en#gid=0>, 2011.
- [44] United States Census Bureau, "Midyear population and density - world - total for selected region." <http://www.census.gov/population/international/data/idb/region.php?N=%20Results%20&T=6&A=aggregate&RT=0&Y=1990&R=1&C=>.
- [45] United States Census Bureau, "Midyear population and density - world - total for selected region." <http://www.census.gov/population/international/data/idb/region.php?N=%20Results%20&T=6&A=aggregate&RT=0&Y=2009&R=1&C=>.
- [46] "A 160 hummingbird - overview." [http://www.boeing.com/boeing/bds/phantom\\_works/hummingbird.page](http://www.boeing.com/boeing/bds/phantom_works/hummingbird.page).
- [47] "Kaman k-max." [http://en.wikipedia.org/wiki/Kaman\\_K-MAX](http://en.wikipedia.org/wiki/Kaman_K-MAX).
- [48] "With outstanding high-hot performance, economic operation, and superior reliability, the k-maxif; aerial truck is built to lift.." <http://www.kaman.com/aerospace/aerosystems/air-vehicles-mro/products-services/k-max/>.
- [49] "Unmanned little bird - overview." <http://www.boeing.com/boeing/rotorcrafter/military/ulb/>.
- [50] "Boeing ah-6." [http://en.wikipedia.org/wiki/Boeing\\_AH-6](http://en.wikipedia.org/wiki/Boeing_AH-6).
- [51] Defense Industry Daily, "Jpads: Making precision air-drops a reality." <http://www.defenseindustrydaily.com/jpads-making-precision-airdrop-a-reality-0678/>, 2012.
- [52] Defense Update, "Precision aerial delivery." [http://defense-update.com/features/du-1-07/feature\\_aerialdelivery.htm](http://defense-update.com/features/du-1-07/feature_aerialdelivery.htm).
- [53] Defense Update, "Sherpa parafoil based aerial delivery system." <http://defense-update.com/products/s/Sherpa-PADS.htm>, 2013.
- [54] Atair Aerospace, "Onyx ultra light dropping system." <http://www.atair.com>.
- [55] MMIST, "Sherpa ranger dropping system." [http://www.mmist.ca/pg\\_ProductsSherpaPadsRanger.php](http://www.mmist.ca/pg_ProductsSherpaPadsRanger.php).
- [56] ParaFly, "Firefly dropping system." <http://www.airborne-sys.com/pages/view/firefly>.
- [57] Atair Aerospace, Inc., "Onyx overview." <http://www.atair.com/onyx/>, 2012.
- [58] AirborneSystems, "Guided precision aerial delivery system." [http://www.airborne-sys.com/files/pdf/firefly-spec\\_sheet-crops.pdf](http://www.airborne-sys.com/files/pdf/firefly-spec_sheet-crops.pdf).
- [59] IFRC, "Shelter kits guidelines." <http://www.ifrc.org/PageFiles/95526/publications/D.03.a.07.%20IFRC%20shelter-kit-guidelines-EN-LR.pdf>.
- [60] IFRC, "Emergency shelter in natural disaster." [https://www.google.com/url?q=http://www.ifrc.org/PageFiles/95528/Shelter%2520in%2520Natural%2520Disasters.pptx&sa=U&ei=SoqMUoW1BI6thQfQ24HgCQ&ved=0CAYQFjAA&client=internal-uds-cse&usq=AFQjCNE42w1PYjB6\\_NxHmFGeKB9GL\\_cKKA](https://www.google.com/url?q=http://www.ifrc.org/PageFiles/95528/Shelter%2520in%2520Natural%2520Disasters.pptx&sa=U&ei=SoqMUoW1BI6thQfQ24HgCQ&ved=0CAYQFjAA&client=internal-uds-cse&usq=AFQjCNE42w1PYjB6_NxHmFGeKB9GL_cKKA).
- [61] Life Cube, Inc., "Life cube." <http://lifecubeinc.weebly.com/life-cube.html>.
- [62] Reaction Cube, Inc., "Reaction housing system." <http://www.reactionhousingsystem.com>.
- [63] P. M. van Tooren, "Ae1-201 a/c preliminary sizing." lecture slides Aerospace Design and Systems Engineering Elements 1, 2010 - 2011.
- [64] unknown, "Intermodal container." <http://en.wikipedia.org/wiki/Intermodalcontainer>, 2013.
- [65] SHIPPING CONTAINER INFO, "Standard iso containers size and type." <http://shipping-container-info.com/size-type-info/widespread-container-size-type>, 2013.
- [66] Lorenzo Shipping Corporation, "Container 01 kmj." <http://upload.wikimedia.org/wikipedia/commons/d/df/Container-01-KMJ.jpg>.
- [67] Global Security, "463l pallet cargo system." <http://www.globalsecurity.org/military/systems/aircraft/systems/463L-pallet.htm>, 2011.
- [68] Boeing, "Cargo pallets containers." <http://www.boeing.com/assets/pdf/commercial/startup/pdf/CargoPalletsContainers.pdf>, March 2012.
- [69] Tech. Sgt. James R. Ferguson, "C-130 hercules." [http://en.wikipedia.org/wiki/File:C-130\\_Hercules-\(2152191703\).jpg](http://en.wikipedia.org/wiki/File:C-130_Hercules-(2152191703).jpg), 1987.
- [70] Compliance Packaging International Ltd., "463l pallets." <http://www.463lpallet.com>.
- [71] US Air Force, "C-130 hercules." <http://www.af.mil/AboutUs/FactSheets/Display/tabid/224/Article/104517/c-130-hercules.aspx>, September 2003.
- [72] e. C. Wilson, "A guide to developing a sustainability strategy and action plan," Marina House, Marina Place, Hampton Wick, August 2007.
- [73] The Associated Press, "Haiti's displaced from the quake now at 320,050." <http://abcnews.go.com/m/story?id=18962089&sid=76>, 2013.
- [74] M. J. RICH, "Advanced materials applications for vtol aircraft." Sikorsky Aircraft, 1969.
- [75] Giovanni de Briganti, "Agustawestland completes aw609 tiltrotor takeover?." <http://www.defense-aerospace.com/article-view/feature/140692/aw-completes-aw609-tiltrotor-takeover.html>, 2012.
- [76] Singular Aircraft, "A new concept of uav." <http://www.singularaircraft.com>, 2013.
- [77] UNESCO, "World water assessment programme (wwap)." <http://www.unesco.org/new/en/natural-sciences/environment/water/wwap/>.

- [78] GenPro Energy Solutions, "Water purification gp sw 500." <http://www.genproenergy.com/water-purification-ro-gpsw500.html>, 2012.
- [79] E. Torenbeek, "Synthesis of subsonic airplane design." Delft University Press, 1982.
- [80] D. P. Raymer, *Aircraft Design: A Conceptual Approach*. Reston, Virginia: American Institute of Aeronautics and Astronautics, Inc., third edition ed., 1999.
- [81] D. G. L. Rocca, "Ae2101-11 aerospace design and systems engineering elements ii." <https://blackboard.tudelft.nl>, 2011.
- [82] D. G. L. Rocca, "Design of unconventional solutions for stability and control : V-tail and canard (addendum 2)," TU Delft faculty of Aerospace Engineering, May 2013.
- [83] A. E. v. D. Ira H. Abbott, *Theory of Wing Sections*. New York: Dover Publications, Inc., 1959.
- [84] Stanford University, "Tail design and sizing." <http://adg.stanford.edu/aa241/stability/taildesign.html>.
- [85] D. G. L. Rocca, "Systems engineering and aerospace design. weight estimation and iterations in a/c design and aircraft balance.," TU Delft faculty of Aerospace Engineering, April 2013.
- [86] J. John D. Anderson, *Fundamentals of Aerodynamics*. 1221 Avenue of the Americas, New York, NY, 10020: McGraw-Hill Series in Aeronautical and Aerospace Engineering, fifth edition in si units ed., 2011.
- [87] D. M. Somers, *Design and Experimental Results for a Natural-Laminar-Flow Airfoil for General Aviation Applications*. No. NASA Technical Paper 1861, Langley Research Center, Hampton, Virginia: NASA, June 1981.
- [88] FAR, "Part 23?airworthiness standards: Normal, utility, acrobatic, and commuter category airplanes." <http://www.ecfr.gov/cgi-bin/text-idx?c=ecfr&sid=63fd55342c8ac60966e76f8e0cd889a0&rgn=div5&view=text&node=14:1.0.1.3.10&idno=14#14:1.0.1.3.10.2.60.10>.
- [89] EASA, "Certification specifications for normal, utility, aerobatic, and commuter category aeroplanes cs-23." [http://www.easa.europa.eu/agency-measures/docs/agency-decisions/2003/2003-014-RM/decision\\_ED\\_2003\\_14\\_RM.pdf](http://www.easa.europa.eu/agency-measures/docs/agency-decisions/2003/2003-014-RM/decision_ED_2003_14_RM.pdf).
- [90] e. M.J.L. van Tooren, "A/c preliminary sizing (t/w-w/s diagram) part 1 of 2," TU Delft faculty of Aerospace Engineering, May 2010.
- [91] P. A. Diaz, "Fed-ex-cessna-caravan." <http://en.wikipedia.org/wiki/File:Fed-Ex-Cessna-Caravan.jpg>, 2007.
- [92] J. Lehle, "Cessna citation mustang n416cm." [http://en.wikipedia.org/wiki/File:Cessna\\_Citation\\_Mustang\\_N416CM.jpg](http://en.wikipedia.org/wiki/File:Cessna_Citation_Mustang_N416CM.jpg), 2007.
- [93] F. Miller, "Cessna 172." <http://www.fromtheflightdeck.com/Reviews/Cessna172/P3200731.jpg>, 2007.
- [94] D. G. L. Rocca, "Wing design - part 3," TU Delft faculty of Aerospace Engineering, October 2011.
- [95] J. Roskam, *Methods for estimating drag polars of subsonic airplanes*. Lawrence, Kansas: The University of Kansas, 1971.
- [96] A. K. Kundu, *Aircraft Design*. 32 Avenue of the Americas New York NY 10013-2473 USA: Cambridge University Press, 2010.
- [97] M. Voskuil, "Ae2104-11 flight and orbital mechanics." <https://blackboard.tudelft.nl>, 2011.
- [98] G. Puntacana, "Punta cana international airport puj." <http://www.puntacanainternationalairport.com/airport-services/airport-information>, 2014.
- [99] Wikipedia, "Propfan." <http://en.wikipedia.org/wiki/Propfan>.
- [100] IHS Jane's, "Janes all the world's aircraft." Jane's Information Group, 2013.
- [101] H. Cohen and G.F.C. Rogers, "Gasturbine theory." Longman Group Limited, 1996.
- [102] Shoreline Aviation, Inc, "Piston engine aircraft vs. turboprop engine aircraft." <http://www.shorelineaviation.net/news---events/bid/50442/Piston-Engine-Aircraft-vs-Turboprop-Engine-Aircraft>, 2011.
- [103] A.K. Kundu, "Aircraft design." Cambridge Aerospace Series, 2010.
- [104] M. Mahony , "Plane takes first flight on 100% biofuel." <http://www.smartplanet.com/blog/intelligent-energy/plane-takes-first-flight-on-100-biofuel/>, 2010.
- [105] J. Reed, "C-17 is first air force jet to cleared to fly on biofuel." <http://defensetech.org/2011/02/11/c-17-is-first-air-force-jet-to-cleared-to-fly-on-biofuel/>, 2011.
- [106] B.W. McCormick, "Aerodynamics of v/stol flight." <http://www.pdas.com/atmos.html>, 1999.
- [107] Rolls Royce Corporation, "Rr300 lightweight turbine power for a new era of aircraft." [http://www.rolls-royce.com/Images/rr300fs\\_tcm92-6710.pdf](http://www.rolls-royce.com/Images/rr300fs_tcm92-6710.pdf), 2007.
- [108] NOAA, NASA, "U.s. standard atmosphere 1976." <https://docs.google.com/file/d/0B2UKsB0-ZMVgWG9mWEJGM1FacDQ/edit?pli=1>, 1976.
- [109] Rolls Royce Corporation, "Model 250-b17f." [http://www.rolls-royce.com/Images/model250\\_turboprop\\_tcm92-14681.pdf](http://www.rolls-royce.com/Images/model250_turboprop_tcm92-14681.pdf), 2009.
- [110] David F. Rogers, "Propeller efficiency rule of thumb." NASA Technical Memorandum 83458, 2010.
- [111] FAA, "Section 925 - propeller clearance." Federal Aviation Regulations, 1996.
- [112] R.M. Plencner, "Propeller performance and weight predictions." NASA Technical Memorandum 83458, 1983.
- [113] B.W. McCormick, "Aerodynamics of v/stol flight." General Publishing Company, Ltd., 1999.
- [114] T. Megson, *Aircraft Structures for Engineering Students*. Elsevier aerospace engineering series, Elsevier Science, 2007.
- [115] D. K. L. Murty, "Multiaxial loading - tresca and von-mises yield criteria." <http://www4.ncsu.edu/~murty/MAT450/NOTES/plasticity.pdf>, August 2004.
- [116] M. C. Niu, *Airframe stress analysis and sizing*. Michael C.Y. NIU's airframe book series, Hong Kong conmlit press ltd., 1997.
- [117] D. S. Severo, "Algor and the macneal proposed standard set of problems to test finite element accuracy." [http://www.caetebr.com/download/macneal\\_tests.pdf](http://www.caetebr.com/download/macneal_tests.pdf), 2000.
- [118] J. Roskam, "Airplane design. pt. 4. layout design of landing gear and systems." Roskam Aviation and Engineering, 1986.
- [119] T. Delft, *AE2207 Production of Aerospace Systems reader*. Delft University of Technology, 2013.

- [120] S. Gudmundsson, "Proadvice 3: Aileron sizing." <http://www.flightlevelengineering.com>, 2014.
- [121] J.A. Mulder et al., "Flight dynamics: Lecture notes." Delft University of Technology, 2013.
- [122] Michael V. Cook, "Flight dynamics principles: A linear systems approach to aircraft stability and control." Butterworth-Heinemann, Elsevier Ltd., 2013.
- [123] W.H. Harman, "Tcas: A system for preventing midair collisions." [http://www.ll.mit.edu/publications/journal/pdf/vol02\\_no3/2.3.7.TCAS.pdf](http://www.ll.mit.edu/publications/journal/pdf/vol02_no3/2.3.7.TCAS.pdf).
- [124] Inmarsat, "Swift broadband." <http://www.inmarsat.com/service-collection/swiftbroadband/>, 2013.
- [125] Inmarsat, "Haiti earthquake aftermath - first responders rely on bcas." [http://www.inmarsat.com/wp-content/uploads/2013/10/Inmarsat\\_Haiti\\_Earthquake\\_Aftermath.pdf](http://www.inmarsat.com/wp-content/uploads/2013/10/Inmarsat_Haiti_Earthquake_Aftermath.pdf).
- [126] Coment industries, "General antenna installation guidelines." <http://www.cobham.com/media/5045/antennainstallationguide.pdf>.
- [127] James R. Wertz, Wiley J. Larson, "Space mission analysis and design." Microcosm Press, Springer, 2007.
- [128] rfcafe, "Atmospheric absorption / attenuation." <http://www.rfcafe.com/references/electrical/atm-absorption.htm>.
- [129] US Department of Commerce, "United states frequency allocations." <http://www.ntia.doc.gov/files/ntia/publications/2003-allocrft.pdf>, 2003.
- [130] Afar communications, "Fcc rules for unlicensed wireless equipment operating in the ism bands." <http://www.afar.net/tutorials/fcc-rules/>.
- [131] Afar communications, "Rf link budget calculator." <http://www.afar.net/rf-link-budget-calculator/>, 2013.
- [132] PHARAD, "Uhf to c-band uav antenna." <http://www.pharad.com/uhf-to-c-band-uav-antenna.html>.
- [133] L-com, "900 mhz sectorized antenna." <http://www.l-com.com/wireless-antenna-900-mhz-sectorized-antenna-array-with-three-120-degree> Accessed 2014.
- [134] Adobe, "Recommended bit rates for live streaming." [http://www.adobe.com/devnet/adobe-media-server/articles/dynstream\\_live/popup.html](http://www.adobe.com/devnet/adobe-media-server/articles/dynstream_live/popup.html), Accessed 2014.
- [135] Meng Fanliang, "Actuation system design with electrically powered actuators." [https://dspace.lib.cranfield.ac.uk/bitstream/1826/6282/1/Meng\\_Fanliang\\_Thesis\\_2010.pdf](https://dspace.lib.cranfield.ac.uk/bitstream/1826/6282/1/Meng_Fanliang_Thesis_2010.pdf), 2011.
- [136] Kevin Ronald McCullough, "Design and characterization of dual electro-hydrostatic actuator." <http://cmht.mcmaster.ca/docs/McCullough%20-%20Design%20and%20Characterization%20of%20a%20Dual%20Electro-Hydrostatic%20Actuator%20-%202011.pdf>, 2011.
- [137] Dominique van den Bossche, "The a380 flight control electrohydrostatic actuators, achievements and lessons learnt." <http://www.icas-proceedings.net/ICAS2006/PAPERS/048.PDF>, 2006.
- [138] Mead info, "Comparison of gear efficiencies - spur, helical, bevel, worm, hypoid, cycloid." <http://www.meadinfo.org/2008/11/gear-efficiency-spur-helical-bevel-worm.html>, 2012.
- [139] The Engineering Toolbox, "Power gained by fluid from pumps or fans." <http://www.engineeringtoolbox.com/pump-fan-power-d-632.html>, accessed 2014.
- [140] Jane's, "Rolls-royce model 250 (m250)." [https://janes.ihs.com/CustomPages/Janes/DisplayPage.aspx?DocType=Reference&ItemId=+++1306238&Pubabbrev=JAE\\_](https://janes.ihs.com/CustomPages/Janes/DisplayPage.aspx?DocType=Reference&ItemId=+++1306238&Pubabbrev=JAE_), accessed 2014.
- [141] MOOG, "Electrohydrostatic actuators." <http://www.moog.com/products/actuators-servoactuators/actuation-technologies/electrohydrostatic/>, Accessed 2014.
- [142] BOSCH, "Can with flexible data-rate." [http://www.bosch-semiconductors.de/media/pdf\\_1/canliteratur/can\\_fd\\_spec.pdf](http://www.bosch-semiconductors.de/media/pdf_1/canliteratur/can_fd_spec.pdf), 2012.
- [143] microcontroller.com, "Can user benefits." [http://microcontroller.com/learn-embedded/CAN1\\_sie/CAN1big.htm](http://microcontroller.com/learn-embedded/CAN1_sie/CAN1big.htm), 1999.
- [144] Arcelect, "Rs232 data interface." <http://www.arcelect.com/rs232.htm>, Accessed 2014.
- [145] CAN in Automation, "CANopen." [https://www.phoenixcontact.com/assets/downloads\\_ed/global/web\\_dwl\\_technical\\_info/CANopen.pdf](https://www.phoenixcontact.com/assets/downloads_ed/global/web_dwl_technical_info/CANopen.pdf), 1999.
- [146] Various contributors, "Nicad vs lead acid." [http://www.airliners.net/aviation-forums/tech\\_ops/read.main/40156/](http://www.airliners.net/aviation-forums/tech_ops/read.main/40156/), Accessed 2014.
- [147] I. Atair Aerospace, "Onyx ultralight overview." <http://www.atair.com/onyx/ul/>, 2012.
- [148] A. M. C. ltr, "Design for air transport and aidrop materiel," 1968. p. 3-4.
- [149] TutorVista, "Free fall with air resistance." <http://physics.tutorvista.com/motion/free-fall.html>, 2013.
- [150] T. E. Toolbox, "Drag coefficient." <http://www.engineeringtoolbox.com/drag-coefficient-d-627.html>, 2013.
- [151] T. W. Knacke, "Parachute recovery systems design manual," tech. rep., US Navy; Recovery System Division Aerosystems Department, 1991.
- [152] R.C.Maydew and C.W.Peterson, "Design and testing of high-performance parachutes," tech. rep., Institute for Aerospace Research, Government of Canada, 1991.
- [153] R. A. Segars, "The degradation of parachutes," tech. rep., US Army; RESEARCH, DEVELOPMENT AND ENGINEERING CENTER, 1990.
- [154] A. M. C. ltr, "Design for air transport and aidrop materiel," 1968. p. 5-43.
- [155] T. Stathopoulos and C. C. Baniotopoulos, "Wind effects on buildings and design of wind-sensitive structures." International Centre For Mechanical Sciences, 2007.
- [156] A. S. of Civil Engineers, "Asce/sei 7 minimum design loads for buildings and other structures." Structural Engineering Institute.
- [157] T. W. Database, "Spruce pine." <http://www.wood-database.com/lumber-identification/softwoods/spruce-pine/>.
- [158] Wikipedia, "A36 steel." [http://en.wikipedia.org/wiki/A36\\_steel](http://en.wikipedia.org/wiki/A36_steel).

